UNIVERSITY
OF SUSSEX

# Comparison of oscillation parameters measured from $\nu_\mu$ and $\bar{\nu}_\mu$ disappearance in the NOvA experiment

**Diana Patricia Méndez Méndez**

A thesis submitted for the degree of

*Doctor of Philosophy*

University of Sussex

Brighton, England

October 2019

I hereby declare that this thesis has not been and will not be submitted in whole or in part to another University for the award of any other degree.

Diana Patricia Méndez Méndez

*Doctoral Thesis*

**Comparison of oscillation parameters measured from $\nu_\mu$ and $\bar{\nu}_\mu$ disappearance in the NOvA experiment**

Author: Diana Patricia Méndez Méndez

Supervisor: Professor Jeffrey John Hartnell

## Abstract

The NOvA experiment is a neutrino oscillation experiment designed to make precise measurements of $\nu_e$ and $\bar{\nu}_e$ appearance and $\nu_\mu$ and $\bar{\nu}_\mu$ disappearance at long distances and GeV energy scales. Using Fermilab's Neutrinos at the Main Injector (NuMI) beam, the experiment is provided with a highly pure and abundant source of either $\nu_\mu$ or $\bar{\nu}_\mu$. NOvA's $\nu_\mu$ and $\bar{\nu}_\mu$ disappearance measurement is particularly sensitive to constraining the $\sin^2\theta_{23}$ vs. $\Delta m^2_{32}$ space of oscillation parameters. Any difference between $\nu_\mu$ and $\bar{\nu}_\mu$ disappearance in vacuum could be an indication of the combination of Charge Conjugation, Parity and Time reversal (CPT) symmetry not being conserved in the neutrino sector or something else beyond our current understanding of physics.

This thesis presents results from two $\nu_\mu$ and $\bar{\nu}_\mu$ disappearance analyses, one where $\sin^2\theta_{23}$ and $\Delta m^2_{32}$ are assumed to be identical as in the standard three neutrino flavour model, and the other where the oscillation parameters can differ between neutrinos and antineutrinos. In the later, the core analysis of this thesis, the parameters $\sin^2\theta_{23}$ and $\Delta m^2_{32}$ are measured using just the information from neutrinos, and the parameters $\sin^2\bar{\theta}_{23}$ and $\Delta\bar{m}^2_{32}$ are measured using just the information from antineutrinos. The results for the mass splitting are $\Delta m^2_{32} = 2.48^{+0.07}_{-0.09} \times 10^{-3}$ eV$^2$ and $\Delta\bar{m}^2_{32} = 2.55^{+0.12}_{-0.13} \times 10^{-3}$ eV$^2$. The results for the mixing angle are $\sin^2\theta_{23} = 0.51$ in the range $[0.45, 0.57]$, and two degenerate best fits for $\sin^2\bar{\theta}_{23}$ at 0.41 and 0.61 in the ranges $[0.38, 0.45]$ and $[0.57, 0.64]$ allowed at 1 $\sigma$. No significant difference between the oscillation parameters measured using $\nu_\mu$ or $\bar{\nu}_\mu$ was found. The data analysed in this thesis was collected between 2014 and 2019, for which the NOvA detectors collected an exposure of $8.85 \times 10^{20}$ and $12.33 \times 10^{20}$ protons-on-target (POT) for the production of the $\nu_\mu$ and $\bar{\nu}_\mu$ beams respectively. This data is about a quarter and a third of what NOvA is expected to collect in $\nu$ and $\bar{\nu}$ mode, respectively.

*To my mom, always.*

*To myself, because I owe me a lot.*

This is the last push, the last stage of Le Tour. I am currently flying at about 11 km over the Atlantic Ocean and it is now when I decide to start writing this little book. Today is the 3rd of July of 2018.

> *I am not very clever but I am very stubborn and this is the proof.*
>
> — Diani Patito

20th of July 2019. It's been a while. I intended to quit many times. Not that I did not have happy times and awesome experiences during these years, because I actually had more than I would want to admit. But this year had many downs and writing was hard. When people ask if what I do is difficult I always say 'No', and sometimes they assume that I must be very intelligent and that is also not the case. Perseverance and dedication are key, which nourish themselves from the will to achieve. But the thing is that science is only part of the story. The PhD journey can be very emotionally draining, and being a foreigner and still feeling like one after all this time hasn't made it any easier. I yearn the music, the colour and the sunshine. I miss doing everything that defined *me* and expressing myself in my mother tongue. I miss my country and it is scary to think that this is what life will be forever.

I also want to dedicate this thesis to the immigrants like me, who have, are or will be pursuing a PhD or some other kind of goal abroad. On top of the intrinsic demands and stress that the goal brings, we are faced with moving to a whole new place and starting a whole new life. We travel a lot and stop having a home. We leave people behind and work to preserve relationships while trying to build new solid ones. We have to find our way into the unfamiliar culture, eat not as tasty food and suck up the weather. We learn to learn, instantly process stuff and communicate on a daily basis in a language that is not our own. Our voices will always have an accent and there will always be someone willing to give us a hard time. And yet we succeed.

# Preface

The data presented in this thesis was obtained with the NOvA experiment, operated by the Fermi National Accelerator Laboratory (Fermilab) in the United States of America. As of 2019, the NOvA Collaboration is made of more than 200 scientists and engineers from all around the world. The main analysis in this thesis was suggested by my supervisor, Professor Jeffrey John Hartnell, who is the lead of the University of Sussex group within the NOvA collaboration.

Chapter 1 introduces the motivation and subject of the thesis.

Chapter 2 presents a briefing of the discovery of neutrino oscillations, sets up the theory behind of the phenomena and presents an overview of the experimental status of the field.

Chapter 3 describes NOvA's neutrino and antineutrino source and its detectors.

Chapter 4 outlines the analysis methodology, from event reconstruction and selection, to the model fit to data. This has been mostly developed by other members of the collaboration.

The information in the first four chapters was sourced from a variety of external publications, public and internal NOvA documentation as well as complemented with my personal work and experience. Several NOvA PhD theses have also been consulted and cited where most appropriate.

Chapter 5 describes the NOvA disappearance analysis in which $\nu_\mu$ and $\bar{\nu}_\mu$ data is combined in a fit to a standard three neutrino flavour model. The first NOvA disappearance analysis to include antineutrino data and to follow the methodology described in this chapter was performed by the author. The results from that analysis were presented at the XXVIII International Conference on Neutrino Physics and Astrophysics (Neutrino 2018). Chapter 5 presents the distributions of selected and simulated $\nu_\mu$ and $\bar{\nu}_\mu$ spectra at the NOvA near and far detectors that include an additional 78% exposure to the antineutrino

beam. The results of the analysis, referred to as *CPTc*, are presented at the end of the chapter and are based on my own work.

Chapter 6 introduces the core analysis of the thesis. The analysis also combines neutrino and antineutrino data but the value of the neutrino and antineutrino oscillation parameters are allowed to differ in the fit. The initial development of the framework for this type of fit was made by Joseph Lozier and Chris Backhouse. NOvA's sensitivity to the oscillation parameters measured with either neutrinos or antineutrinos are presented. An exaggerated uncertainty on the beam wrong sign component, the $\bar{\nu}_\mu$ in the $\nu_\mu$ beam and vice versa, and its effect in the analysis is evaluated and the results shown. The content in this chapter is based on my own work.

Chapter 7 presents near detector data and simulation with a focus on the wrong sign component, and presents the results from the separate extraction of neutrino and antineutrino oscillation parameters. These results use the same data from Chapter 5 and are my own work.

Chapter 8 summarises and concludes this thesis.

# Contents

# List of Figures

# List of Tables

# Chapter 1

# Introduction

Ever since their detection, neutrinos have proved to be out of the ordinary. The existence of the neutrino was proposed by Wolfgang Pauli in 1930 as the solution to the continuous $\beta$ decay spectrum observed more than a decade before. Given that neutrinos rarely interact with matter, their detection is challenging so it was not until 1956 that the existence of the neutrino was finally confirmed. A lot has been learnt and many more questions have arisen since the discovery. Nowadays it is known that at least three neutrino types or flavours exist, and that they can change back and forth between each other in a phenomenon known as *neutrino oscillations*.

Neutrino oscillations were first proposed by Bruno Pontecorvo in 1957. Later on, the theory was modified and extended by Maki, Nakagawa and Sakata, who suggested transitions between neutrino flavours instead of between neutrinos and antineutrinos. Neutrino oscillations is a phenomenon of quantum interference where the neutrino flavours, $\nu_e, \nu_\mu$ and $\nu_\tau$, are superpositions of the mass eigenstates $\nu_1, \nu_2$ and $\nu_3$. A variety of experiments have been built in the last three decades to measure neutrino oscillations and the first strong evidence of them occurring was provided in 1998 by the Super-Kamiokande detector and by SNO in 2002. Constraints on the neutrino mixing angles ($\theta_{ij}$) and their mass squared differences ($\Delta m^2_{ij}$) have been made since then. However, the octant of the largest mixing angle, the neutrino mass ordering and the value of the charge parity violation phase $\delta_{CP}$ have not yet been determined.

NOvA is a long baseline neutrino oscillation experiment that looks for oscillations with Fermilab's NuMI beam in both $\nu_\mu$ and $\bar{\nu}_\mu$ mode. NOvA observes the $\nu_\mu$ and $\bar{\nu}_\mu$ disappearance and $\nu_e$ and $\bar{\nu}_e$ appearance oscillation channels using a 300 ton Near Detector and a 14 kiloton Far Detector placed 810 km away from each other. NOvA's disappearance search is particularly sensitive to constraining the $\sin^2\theta_{23}$ vs. $\Delta m^2\theta_{32}$ space. In this thesis, NOvA's data is analysed in a model of three neutrino flavours to extract $\nu$ and $\bar{\nu}$ oscillation parameters via the disappearance channel with only the information of the neutrinos or only antineutrinos.

The structure of this thesis is as follows. Chapter 2 presents an historical introduction to the discovery of the neutrinos and of neutrino oscillations. The formalism of neutrino oscillations is presented in the same chapter, with a focus on the elements relevant for the NOvA experiment.

The experimental status of the field is summarised at the end of Chapter 2. The neutrino and antineutrino beam source and the NOvA detectors are described in Chapter 3. The analysis methodology is described in Chapter 4, which starts with the event reconstruction and selection, followed by the estimation of the predictions at the far detector and systematic uncertainties, and concludes with the oscillation model fit to data. Chapter 5 presents the NOvA disappearance analysis which combines neutrino and antineutrino beam data assuming CPT invariance. The results from that analysis are shown at the end of the same chapter. The main analysis developed for this thesis, where independent neutrino and antineutrino oscillations are allowed in the fit to data, is introduced in Chapter 6. In this chapter, the experimental sensitivity and the impact of the antineutrinos in the neutrino beam and vice versa in the extraction of the parameters is assessed. The results from the separate extraction of neutrino and antineutrino parameters are shown in Chapter 7. Chapter 8 presents the conclusions from the work in this thesis.

# Chapter 2

# Neutrino oscillations

This chapter reviews the history and theory of neutrino oscillations and summarizes the experimental status of the field. Section 2.1 presents a brief history of the neutrino discovery and the first evidence of neutrino oscillations. The theory of neutrino oscillations is delineated in § 2.2. The current measurements of neutrino oscillations are summarized in § 2.3.

## 2.1 Discovery of the neutrino and neutrino mixing

The hunt for what is now called the *neutrino* started at the beginning of the 20th century. Three particles were known at that time, namely the proton, electron and photon, which are involved in the radioactive $\alpha, \beta$ and $\gamma$ decays respectively. The $\alpha$ and $\gamma$ decays had been studied and discrete energy lines were observed. The $\beta$ decay was thought to also be a two-body process where an electron was suddenly ejected from an atom leaving a new nuclei ($N \rightarrow N' + e$). Thus it came as a surprise in 1914 when James Chadwick measured a continuous spectrum from the $\beta$ decay of $^{201}$Bi [1]. This observation implied that the principle of energy conservation was violated.

Neutrinos were first postulated by Wolfgang Pauli in 1930 [2] to explain the continuous energy spectrum of the $e$ emitted in the $\beta$ decay, while preserving the principle of energy and angular momentum conservation. Initially called *neutron*, the new particle would exist inside the atomic nuclei and be emitted together with an electron in a three body $\beta$ decay ($N \rightarrow N' + e + \nu$). Besides being electrically neutral, the particle should have a mass of at most $10^{-2}$ times that of the proton and have spin $\frac{1}{2}$. In 1934, Erico Fermi used this particle to complete his theory of beta decay [3] and renamed it *neutrino* to distinguish it from the neutron discovered two years before [4].

### 2.1.1 First detection

Fermi's theory implied that the neutrinos could be detected via the *inverse $\beta$ decay* process $\bar{\nu} + p^+ \rightarrow n + e^+$. Bethe and Pearls [5] estimated that the antineutrino cross-section was $\sigma_{\bar{\nu}} \leq 10^{-44}$ cm$^2$ for a mean neutrino energy of about 2 MeV. This cross-section meant that the

neutrino had a mean free path length of thousands of light years in water thus neutrinos were thought to be impossible to detect. However, Bruno Pontecorvo realised that their detection could be possible. A few neutrino events per day could be detected with a 1 ton mass detector exposed to a flux of 10 $\nu/\mathrm{cm}^2/\mathrm{s}$. This flux could be achieved at about 10 meters from a nuclear reactor core.

The first neutrinos were detected in 1956 by Cowan and Reines [6]. The signature signal of $\bar{\nu}_e$ was identified by the ionization and annihilation of a final-state positron as the prompt signal, and a delayed $\gamma$ ray signal from neutron capture. Their experiment not only confirmed the existence of the neutrino but introduced an experimental technique still used today to detect neutrinos.

In 1962, Lederman, Schwartz and Steinberg showed that the neutrinos produced by the $\pi^{\pm}$ decay and in association with a muon were not the same as the neutrinos observed in the $\beta$ decay [7]. By this time, the difference between $\nu_e$ and $\bar{\nu}_e$ was already established [8]. Thus a second type of neutrino, the $\nu_\mu$, had been discovered. Further ahead, the scheme of the three generations of particles in the Standard Model was pointed out by the discovery of the tau lepton in 1975 [9] and with the discovery of the top quark in 1995 [10, 11]. This suggested the existence of a third neutrino, the $\nu_\tau$, which was finally detected in 2000 by the DONUT experiment [12].

### 2.1.2 Evidence of neutrino oscillations

Neutrino oscillations were first postulated by Bruno Pontecorvo in 1957 [13] as transitions between neutrinos and antineutrinos in analogy to the $K^0/\bar{K}^0$ oscillations. With the discovery of the muon neutrino, Maki, Nakagawa and Sakata [14] suggested that transitions between neutrino flavours could happen if the neutrinos had mass and if the definite neutrino flavour and mass states were related via a linear transformation, similar to a change of basis. Almost forty years later, the idea of *neutrino mixing* or *oscillations* was the only explanation left standing to observed deficits of solar and atmospheric neutrinos.

Between 1960 and 1970, Ray Davis and collaborators [15] conducted experiments to measure the flux of neutrinos from the Sun. The experiment was located underground in the South Dakota Homestake mine and consisted of a tank with chlorine solution capable of neutrino capture ($\nu_e + {}^{37}\mathrm{Cl} \rightarrow {}^{37}\mathrm{Ar} + \mathrm{e}^-$). The atoms of argon were counted and used as a measure of the neutrino flux. The reported experimental rate was about two thirds less than what was expected from the Standard Solar Model (SSM). This large discrepancy, known as the *solar neutrino problem*, was initially believed to be an experimental flaw. More experiments were built a couple of decades later to measure the solar neutrino flux and corroborate or refute the measurements. GALLEX [16] and its succesor GNO [17], and SAGE [18] collected solar neutrino data using a different reaction ($\nu_e + {}^{71}\mathrm{Ga} \rightarrow {}^{71}\mathrm{Ge} + \mathrm{e}^-$) than that used by Davis and had similar results.

In 1998, Super Kamiokande (or Super-K) showed evidence of a difference between the upwards and downwards flux of $\nu_\mu$ produced by cosmic ray interactions in the upper atmosphere [19]. The difference proved the disappearance of muon neutrinos as the neutrinos arriving from above the

detector have no time to oscillate. Super-K also showed a neutrino energy dependance on the zenith angle [20]. This phenomena is understood as neutrinos traversing the earth at different angles travel different distances thus having different oscillation probabilities. The final resolution to the solar neutrino problem was provided by the SNO experiment which measured the $^8$B solar spectrum. The SNO detector was a heavy water Cherenkov detector able to discern $\nu_e$ Charged Current (CC) interactions and also measure Neutral Current (NC) and Elastic Scattering (ES) interactions of the three active neutrino flavours. What was found with SNO is that the total rate of NC events was consistent with the SSM but the $\nu_e$ flux was significantly lower [21].

Neutrino oscillations were confirmed with the Super-K and SNO results and the 2015 Physics Nobel Prize was awarded to Takaaki Kajita and Arthur McDonald, Super-Kamiokande and SNO collaborators respectively, *"for the discovery of neutrino oscillations, which shows that neutrinos have mass"* [22].

## 2.2 Theory

Neutrinos interact in one of the three states of the weak interaction, namely $\nu_e, \nu_\mu$ and $\nu_\tau$. These interactions are mediated by the electrically charged $W^\pm$ boson or by the neutrally charged $Z$ boson. The latter and the former case are CC and NC interaction, respectively. Figure 2.1 shows the Feynman diagrams for the CC and NC neutrino interactions. In the case of CC interactions, the neutrinos and charged leptons only couple in doublets of the same flavour thus a neutrino interacting through the $W^\pm$ will produce a charged lepton of the same flavour, and vice versa. The flavour eigenstates are orthogonal and diagonalize the weak interaction Hamiltonian.

While the flavour of a neutrino can be known upon its creation or interaction, neutrinos propagate through space with a definite eigenstate of mass, $\nu_1, \nu_2$ or $\nu_3$. The set of mass eigenstates are a basis for the free particle Hamiltonian. The non-zero probability of a neutrino being produced in one flavour and detected as another is a quantum phenomena known as *neutrino oscillations* and resides on the relationship between the neutrino states of flavour and mass.

Given the flavour and the mass bases, the flavour eigenstates $|\nu_\alpha\rangle$ can be expressed as a linear combination of the mass eigenstates $|\nu_k\rangle$ via a unitary matrix $U$, such that

$$|\nu_\alpha\rangle = \sum_k U^*_{\alpha k} |\nu_k\rangle \qquad (\alpha = e, \mu, \tau)\,, \tag{2.1}$$

where $U$ is the leptonic mixing matrix commonly known as the PMNS matrix [13, 14]. The $U_{\alpha k}$ element of this matrix describes the coupling strength between the flavour eigenstate $\alpha$ and the mass eigenstate $k$. The PMNS matrix would be the identity matrix if the neutrinos did not oscillate.

### 2.2.1 Oscillations in vacuum

The basics of neutrino oscillations are delineated in this section and follow the derivation in [23, 24]. The oscillation phenomena is considered to occur in vacuum, and the mass eigenstates are treated


**(a)** Charged current interaction **(b)** Neutral current interaction

**Figure 2.1:** Diagrams of the neutrino weak interactions. The Charged Current (CC) (left) and Neutral Current (NC) (right) interactions are mediated by the $W^{\pm}$ and the $Z^0$ boson, respectively.

as well localized plane waves in space and time.

Consider a neutrino in a definite state of flavour $\alpha$ at a time $t_0$, which is a superposition of mass eigenstates with three-momentum $\mathbf{p}$

$$|\nu_\alpha(t_0)\rangle = \sum_i U^*_{\alpha i}|\nu_i(\mathbf{p})\rangle. \tag{2.2}$$

As the mass eigenstates are eigestates of the free Hamiltonian,

$$\hat{H}|\nu_i(\mathbf{p})\rangle = E_i(\mathbf{p})|\nu_i(\mathbf{p})\rangle, \quad E_i(\mathbf{p})^2 = \mathbf{p}^2 + m_i^2. \tag{2.3}$$

Thus, the neutrino state at time $t \neq t_0$ is determined by the time evolution of the mass eigenstates,

$$|\nu_\alpha(t)\rangle = e^{-i\hat{H}(t-t_0)}|\nu_\alpha(t_0)\rangle = \sum_i U^*_{\alpha i} e^{-iE_i(\mathbf{p})(t-t_0)}|\nu_i(\mathbf{p})\rangle, \tag{2.4}$$

where it has been used that the time evolution operator from $t_0 \to t$ is given by $e^{-i\hat{H}(t-t_0)}$. Therefore, the probability that at time $t$ the neutrino originally in flavour state $\alpha$ is in a state of flavour $\beta$ is

$$\begin{aligned} P(\nu_\alpha \to \nu_\beta)(t) &= \left|\langle\nu_\beta|\nu_\alpha(t)\rangle\right|^2 \\ &= \left|\sum_i U_{\beta i} U^*_{\alpha i} e^{-iE_i(\mathbf{p})(t-t_0)}\right|^2, \end{aligned} \tag{2.5}$$

where the orthogonality relation $\langle\nu_i(\mathbf{p})|\nu_j(\mathbf{p})\rangle = \delta_{ij}$ has been implemented. Using the fact that the neutrinos are ultra-relativistic, $L \simeq (t - t_0)$ and

$$E_i(\mathbf{p}) - E_j(\mathbf{p}) \simeq \frac{1}{2}\frac{m_i^2 - m_j^2}{|\mathbf{p}|} + \mathcal{O}(m^4). \tag{2.6}$$

Defining

$$\Delta m^2_{ij} \equiv m_i^2 - m_j^2, \tag{2.7}$$

the probability can be expressed as

$$P(\nu_\alpha \to \nu_\beta) = \sum_{i,j} U^*_{\alpha i} U_{\beta i} U_{\alpha j} U^*_{\beta j} e^{-i\frac{\Delta m^2_{ji} L}{2|\mathbf{p}|}}. \tag{2.8}$$

This last expression can be manipulated using the properties of unitary matrices and further simplified with the use of two other facts: the complex phases where $i = j$ vanish as $\Delta m^2_{ii} = 0$, and terms where $i < j$ are complex conjugates of those where $i > j$. Defining $W^{ij}_{\alpha\beta} \equiv [U_{\alpha i} U^*_{\beta i} U^*_{\alpha j} U_{\beta j}]$ and approximating $|\vec{p}| \simeq E_\nu$, Equation 2.8 becomes

$$\begin{aligned} P(\overset{(-)}{\nu}_\alpha \to \overset{(-)}{\nu}_\beta) = \delta_{\alpha\beta} \quad & -4 \sum_{j>i} \mathrm{Re}[W^{ij}_{\alpha\beta}] \sin^2\left(\frac{\Delta m^2_{ij} L}{4E_\nu}\right) \\ & \mp 2 \sum_{j>i} \mathrm{Im}[W^{ij}_{\alpha\beta}] \sin\left(\frac{\Delta m^2_{ij} L}{2E_\nu}\right), \end{aligned} \tag{2.9}$$

where the plus(minus) sign in the last term of the equation applies to $\nu(\bar{\nu})$. This expression shows that the probability of neutrinos transitioning between flavours is not only governed by the elements of the $U$ matrix, but also by the squared mass differences $\Delta m^2_{ij}$ thus at least one neutrino mass should be non-zero for the transitions to occur. Equation 2.9 also shows that the probability is a function of $L/E$ and so it *oscillates*, hence the name of *neutrino oscillations*. In Equation 2.9, the case where $\alpha \neq \beta$ is called *appearance probability* of $\nu_\beta$, as the flavour state at time $t$ is different from that of the initial state. If $\alpha = \beta$, the equation is referred to as *disappearance* or *survival probability*. In the disappearance case, the imaginary piece drops out and the probability equation can be simplified further

$$P(\overset{(-)}{\nu}_\alpha \to \overset{(-)}{\nu}_\beta) = \delta_{\alpha\beta} \quad -4 \sum_{j>i} |U_{\alpha i}|^2 |U_{\alpha j}|^2 \sin^2\left(\frac{\Delta m^2_{ij} L}{4E_\nu}\right) \tag{2.10}$$

Given the combined influence of the travelled distance $L$, neutrino energy $E$ and mass splittings, it is often the case that the oscillation probabilities are largely determined by a dominant term of the $U$ matrix. The two neutrino flavour approximation can be instructive in this case, as the oscillations are determined by only one mixing angle and one mass squared difference.

### Two neutrino flavour approximation

In a two neutrino flavour model, the mixing matrix is a real two dimensional rotation matrix

$$U = \begin{pmatrix} \cos\theta & \sin\theta \\ -\sin\theta & \cos\theta \end{pmatrix}. \tag{2.11}$$

Restoring the factors of $\hbar$ and $c$ in Equation 2.10 and applying the appropriate unit conversions, the oscillation probabilities are given by

$$P(\nu_\alpha \to \nu_\beta) = \sin^2 2\theta \, \sin^2\left(1.27 \frac{\Delta m^2(\mathrm{eV}^2)\,\mathrm{L(km)}}{E_\nu(\mathrm{GeV})}\right), \quad \alpha \neq \beta. \tag{2.12}$$

$$P(\nu_\alpha \to \nu_\alpha) = 1 - P(\nu_\alpha \to \nu_\beta). \tag{2.13}$$

The equations above show the sinusoidal form of the probabilities, where the mixing angle $\theta$ and the mass squared difference $\Delta m^2$ determine the amplitude and the period of the oscillations respectively.

Neutrino oscillations would ideally be studied with a varying baseline and with a monoenergetic particle source. In practice, the mass of the neutrino detectors are of the order of tons so the baseline is kept fixed and the oscillations are studied as a function of neutrino energy. Figure 2.2 shows the oscillation probability curves from a two neutrino model as a function of baseline and energy. Subfigure 2.2a shows the appearance probability as a function of baseline $L$, where the oscillation period $L_{\text{osc}}$ is defined by

$$L_{\text{osc}}\ (\text{km}) = \pi \frac{\text{E}_\nu(\text{GeV})}{1.27\Delta\text{m}^2(\text{eV}^2)}. \tag{2.14}$$

Oscillation experiments can be optimized so $E/L$ is of the same order as $\Delta m^2$, thus the position of the first oscillation maxima, from left to right in Subfigure 2.2b, can provide the information about the mass splitting as

$$E_{\text{max}}(\text{GeV}) = 1.27 \frac{\Delta\text{m}^2(\text{eV}^2)\text{L(km)}}{\pi/2}. \tag{2.15}$$

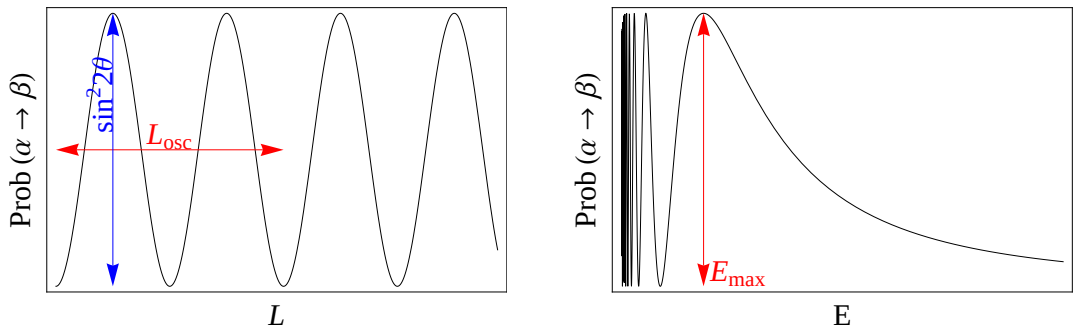


**(a)** Appearance probability as a function of baseline $L$, at a fixed neutrino energy.

**(b)** Appearance probability as a function of neutrino energy $E$, at a fixed baseline.

**Figure 2.2:** Neutrino oscillation probability in the two neutrino flavour approximation [25]. The appearance probability curves are shown as a function of baseline $L$ and energy $E$.

### Three neutrino model

In the Standard Model of three neutrino flavours, the PMNS matrix $U$ is a $3 \times 3$ matrix which describes the coupling strength between the flavour and mass eigenstates. Explicitly expanding Equation 2.1,

$$\begin{pmatrix} \nu_e \\ \nu_\mu \\ \nu_\tau \end{pmatrix} = \begin{pmatrix} U_{e1} & U_{e2} & U_{e3} \\ U_{\mu 1} & U_{\mu 2} & U_{\mu 3} \\ U_{\tau 1} & U_{\tau 2} & U_{\tau 3} \end{pmatrix} \begin{pmatrix} \nu_1 \\ \nu_2 \\ \nu_3 \end{pmatrix}. \tag{2.16}$$

$U$ is a unitary matrix and it would be equivalent to the identity matrix if a specific flavour eigenstate $\nu_\alpha$ corresponded to a specific mass eigenstate $\nu_i$. However, the flavour eigenstates are a superposition of the mass eigenstates and vice versa. In the three neutrino model, $U$ is parametrized in terms of three real mixing angles $\theta_{ij}$, one complex CP violating phase $\delta$ and two Majorana phases $\alpha_{ij}$, such that $U$ can be expanded as [26]

$$\begin{aligned} U &= \begin{pmatrix} 1 & 0 & 0 \\ 0 & c_{23} & s_{23} \\ 0 & -s_{23} & c_{23} \end{pmatrix} \begin{pmatrix} c_{13} & 0 & s_{13}e^{-i\delta_{CP}} \\ 0 & 1 & 0 \\ -s_{13}e^{i\delta_{CP}} & 0 & c_{13} \end{pmatrix} \begin{pmatrix} c_{12} & s_{12} & 0 \\ -s_{12} & c_{12} & 0 \\ 0 & 0 & 1 \end{pmatrix} \begin{pmatrix} 1 & 0 & 0 \\ 0 & e^{i\frac{\alpha_{21}}{2}} & 0 \\ 0 & 0 & e^{i\frac{\alpha_{31}}{2}} \end{pmatrix} \\ &= \begin{pmatrix} c_{12}c_{13} & s_{12}c_{13} & s_{13}e^{-i\delta_{CP}} \\ -s_{12}c_{23} - c_{12}s_{23}s_{13}e^{i\delta_{CP}} & c_{12}c_{23} - s_{12}s_{23}s_{13}e^{i\delta_{CP}} & s_{23}c_{13} \\ s_{12}s_{23} - c_{12}c_{23}s_{13}e^{i\delta_{CP}} & -c_{12}s_{23} - s_{12}c_{23}s_{13}e^{i\delta_{CP}} & c_{23}c_{13} \end{pmatrix} \times \mathrm{diag}\left(1, e^{i\frac{\alpha_{21}}{2}}, e^{i\frac{\alpha_{31}}{2}}\right), \end{aligned} \tag{2.17}$$

where $s_{ij} \equiv \sin\theta_{ij}$ and $c_{ij} \equiv \cos\theta_{ij}$. Because of the diagonal nature of the last sub-matrix, the Majorana phases are not observable in neutrino oscillations and can be ignored.

Defining $\Delta_{ij} \equiv \Delta m^2_{ij} L/4E$, the relevant disappearance and appearance oscillation probabilities for NOvA can be expressed as

$$\begin{aligned} P(\nu_\mu \to \nu_\mu) &\approx 1 - 4|U_{\mu 3}|^2(|U_{\mu 1}|^2 + |U_{\mu 2}|^2)\sin^2\Delta_{32} \\ &\approx 1 - 4s^2_{23}(1 - s^2_{13})(c^2_{23} + s^2_{23}s^2_{13})\sin^2\Delta_{32} \\ &\approx 1 - 4s^2_{23}c^2_{23}\sin^2\Delta_{32} + 4\mathrm{s}^2_{23}\mathrm{s}^2_{13}(\mathrm{c}^2_{23} - \mathrm{s}^2_{23})\sin^2\Delta_{32} \\ &= 1 - \sin^2 2\theta_{23}\sin^2\Delta_{32} + 4\sin^2\theta_{23}\sin^2\theta_{13}\cos^2 2\theta_{23}\sin^2\Delta_{32}, \end{aligned} \tag{2.18}$$

$$P(\overset{(-)}{\nu}_\mu \to \overset{(-)}{\nu}_e) = P_{atm} + P_{sol} + 2\sqrt{P_{atm}P_{sol}}(\cos\delta\cos\Delta_{32} \overset{(+)}{-} \sin\delta\sin\Delta_{32}), \tag{2.19}$$

where

$$\sqrt{P_{atm}} \equiv \sin\theta_{23}\sin 2\theta_{13}\sin\Delta_{32} \tag{2.20}$$

$$\sqrt{P_{sol}} \equiv \cos\theta_{23}\sin 2\theta_{12}\sin\Delta_{21} \tag{2.21}$$

and higher order terms of $s^2_{13}$ have been dropped given the known small value of this parameter. The approximation $|\Delta m^2_{32}| \approx |\Delta m^2_{31}|$, referred to as the *one mass scale dominance* (OMSD), has also been made as it has been experimentally shown that $|\Delta m^2_{21}|$ is small with respect to $|\Delta m^2_{32}|$ and $|\Delta m^2_{31}|$. Furthermore, $\Delta m^2_{31} = \Delta m^2_{32} + \Delta m^2_{21}$ which means that there are only two independent mass splittings. Thus, the oscillation probabilities are determined by the following six parameters

- 3 mixing angles: $\theta_{12}, \theta_{13}, \theta_{23}$

- 2 mass splittings: $\Delta m^2_{21}, \Delta m^2_{32}$
- 1 CP phase $\delta_{CP}$

The CP phase represents the amount of CP violation, where the CP conserving values are $\delta_{CP} = 0, \pi$. The mixing angles define the amplitude of the oscillation. The mass squared differences define the frequency of the oscillation and the energy position of the oscillation maxima. For historic and experimental reasons, $\Delta m^2_{21}$ and $\theta_{12}$ are known as the solar parameters, $\Delta m^2_{32}$ and $\theta_{23}$ are referred to as the atmospheric parameters and $\theta_{13}$ is the reactor neutrino mixing angle. The case where $\Delta m^2_{32} > 0$ ($\Delta m^2_{32} < 0$) is referred to as *normal hierarchy (inverted hierarchy)* and would be the consequence of $\nu_3$ being the heaviest (lightest) of the mass eigenstates. Figure 2.3 shows a graphic representation of the elements of $U$, ignoring $\delta_{CP}$, and the neutrino mass ordering scenarios.

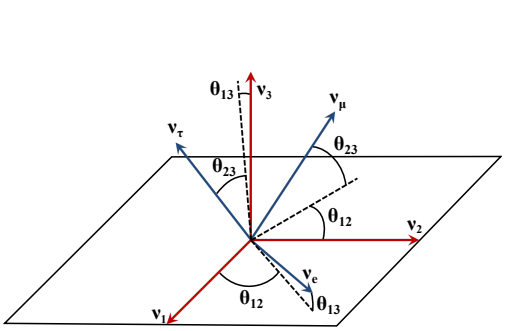


**(a)** Representation of the neutrino mixing matrix elements between the flavour eigenstates $(\nu_\mu, \nu_e, \nu_\tau)$ and mass eigenstates $(\nu_1, \nu_2, \nu_3)$

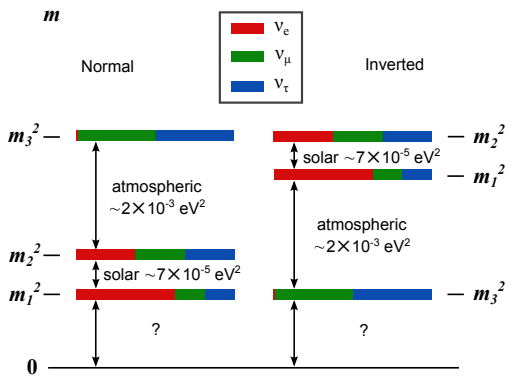


**(b)** Neutrino mass hierarchy schemes, where the normal (inverted) mass hierarchy scenario is characterized by $\Delta m^2_{32} > 0$ ($\Delta m^2_{32} < 0$)

**Figure 2.3:** Graphic representation of neutrino mixing in the three neutrino flavour model.

It is important to note that the $\nu_\mu$ disappearance probability is symmetric with respect to $\theta_{23} = \pi/4$, or degenerate with respect to the interchange $\theta_{23} \leftrightarrow \pi/2 - \theta$ [26]. This is clearly seen in Equation 2.13 from the two flavour approximation. Thus, at first order and in the vacuum approximation, the $\nu_\mu$ disappearance channel alone is not sensitive to determining the octant of $\theta_{23}$.

Mixing between the muon and tauon neutrino flavours would be maximal if $\sin^2\theta_{23} = 0.5$, thus $\cos^2\theta_{23} \simeq 0.5$. In this case, $U_{\mu 3} = U_{\tau 3} = \frac{1}{2}c_{13}$. These two elements of the PMNS matrix define the amount of $\nu_\mu$ and $\nu_\tau$ contained in $\nu_3$. The case where $\theta_{23} = \pi/4$ is known as *maximal mixing* and means that the third mass eigenstate has equal parts of $\nu_\mu$ and $\nu_\tau$ which could potentially point to a fundamental symmetry in the lepton sector. If $\theta_{23} > \pi/4$ ($\theta_{23} < \pi/4$), the amount of $\nu_\mu$ is larger (smaller) than the amount of $\nu_\tau$ in $\nu_3$ and the value of $\theta_{23}$ is said to be in the *upper (lower) octant*.

### 2.2.2 Matter effect

The expressions of the oscillation probabilities presented in § 2.2.1 assume neutrino oscillations in vacuum. However, even though very weakly, neutrinos interact with particles and their interactions can be affected by high density matter in a way that is not the same for all the flavours. Because matter is made of electrons and not positrons (nor muons or tauons), CC coherent forward scattering of neutrinos off electrons in matter is only available to electron flavour neutrinos and the $\nu_e$ and $\bar{\nu}_e$ interaction amplitudes are different. Figure 2.4 illustrates those interactions. This *matter effect*, is known as the MSW effect [27, 28] and affects the oscillation probabilities. The electrons in matter contribute with a potential term

$$V_e = \pm\sqrt{2} G_F N_e, \tag{2.22}$$

where $G_F$ is Fermi's constant and $N_e$ is the electron density in matter. The positive (negative) sign of $V_e$ corresponds to the neutrinos (antineutrinos). This potential adds an additional term to the Schrodinger equation thus affects the time evolution of the flavour eigenstates and the oscillation probabilities differ from those in vacuum. Considering the two neutrino approximation case, the equations of motion in the presence of matter are written as [24, 29]

$$\begin{aligned} i\frac{d}{dt}\begin{pmatrix} \nu_e \\ \nu_\mu \end{pmatrix} &= \left[ U \begin{pmatrix} \frac{m_1^2}{2E} & 0 \\ 0 & \frac{m_2^2}{2E} \end{pmatrix} U^\dagger + \begin{pmatrix} V_e & 0 \\ 0 & 0 \end{pmatrix} \right] \begin{pmatrix} \nu_e \\ \nu_\mu \end{pmatrix} \\ &= \frac{1}{4E} \begin{pmatrix} -\Delta m^2 \cos 2\theta \pm 4EV_e & \Delta m^2 \sin 2\theta \\ \Delta m^2 \sin 2\theta & \Delta m^2 \cos 2\theta \end{pmatrix} \begin{pmatrix} \nu_e \\ \nu_\mu \end{pmatrix}. \end{aligned} \tag{2.23}$$

The last $2 \times 2$ matrix in this equation is the flavour basis Hamiltonian $H$ in matter. This can be diagonalized according to $H_M = U_M^\dagger H U_M$, where $H_M$ is the effective Hamiltonian in the mass basis and $U_M$ is the effective mixing matrix. Explicitly,

$$H_M = \frac{1}{2} \begin{pmatrix} -\frac{\Delta m_M^2}{2E} & 0 \\ 0 & \frac{\Delta m_M^2}{2E} \end{pmatrix} \tag{2.24}$$

$$U_M = \begin{pmatrix} \cos\theta_M & \sin\theta_M \\ -\sin\theta_M & \cos\theta_M \end{pmatrix}, \tag{2.25}$$

where the effective mixing angle $\theta_M$ and mass splitting $\Delta m_M^2$ in matter are given by

$$\sin 2\theta_M \equiv \frac{\sin 2\theta}{A_M} \tag{2.26}$$

$$\Delta m_M^2 \equiv \Delta m_{21}^2 A_M \tag{2.27}$$

$$A_M \equiv \sqrt{\left( \cos 2\theta \mp \frac{2EV_e}{\Delta m_{21}^2} \right)^2 + \sin^2 2\theta}. \tag{2.28}$$

In these expressions, $\Delta m^2_{21}$ and $\theta$ denote the mass splitting and the mixing angle in vacuum, and the negative (positive) sign in $A_M$ corresponds to the neutrinos (antineutrinos). The solution to the equations of motion in vacuum is recovered as the electron density approaches zero, as the additional potential $V_e$ is directly proportional to such density. Therefore, for experiments with low energy neutrinos or low matter density, the oscillation probabilities in vacuum are a good approximation.

The matter effect in the case of three neutrino flavor oscillations is considerably more complicated. However, the conclusion is the same. The effective neutrino mass changes and the oscillation probabilities are different between neutrinos and antineutrinos. In the three neutrino case, the mixing angle $\theta_{13}$ is replaced in the oscillation probabilities by [30]:

$$\sin^2 2\theta_M = \frac{\sin^2 2\theta_{13}}{\sin^2 2\theta_{13} + (A - \cos 2\theta_{13})^2}. \tag{2.29}$$

where $A$, the *magnitude* of the matter effect, is defined as

$$A \equiv \pm 2\sqrt{2} G_F N_e E_\nu / \Delta m^2_{31}, \tag{2.30}$$

and the top (bottom) sign refers to neutrinos (antineutrinos). How the interactions in matter affect the appearance and disappearance channels for the specific experimental parameters of NOvA are further discussed in § 5.4.2.

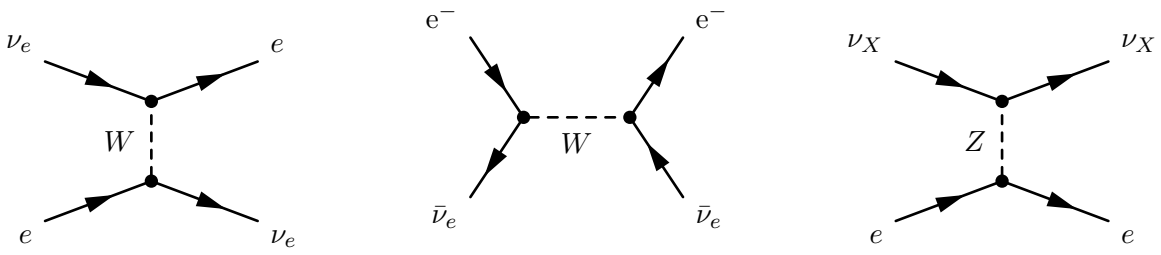


**(a)** Charge current scattering of an electron neutrino on an electron.

**(b)** Charge current scattering of an electron antineutrino on a electron.

**(c)** Neutral current scattering of a neutrino on an electron.

**Figure 2.4:** Diagrams of charge current (left and middle) and neutral current (right) coherent scattering of neutrinos on electrons.

## 2.3 Experimental status

Neutrino oscillation experiments set constraints on the values of the six parameters that govern the neutrino mixing, namely the mixing angles $(\theta_{12}, \theta_{13}, \theta_{23})$, mass splittings $(\Delta m^2_{21}, \Delta m^2_{32} \simeq \Delta m^2_{31})$ and $\delta_{CP}$, and the neutrino mass hierarchy. Significant progress has been made in the field but many questions remain unanswered. Measurements with limited sensitivity to the CP violating

phase $\delta_{CP}$ have been made but its actual value remains unknown. The absolute values of the two mass splittings have been measured and the positive sign of $\Delta m^2_{21}$ has been determined, but the neutrino mass ordering has not yet been resolved. Current measurements of the $\sin^2\theta_{23}$ favour values of about 0.5 but the octant of $\theta_{23}$ is yet unknown.

The oscillation parameters are constrained using natural neutrino sources, such as the sun and atmosphere, or artificial sources, such as nuclear reactors and accelerators. Each source produces neutrinos of different flavours and energies, which make experiments sensitive to measuring a particular set of parameters. A summary of the results from global fits to experimentally measured values of the neutrino oscillation parameters is give in Table 2.1.

This section presents a summary of the measurements of the neutrino mixing parameters with a focus on the currently running experiments that have set the constraints. Section 2.3.5 is dedicated to NOvA's latest public oscillation results, which includes the first set of antineutrino beam data. The separated measurements of $\nu_\mu$ and $\bar{\nu}_\mu$ disappearance by the MINOS and T2K experiments are presented in section § 2.3.6.

### 2.3.1 Measurement of $\theta_{13}$

Nuclear facilities provide an abundant $\bar{\nu}_e$ flux and reactor experiments have measured the value of $\theta_{13}$ via the $\bar{\nu}_e$ disappearance channel. Electron antineutrinos are created from the nuclear fission of elements like $^{235}$U, $^{238}$U, $^{239}$Pu and $^{241}$Pu, which are commonly used in commercial power reactors. Even today, these neutrino experiments follow the inverse $\beta$ decay detection strategy of the original Reines and Cowan experiment.

The reactor neutrino mixing angle was believed to be equal to zero or very close to that value. Three experiments were proposed around 2006 to measure $\theta_{13}$ at distances of about 1-2 km. In late 2011, the Double-Chooz experiment [32] observed an antineutrino flux deficit which was explained by $\theta_{13}$ being different to zero. The Daya Bay experiment soon after reported a 5 $\sigma$ evidence of $\theta_{13}$ being non-zero [33], which was later on confirmed by the RENO experiment at 4.9 $\sigma$ [34]. These results are one of the particle physics milestones. Since then, increased statistics and experimental improvements have made $\theta_{13}$ the most precisely known neutrino mixing angle despite it being the smallest.

**Daya Bay** consists of 8 identically-designed antineutrino detectors arranged in two near detector halls (EH1 and EH2), each containing two detectors, and one far detector hall (EH3), which houses four detectors. The detectors measure the antineutrino flux from six reactor cores of one of the most powerful nuclear complexes in the world. The EH1(EH2) is located at about 365 m(505 m) from two(four) of the cores. The average baseline to the EH3 over all the cores is about 1663 m. The scintillator technology is used in all detectors with a gadolinium-doped liquid scintillator. Daya Bay has recently published an updated fit to its data including 1958 days of operation and set up constraints in the $\sin^2 2\theta_{13}$ vs. $\Delta m^2_{32}$ space [35]. The results were obtained with the exact total disappearance probability equation, and with an approximation to

| | | Normal Ordering (best fit) | | Inverted Ordering ($\Delta\chi^2 = 4.7$) | |
|---|---|---|---|---|---|
| | | bfp $\pm 1\sigma$ | $3\sigma$ range | bfp $\pm 1\sigma$ | $3\sigma$ range |
| without SK-atm | $\sin^2\theta_{12}$ | $0.310^{+0.013}_{-0.012}$ | $0.275 \to 0.350$ | $0.310^{+0.013}_{-0.012}$ | $0.275 \to 0.350$ |
| | $\theta_{12}/^\circ$ | $33.82^{+0.78}_{-0.76}$ | $31.61 \to 36.27$ | $33.82^{+0.78}_{-0.76}$ | $31.61 \to 36.27$ |
| | $\sin^2\theta_{23}$ | $0.580^{+0.017}_{-0.021}$ | $0.418 \to 0.627$ | $0.584^{+0.016}_{-0.020}$ | $0.423 \to 0.629$ |
| | $\theta_{23}/^\circ$ | $49.6^{+1.0}_{-1.2}$ | $40.3 \to 52.4$ | $49.8^{+1.0}_{-1.1}$ | $40.6 \to 52.5$ |
| | $\sin^2\theta_{13}$ | $0.02241^{+0.00065}_{-0.00065}$ | $0.02045 \to 0.02439$ | $0.02264^{+0.00066}_{-0.00066}$ | $0.02068 \to 0.02463$ |
| | $\theta_{13}/^\circ$ | $8.61^{+0.13}_{-0.13}$ | $8.22 \to 8.99$ | $8.65^{+0.13}_{-0.13}$ | $8.27 \to 9.03$ |
| | $\delta_{CP}/^\circ$ | $215^{+40}_{-29}$ | $125 \to 392$ | $284^{+27}_{-29}$ | $196 \to 360$ |
| | $\frac{\Delta m^2_{21}}{10^{-5}\ \mathrm{eV}^2}$ | $7.39^{+0.21}_{-0.20}$ | $6.79 \to 8.01$ | $7.39^{+0.21}_{-0.20}$ | $6.79 \to 8.01$ |
| | $\frac{\Delta m^2_{3\ell}}{10^{-3}\ \mathrm{eV}^2}$ | $+2.525^{+0.033}_{-0.032}$ | $+2.427 \to +2.625$ | $-2.512^{+0.034}_{-0.032}$ | $-2.611 \to -2.412$ |
| | | Normal Ordering (best fit) | | Inverted Ordering ($\Delta\chi^2 = 9.3$) | |
| | | bfp $\pm 1\sigma$ | $3\sigma$ range | bfp $\pm 1\sigma$ | $3\sigma$ range |
| with SK-atm | $\sin^2\theta_{12}$ | $0.310^{+0.013}_{-0.012}$ | $0.275 \to 0.350$ | $0.310^{+0.013}_{-0.012}$ | $0.275 \to 0.350$ |
| | $\theta_{12}/^\circ$ | $33.82^{+0.78}_{-0.76}$ | $31.61 \to 36.27$ | $33.82^{+0.78}_{-0.75}$ | $31.62 \to 36.27$ |
| | $\sin^2\theta_{23}$ | $0.582^{+0.015}_{-0.019}$ | $0.428 \to 0.624$ | $0.582^{+0.015}_{-0.018}$ | $0.433 \to 0.623$ |
| | $\theta_{23}/^\circ$ | $49.7^{+0.9}_{-1.1}$ | $40.9 \to 52.2$ | $49.7^{+0.9}_{-1.0}$ | $41.2 \to 52.1$ |
| | $\sin^2\theta_{13}$ | $0.02240^{+0.00065}_{-0.00066}$ | $0.02044 \to 0.02437$ | $0.02263^{+0.00065}_{-0.00066}$ | $0.02067 \to 0.02461$ |
| | $\theta_{13}/^\circ$ | $8.61^{+0.12}_{-0.13}$ | $8.22 \to 8.98$ | $8.65^{+0.12}_{-0.13}$ | $8.27 \to 9.03$ |
| | $\delta_{CP}/^\circ$ | $217^{+40}_{-28}$ | $135 \to 366$ | $280^{+25}_{-28}$ | $196 \to 351$ |
| | $\frac{\Delta m^2_{21}}{10^{-5}\ \mathrm{eV}^2}$ | $7.39^{+0.21}_{-0.20}$ | $6.79 \to 8.01$ | $7.39^{+0.21}_{-0.20}$ | $6.79 \to 8.01$ |
| | $\frac{\Delta m^2_{3\ell}}{10^{-3}\ \mathrm{eV}^2}$ | $+2.525^{+0.033}_{-0.031}$ | $+2.431 \to +2.622$ | $-2.512^{+0.034}_{-0.031}$ | $-2.606 \to -2.413$ |

**Table 2.1:** Three-flavour oscillation parameters from fits to global data reported in [31]. The best fit values under the normal and inverted hierarchy are shown in the left and right columns, respectively. The upper (lower) table shows the results without (with) the constraints set by the SuperKamiokande atmospheric data.

the $\bar{\nu}_e$ disappearance expression for the effective neutrino mass squared difference $\Delta m^2_{ee}$ [1]. In these cases, the measurement of $\sin^2 2\theta_{13}$ is independent of the neutrino mass ordering. Figure 2.5 shows Daya Bay's latest result, which prefers a value of $\sin^2 2\theta_{13} = 0.085 \pm 0.003$ and $\Delta m^2_{ee} = 2.522^{0.068}_{0.070} \times 10^{-3}$ eV$^2$. Complementary best fits were found at $\Delta m^2_{32} = 2.471^{0.068}_{0.070} \times 10^{-3}$ eV$^2$ and $\Delta m^2_{32} = -2.575^{0.068}_{0.070} \times 10^{-3}$ eV$^2$ for normal and inverted mass ordering respectively. The experiment will continue taking data until 2020 when it is expected to achieve a 3% precision measurement of $\sin^2 2\theta_{13}$.

The Reactor Experiment for Neutrino Oscillations (RENO) in South Korea, and the Double Chooz experiment in France, also currently measure antineutrino fluxes from nuclear reactors for which they also use Gadolinium-doped liquid scintillator detectors. Both collaborations presented updated results at the Neutrino 2018 Conference [37]. **RENO** is located in the vicinity of the Hanbit Nuclear Power Plant and uses a near detector placed at 294 m from the center of six reactor cores, and a far detector at 1383 m. RENO's latest results [38] with data collected between August 2011 and and February 2018 have a best fit at $\sin^2 2\theta_{13} = 0.0896 \pm 0.0048(\text{stat}) \pm 0.0047(\text{syst})$ and $\Delta m^2_{ee} = 2.68 \pm 0.012(\text{stat}) \pm 0.07(\text{syst}) \times 10^{-3}$ eV$^2$. **Double Chooz** operates using the antineutrino flux of two thermal power reactors of the Chooz Nuclear Power Plant and has the shortest of the reactor baselines with the far detector placed at 1050 m from the reactor cores. Double-Chooz last analysis prefers a best fit at $\sin^2 2\theta_{13} = 0.105 \pm 0.014$ [39].

Long-baseline oscillation experiments, such as MINOS, T2K and NOvA, use the knowledge of $\theta_{13}$ as a constraint in their analyses due to the precision of the measurements provided by the reactor experiments. However, with much less sensitivity, they have the potential to determine the value of $\theta_{13}$. T2K's last explicitly quoted results for normal hierarchy are $\sin^2\theta_{13} = 0.0248$ [40] and $\sin^2\theta_{13} = 0.0219^{0.0208}_{0.0233}$ [41] with a neutrino only and with neutrino plus antineutrino data respectively.

### 2.3.2 Measurement of $\theta_{12}$ and $\Delta m^2_{21}$

Oscillation experiments such as Super-Kamiokande, SNO and Borexino, detect neutrinos originating from nuclear fusion reactions in the sun and measure the oscillation parameters $\theta_{12}$ and $\Delta m^2_{21}$. The solar $\nu_e$ flux oscillates as it propagates out of the Sun's core. The detected $\nu_e$ spectra, dominated by $^8$B decays, is compared to the SSM expectation and is fit to an oscillation model. KamLAND, an experiment measuring oscillations of antielectron neutrinos from nuclear reactors, is also sensitive to measuring the solar parameters.

The **Super-Kamiokande** (Super-K) detector was one of the first experiments to provide

[1] Insted of the $\bar{\nu}_e$ survival probability given by $P(\bar{\nu}_e \rightarrow n\bar{u}_e) = 1 - \cos^4\theta_{13}\sin^2 2\theta_{12}\sin^2\Delta_{21} - \sin^2 2\theta_{13}(\cos^2\theta_{12}\sin^2\Delta_{32} + \sin^2\theta_{12}\sin^2\Delta_{32})$, Daya Bay uses the approximation $P(\bar{\nu}_e \rightarrow \bar{\nu}_e) \simeq 1 - \cos^4\theta_{13}\sin^2 2\theta_{12}\sin^2\Delta_{21} - \sin^2 2\theta_{13}\sin^2\Delta_{\text{ee}}$ for its measurement, where $\Delta_x = \Delta m^2_x \frac{L}{4E}$. Although $\Delta m^2_{ee}$ is not a fundamental parameter, it has the advantage of being independent of the neutrino mass ordering and the solar parameters. See Appendix in [36] for more details.

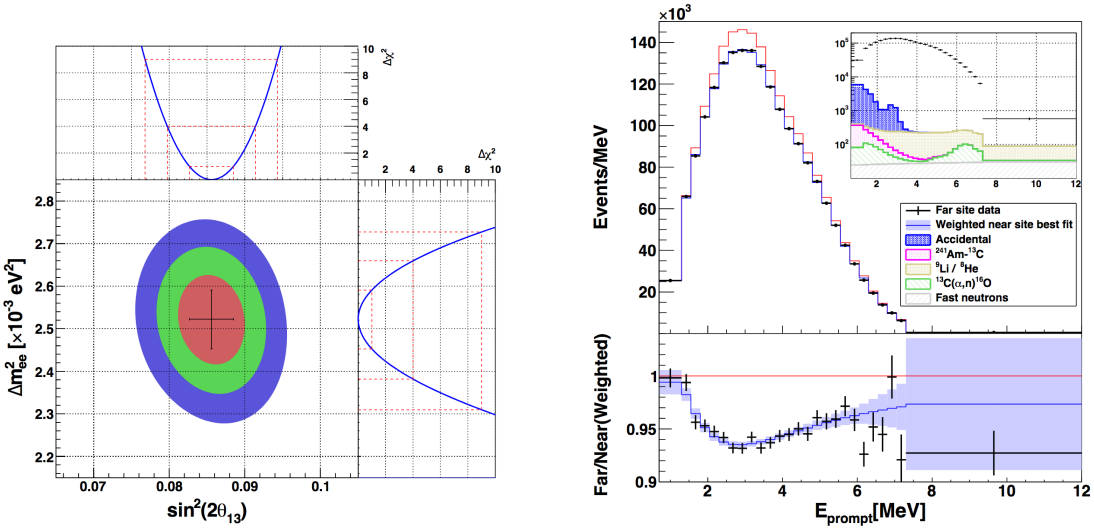


**Figure 2.5:** Daya-Bay results for the measurement of $\sin^2 2\theta_{23}$ and $\Delta m^2_{ee}$ and spectra of selected events at the far detector from 1958 days of operation, as published in [35]. Left: Allowed regions at the 1, 2 and 3 $\sigma$ levels in the $\sin^2 2\theta_{23}$ vs. $\Delta m^2_{ee} \times 10^{-3}$ eV$^2$ space, and respective $\Delta\chi^2$ profiles. The best fit point is shown in black with one-dimensional uncertainties. Right: The top panel shows the energy spectra of selected events (black) and the prediction including (blue) or excluding (red) the best-fit oscillation parameters at the far detector. The bottom panel shows the data/prediction ratios at the best fit (blue) and without oscillations (red). The shaded area represents the total uncertainty on the prediction and the error bars represent the statistical uncertainty on the data.

strong evidence of the solution to the solar neutrino problem. Super-K has been collecting solar neutrino data since 1996 and has observed the flux from the solar $^8$B decays. The detector is located inside the Kamioka mine in Japan and is the world's largest water Cherenkov detector, with a 22.5 kton fiducial volume. **SNO** used a spherical tank of heavy water, located at a depth of 2092 m inside the Vale's mine in Canada. It was also designed to measure the $^8$B solar spectrum and operated as the SNO experiment between 1999 and 2006. The SNO detector is being upgraded into the SNO+ experiment which will use liquid scintillator to detect lower energy solar neutrinos with a reduced background among other neutrino physics searches [42]. **Borexino**, a running experiment since 2007, is another experiment that uses a spherical liquid scintillator detector in the Gran Sasso Laboratory. Figure 2.6 shows the wide range of solar fusion reactions neutrino spectra.

**KamLAND** is a long baseline reactor experiment, which uses a 1 kton liquid scintillator spherical detector to measure the antineutrino flux from 53 nuclear reactors with an average baseline of 180 km. It is also sensitive to measuring the solar parameters and complements the solar experiments to constrain the $\sin^2\theta_{12}$ vs. $\Delta m^2_{21}$ space. KamLAND's own best fit is at $\sin^2\theta_{12} = 0.316^{+0.034}_{-0.026}$ and $\Delta m^2_{12} = 7.54^{+0.19}_{-0.17} \times 10^{-5}$ eV$^2$, which is the best current measurement of the solar mass splitting. However, KamLAND's results are in tension with Super-Kamiokande

and SNO at the 2 $\sigma$ level. Figure 2.7 displays the most recent results from combined fits between radiochemical solar neutrino experiments [15, 43, 44], Borexino, SNO, KamLAND and Super-K.

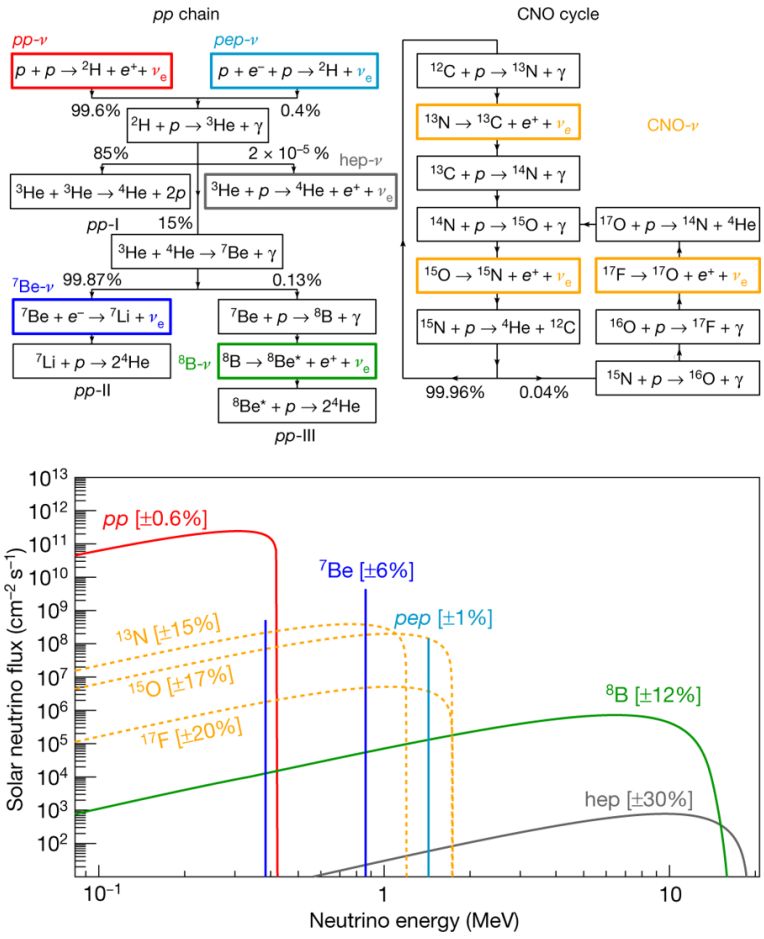


**Figure 2.6:** Nuclear fusion sequences and neutrino energy spectrum from [45]. The largest contribution to the solar neutrino flux arises from the proton-proton chain $p + p \rightarrow {}^{2}_{1}H + e^{+} + \nu_e$.

### 2.3.3 Measurement of $\theta_{23}$ and $\Delta m^2_{32}$

Several experiments have set constrains on the values of $\sin^2\theta_{23}$ and $\Delta m^2_{32}$ through the $\nu_\mu$ disappearance and $\nu_e$ appearance channels, particularly Super-K, T2K, MINOS, IceCube and NOvA. The results from the later are presented separately in 2.3.5. These experiments will be briefly mentioned and their results summarised in this section. Figure 2.8 shows the latest experimental constraints to the $\sin^2\theta_{23}$ and $\Delta m^2_{32}$ parameters, where it can be seen the experiment's measurements are in agreement at the 90% confidence level. Additionally, the Daya Bay experiment has measured the disappearance of $\bar{\nu}_e$ which yields the most precise measurement of the mass splitting in the atmospheric scale. In normal (inverted) hierarchy, the data prefers a best fit in $\Delta m^2_{32} = 2.471^{+0.068}_{-0.070}(-2.575^{+0.068}_{-0.070}) \times 10^{-3}$ eV$^2$.

In addition to solar neutrinos, **Super-K** detects accelerator and atmospheric neutrinos. This detector serves as a 2.5° off-beam axis far detector for the **T2K** (Tokai-to-Kamioka) experiment, which is a 295 km baseline accelerator experiment that detects neutrinos from a $\nu_\mu$ and $\bar{\nu}_\mu$

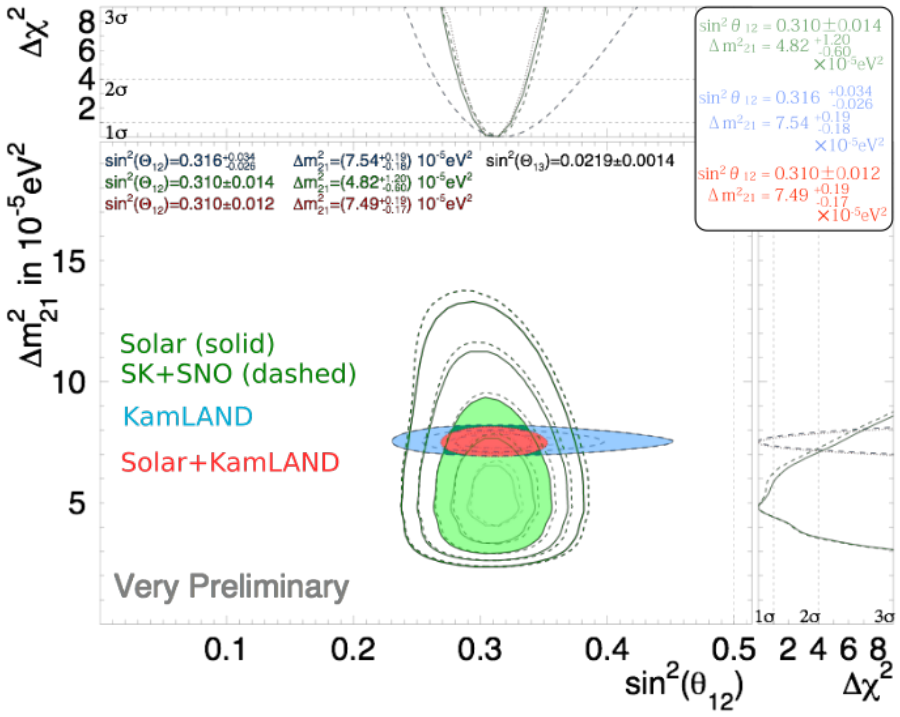


**Figure 2.7:** Constraints on the solar neutrino parameters $\sin^2\theta_{12}$ and $\Delta m^2_{21}$ obtained by Super-Kamiokande [46] and other solar and reactor experiments. The lines in the $\sin^2\theta_{12}$ vs. $\Delta m^2_{21}$ space show different levels of $\sigma$ contours and the shaded areas correspond to the 3 $\sigma$ confidence regions. The significance of each measurement is shown in terms of $\Delta\chi^2$ in the right and top panels. The solid green lines correspond to the combined result of Super-Kamiokande and all solar experiments, and the dashed green lines show the Super-Kamiokande results combined with SNO. The blue and red lines are the results of KamLAND, and of KamLAND with all solar experiments, respectively.

beam. T2K also uses one on-axis and one off-axis solid near detector for its measurements. The near detectors are situated in the J-PARC facility at a distance of 280 m of the neutrino source. T2K's lastest combined appearance and disappearance result uses data from the neutrino and antineutrino beams, and its best fits in $\sin^2\theta_{23}$ and $\Delta m^2_{32}$ are $0.526^{+0.032}_{-0.036}(0.530^{+0.030}_{-0.034})$ and $2.463^{+0.071}_{-0.070}\times10^{-3}(2.432\pm0.070\times10^{-3})$ eV$^2$ respectively, for normal (inverted) mass ordering [47].

The Main Injector Neutrino Oscillation Search (**MINOS**) was the second long-baseline accelerator experiment, just after K2K [48]. MINOS began collecting data in 2005 from Fermilab's Neutrinos at the Main Injector (NuMI) beam. The MINOS near detector was located about 1 km from the beam target, and the far detector at 735 km from it. These detectors were functionally identical magnetized tracking calorimeters with vertical steel planes and alternating planes of scintillator strips with a ±45° orientation. The MINOS+ phase was an upgrade of the original MINOS project, with a more intense and energetic neutrino beam, and was in operation between 2013 and 2017. The MINOS/MINOS+ collaboration has completed a new analysis which result disfavours maximal mixing by 1.1 $\sigma$ and their best fit to data is at $\sin^2\theta_{23} = 0.42$ and $\Delta m^2_{32} = 2.42\times10^{-3}$ eV$^2$.

The **IceCube** Neutrino Observatory at the South Pole, also sets limits in the $\sin^2\theta_{23}$ vs. $\Delta m^2_{32}$ space using atmospheric neutrinos from all directions and with high reconstructed energies between 5 and 56 GeV. The Ice-Cube detector is made of PMTs arranged in vertical strings and distributed inside the arctic ice to cover a 1 km$^3$ volume. It uses a more densely instrumented region, the *DeepCore*, at the center of the detector which allows the detection of less energetic interactions (lower than 5 GeV). IceCube's lastest results [49] have a best fit to data in $\Delta m^2_{32} = 2.31^{+0.11}_{-0.13}(-2.32) \times 10^{-3}$ eV$^2$ and $\sin^2\theta_{23} = 0.51^{+0.07}_{-0.09}(0.51)$ for the normal (inverted) ordering.

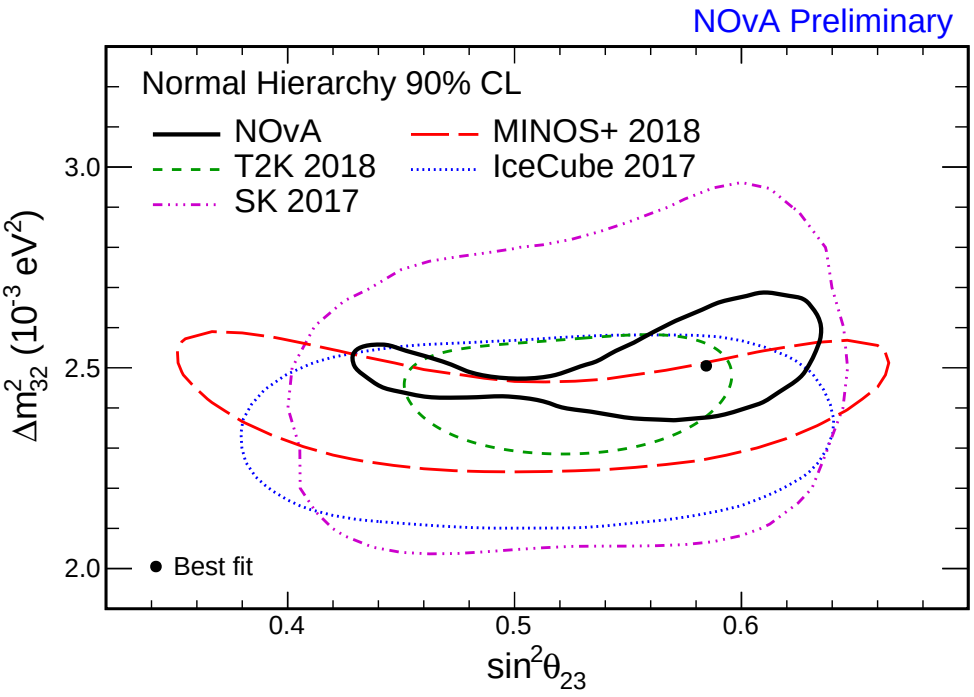


**Figure 2.8:** 90% confidence level contour from NOvA's 2018 joint fit with neutrino + antineutrino data with exposure to $8.85 + 6.89 \times 10^{20}$ POT, with systematics and Feldman-Cousins corrections applied. The latest results from MINOS+ [50], T2K [47], Super-Kamiokande [51] and IceCube [49] are plotted for reference.

### 2.3.4 Constraints on $\delta_{CP}$

The determination of the Charge-Parity symmetry in the lepton sector offers a door to understanding the matter-antimatter asymmetry in the universe, and it can be accessed by studying any difference between neutrino and antineutrino oscillations. The NOvA, MINOS and T2K experiments have constrained the value of $\delta_{CP}$ via the appearance of $\nu_e$ and $\bar{\nu}_e$ and the disappearance of $\nu_\mu$ and $\bar{\nu}_\mu$. However, these constraints are in tension between each other and are yet to reach higher significance. The Deep Underground Neutrino Experiment (DUNE) [52] could be able to determine if CP is violated with a 5 $\sigma$ significance after 7 years of data collection [53]. The Hyper-Kamiokande experiment can determine CP violation at 3 $\sigma$ for 80% of the possible values of $\delta_{CP}$ within the first 10 years of operation [54].

### 2.3.5 NOvA joint appearance and disappearance results

NOvA is one of the leading experiments to set limits on the still unknown values of the octant of $\theta_{23}$, the neutrino mass ordering and the CP violation phase. The constraints of the value of $\theta_{13}$ set by the reactor experiments play an important role as it's non-zero value makes these measurements possible via the appearance of $\nu_e$ and $\bar{\nu}_e$. NOvA has performed a joint appearance and disappearance fit to data, using its full exposure to the NuMI beam in neutrino and antineutrino mode. Figure 2.10a shows a plot of NOvA's data as a function of neutrino and antineutrino events. The ellipses help visualize NOvA's preference for a given combination of neutrino oscillation parameters for a given number of selected electron neutrino and antineutrino candidates at the Far Detector (FD).

Figure 2.9 shows the reconstructed energy spectra of selected electron neutrino and antineutrino events at NOvA's FD. The experiment observed 58 $\nu_e$ and 18 $\bar{\nu}_e$ events from an exposure to $8.85\times10^{20}$ Protons On Target (POT) for a $\nu_\mu$ beam and $6.9\times10^{20}$ POT for a $\bar{\nu}_\mu$ beam respectively, over an expectation of 15 and 5.3 background interactions. This result is a 4 $\sigma$ evidence of electron antineutrino appearance, which is the first observation of its kind at this high level of significance. The disappearance analysis selected 113 $\nu_\mu$ and 65 $\bar{\nu}_\mu$ events. The constraints to the space of oscillation parameters from NOvA's combined appearance and disappearance fit to neutrino and antineutrino data are shown in Figures 2.8 and 2.10. The best fit occurs at $\sin^2\theta_{23} = 0.58 \pm 0.03$, $\Delta m^2_{32} = 2.51^{+0.12}_{-0.08}\times10^{-3}$ eV$^2$ and $\delta_{CP} = 0.17\pi$ in the normal ordering (NH). A detailed description of the experimental design of NOvA is presented in the next chapter.

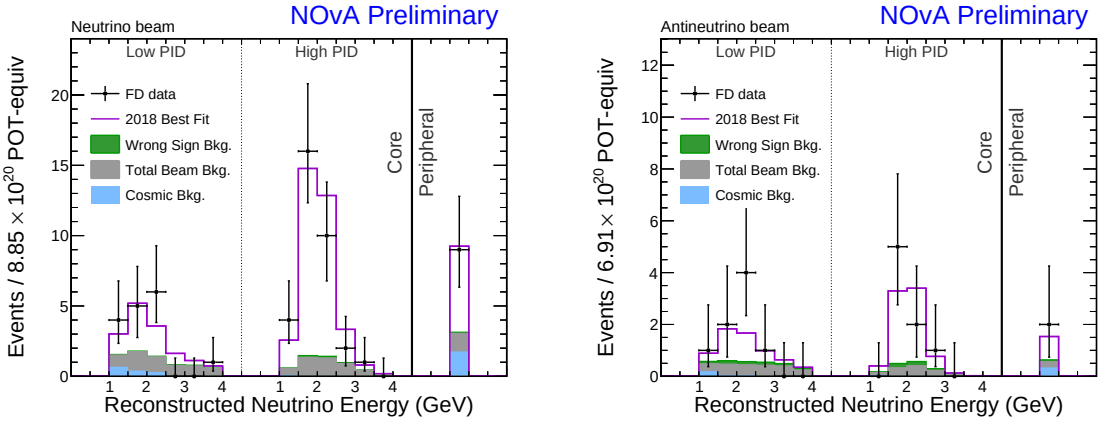


**(a)** Energy spectrum of selected $\nu_e$ events at the FD from the neutrino beam.

**(b)** Energy spectrum of selected $\bar{\nu}_e$ events at the FD from the antineutrino beam.

**Figure 2.9:** Reconstructed energy spectra of the $\nu_e$ and $\bar{\nu}_e$ selected events at NOvA's FD [55].

### 2.3.6 Comparison between $\nu_\mu$ and $\bar{\nu}_\mu$ disappearance

In a disappearance channel, the action of T does not change the oscillation

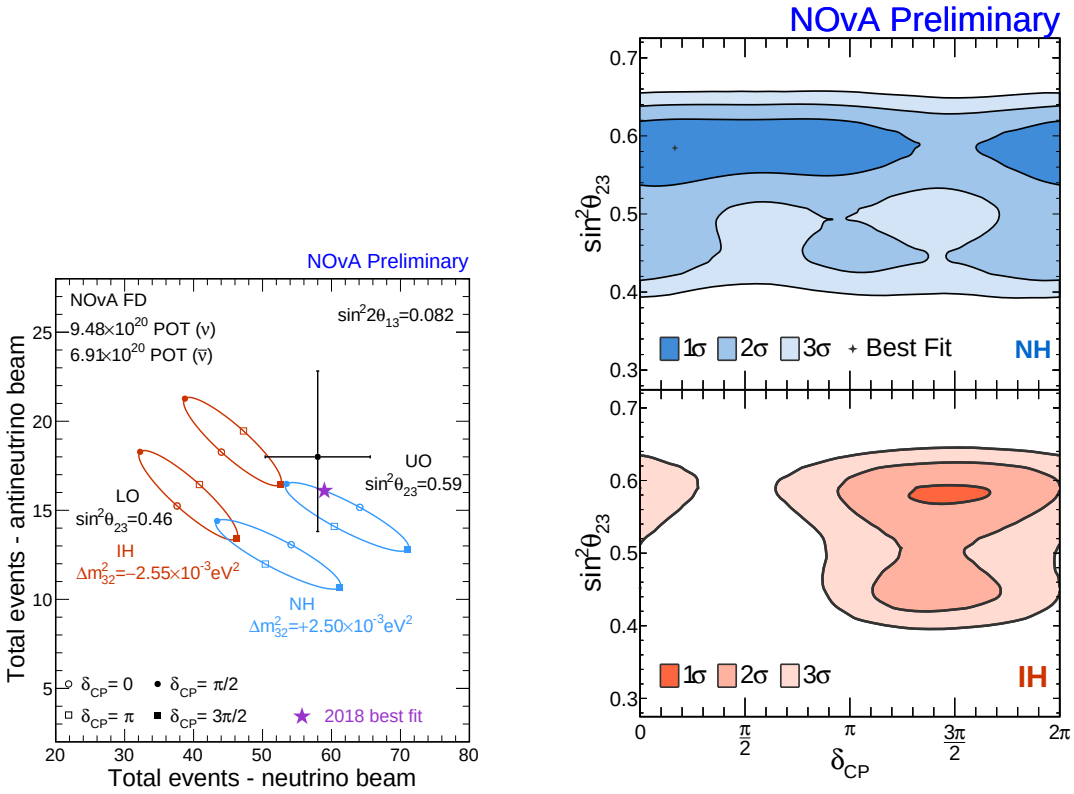


**(a)** Ellipses as a function of $\delta_{CP}$, for normal and inverted ordering in blue and red, respectively. The octant preference of $\theta_{23}$ give two possible scenarios: the figures at the bottom(top) correspond to $\theta_{23}$ in the lower(upper) octant.

**(b)** 1,2 and 3 $\sigma$ contours in the $\sin^2\theta_{23}$vs. $\delta_{CP}$ parameter space in the normal (top panel) and inverted hierarchy (bottom panel) scenarios. The best fit point is shown by the black marker.

**Figure 2.10:** NOvA results from $\nu_e$ appearance and $\nu_\mu$ disappearance including first data set from the antineutrino beam as presented in [55].

$$T(\nu_x \to \nu_x) = \nu_x \to \nu_x \tag{2.31}$$

As T does not have any effect on the physical situation, CP can not manifest itself if CPT is conserved:

$$\begin{aligned} CPT(\nu_{\mu,L} \to \nu_{\mu,L}) &= CP(\nu_{\mu,L} \to \nu_{\mu,L}) \\ &= C(\nu_{\mu,R} \to \nu_{\mu,R}) \\ &= (\bar{\nu}_{\mu,R} \to \bar{\nu}_{\mu,R}) \end{aligned} \tag{2.32}$$

thus a difference between the $\nu_\mu$ and the $\bar{\nu}_\mu$ disappearance rates in vacuum,

$$P(\nu_{\mu,L} \to \nu_{\mu,L}) \neq P(\bar{\nu}_{\mu,R} \to \bar{\nu}_{\mu,R}), \tag{2.33}$$

would be an indication of CPT violation. In matter, the $\nu$ and $\bar{\nu}$ survival probabilities differ for neutrinos and antineutrinos and can mimic CPT violation. However, the differences are small with the experimental conditions of experiments such as MINOS, T2K and NOvA.

MINOS is able to differentiate positively from negatively charged muons, which allowed the inclusion of 7.88 kton-years of atmospheric data to its measurements on top of the collected samples from $\nu_\mu$ and $\bar{\nu}_\mu$ beams achieved from an exposure to $10.71 \times 10^{20}$ POT and $3.36 \times 10^{20}$ POT respectively [56]. MINOS $\nu$ and $\bar{\nu}$ separated analysis yield $\Delta m^2 = 2.41^{+0.09}_{-0.10} \times 10^{-3}$ eV$^2$ and $\sin^2 2\theta = 0.950^{+0.035}_{-0.036}$ assuming CPT conservation. Allowing different oscillations between neutrinos and antineutrinos, the experiment best fit result was $\Delta \bar{m}^2 = 2.50^{+0.23}_{-0.25} \times 10^{-3}$ eV$^2$ and $\sin^2 2\bar{\theta} = 0.97^{+0.03}_{-0.08}$ for antineutrino oscillations, and a difference between the mass squared splitting for $\nu$ and $\bar{\nu}$ of $\Delta m^2 - \Delta \bar{m}^2 = 0.12 \times 10^{-3}$ eV$^2$ that was not significant.

The T2K experiment has also published measurements of $\Delta m^2_{32}, \Delta \bar{m}^2_{32}, \sin^2\theta_{23}$ and $\sin^2\bar{\theta}_{23}$ from a combined $\nu_\mu + \bar{\nu}_\mu$ disappearance analysis [57]. Using $7.482 \times 10^{20}$ POT and $7.471 \times 10^{20}$ POT in neutrino and antineutrino beam mode respectively, the reported best fits in normal mass ordering are $\sin^2\theta_{23} = 0.51^{+0.08}_{-0.07}$ and $\Delta m^2_{32} = 2.53 \times^{+0.15}_{-0.13} \times 10^{-3}$ eV$^2$ for neutrinos and $\sin^2\bar{\theta}_{23} = 0.42^{+0.25}_{-0.07}$ and $\Delta \bar{m}^2_{32} = 2.55^{+0.33}_{-0.27} \times 10^{-3}$ eV$^2$ for antineutrinos. These measurements agree within errors, but a slight $\theta_{23}$ octant preference is present in the fit for the antineutrino parameter. These best fit values reported by the T2K experiment will be used later on in this document for a comparison with the NOvA disappearance only results for a separate measurement of the neutrino and antineutrino oscillation parameters.

The MINOS and T2K experiments have provided measurements of the $\theta_{23}$ and $\Delta m^2_{32}$ parameters with $\nu_\mu$ and $\bar{\nu}_\mu$ disappearance, whose best fit values are consistent with each other. No significant differences between the $\nu$ and $\bar{\nu}$ values are present at the 1 $\sigma$ level. The results of these analysis are shown in Figure 2.11.

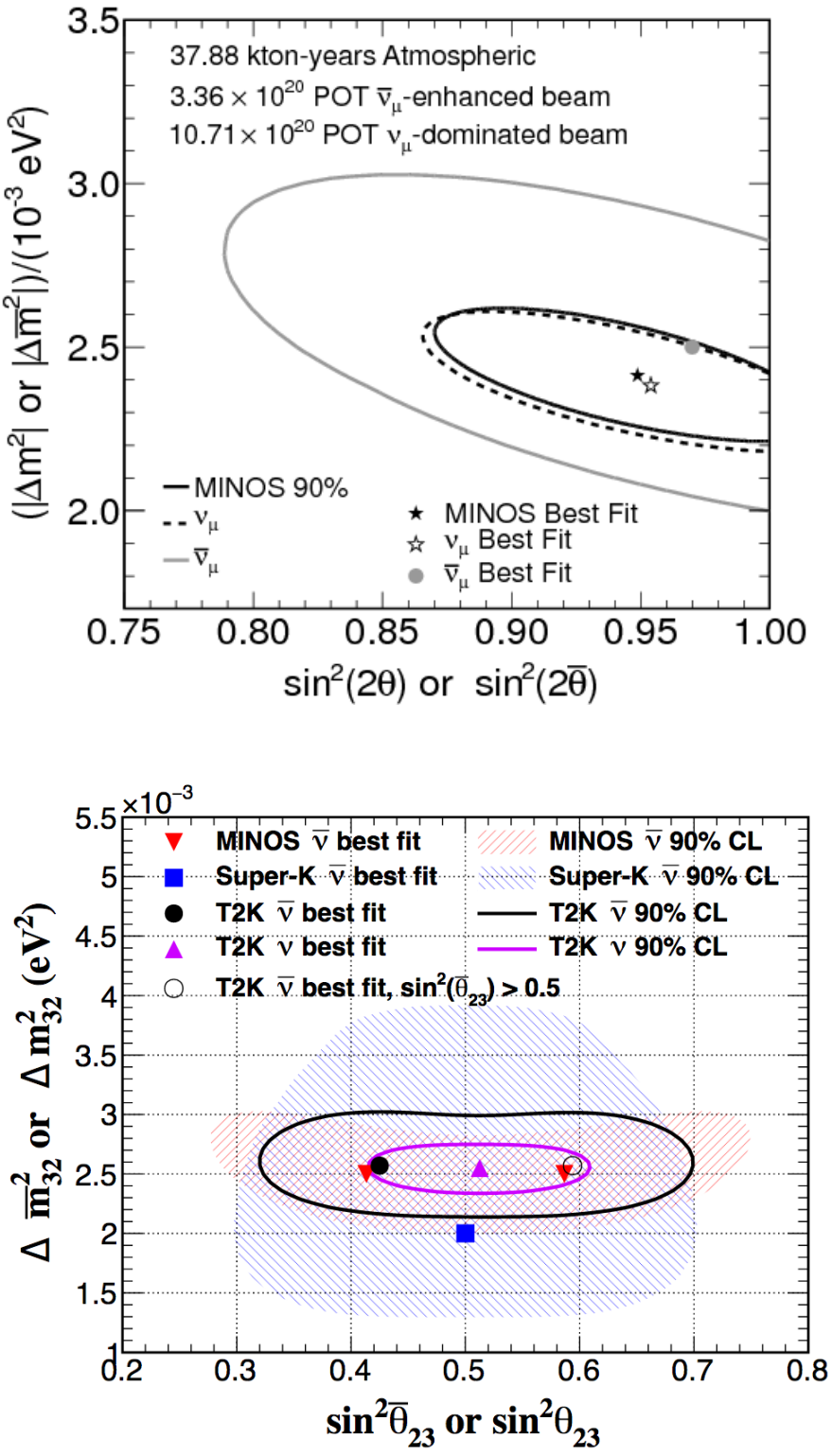


**Figure 2.11:** 90%C.L. allowed regions of the $\sin^2 2\theta$ vs. $\Delta m^2$ parameter space from the MINOS experiment [56], and constrains on $\sin^2\theta_{23}$ vs. $\Delta m^2_{32}$ and $\sin^2\bar{\theta}_{23}$ vs. $\Delta\bar{m}^2_{32}$ from T2K [57] assuming different and identical neutrino and antineutrino oscillations.

# Chapter 3

# The NOvA Experiment

The NOvA experiment is a neutrino oscillation experiment designed to make precise measurements of $\nu_e + \bar{\nu}_e$ appearance and $\nu_\mu + \bar{\nu}_\mu$ disappearance at long distances and GeV energy scales. For this purpose NOvA uses Fermilab's Neutrinos at the Main Injector (NuMI) beam, which provides a highly pure and abundant source of either $\nu_\mu$ or $\bar{\nu}_\mu$. The experiment consists of two identically functional detectors placed at 14 mrad off the neutrino beam axis. The 300 tonne Near Detector (ND) is located 1 km from the NuMI target, on-site at Fermilab. At this distance the neutrinos have not yet oscillated. The Far Detector (FD), where the oscillation phenomenon is measured, is located near Ash River, Minnesota at 810 km from the NuMI target. The baseline and off-axis configuration was chosen to produce a narrow energy flux at around the first oscillation maxima at the location of the far detector, and therefore to enhance the experiment's sensitivity to observing neutrino appearance and disappearance. With near identical detector construction, the common systematic uncertainties largely cancel upon a comparison of ND and FD measurements.

This chapter summarizes the details of the NOvA experiment. The neutrino source is described in section § 3.1, followed by the design and installation of the detectors in § 3.2. Section § 3.3 goes through the data acquisition and presents the datasets used for the analysis in this thesis. The beam and detector simulation is described in section § 3.4. The detailed design of the NOvA experiment is documented in the Technical Design Report (TDR) [58].

## 3.1 The NuMI Beam

This section describes NOvA's neutrino and antineutrino source, the Neutrinos at the Main Injector (NuMI) beam located at the Fermi National Accelerator Laboratory (Fermilab). The production of the beam can be summarized by three stages:

- A primary beam of protons.
- A secondary meson beam.
- A decay pipe and the final neutrino beam.

The process begins at Fermilab's Linear Accelerator (LINAC) and continues via a syncrotron accelerator (Booster). Protons then enter the Recycler ring where multiple particle batches are stacked for increased intensity before being sent to the Main Injector (MI). Each group of batches (*spill*) are extracted to the MI in a single-turn, and accelerated further before being sent to the NuMI target hall to produce the neutrino or the antineutrino beam. The layout of Fermilab's accelerator complex is shown in Figure 3.1 and is described more in detail in [59]. The NuMI beam layout is shown in Figure 3.2.

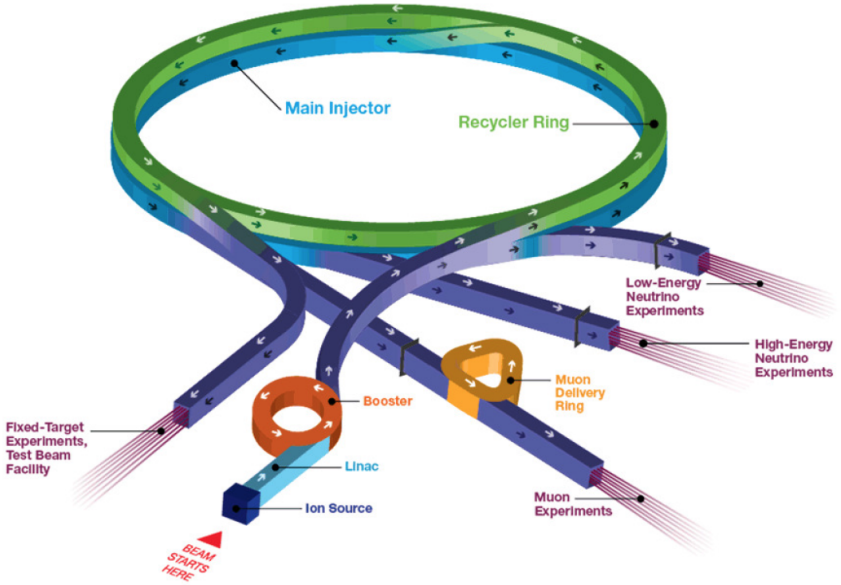


**Figure 3.1:** Layout of Fermilab's accelerator complex. The LINAC, Booster, Recycler and MI are used for the high energy neutrino experiments. Source [60].

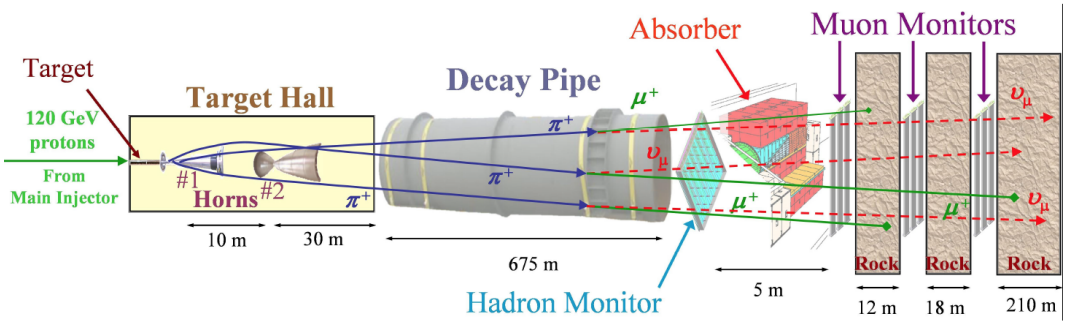


**Figure 3.2:** Layout of the NuMI beam, showing the target hall, decay pipe and Absorber [61].

### 3.1.1 Primary proton beam

Producing the 120 GeV protons for NuMI employs several accelerators. The first stage begins with the ion source which generates a 35 keV $H^-$ ion beam. Next, these ions are accelerated up to 400 MeV by making use of alternating electric fields along a 150 m Linear Accelerator (LINAC). Then, a thin carbon foil stops the electrons leaving only free protons to enter the Fermilab's

syncrotron accelerator (Booster), a circular accelerator (synchrotron) of 152 m diameter, which operates at 15 Hz at about 6 m under the ground.

The proton beam entering the Booster is accelerated until it reaches an energy of 8 GeV and is then extracted and sent to the Recycler. Each Booster batch has a duration of about 1.6 $\mu$s and consists of about $4 \times 10^{12}$ protons. Due to the MI and Recycler being 7 times the diameter of the Booster, they can accommodate up to 7 batches. In practice, one of the slots is used to allow for the pulse kicker rise time. The Recycler uses a slip-stacking technique meaning that two batches are combined into one. In total 6+6 batches are slip-stacked before sending them to the MI where the protons are accelerated to 120 GeV. While the Recycler accumulates protons from the Booster, the MI accelerates the particles from the previous batches. This parallelized accumulation and acceleration technique was a key part of achieving the proton intensity for which NOvA was designed.

Each beam *spill* with a duration of 10 $\mu s$, formed by 6+6 slip-stacked batches of 120 GeV protons, is extracted every 1.33 s from the MI and bent down to point to the NuMI target hall. After traveling about 350 m the protons enter the target hall which is located approximately 41 m underground.

### 3.1.2 Secondary meson beam

The secondary beamline consists of four parts: a target, a focusing system, a decay region and an absorber. After arrival in the target hall, the primary proton beam impacts a 1 m long target. The target consists of graphite, segmented into 48 fins which are brazed to water cooled steel pipes. This design maximises the hadron production and minimises the number of secondary meson interactions while withstanding the 700 kW beam power.

The hadrons produced by the proton interactions on the target, mostly $\pi$ and $K$, need to be focused to maximise the number of usable neutrinos or antineutrinos. The focusing is achieved by placing two magnetic horns right after the target, which operate in two modes to focus either positive or negatively charged particles. A pulsed current of 175 kA is supplied to the horns in coincidence with the beam spills, Forward Horn Current (FHC) and Reversed Horn Current (RHC) for a neutrino or antineutrino beam respectively.

The two horn array has increased the focusing efficiency by 50% if compared to a system with a single magnetic horn. Hadrons with a low transverse momentum are unaffected by the horns as they pass straight along the beam axis, where there is no magnetic field. Similarly, the hadrons focused by the first horn do not significantly change their trajectories in the second horn. Hadrons that are either under or over focused by the first horn are focused by the second horn. The focused beam of mesons then travels to the decay region.

### 3.1.3 Decay pipe and neutrino beam

Once they have been focused, the secondary mesons enter a decay pipe 676 m long where they have time to decay into tertiary mesons, leptons and neutrinos. The decay pipe is filled with helium due to its long interaction length.

When the horns are in neutrino mode, the beam of mesons is largely formed by $\pi^+$ with energies of around 8 GeV. Those pions in turn produce a tertiary beam of almost completely pure $\nu_\mu$ when they decay via their dominant mode $\pi^+ \to \mu^+\nu_\mu$ (branching ratio 99.98%). Positive kaons also contribute to the muon neutrino flux via $K^+ \to \mu^+\nu_\mu$ (branching ratio 63.55%). The majority of the $\mu^+$ daughters of the $\pi^+$ make it to the end of the decay region to be absorbed by the rock. Nevertheless there is a chance that some of the $\mu^+$ decay via $\mu^+ \to e^+\bar{\nu}_\mu\nu_e$, therefore contaminating the beam with $\nu_e$. Furthermore, $K^+$ and $K^0$ can decay through $K^+ \to \pi^0 e^+\nu_e$ and $K^0 \to \pi^\pm e^\mp\nu_e$. The decay modes of the charged particles listed above are all charge conjugated when the magnetic horns operate in antineutrino mode.

Downstream of the decay pipe is the Absorber made of aluminium, steel and concrete, which functions to absorb any undesirable beam such as primary and secondary protons that did not interact earlier in the beamline. The Absorber also stops secondary mesons which did not decay in flight as well as $e^-, n$ and $\gamma$ particles. The muon rate is suppressed by an additional barrier, the Muon Shield, which consists of 240 m of rock between the end of the decay pipe and the ND hall.

### 3.1.4 Off-axis beam

NOvA was designed to exploit the off-axis technique to enhance the $\nu_\mu$ or the $\bar{\nu}_\mu$ flux in the maximum oscillation energy region. Pions and kaons decay isotropically in their rest frame producing mono-energetic neutrinos. When these particles are boosted, the resulting flux $\Phi$ and energy $E_\nu$ of neutrinos from meson decay in flight, in the reference frame of the laboratory, is given by [62]

$$\Phi = \left[\frac{2\gamma}{1+\gamma^2\theta^2}\right]^2 \frac{A}{4\pi z^2}, \tag{3.1}$$

$$E_\nu = E_{\pi,K}\frac{1-\frac{m_\mu^2}{m_{\pi,K}^2}}{1+\gamma^2\theta^2}, \tag{3.2}$$

where $E_{\pi,K}$ and $m_{\pi,K}$ denote the energy and mass, respectively, of the parent pion ($\pi$) or kaon ($K$) and $\gamma = E_{\pi,K}/m_{\pi,K}$. $A$ is the area of a detector placed at a distance $z$ from the decaying particle, $\theta$ is the angle between the parent and the neutrino directions. These functions are plotted in Figure 3.3 for a range of pion and kaon energies and for different angles with respect to the beam axis. The location of the NOvA detectors was chosen to be 14 miliradians from the central beam axis. As can be seen in Figure 3.4, this enhances the neutrino energy spectrum at around 2 GeV, which is key to the experiment as the oscillation maximum is expected to occur at about 1.6 GeV for NOvA's baseline.

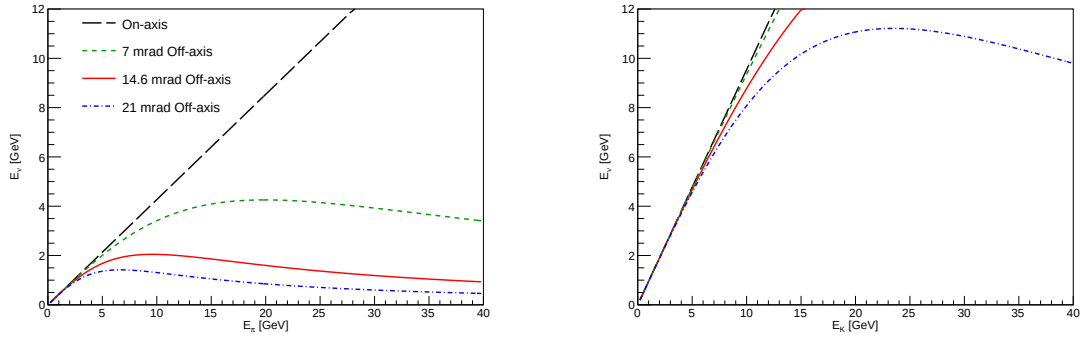


**Figure 3.3:** Neutrino energy as a function of the parent particle's energy. The spectra for neutrinos produced from the decay of a pion or kaon are shown on the left and right, respectively, for different angles from the NuMI beam axis.

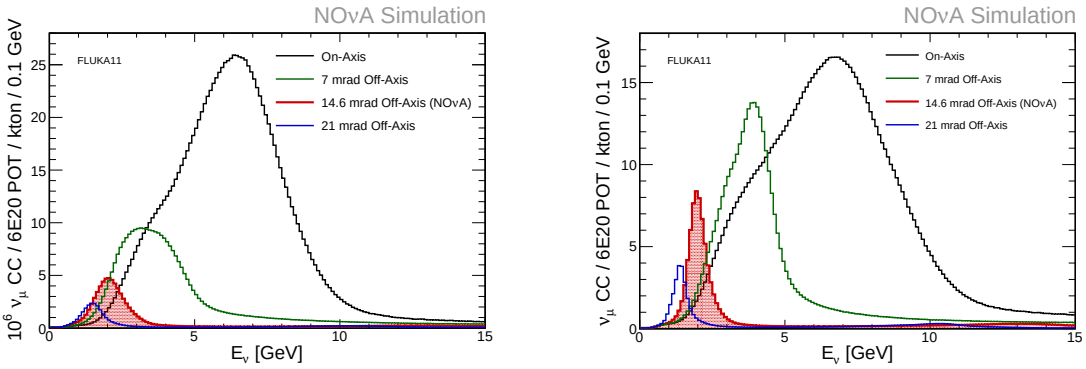


**Figure 3.4:** Reconstructed energy spectra for $\nu_\mu$ CC at the ND(left) and at the FD(right) at different angles from the NuMI beam axis.

### 3.1.5 Data taking and exposure

The beam delivered since February 2017 for NOvA has been at 700 kW with $4.9\times10^{13}$ protons per pulse. This is a new high intensity record, which positions NuMI as the most powerful neutrino beam in the world. Figure 3.5 shows the total accumulated Protons On Target (POT) from 2014 until February 2019: $9.5\times10^{20}$ POT have been delivered with the beam in neutrino mode and $12.3\times10^{20}$ POT in antineutrino mode. Table 3.1 displays the FD beam livetime and the number of protons on target per periods and beam modes as used for NOvA's oscillation analyses. The data recorded during these periods is analyzed in this thesis.

## 3.2 The NOvA Detectors

The NOvA detectors are functionally identical structures designed with the purpose of detecting neutrino interactions with the main difference between them being their size and location with respect to the surface. Contrary to other particle physics experiments, the detectors are not subject to a magnetic field which would help with charged particle identification. To be able to tackle the challenge of particle identification, NOvA not only relies on a highly pure NuMI beam,

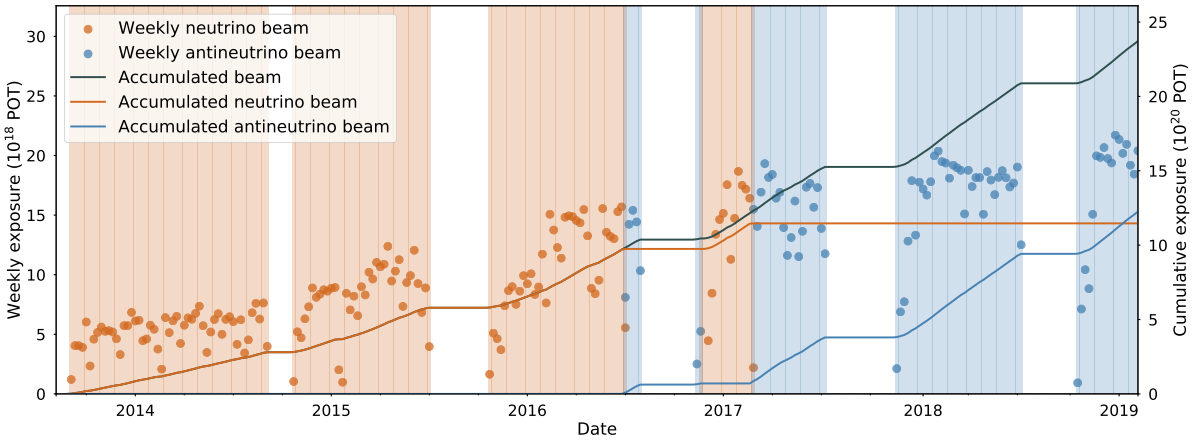


**Figure 3.5:** NOvA's beam exposure vs. time. Timeline showing the weekly POT delivered for NOvA's neutrino beam (orange dots) and antineutrino beam (blue dots) from the start of the physics data taking to the end of February 2019. The cumulative POT for the neutrino and antineutrino beam are shown in solid orange and blue lines, respectively. The total accumulated POT is represented by the grey line [61].

but also relies on having a granularity fine enough to distinguish shower inducing interactions (such as $e^-$) from non-showering particle tracks (such as muons, protons and charged pions). This granularity is achieved by segmenting the detectors.

The NOvA detectors are tracking calorimeters made of Polyvinyl Chloride (PVC) and organic liquid scintillator, giving a 65% active mass. The basic detector design is a long plastic unit filled with the liquid scintillator and containing a Wavelength Shifting (WLS) fiber to capture scintillation light. These plastic units, called *cells*, are the smallest detector components from which the data is read out.

The light collected and transmitted along the fibre is converted into an electronic signal by an Avalanche Photo-diode (APD) at its far end. The signal from the APD is then digitized by an ADC. Using the average expected APD response, integrated charge from the Analog Digital Converters (ADCs) are converted to units of Photo-Electron (PE) using a simple conversion factor. Signals are recorded which coincide with the NuMI spills as well as some that are outside of it for which data-driven triggers are used.

This section begins by describing the common features to the NOvA detectors and then proceeds to describe the particular characteristics of each one.

### 3.2.1 The Cell

PVC structures are extruded to form 16 cells. These cells are filled with liquid scintillator and light is collected by a looped WLS fiber that runs all along the cell and back as shown in Figure 3.6. Each cell has a transverse area of 3.8 × 5.9 cm, and a length of 4 m in the ND and 15.5 m in the FD. This difference in length results in a larger light attenuation in the FD than in the ND,

| Period | Beam Mode | POT ($\times 10^{20}$) | Livetime (s) |
|---|---|---|---|
| Period 1 (February 2014 - September 2014) | Neutrino | 1.23 | 128.1 |
| Period 2 (November 2014 - July 2015) | Neutrino | 2.64 | 119.0 |
| Period 3 (October 2015 - June 2016) | Neutrino | 3.85 | 138.9 |
| Period 4 (June - July + November 2016) | Antineutrino | 0.66 | 19.6 |
| Period 5 (November 2016 - February 2017) | Neutrino | 1.76 | 51.9 |
| Period 6 (February 2017 - July 2017) | Antineutrino | 3.06 | 76.3 |
| Period 7 (November 2017 - July 2018) | Antineutrino | 5.38 | 136.97 |
| Period 8 (October 2018 - February 2019) | Antineutrino | 3.23 | 84.23 |

**Table 3.1:** FD beam livetime and number of protons on target used in the analysis with the beam in neutrino and in antineutrino mode per period of data taking. Every year, the accelerator complex goes into a summer shutdown; the dates in parenthesis are the periods when NuMI was in operation.

that has to be corrected for by the calibration (see § 4.3).

The layout of the detectors is relatively simple. Two PVC extrusions are glued together to form a module with 32 cells. Multiple modules are used to form planes which are placed orthogonally one after the other allowing for 3D particle track reconstruction. Each cell is read-out by attaching both ends of the WLS fibres to one of the 32 pixels of an APD.

The NOvA design is influenced by the material properties of the PVC. Unlike other experiments, NOvA's structure, made of plastic, stresses more easily than, for example, metals and yet it has to withstand the interior hydrostatic pressure of up to 15.7 meter columns of scintillator. Therefore the extrusions were designed with rounded interior corners to minimise the stress and the creep.

### 3.2.2 Liquid Scintillator

The liquid scintillator, the active material, corresponds to approximately 65% of the detector's mass. This scintillator is a solution which consists of three elements, each with a specific purpose,

- Scintillator, which emits light in the UV region, peaking between 360 - 390 nm, when ionised by an particle interacting within the cell.
- Wave-shifters, which absorb and shift the light produced by the scintillator into the visible region, between 400 - 450 nm, so it can be absorbed by the WLS fibres.
- Solvent, which is mineral oil acting as a stabiliser and provides the bulk of the material.

Other components such as an anti-oxidant and an anti-static element complete the scintillator blend. The anti-oxidant Vitamin E helps prevent the scintillator from losing its transparency. The anti-static Stadis-425 is added to make the filling of the detectors safer. The liquid scintillator composition is detailed in Table 3.2.

The scintillator temperature differs between detectors due to their different operation temperatures: The temperature of the blend in the ND is 18.3 °C, for a $\rho = 0.859$ g/cm$^3$, and in the FD is

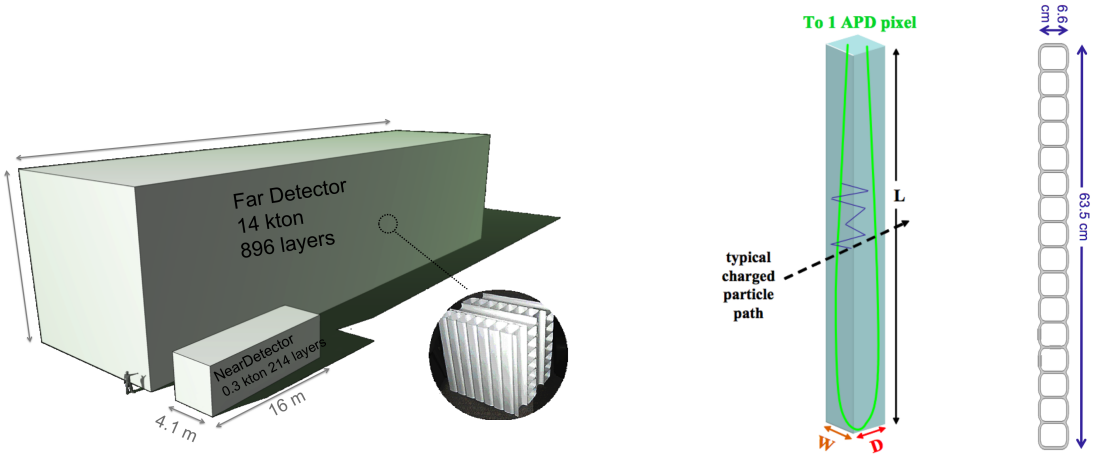


**Figure 3.6:** Detector and cell schematics. The NOvA detectors are identically functional structures made of vertical and horizontal PVC planes (left). These planes are composed by cells which are the detectors' elementary units (shown on the right). When a charged particle interacts with the active material, it induces scintillation light (represented by the blue line in the middle diagram); this light bounces around until it is absorbed by the fiber which transmits the re-emitted WLS light to an APD.

| Component | Purpose | Mass fraction |
|---|---|---|
| Mineral oil | Solvent | 94.63% |
| Pseudocumene | Scintillant | 5.63% |
| PPO | Wave-shifter | 0.14% |
| bis-MSB | Wave-shifter | 0.002% |
| Stadis-425 | Anti-static | 0.001% |
| Vitamin E | Anti-oxidant | 0.001% |

**Table 3.2:** NOvA scintillator composition [63].

20.6 °C for a $\rho = 0.860$ g/cm$^3$. In total, 29,616 gallons of scintillator fill the Near Detector (ND) and 3,213,660 gallons fill the Far Detector (FD).

### 3.2.3 Optical Fiber

The optical fiber contains wave-length shifting agents and it is multi-clad to facilitate and maximise the internal reflection. The fiber core material is polystyrene mixed with R27 dye with refractive index n = 1.59 making it less refracting than the outer layers made of acrylic (n = 1.49) and fluorinated-polymer (n = 1.42). The total diameter of the Wavelength Shifting (WLS) fiber is 0.7 mm, with both outer-most materials accounting for about 3% of it.

The liquid scintillator emits light in the 400-450 nm range which is absorbed by the optical fiber and shifted to blue-green wavelengths between 490 nm and 550 nm. This shifting ensures that even though the internally reflected light has to travel 15.7 m in the FD, light in the range

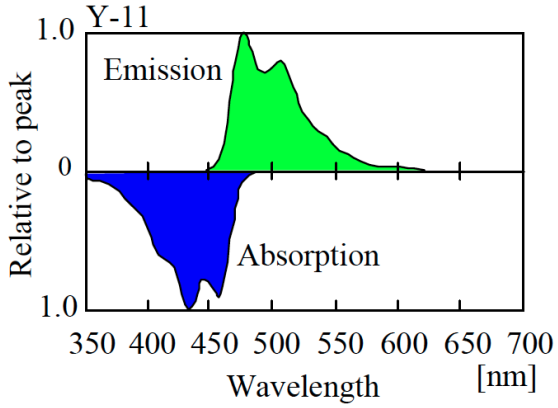


**Figure 3.7:** NOvA's optical fiber absorption and emission spectra. The dye in the optical fiber absorbs the violet light emitted by the liquid scintillator and re-emits it in the blue-green range. Wavelengths below 500 nm are highly attenuated due to the overlapped emission and absorption spectra [58].

of 520 - 550 nm will still be measurable. As can be seen from NOvA's optical fiber absorption and emission spectra in Figure 3.7, wavelengths below about 500 nm are attenuated due to the overlap between the two spectra. Each single fiber is looped inside a Polyvinyl Chloride (PVC) cell. This design allows light traveling in both directions along the cell to be collected. Given the light produced, a measurable signal requires a good quantum efficiency for green light which is achieved by using an Avalanche Photo-diode (APD).

### 3.2.4 Photodetectors and Electronics

The NOvA electronics have to satisfy slightly different criteria in each detector. In the FD, the readout should be able to collect information from events happening within the Neutrinos at the Main Injector (NuMI) spill as well as record cosmic ray events used for calibration and monitoring. In the ND, the electronics have to be capable enough to allow the multiple particle interactions induced by the neutrino beam. to be separated. In both detectors, the readout should have a high quantum efficiency for the light signal and low noise to be able to measure the light from the end of the cell far away from the readout.

With these considerations in mind, the NOvA photodetectors were chosen to be Hamamatsu APDs. These APDs have a quantum efficiency of 85% in the 500 - 550 nm region and currently operate at a gain of 100 and 150 in the ND and in FD, respectively; the higher gain in the FD is to increase the signal to noise ratio. The thermal creation of electron-hole pairs is minimized by each APD carrying its own Thermoelectric Cooler (TEC) to keep it operating at - 15 °C and therefore mitigate the dark noise.

APDs use the photoelectric effect to convert light into an electrical signal. Each absorbed photon can excite an electron which is drifted by a potential difference and then causes an electron avalanche. These electrons are collected, amplified, and digitized by a coupled Front End Board (FEB), which sends its data onwards to a Data Concentrator Module (DCM) and then to a farm of

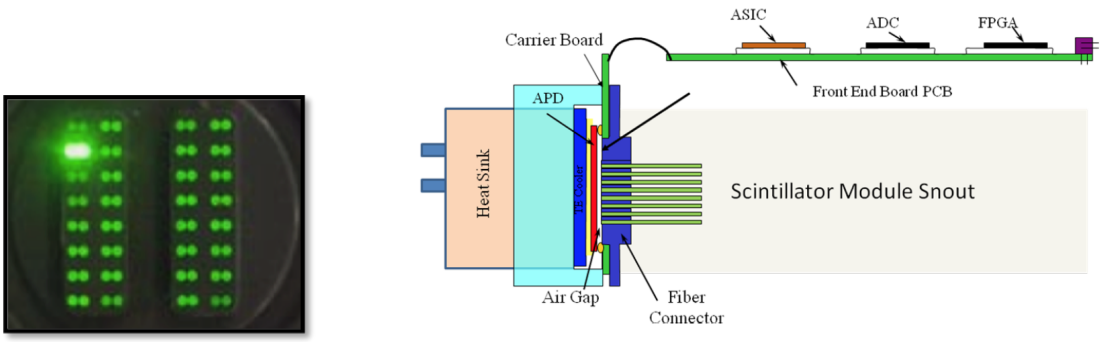


**(a)** Array of fiber ends **(b)** Electronics schematic [64].

**Figure 3.8:** Array of fiber ends from a 32 cell module (left) and a schematic showing the fiber ends connected to a cooled 32-pixel APD(right). Each APD is coupled to a Front End Board (FEB) which carries an ADC, an Application Specific Integrated Circuit (ASIC) and a Field Programmable Gate Array (FPGA).

PCs. Figure 3.8 shows an schematic of the electronics, where a module's fiber ends are connected to an APD coupled to a FEB.

### 3.2.5 Detector assembly

The PVC extrusions were assembled into modules at the Module Factory at University of Minnesota, Minneapolis, where they were tested and assembled with other detector components. The modules were sealed with an end-plate made with the same PVC material moulded to fit and cover the cross-section of the 32 cells of the module where the fiber loops end. Additionally, the end of the modules were sealed with center and side seals. On the other side, the top modules were sealed with a manifold cover, a snout and an electronics box; the latter houses one APD and one FEB per module, the snout contains one port for ventilation and a second port for filling the module with the liquid scintillator. The bottom and top covers, the raceways and snouts are composed of black injection plastic to minimise light reflexion and to reduce cross-talk between channels. This design is shown in Figure 3.9. Once the modules were assembled, they were tested for leaks. Once they passed the tests, the modules were shipped to Ash River or to Fermilab to begin the detector construction.

#### Near Detector

The NOvA ND is located 105 m below the surface at Fermilab, in a cavern adjacent to the MINOS and MINERvA experiments hall area. The ND is placed at around 1015 m from the target hall and at 14.6 miliradians from the NuMI beam axis. This 300 ton detector has a front face of 4.2 m x 4.2 m and a length, in the direction of the beam, of 15.8 m. The ND is divided in one *fully active region* and a *muon catcher*. Planes in the fully active region are formed by 3 modules and 24 of such planes form a *block*. There are 8 of these blocks in the ND. The muon catcher was added to the downstream end of the ND to contain muons that will otherwise escape the detector. This is

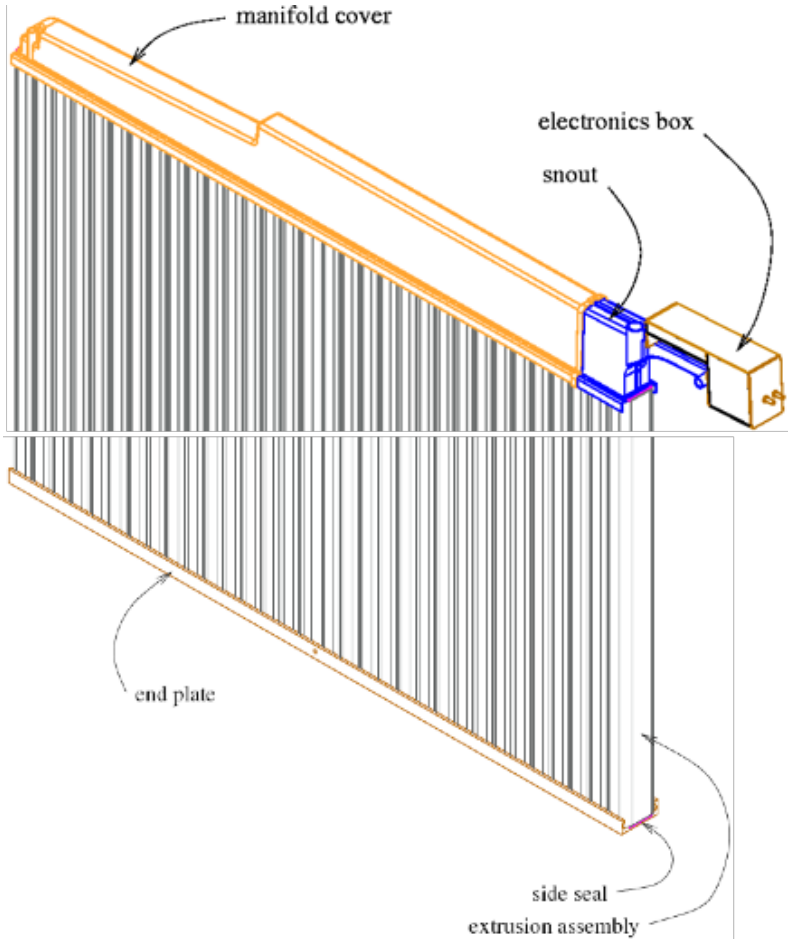


**Figure 3.9:** NOvA module structure. Each PVC plane is structured in groups of 32 cells, which share the same electronics readout [58].

made of ten layers of 10 cm thick steel planes combined with eleven pairs of one vertical and one horizontal plastic plane. As they were re-used from the Near Detector On Surface (NDOS)[1], the steel planes are three modules wide and two modules high. Therefore, the vertical plastic modules are only of 2/3 of the usual height to match the steel planes. The total ND structure has 214 planes and 20,192 cells.

Each block was assembled on the surface and mounted on wheels. A cradle was built around the erected blocks for easy and safe transportation to the NOvA site in Fermilab, where they were lowered down though the existing shaft within the building. Once underground, the blocks were moved with the wheels into the NOvA ND hall. Figure 3.10 shows a front and a back view of the fully assembled ND.

### Far Detector

The NOvA FD is located in a building on the surface in a site specially constructed for this purpose near Ash River, MN, with the beam traveling upwards at an angle of 3°. This 14 kton detector

[1]Near Detector On Surface (NDOS) was the NOvA prototype detector.

**Figure 3.10:** Front(left) and back(right) view of NOvA's near detector. The Muon Catcher can be seen at the rear of the detector [60].

has a cross-section area of 15.5 m x 15.5 m and a length of 60 m, which makes it the largest plastic structure on Earth. In the FD, each plane is formed by 12 modules, and 32 of such planes form a *block*. There are 28 blocks in the FD for a total of 896 planes and 344,064 cells.

The modules were transported to the FD site and assembled in the south-end of the detector hall. The first step to build the FD detector was lifting each module with the help of a crane to build the planes. The blocks were assembled on the block pivoter, which is a movable platform. This device moved every block horizontally to the furthest end of the detector hall and then pivoted the structure into a vertical position. The pivoter then goes back to the assembly area in its horizontal position. Figure 3.11 shows the FD being assembled with the pivoter. The construction of the FD was modular and took place in multiple stages during the first period of data taking in 2014.

Due to its surface location, the FD is subject to about 150 kHz of cosmic ray induced events. The cosmic muons are used as a standard candle for the detector calibration but are also a background for the oscillation analyses. With this in mind, the detector building is first shielded with 122 cm of concrete and 15 cm thick overburden of barite. Together, the concrete and the barite provide 12 radiation lengths of shielding which is enough to significantly reduce the cosmic ray interactions. Particle identification and containment are also used to mitigate this source of background, as described in section § 4.4.

**Figure 3.11:** Assembly of NOvA's far detector. The pivoter can be seen carrying a block to the back of the detector hall (left) and moving it into an upwards position before positioning it infront of a previously assembled block [60].

## 3.3 Data Acquisition and Timing

The aim for the Data Acquisition (DAQ) system is to read-out, digitize and archive the data for physics events of interest. NOvA's DAQ has the same architecture at both detectors since they share the same readout system. The detectors operate in constant readout mode and therefore a set of *filters* has to be applied to the collected data with each detector having its own challenges. The FD has a higher background rate not only because of its size but because of the large cosmic flux on the surface, which has a rate of about 120 kHz[2]. In the ND, approximately 5-10 neutrinos interact per 10 $\mu$s beam spill. The ND samples each channel every 125 ns to handle the higher rate of beam induced events. This sampling is four times faster than the FD readout speed. Being small in size, the average data rate at the ND is still lower than in the FD.

The pulse shaping, digitisation and pedestal subtraction happen at the FEB level which continuously reads the pulses from 32 channels. Data Concentrator Modules (DCMs) concentrate the hit information from 64 FEBs into a same time-slice. One Master Timing Unit (MTU) and ten Timing Distribution Units (TDUs) serve as timing and command systems for the DCMs. This ensures that every channel is stamped according to the same internal time and it also keeps the global detector time synchronised with an external GPS time. The DCM then transmits the data packets through a Gigabit Ethernet port to a PC from where it is buffered. A trigger system decides which data to keep. Three kinds of triggers are described below [65]. All the NOvA triggers store data for a time interval which is a multiple of 50 $\mu$s.

### Clock triggers

These store data around a specific point in time.

- NuMI data trigger: Records a 550 $\mu$s long readout centered around the 10 $\mu$s beam spill window. The triggering information is a GPS timestamp from the accelerator system.

[2]Between 60-70 cosmic rays interact in the FD within a 550 $\mu$s window.

**Signal triggers**

Receive an external signal to store data for a determined time interval.

- Cosmic pulser trigger: Stores readouts at 10 Hz in the FD for 550 $\mu$s. The data is used for calibrating the detector and in estimates of the cosmic background in the analyses.

**Data-driven triggers**

Store data during the period of time that the data satisfies specific conditions.

- DDActivity trigger: Collects readouts upon any significant activity in the ND during a 50$\mu$s period. The stored data are used for calibration and to evaluate the running conditions independently of any beam activity.
- DDEnergy trigger: Collects readouts during a 50 $\mu$s window or more if the condition keeps being fulfilled. The trigger condition is the data surpassing some total charge threshold.
- SNEWS trigger: Takes tens of seconds long readouts when receiving an alert of potential supernovae signals in our galaxy provided by the SuperNova Early Warning System [66].

### 3.3.1 FD Timing Peak

The precise synchronisation of the FD with the NuMI beamline spills is of vital importance for rejection of cosmic background in the oscillation analyses. The operation of the NOvA DAQ and triggers requires knowledge of the flight path of the neutrinos that are generated in the NuMI. Knowledge of this length allows for the computation of the propagation time required for the neutrinos to travel from their source to the FD. This propagation time is used to set the time delay used in the trigger system that determines the start point of time window for which a NuMI beam trigger is issued. NOvA uses a monitoring tool [67, 68] to verify that the FD is seeing neutrinos inside the expected time window above the background expectation, and that the signal count is consistent with the expected rate. The NuMI spill duration is nominally 10 $\mu s$ and the expected position of the neutrino interaction peak is expected inside a window ranging from 217 $\mu s$ to 229 $\mu s$ from the start of the 550 $\mu s$ long DAQ readout window.

An example of the FD timing peak monitoring tool is presented in Figure 3.12 where a distribution of selected events as a function of slice time ($\mu s$) is shown for an exposure to $3.14\times10^{20}$ POT for the antineutrino beam collected between February and July 2017. A dedicated selection algorithm is used to select events, which is different to what is used in the analyses to speed up performance. The red histogram is the total MC prediction and the lower and upper uncertainty boundary is defined with the normal or inverted mass hierarchy hypothesis. The breakdown into expected $\nu_\mu$, $\nu_e$ and NC events are represented by the solid blue, green and grey lines respectively. The background is shown by the dotted blue line, which is estimated from cosmic data. The Poisson probability of observing the number of events in the peak vs. time, given the background

estimate, is compared to a rough estimate based on the total beam exposure, and serves as a crosscheck of the detector performing as expected.

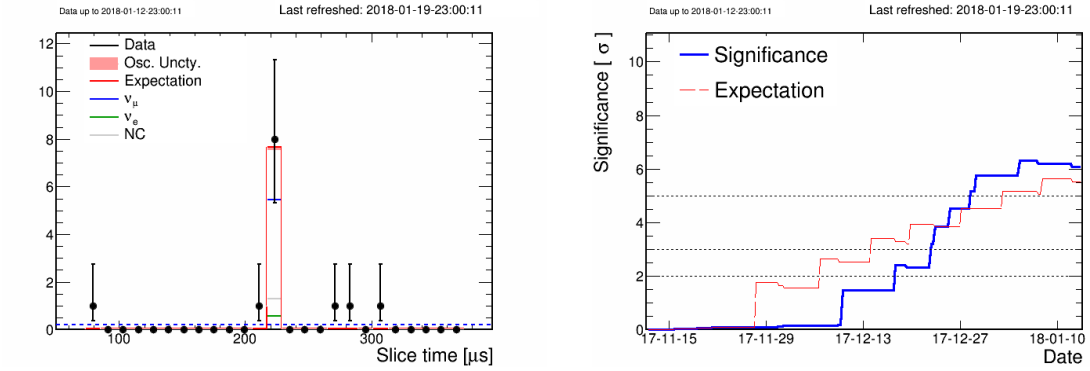


**Figure 3.12:** Far detector time peak monitoring distributions. Left: Far detector timing peak distribution of selected events as a function of slice time ($\mu s$) for an exposure to $3.14\times10^{20}$ POT with RHC beam mode. Right: Significance of the signal in the peak vs. time, compared to the expectation.

## 3.4 Simulation

Simulations are an essential tool for physics modeling and hypothesis testing. The NOvA experiment relies on predictions of the beam flux, on neutrino interactions and on the detectors' response to particles produced by the neutrinos. These simulation components are summarized in this section.

### 3.4.1 Beam

The simulation of the neutrino flux starts with a model of hadron production in the target using Geant 4.10.1 [69]. A detailed description of the NuMI beam line geometry and material composition was developed in a Geant4 based simulation called G4NuMI [70], which models the hadron focusing, interactions and decays along the beam. The simulation stores the flavour and kinematics from final state particles, as well as ancestor information.

The output neutrino flux is corrected using the Package to Predict the Flux (PPFX) developed by the MINERvA collaboration for the NuMI beam [71]. This package provides a re-weight and computes the uncertainties on the hadron production spectrum using constraints from hadron-nucleon collisions on thin targets. Figure 3.13 shows the neutrino flux at both detectors, for the neutrino and antineutrino beam configuration with PPFX corrections. It can be seen that the relative amount of $\bar{\nu}_\mu$ in the FHC configuration is lower than the $\nu_\mu$ in RHC. The contamination of $\bar{\nu}_\mu$ in the $\nu_\mu$ beam, and vice versa, is known as the *wrong-sign* component and is important for the analysis presented in this thesis.

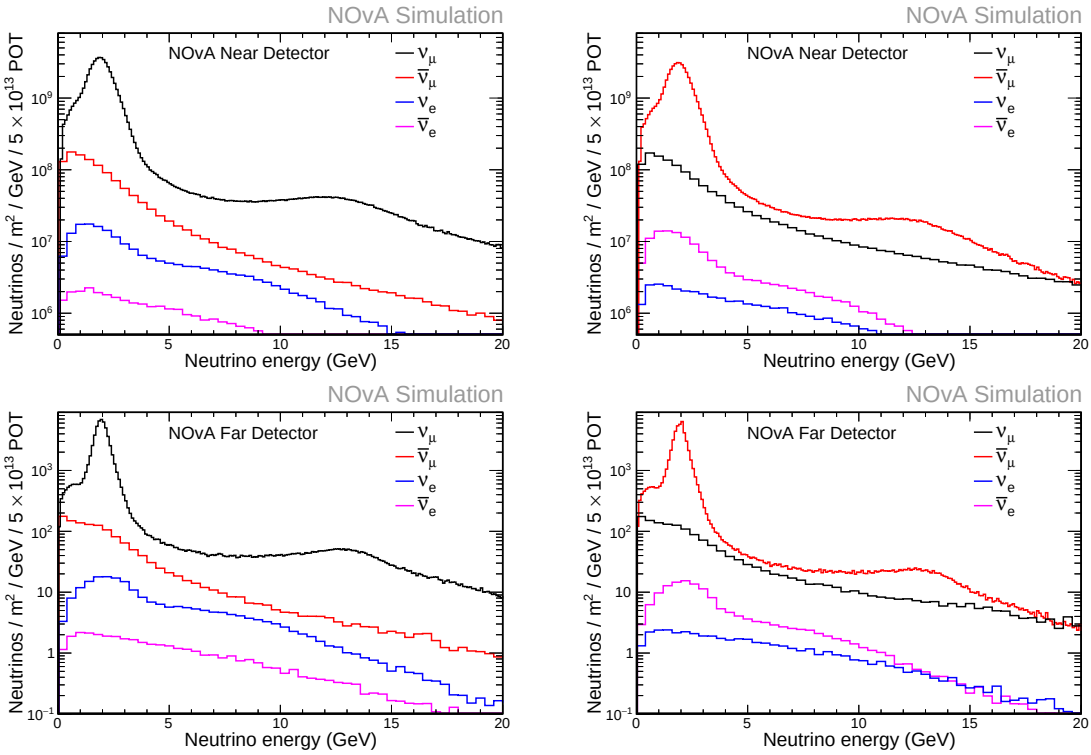


**Figure 3.13:** Predicted neutrino flux components with PPFX corrections applied at the ND(top) and FD(bottom) for the NuMI beam in Forward Horn Current (FHC, left) and Reversed Horn Current (RHC, right) configurations [61].

### 3.4.2 Interactions and Cross-section

The GENIE 2.12.2 event generator [72] is used to simulate neutrino interactions in and outside of the NOvA detectors using the predicted flux and detector geometry as input. NOvA applies weights to the GENIE simulation driven by external theory and experimental data as well as our own ND data.

The single nucleon Quasi-elastic (QE) cross-section calculated by GENIE is corrected with a Random Phase Approximation (RPA) nucleon charge screening model [73]. The RPA model is also applied to Resonance events. A 10% increase to non-resonant (Deep Inelastic Scattering (DIS)) events with Final state hadronic mass (W)$>$ 1.7 GeV is applied based on ND data. A 2-dimensional fit to data in hadronic energy and transferred 3-momentum space is performed to obtain weights for Meson Exchange Current (MEC) events, specifically 2 protons-2 holes (2p2h) events. The individual effects of the cross-section tuning are shown in Figure 3.14 on visible hadronic energy. The MEC tuning is separately performed for neutrinos and antineutrinos.

The Cosmic-ray Shower Library (CRY) generator [74] is used to simulate particles from cosmic ray showers in the NOvA detectors, which are used for calibration. Primary and secondary particles are simulated in the 1 GeV $-$ 100 TeV and 1 MeV $-$ 100 TeV range respectively.

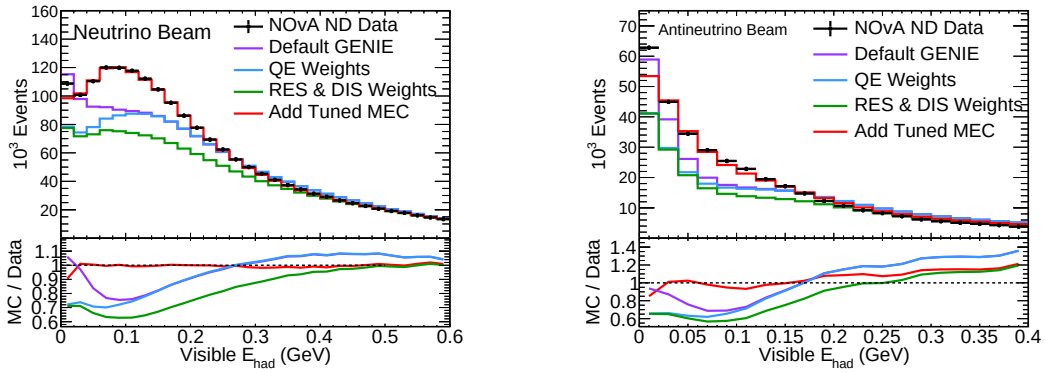


**Figure 3.14:** NOvA's cross-section tuning stages in reconstructed visible hadronic energy for selected $\nu_\mu$-CC events at the ND for the neutrino(left) and antineutrino(right) beam configurations, where the default GENIE 2.12.2 prediction is shown in purple. The effect of the RPA reweight on QE events (blue) is followed by a correction to the RES production and by a 10% increase of DIS cross-section with high W (green). The last data-driven correction is applied to MEC events (red). RPA corrections are constraints from theory and external measurements; DIS and MEC are constrained by NOvA's ND data [61].

### 3.4.3 Detector

Once the particle production from a neutrino interaction has been simulated, the propagation and energy loss of the particles within the detectors is modelled with GEANT4 [69]. The energy deposition is computed for every cell. The resulting energy from ionization is stored as FLSHits which represent the true energy deposited in the active detector material. NOvA specific software modules use this information to evaluate the light production and transport through the fibers to collection in the APDs, the electronics noise modeling, as well as the subsequent FEB response.

# Chapter 4

# Analysis methodology

Neutrino oscillation measurements often substantially benefit from placing a detector close to the neutrino production point, and a second detector far away enough to allow sufficient time for the lepton flavour change as the neutrinos propagate through space. This strategy has the advantage of reducing systematic uncertainties. In NOvA's disappearance analysis, the $\nu_\mu$ and $\bar{\nu}_\mu$ spectra at the ND are compared to those at the FD after beam divergence and acceptance corrections. A deficit between the expected number of events without oscillations and what is actually observed at the FD is the signal.

The oscillation results from the NOvA experiment involve the following calculations and measurements:

- **Measurement of selected neutrino interactions at the ND**, from real and simulated data. This information provides reconstructed energy spectra of selected unoscillated neutrino interactions.
- **Nominal prediction at the FD**, is the product of a series of steps including beam decomposition into signal and background, data/MC corrections and oscillation probability event weights.
- **Measurement of selected neutrino interactions at the FD**. This information yields a reconstructed energy spectra of selected events at the FD after oscillations.
- **Fit to model** The data is compared to the predictions at the FD according to a model at a range of specific values of the oscillation parameters and systematic uncertainties.

The work outlined in this thesis focuses on the $\nu_\mu$ CC disappearance analysis. This chapter expands on the procedure outlined above starting from NOvA's analysis software described in § 4.1. The event and energy reconstruction are explained in § 4.2 and § 4.3 respectively. The particle identification algorithms and selection of $\nu_\mu$ and $\bar{\nu}_\mu$ CC events are described in § 4.4, followed by an explanation of the analysis binning in § 4.5. The calculation of the FD cosmic background is described in § 4.6 and the procedure to compute the predictions at the FD is described in § 4.7.

Section § 4.8 gives a summary of the systematic uncertainties considered in the disappearance analysis. Finally, the oscillation model fit to data is explained in § 4.9.

## 4.1 Analysis Software

The NOvA experiment has developed the CAFAna framework [75], which provides diverse classes and functions from plotting basic spectra to fitting algorithms for oscillation analyses. CAFAna uses ND and FD Common Analysis Format (CAF) files[1] from both data and MC which are used to produce histograms. The fit is done using such histograms made from nominal simulated events as well as histograms that capture the effect of systematic uncertainties. This strategy speeds up the fitting. Histogram classes from the data analysis software ROOT [76] are accessed by CAFAna for this purpose.

The analysis presented in this document has been performed using the CAFAna framework. All the spectra including the nominal and systematically shifted predictions at the FD were created with this same software. MINUIT [77], a numerical minimization package, is also accessed through CAFAna and used for the fits to simulated and real FD data.

## 4.2 Event reconstruction

The general goal of the reconstruction process is to take the APD signal information and transform it into physically meaningful variables, such as neutrino position, energy and particle identifiers, which can be used for the analyses. This information is also used to reject other detector activity, such as noise and interactions originating outside of the detectors.

The event reconstruction for all the NOvA analyses begins with the collection of above APD threshold signals recorded as **raw hits** per cell. The raw hits store pixel information such as the ADC charge, which is a measure of energy deposition, plane and cell identifiers as spatial coordinates, and a time stamp as temporal coordinate. These hits are grouped by trigger type, detector, run and subrun numbers, and stored in data files. Monte Carlo simulation files contain the same attributes plus the information with which the events were generated[2], which is mapped to reconstructed objects. Next, the knowledge of the detector response is used to convert the raw data into **calibrated hits**, called *CalHits*. Up to this point it is still undetermined if the recorded cell activity is due to electronics noise, *noise hit*, or by an actual particle interaction, *signal hit*.

The data is clustered into sets of hits which are close in space and time. This process, referred to as *slicing*, groups hits using the density-based Slicer4D clustering algorithm [78, 79] to form a *slice*. This algorithm separates hits found in the same high-density space-time region from hits that are isolated, the latter being labeled as noise. For the oscillation analyses, we are interested

[1] CAF files contain information from the simulated flux such as parenthood, physics and kinematics variables stored as ntuples of the data analysis software ROOT.

[2] This is known as *truth information*.

in both beam events and the cosmic rays (either to reject them or to use them for calibration). For this purpose, the slices are input to two reconstruction algorithms: a Kalman tracker used to isolate and measure the muon in $\nu_\mu$ and $\bar{\nu}_\mu$ CC candidates, and a cosmic tracker used for the identification of cosmogenic events. These algorithms are described below.

Given that the cells span the full width of the detectors, each cell hit can only give 2-dimensional information about the particle trajectory. To achieve a 3-dimensional event reconstruction, the reconstruction methods use two 2-dimensional reference systems with a common axis. The common $z-$axis runs parallel to the beam axis. The $x-$axis and the $y-$axis are horizontal and vertical traverse coordinates respectively. Therefore, a top view of the detector, referred to as *x-view*, is provided by the location of the vertical cells in the $x-z$ plane. A side view of the detector, referred to as *y-view*, is provided by the location of the horizontal cells in the $y-z$ plane. Figure 4.1 shows a schematic of the NOvA detectors which explains the two detector views.

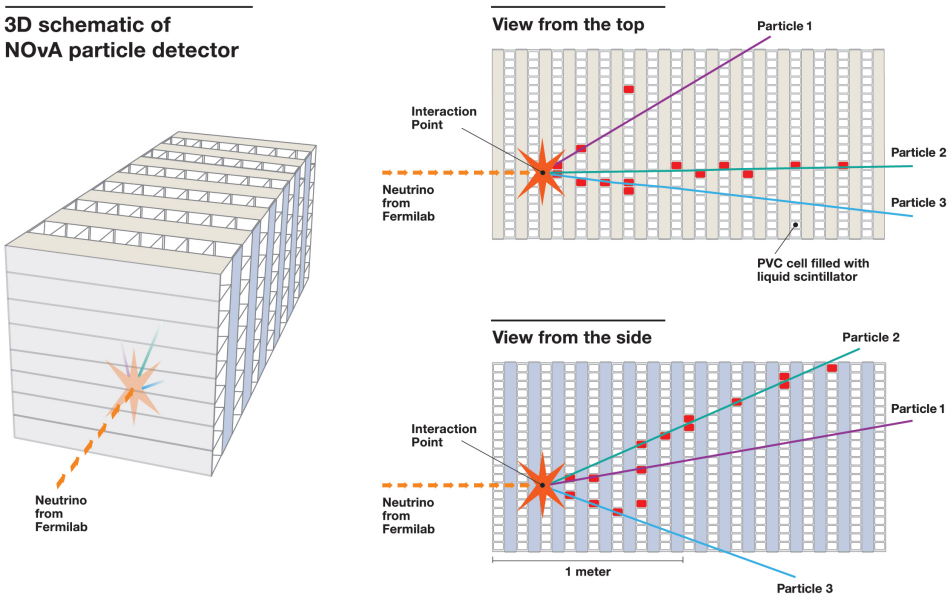


**Figure 4.1:** Schematic of the NOvA detector showing the array of horizontal and vertical planes. The alternating plane orientations allow for a 3-dimentional track reconstruction when combining the top and side detector views [60].

### 4.2.1 Kalman tracker

The Kalman tracker [80] uses a technique based on the Kalman filter algorithm [81] to reconstruct individual particle tracks within a slice. Narrow and straight tracks with little scattering are the characteristic signature from $\mu^{+,-}$ interactions, which are used to identify $\nu_\mu$ and $\bar{\nu}_\mu$ events. This method separately reconstructs tracks for each of the two 2-dimensional detector views. Later on, the detector views are matched into a single 3-dimensional track. The tracking process starts from the downstream end of the detector, where the tracks are on average more separated from each other. Slice hits are added to the track and the propagation is continued in the upstream direction

until no more hits satisfy the filter separation and probability conditions. Next, the propagation is reversed to recover any missing hits from the first scan. An example event at the FD with tracks reconstructed with the Kalman tracker is shown in Figure 4.2.

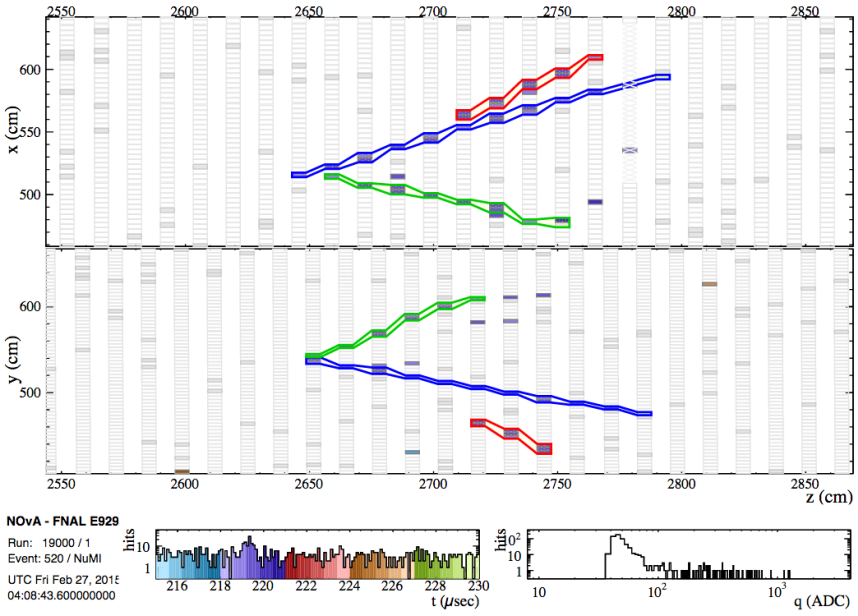


**Figure 4.2:** Example of simulated reconstructed tracks at the FD implementing the Kalman tracker algorithm. Each colour represents an individual track which is part of a single event. The $x-z$ and $y-z$ views of the detector are shown at the top and bottom halves of the image [80].

### 4.2.2 Cosmic tracker

The cosmic tracker [82] uses a sliding-window tracking algorithm to fit a single line to downward going particles traversing the detectors. This method was designed to quickly process single-particle events due to cosmic ray activity. The algorithm begins with a set window of $n$ planes in the $z$ direction. A straight line fit is performed to the hits contained in this window of planes, where the hits consistent with the best fit are added to a two dimensional track. This process is repeated after moving the window one plane at a time in the downstream direction, and it ends once all the planes in the slice have been covered. Similarly to the Kalman tracker, the cosmic tracker first reconstructs particle tracks in each of the detector views and then matches them together for a 3D track event reconstruction.

## 4.3 Energy reconstruction

The total energy of reconstructed $\nu_\mu$ and $\bar{\nu}_\mu$ CC candidate events is calculated by energy estimators which separate the muon from the hadronic component in the interaction. The $E_{\nu_\mu}(E_{\bar{\nu}_\mu})$ reconstructed energy of a $\nu_\mu$ ($\bar{\nu}_\mu$) interaction in the NOvA detectors is estimated from the $\mu(\bar{\mu})$ energy, $E_{\mu(\bar{\mu})}$, and the sum of the hadronic system energy, $E_{Had}$, such that

$$E_{\nu_\mu,\bar{\nu}_\mu} = E_{\mu,\bar{\mu}} + E_{Had}, \tag{4.1}$$

where $E_{\mu(\bar{\mu})}$ is estimated from track length and the $E_{Had}$ is obtained from calorimetry by summing the visible calibrated energy of each cell of the hadronic system. The calorimetric energy calibration is described in the following subsection.

Figure 4.3 shows the linear piece-wise fits used to convert simulated to reconstructed muon track length, and visible to reconstructed hadronic energy. The events in NOvA have an average muon and hadronic resolution of about 3.5% and 30%, respectively. The energy resolution of neutrino events selected for the disappearance analysis with the beam in FHC (RHC) mode is 9.1% (8.1%)[3]. As expected, a predominantly $\bar{\nu}_\mu$ sample has a better energy resolution due to the lower hadronic energy fraction of those events.

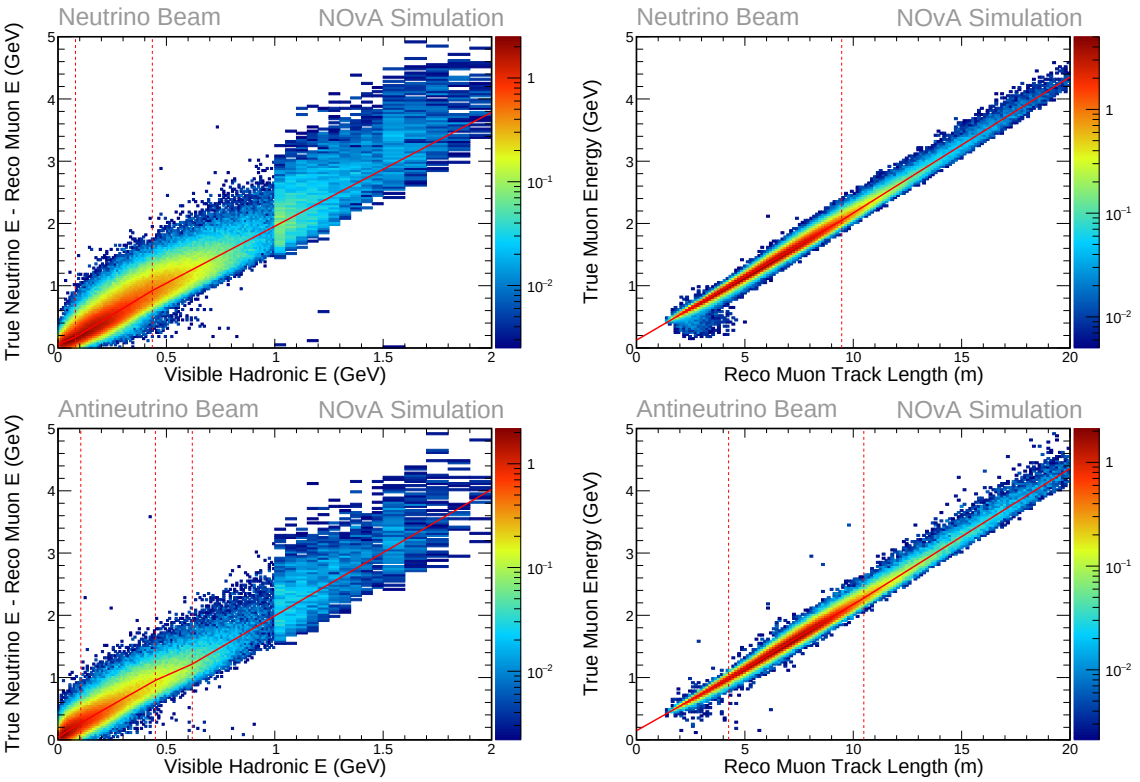


**Figure 4.3:** Linear piece-wise fits for the estimation of the hadronic (left) and muon energy (right) at the FD, for the beam in the FHC (top) and RHC (bottom) beam mode. The linear piece-wise fits are shown by the solid red line. These lines on the left plots are overlaid with the density distribution of (true neutrino energy - reconstructed muon energy) vs. (visible hadronic energy), and those on the right plots are overlaid with the density distribution of true muon energy vs. reconstructed muon track length on which the fit was performed [61].

[3]These numbers are the raw RMS value of (reconstructed-true)/true neutrino energy for selected true $\nu_\mu$ and $\bar{\nu}_\mu$ CC events.

### 4.3.1 Calorimetric energy calibration

Cosmic ray muons are a source of fairly uniform energy deposits across the detectors and therefore are used for the calorimetric energy calibration. Cosmic muons are easily identified by downward going tracks and their energy loss by ionization is well understood from the Bethe-Bloch equation. The tracks used for calibration are required to pass quality cuts to remove those with badly reconstructed positions, and only *tricells* are selected. Tricell hits are defined as cell hits having an adjacent hit in the two neighbouring cells as sketched in Figure 4.4. This requirement ensures that the path length inside of the central cell can be determined with accuracy and decreases the probability of using noise hits.

The detector calorimetric calibration is separated in two steps. The first step is the relative calibration, that attempts to ensure the detector response is independent of the position of the registered activity. Once the detector position dependency has been removed, the absolute calibration follows. This second calibration step uses stopping muons to provide conversion factors that translate energy deposits into physically meaningful units of GeV. The relative and absolute calibrations are described next.

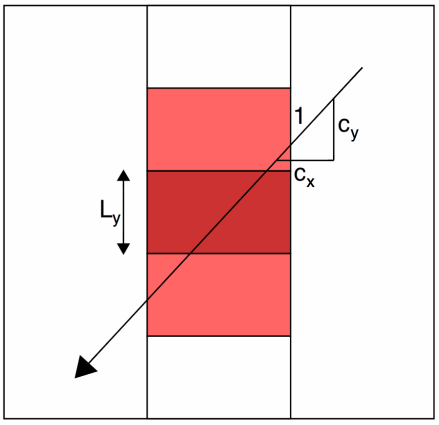


**(a)** Schematic of a tricell hit. The dark-red cell is selected because each of its neighbours is hit. The path length is the width of the cell $L_y$ divided by the direction cosine $c_y$.

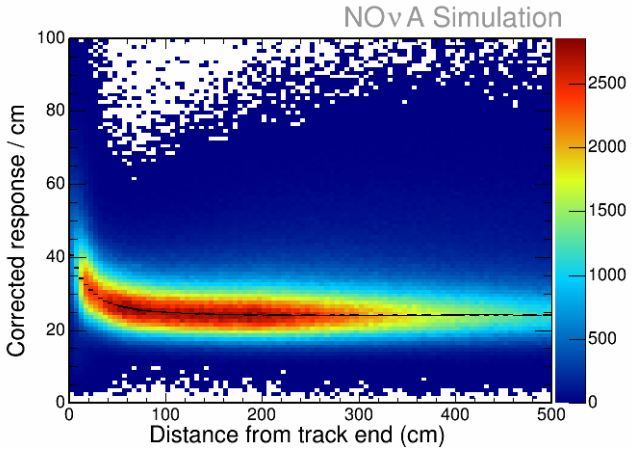


**(b)** Simulated detector response vs. distance to the end of the track. Tricell density is represented by colour. Only tricell hits within 100-200 cm from the track end are used for the absolute calibration.

**Figure 4.4:** Schematic of a tricell hit (left) and simulated detector response (right) [61].

#### Relative calibration

The charge output from NOvA's APDs is digitised by Analog Digital Converters (ADCs). Using the average expected APD response, integrated charge from the ADCs are converted to units of Photo-Electrons (PEs) and used as input for the first calorimetric calibration stage.

There are three effects that affect the PE counting, namely threshold, shielding and attenuation

effects. The first is based upon the electronic threshold, which can lead to a mis-counting of hits. This is a consequence of lower energy hits having to undergo a fluctuation upwards to be detected. Self shielding means that the muon's energy deposition is not uniform across the detectors, as less energetic particles are less likely to make it to the bottom of the detector. Light attenuation occurs as light travels through the Wavelength Shifting (WLS) fibers. The light from ionization at the far end of the cells will travel a longer distance than that of activity closer to the read-out. This effect is larger at the FD. The relative calibration aims to correct these effects and remove any hit position dependence.

The relative calibration [83] is made at the cell level and for each detector and period of data collection. It first creates threshold and shielding correction factors as a function of view and $W$ position defined from the center of the cell. These corrections are applied before attenuation corrections. The attenuation calibration then provides fit functions to translate number of PE to corrected PE. Figure 4.5 shows a example of attenuation correction at the FD .

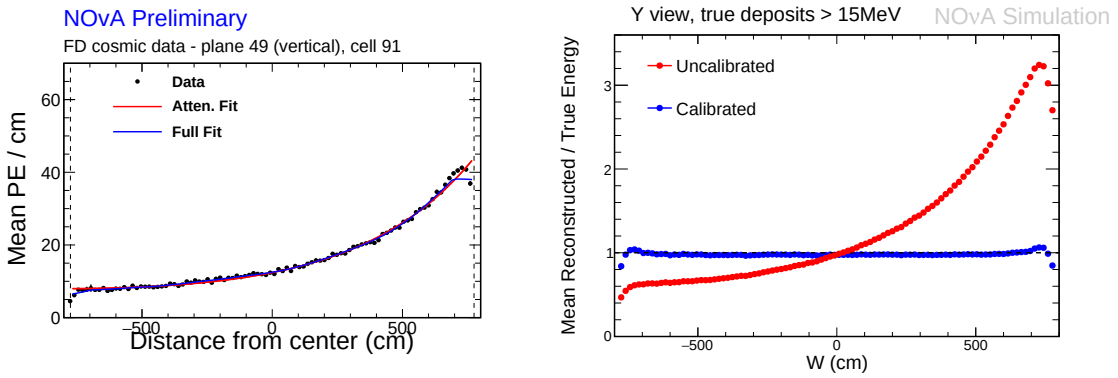


**(a)** Fit **(b)** Correction

**Figure 4.5:** Example of fit for light attenuation correction at the FD. Left: Profile of simulated detector response over centimeter as function of hit position with respect to the center of the cell, $W$, where a fit to data (black dots) is performed. Right: Profile of simulated reconstructed over true energy as function of $W$, where simulated hits pre and post attenuation calibration are shown in red and blue dots respectively [61].

### Absolute calibration

The calorimetric energy calibration, or absolute calibration, provides factors to convert the detector response to energy in GeV units. The average cosmic muon energy loss varies by only 1.8% in the 100-200 cm region from the end of the track. This range sits right on the minimum energy loss region and away from the end point so tricell hits within that distance of the track end are selected at this stage.

The results of the stopping muon calibration are expressed by defining Muon Energy Units (MEUs). The MEU is defined as the mean detector response in units of PECorr (or simulated energy deposition in MeV) to a stopping muon tricell hit within the track window divided by the length of the track inside the cell. Three MEU values are defined for each detector and period of

data taking and simulation: the detector response in the data, the detector response in the MC and the simulated energy deposition in the MC. The energy scale factor to convert PECorr to GeV is explicitly calculated as

$$\text{Calorimetric energy scale} = \frac{MEU_{truth}}{MEU_{reco}} \tag{4.2}$$

where $\text{MEU}_{truth}$ and $\text{MEU}_{reco}$ are the mean of the distributions of MeV/cm (in MC) and PECorr/cm (in both data and MC) respectively. Figure 4.6 shows an example of MEU distributions used the calibration, and the result of their application for the absolute calibration.

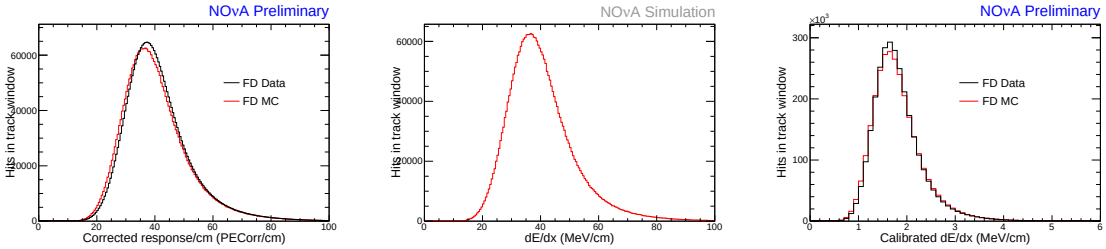


**Figure 4.6:** Uncalibrated and calibrated detector response spectra as used for the calorimetric energy scale calibration at the FD, with data represented in black and Monte Carlo in red. The distribution of data and simulated tricell hits as a function of corrected detector response is shown at the left, and the distribution of simulated tricell hits as a function of true energy deposited is shown in the middle. The mean of these three distributions is used to convert corrected PE into GeV units and the resultant distributions of calibrated data and simulated tricell hits are shown at the right [84].

## 4.4 Event Selection

The event selection is divided into four groups of cuts with a specified purpose. Data quality cuts are applied to the samples to ensure that they pass some basic requirements. Containment cuts ensure that secondary particles carrying energy out of the detector are not counted as signal. Therefore, only events whose full interaction energy is deposited in the detector are accounted for. Events that are likely a product of cosmic activity are also removed from the sample by a cosmic rejection cut. Particle identifiers are used to reduce the background and to look for events whose topology matches that of a $\nu_\mu$ or $\bar{\nu}_\mu$ CC events. Figure 4.7 shows a chart demonstrating the change in number of selected events as the quality, containment, cosmic and particle identification cuts are applied in sequence. These cuts are described in more detail below.

### 4.4.1 Data quality

The data quality event cuts account for possible electronics and data acquisition issues, as well as for changes in the state of the detector during the data collection. These cuts also provide a first pass to well reconstructed events. The selection requires at least 20 hits in the slice, activity in four contiguous planes and at least one track with a non-zero ReMId score [85] (see § 4.4.4 for ReMId

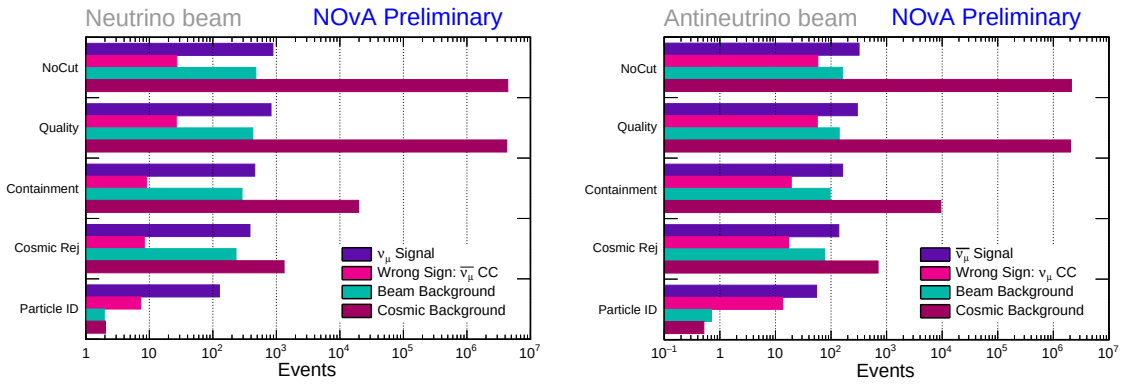


**Figure 4.7:** Bar chart showing the change in number of selected events from the FHC(left) and RHC(right) beam as the quality, containment, cosmic and particle identification cuts are sequentially applied to FD oscillated predictions and cosmic data. The predicted number of events and the wrong sign component are represented by the purple and pink bars respectively. The predicted beam background is shown in light green and the cosmic data background is shown in dark red [61].

definition). It also removes events occurring with a drop out DCM during the spill. Likewise, the selection cuts out events where there is an excess of tracks stopping at DCM edge boundaries, which could mean that the DCM is not synchronized with the rest of the detector [86].

In addition to the basic data quality selection, other criteria ensure that the beam conditions are within acceptable bounds. The *good spill* selection requires a vertical and horizontal spill position with respect to target center between -2 mm and 2 mm, spill width in the range (0.57,1.5) mm, horn current in the range (-202, -198) kA and spill POT $> 2 \times 10^{12}$ [87].

### 4.4.2 Containment

A set of containment cuts are applied with the purpose of selecting events where their energy is fully deposited within the detectors, and to reject background from cosmogenic events or neutrino-induced activity originating outside of the detectors. The containment selection differs between detectors given their particular size, geometry and cosmic ray rate.

The containment requirement in the ND are for any showers to be fully contained in the detector, with the shower start and end positions in the -180 cm$< x, y <$180 cm range, and in 20 cm$< z <$1525 cm. In addition, the primary track is required to start(end) at $z <$1100(1275) cm. A loose track projection cut requires at least 5(10) hit-less planes projected forwards(backwards) from the track end(start) to the edge of the detector. Given that the height of the muon catcher is 2/3 of the main active region, tracks which are estimated to have crossed the top 1/3 *air gap* are also rejected.

At the FD, events with activity too close to the detector edges[4] or with a projected distance from a track end to the edge of less than 6 cells, are rejected. The projection cut in this case requires at least 6 hit-less planes projected forwards (backwards) from the track end (start) to the

[4]60 cm to the top, 12 cm to the bottom or west, 16 cm to the east, 18 cm to front or back

edge of the detector. In addition to the containment selection, additional physics variables are applied at the FD: Kalman track angle $> 0.5$, projected transverse momentum $< 0.9$ and less than 400 hits in the slice. These criteria allow further rejection of largely vertical events, which are most likely cosmic background.

### 4.4.3 Cosmic rejection

Cosmic rays are one of the largest potential sources of background to the disappearance analysis as a cosmic muon can mimic the $\nu_\mu$ and $\bar{\nu}_\mu$ signatures. Furthermore, the FD is located at the surface and cosmic muons interact inside it at a high rate. A supervised learning regression model Boosted Decision Tree (BDT) is used for cosmic rejection [88]. This BDT is a Particle Identifier (PID) that relies on information from the cosmic and Kalman tracks, and on the ReMId and CVN cosmic scores (see § 4.4.4 for definition of ReMId and CVN). The BDT is trained on Monte Carlo simulations and cosmic trigger for data. The algorithm takes Kalman tracks with the highest ReMId in the slice, which serves to identify the primary lepton. It also uses reconstructed variables such as the angle between the lepton and the neutrino, the direction and length of the muon track, the maximum height of activity within the detector, the number of cells projected from the start (end) of the track backwards (forwards) to the edge of the detector, and the number of hits in the selected Kalman track and in the slice. Additionally, the CVN cosmic score is input to the training. A ReMId$> 0.75$ pre-selection plus containment cuts are applied to the signal to remove cosmic like events. The $\nu_\mu$ and $\bar{\nu}_\mu$ selection requires events with values of **BTD**$> 0.53$. The cosmic rejection is only applied at the FD.

### 4.4.4 Particle Identification

NOvA's disappearance analysis uses a combination of Particle Identifiers (PIDs) to discriminate between signal and background. Two PID, ReMId and CVN, are used to accurately identify neutrino interactions with a muon-like particle in the final state for the identification of $\nu_\mu$ and $\bar{\nu}_\mu$ CC events. Figure 4.8 shows an example of a simulated $\nu_\mu$ CC, $\nu_e$ CC and NC event at the FD. $\nu_e$ CC events are typically accompanied by an electromagnetic shower coming from the final state electron. The $\pi^{+,-}$ are very occasionally mistaken for muons when they come from $\nu_e$ CC interactions. NC interactions, where $\pi^{+,-}$ are produced, can be misidentified as a $\mu^{+,-}$. NC interactions can also produce a $\pi^0$ which can shortly decay into two $\gamma$ with undistinguished independent tracks. This is not an issue to identify $\nu_\mu$ CC events but it is for $\nu_e$ CC.

#### Convolutional Visual Network

Convolutional Visual Network (CVN) [89] is an event classifier based on a Convolutional Neural Network (CNN), which mimics how the brain transmits information and performs decisions. The identifier takes each detector view of the event before any further reconstruction, and treats each as an image. Each cell in the event corresponds to a pixel in the image, and each pixel is assigned

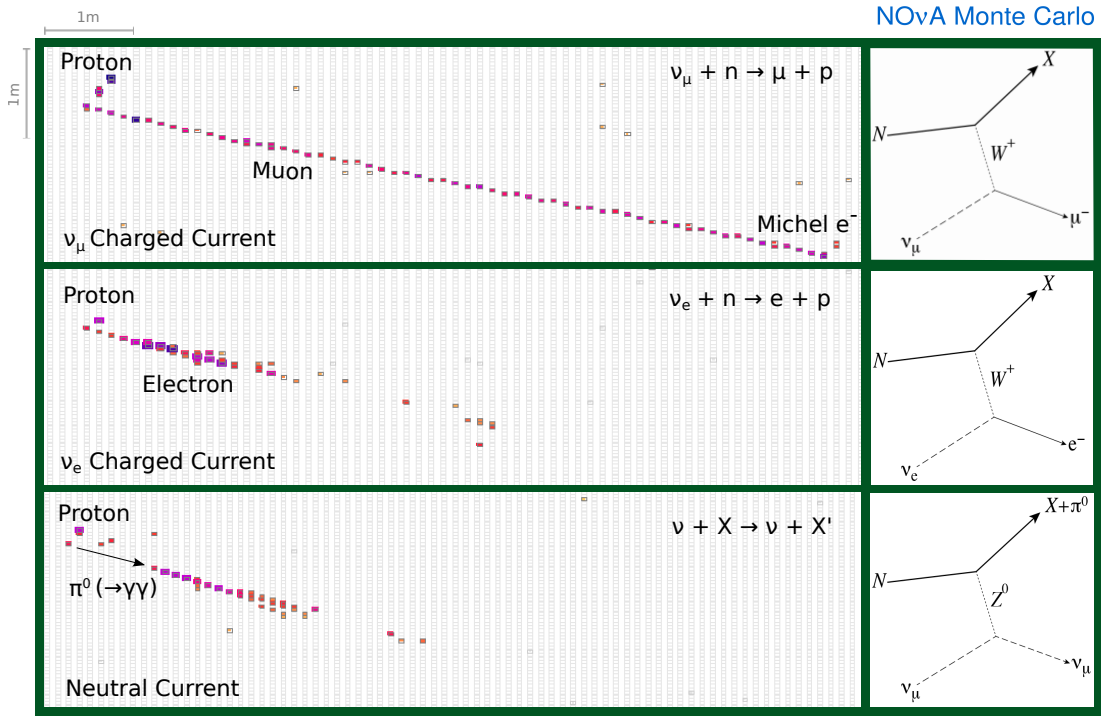


**Figure 4.8:** Simulated event topologies in the NOvA FD, from $\nu_\mu$ CC (top), $\nu_e$ CC (middle) and NC (bottom) events. The simulation assumes a 2.15 GeV neutrino interacting at the FD and the consequent production of a 0.78 GeV proton plus other particles(s). The cells are coloured by charge deposition [61].

an intensity which is proportional to the calibrated charge.

The classifier is trained over simulated events and cosmic ray data, and performed independently for the FHC and RHC beam modes. The training and data samples are passed into a simplified GoogLeNet [90] network architecture to decrease the required computational resources while preserving the recognition performance. Figure 4.9 shows an example of features extracted from a neutrino interaction, from which CVN can identify features such as a muon track, electromagnetic showers and hadronic activity. Separate trainings are performed for $\nu_\mu$ CC, $\nu_e$ CC, NC and cosmic events. An event is assigned a score in the (0,1) range, where the closer to 1 the more the event resembles one of the listed interactions. The $\nu_\mu$ CVN PID output is also shown in Figure 4.9. The $\nu_\mu$ + $\bar{\nu}_\mu$ selection requires events with values of **CVN**$> 0.7$ and values of **2017 CVN**$> 0.1$, where the later refers to the PID output value from the 2017 analysis training. The later cut was introduced after observing a decrease of almost 50% in the cosmic induced background at the FD, with almost no loss of signal [91].

### ReMId

Reconstructed Muon Identification (ReMId) [93] is a k-Nearest Neighbour (kNN) classifier which takes the track related variables to assign a score to an event depending on its $\nu_\mu$ or $\bar{\nu}_\mu$ CC likeness. Four variables are used for this process: $dE/dx$ log-likelihood (LL), scattering LL, track length

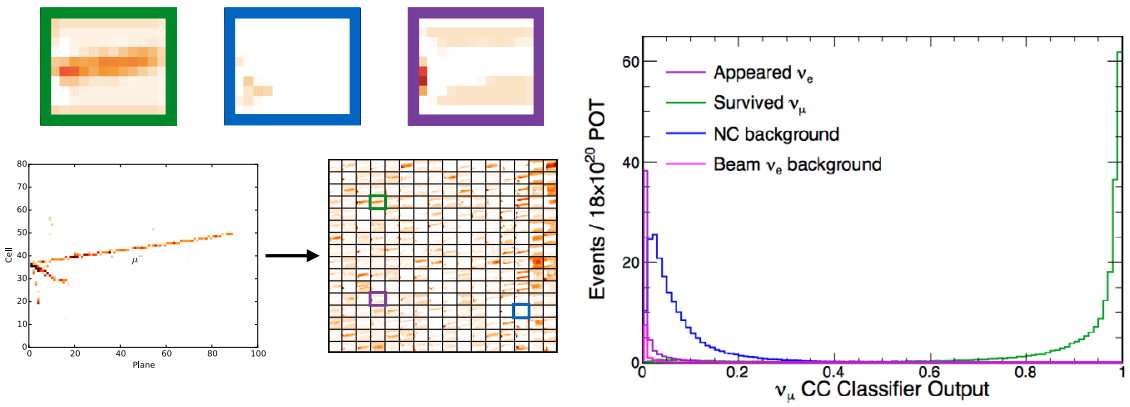


**(a)** Input image to CVN from a simulated $\nu_\mu$ CC event at the FD (bottom left) and the feature maps extracted from the event (bottom right). CVN identifies features such as a muon track, electromagnetic showers or hadronic activity(green, blue and purple boxes at the top, respectively).

**(b)** CVN output score. The distribution of scores for simulated $\nu_\mu$ CC candidates are shown in green. Simulated NC events, and intrinsic beam and appeared $\nu_e$ backgrounds are represented by the blue, purple and pink distributions [92].

**Figure 4.9:** Example of an input event and features extrated from the CNN (left) for the CVN classifier and distribution of scores (right) given to simulated events at the FD [92].

and plane fraction.

The **dE/dx LL** uses the energy deposited by a charged particle per unit length in the detector. The $\mu^{+,-}$ and $\pi^{+,-}$ expected $dE/dx$ profiles are different. In the case of the muons, the $dE/dx$ curve follows the Bethe-Bloch equation as a function of the particle's energy, and it differs from that of a pion in that the later is described by a combination of the Bethe-Bloch process and hadron scattering. In a similar way, the **scattering log-likelihood** looks at deviations of the track from a straight line. As the NOvA detectors are not magnetized, the muons can only deviate from a straight line due to Coulomb scattering. Pion tracks can additionally scatter through strong interactions. Therefore, the $dE/dx$ and scattering log-likelihood tests the muon or pion hypothesis and assigns a score to the event. Pions generally have shorter tracks while the muons can be recognized by longer tracks. Therefore, the reconstructed **track length** provides additional particle identification. Some cells have both muons and pions or protons pass-through. Consequently, the number of planes with no hadronic activity out of the total number of planes in the event, **non-hadronic plane fraction**, is a measure of the hadronic nature of the event as the larger the fraction the less hadronic the interaction. The non-hadronic plane fraction is also used by ReMId.

ReMId is trained with simulated muon tracks from $\nu_\mu$ CC events and tracks from NC events, which play the role of signal and background, respectively. Figure 4.10 shows the kNN output

numbers which range between 0 and 1, where the higher the outcome the more likely an event is to be the result of a $\nu_\mu$ or $\bar{\nu}_\mu$ CC interaction. The spikes in the plane fraction distribution arise from the discrete nature of the number of planes crossed and the number of planes with $dE/dx$ measurements [94]. The $\nu_\mu$ + $\bar{\nu}_\mu$ CC selection requires events with values of **ReMId**> 0.7.

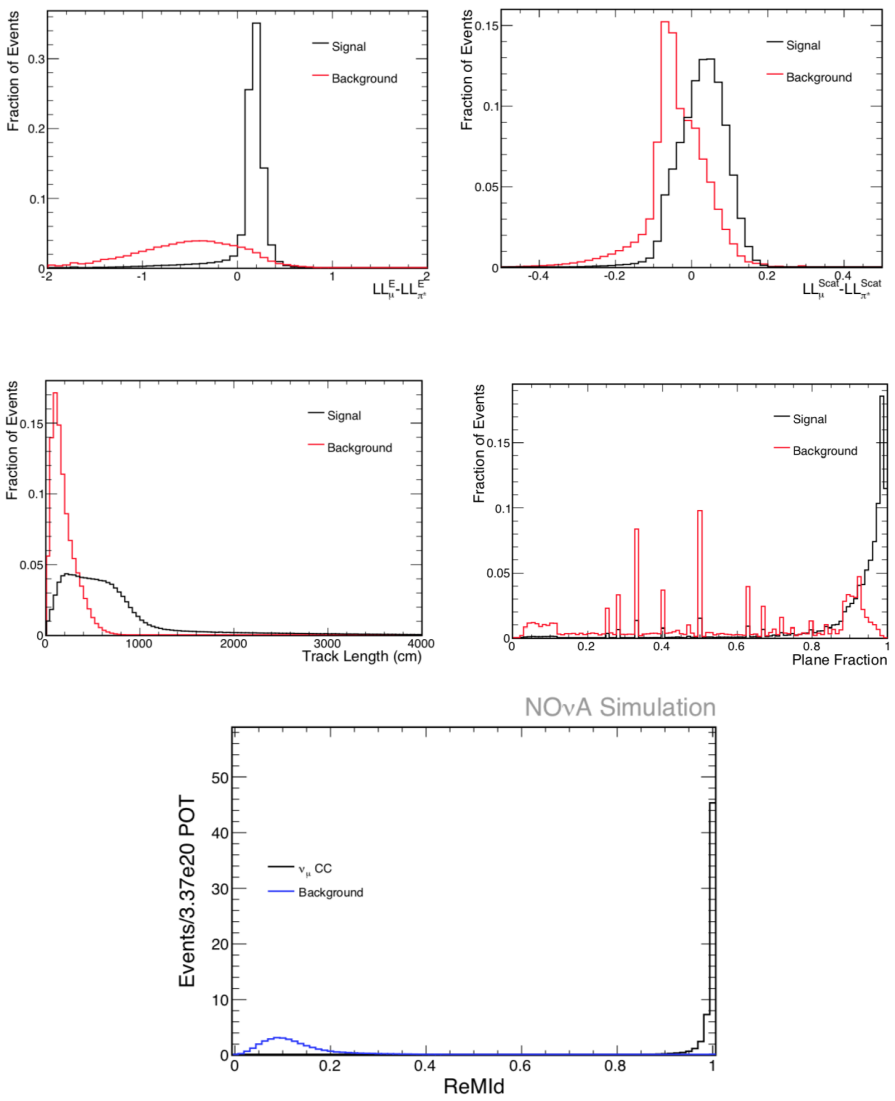


**Figure 4.10:** Distributions of input variables and output scores from the ReMId PID FD from the beam in FHC mode. The simulated distributions of the kNN input variables: $dE/dx$ log-likelihood, scattering likelihood, track length and plane fraction are displayed at the top two rows. The result from the kNN algorithm is a ReMId score between 0 and 1, shown at the bottom [94].

## 4.5 Analysis Binning

Given that the $E_{\mu^{+,-}}$ and $E_{Had}$ energy resolution is 3.5% and a 30% respectively, the hadronic energy fraction $E_{Had}/E_\nu$ provides a measure of event energy resolution. The prediction of $\nu_\mu$CC events at the FD in absence of oscillations is used to divide the real and simulated near and

far detector data such that 25% of the events are placed in one of four *quartiles* of hadronic energy fraction or *energy resolution bins*. Two mutually exclusive distributions of hadronic energy fraction vs. reconstructed neutrino energy, one for the FHC and one for the RHC mode, are used to determine the boundaries that separate the samples into quartiles. With this approach, events with a low hadronic component are placed in the 1st quartile, or best energy resolution bin, and highly hadronic events are placed in the 4th quartile, or worst resolution bin. This strategy is important for the $\nu_\mu$ and $\bar{\nu}_\mu$ analysis as events with worse (better) energy resolution are more (less) likely to migrate between bins of reconstructed neutrino energy, which smears out oscillations.

The analysis presented in this thesis uses quartile boundaries computed with all the available FD Monte Carlo up to Summer 2018: periods 1,2,3 and 5 for FHC, and periods 4 and 6 for RHC. Figure 4.11 shows the density distribution of selected true $\nu_\mu$ and $\bar{\nu}_\mu$ CC events, as a function of hadronic energy fraction vs. reconstructed neutrino energy, which are used to determine the quartile boundaries for the FHC and RHC specific samples. These density plots show that the RHC boundaries occur at lower hadronic energy fractions than those for FHC, which is expected due to the left-handed nature of the weak interaction. The neutrino energy resolution for each FHC (RHC) quartile is, from 1st to 4th, 5.8% (5.5%), 7.8% (6.8%), 9.9% (8.3%), 11.7% (10.8%).

The reconstructed energy binning has been optimised for the disappearance analysis. Narrow bins are used around NOvA's maximum disappearance region, and wider bins where the oscillation is expected to have less significance in the fit [95]. A total of 19 bins of reconstructed energy are used in the (0,5.0) GeV range with the specific bin edges at (0, 0.75, 1, 1.1, 1.2, 1.3, 1.4, 1.5, 1.6, 1.7, 1.8, 1.9, 2, 2.25, 2.5, 2.75, 3, 3.5, 4, 5) GeV.

The ND and FD samples are both split into quartiles following the same boundaries, and each population uses the reconstructed neutrino energy binning. Therefore, a total of $4 \times 2$ energy spectra (4 quartiles for each of the two beam modes) are implemented in the analysis. This results in a fit to $4 \times 19$ or $8 \times 19$ bins, the former in the case of a fit to a single beam data set and the later case for a combined fit with data from the neutrino and antineutrino beams.

## 4.6 Estimation of Cosmic Induced Events at the FD

It is possible for some amount of cosmics to pass the cosmic BDT cut and make it into the analysis sample (see § 4.4.3 and Figure 4.7). A data-driven cosmic background prediction is computed with real FD operating conditions during the collection of beam data. The data from two triggers is used and required to pass the $\nu_\mu$ and $\bar{\nu}_\mu$ selection. Data from the **NuMI trigger** sidebands[5] is used to provide a count of selected events outside of the beam spills. This number is scaled by time to match the sum of beam spill time windows. A reconstructed energy spectrum is constructed from the **cosmic trigger** sample and is area normalized by the number of expected

[5]Refers to time intervals inside of the 550 $\mu s$ time window triggered by the NuMI spill but away from the start and end of the 10 $\mu s$ beam spill.

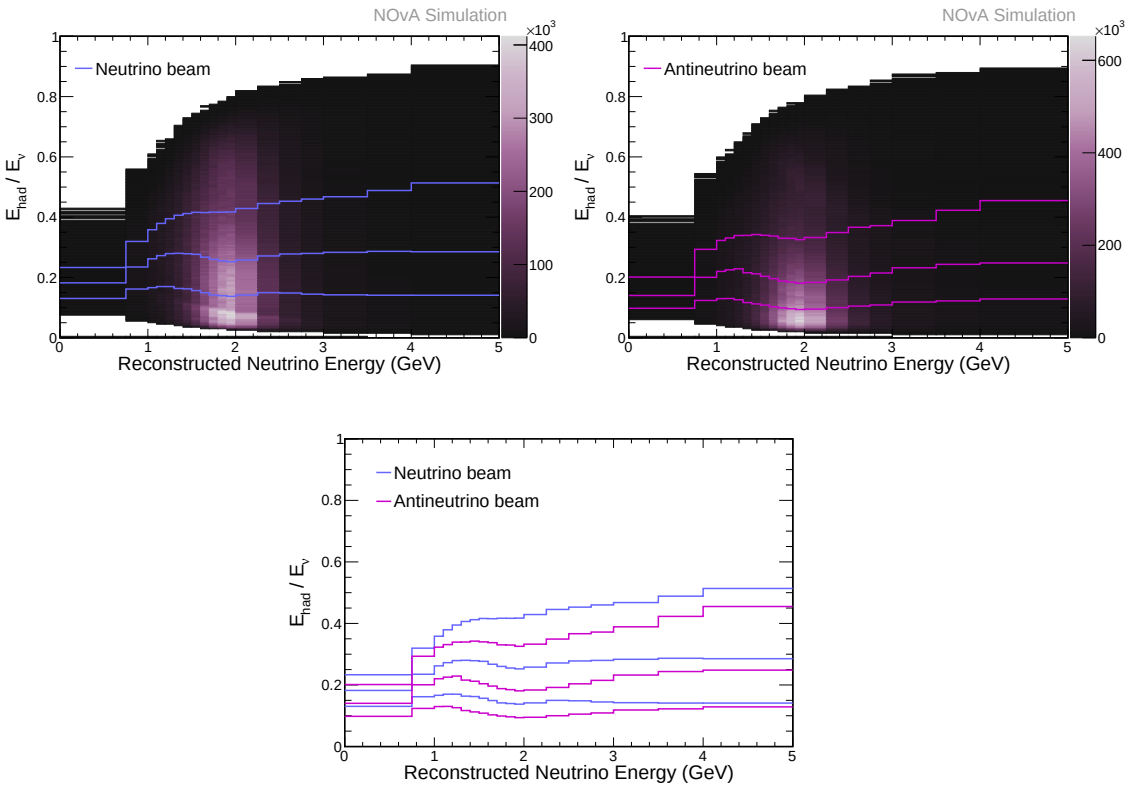


**Figure 4.11:** Histogram of reconstructed neutrino energy vs. hadronic energy fraction for selected muon neutrino and antineutrino Monte Carlo events in the FD. The pixel colours represent event density. The solid lines show the bin boundaries that split the neutrino and antineutrino samples into 4 quartiles (top left and top right, respectively). The quartile boundaries for FHC (blue) and RHC (pink) events are shown together in the bottom plot to emphasize the difference between the neutrino and antineutrino samples.

events. This approach is taken as the cosmic trigger data has almost 10 times the statistics of the NuMI sidebands so it provides a more accurate shape of the cosmic background distribution. This procedure is performed for the FHC and RHC beams, and is separated by bins of hadronic energy fraction.

## 4.7 Predictions at the FD

NOvA's strategy for computing accurate prediction of reconstructed neutrino energy spectra at the FD relies on ND data measurements to constrain the simulation. A *decomposition* technique uses the Monte Carlo to assign fractions of the selected ND data events to the neutrino flavour components in the simulation, such as $\nu_\mu$ and $\bar{\nu}_\mu$. An *extrapolation* technique is used following the results from the ND decomposition and oscillation probability weights are applied to each beam component. This means that the neutrinos and antineutrinos can be oscillated differently. This strategy provides improved estimates of the $\nu_\mu$ or $\bar{\nu}_\mu$ signal at the FD and has the advantage of cancelling the systematic uncertainties that have a similar effect at both detectors. The error on the oscillation parameter measurements is reduced as a result.

The simulation of the oscillated FD spectra uses CAF files. These files are separated by detector and beam configuration. The simulated nominal ND sample is stored in files called ND *non swap*. There are three kinds of simulated samples for the FD: samples which are predominantly $\nu_\mu$ and $\bar{\nu}_\mu$ events, samples where $\nu_\mu$ ($\bar{\nu}_\mu$) have been replaced with $\nu_e(\bar{\nu}_e)$ and vice versa, and samples where $\nu_\mu(\bar{\nu}_\mu)$ have been swapped for $\nu_\tau(\bar{\nu}_\tau)$. These files are referred to as FD *non swap, flux swap* and *tau swap* respectively. The FD flux swap sample assumes that all the $\nu_\mu$ and $\bar{\nu}_\mu$ oscillated into $\nu_e$ and $\bar{\nu}_e$ to simulate the appearance signal. The FD tau swap sample follows the same idea for appeared $\nu_\tau$ and $\bar{\nu}_\tau$. Oscillation probability weights are applied to each event to normalise the distributions to the required level. Figure 4.12 shows a cartoon of the whole extrapolation procedure. This process is performed separately for each beam mode and quartile. A detailed description of the procedure can be found in Appendix A.

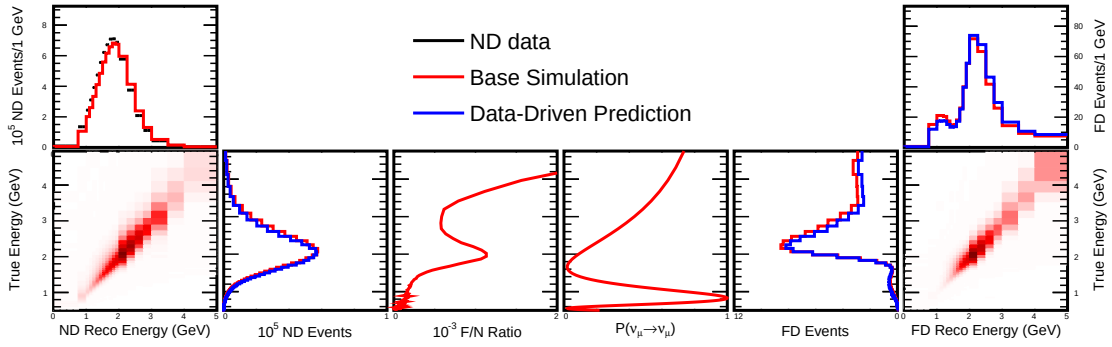


**Figure 4.12:** Diagram illustrating the steps to obtained FD predictions from ND constraints from left to right. The ND data is used to correct the nominal prediction. A matrix is used to convert the spectra from reconstructed to true energy. The information is weighted according to oscillation probabilities and far over near detector ratios. A true-to-reconstructed energy matrix is applied to the spectra to obtain the final predictions at the FD [61].

## 4.8 Systematic uncertainties

The disappearance analyses presented in this thesis incorporate systematic uncertainties that can impact the result. These uncertainties can be broadly separated into four categories: flux, cross sections, detector response and calibration, and miscellaneous, which are separately described in this section. These systematics are defined as absolute (correlated) if they apply to both detectors, or as relative (uncorrelated) if they are due to differences between the detectors.

The treatment of the uncertainties takes one of two approaches. If a re-weighting accurately describes a systematic behavior, then a weight is applied to events based on a combination of variables and conditions stored in the Monte Carlo files. This procedure reduces the computational resources required for the evaluation of the systematic. If a simple re-weighting is not enough to describe the behavior, new simulation samples are produced with shifts according to the uncertainty

and/or the reconstruction chain is run again. The former(later) type of systematics are usually referred to as *weight(file) systematics* within the experiment.

The results of the weight and file systematics are neutrino energy spectra shifted by $\pm 1, 2, 3\ \sigma$ from the central simulation values. The systematics can modify the number of events in each bin or move events between energy bins and/or quartiles. The shifted spectra are incorporated into the analysis using the exact same decomposition and extrapolation procedures.

### 4.8.1 Flux

The flux systematics include the hadron production uncertainties, which account for the production rates of kaons and pions from the collision of protons on the carbon target, and the beam focusing uncertainty. The hadron production uncertainty is derived from PPFX [71]. The uncertainties on the PPFX central values are chosen from 100 randomly generated scenarios or *universes* with different proton-target cross-sections incorporated from theory and experimental constraints, and are stored in CAFAna files as weights. These universes are used to generate covariance matrices that describe the uncertainty in the flux, and are collapsed into a smaller set of uncorrelated weights via a Principle Component Analysis (PCA). The 5 Principle Components (PCs) presenting the largest FD/ND ratio variance are included in the analysis. The beam focusing uncertainty also implements the Principle Component Analysis (PCA) approach by taking into account other aspects that can affect the beam production, such as the target position, the horn current and the magnetic field in the decay pipe. This uncertainty is calculated by quantifying the change in the flux under different parameter assumptions in the simulation, and for each of the 100 hadron production universes [96].

### 4.8.2 Cross section

The cross-section uncertainties are divided in two groups. One is the group of the *large* systematics, which arise from direct re-weighting. A second group is that of the *small* systematics, which are implemented using a PCA procedure.

Three uncertainties are considered for the Meson Exchange Current (MEC) interactions, which are supported by experimental and theoretical models [97]. Two of the uncertainties capture the true neutrino energy dependence and the final state nucleon-nucleon composition. A third uncertainty is associated to the kinematics of MEC events. These uncertainties are uncorrelated between $\nu$ and $\bar{\nu}$, meaning that there are a total of six MEC uncertainties. Other uncertainties motivated from experimental data include a 5% $M_A^{QE}$ uncertainty to cover the tension between the GENIE values and the most recent results from bubble chamber data on deuterium. A DIS systematic is motivated by NOvA's ND data/MC disagreement, where a 10(50)% uncertainty is assigned to DIS events with Final state hadronic mass (W)$>$ 3(W$<$ 3) GeV. A 60% uncertainty is also added to the $\nu_\tau$ cross section taken from the OPERA experiment measurements [98].

The remaining cross-section and Final State Interaction (FSI) systematic uncertainties are taken from the GENIE parameters, or *knobs* [72]. These knobs are varied simultaneously and

used to generate an ensemble of 1,000 universes for the PCA approach, from which the first 5 Principle Components are input to the analysis [99]. The systematic uncertainties summarized by this procedure are the small GENIE systematics.

### 4.8.3 Detector response, calibration and energy scale

The amount of light produced by a charged particle in a scintillator involves the effect of both scintillation and Cherenkov radiation. The **light level** systematic is evaluated with three special file samples which assume alternative detector light models before running the event reconstruction. Motivated by an observed 2% $dE/dx$ discrepancy between ND data and simulation, for muons relative to protons, one dataset assumes an increased Cherenkov light collection efficiency while reducing the standard scintillation light production. The light output is then tuned to match the Monte Carlo muons to the data [100]. The other two samples are simulated assuming a $\pm 10\%$ shift in the scintillator light levels, while compensating with a $\mp 10\%$ shift in the absolute calibration constants. This provides information for evaluating the effect of the hits that miss or pass the threshold level.

The **energy calibration** uncertainty is quantified from the difference between post-calibrated data and simulated events, such as beam muons, Michel electrons[6], reconstructed $\pi^0$ mass peaks [101] and protons. The largest of the discrepancies was measured with protons and is used as the calibration uncertainty. It was found that the detector response to protons in data is lower than that of the Monte Carlo by 5%. The effect of the 5% calibration uncertainty is evaluated by reusing the simulated samples but with a 5% change in the absolute calibration constants before the reconstruction is performed. This procedure maintains a constant number of hits while shifting their energies up or down. The FD sample of beam events is not large enough to evaluate this systematic so the same uncertainty is assumed for the FD. A comparison between reconstructed and true energy of simulated cosmic hits as function of position in the cell has shown a disagreement when not only tricell hits are used for the detector calibration. The discrepancy is interpreted as a position dependent or *shape* calibration uncertainty [102] and is evaluated by generating special Monte Carlo samples.

A **muon energy scale** systematic is constructed by considering the uncertainties on the detectors particular structure and composition, and the uncertainty on the Bethe-Bloch equation parameters that go into the GEANT4 simulation [103]. The absolute(relative) muon energy scale uncertainty is a flat 0.94(0.27)% for events stopping in the active scintillator region. However, the uncertainty for events that stop in the ND muon catcher is the sum in quadrature with a 0.69(0.75)% additional uncertainty on the track segment in the muon catcher. The relative muon energy scale uncertainty is 0.27% for the majority of events. These relative uncertainties are applied at both detectors by shifting the event's muon or hadronic energy by half the uncertainty in opposite directions [104].

[6] A Michel electron is an electron produced from a muon's decay at rest $\mu^- \rightarrow e + \bar{\nu}_e + \nu_\mu$.

### 4.8.4 Other uncertainties

#### Normalization

The particles from neutrino-induced interactions originating outside of the ND may be detected inside of it during the beam spill. These interactions can overlay on true contained interactions, which can cause them to fail the containment criteria and be lost in the selection. To quantify this effect, single Monte Carlo events are overlaid on real and simulated beam spills. The selection efficiency is then examined and the difference between the overlaid samples is assigned as part of the uncertainty. The total *normalization* uncertainty is the sum in quadrature of 0.26% uncertainty in the detector mass, a 0.5% uncertainty on the POT counting and a 1.3(0.3)% selection difference in the FHC(RHC) beam mode. This results in a 1.44% and 0.64% normalization systematic for the FHC and RHC modes respectively. The difference between these uncertainties is attributed to the less hadronic nature of events in the antineutrino beam [105].

#### Neutrons

Neutrons are more prominent in $\bar{\nu}$ interactions so comparison between $\nu$ vs. $\bar{\nu}$ oscillations requires special attention to the detector response to these particles. Discrepancies between data and Monte Carlo in RHC neutron-rich samples motivated an uncertainty which scales the amount of true deposited energy of a subset of simulated neutrons to cover the discrepancy at energies below 0.3 GeV. The result is a 0.5(1.0)% shift of the mean $\bar{\nu}$ ($\nu$) reconstructed energy.

#### Backgrounds

The $\bar{\nu}_\mu(\nu_\mu)$ component in the FHC(RHC) beam configuration is referred to as *wrong sign*. The uncertainty on this component is handled as part of the flux and cross section uncertainties and is about 10%. Data driven checks provide evidence that these uncertainties are reasonable. The checks include the measurement of the amount of $\nu_\mu$ contamination in the RHC beam using the fact that the primary tracks of $\nu_\mu$ CC, $\bar{\nu}_\mu$ CC and NC events produce neutrons with different probabilities [106]. Most of the neutrons produced from the RHC beam are due to negatively charged muons (from $\nu_\mu$ CC events) coming to rest and being captured by a nucleus. This process releases one or more neutrons, which are detected via delayed nuclear capture. Stopping positive muons produced from $\bar{\nu}_\mu$ interactions are not captured by nuclei. This study estimated that the scale of the $\nu_\mu$ component in the RHC beam is $1.05 \pm 0.12$ of the nominal simulation.

Additional backgrounds include NC events, for which the cross-section uncertainty is taken from GENIE. However, the uncertainty in the NC events is dominated by the results from the calibration systematic files, which presumably change the PID values thus increasing the acceptance of these events. The $\nu_\tau$ production is assigned a 100% uncertainty but its small contribution to the beam flux makes it of little impact to the analysis.

## 4.9 Oscillation model fit to data

The measurement of the neutrino oscillation parameters is achieved through the comparison between the FD data and a FD prediction from a three-neutrino oscillation model. Given the expectation $\vec{e}$ for a vector $\vec{\theta}$ of oscillation parameter values, and an observation $\vec{o}$ of events at the FD, the Poisson log-likelihood function [107]

$$-2\ \log\lambda(\vec{\theta}) = 2\sum_{i}^{bins} e_i(\vec{\theta}) - o_i + o_i \log\frac{o_i}{e_i(\vec{\theta})} \tag{4.3}$$

is computed at each point of a chosen grid in the $\Delta m^2_{32}$ vs. $\sin^2\theta_{23}$ space, where $e_i$ and $o_i$ are the predicted and detected number of events, respectively, in the $i$-th bin of reconstructed neutrino energy. For what follows, equation 4.3 is identified as a $\chi^2$ of $k$ independent random variables or bins and is approximated by a Gaussian distribution as $k \to \infty$. This $\chi^2$ statistic is used to determine the goodness of fit and the significance of the oscillation measurements.

Equation 4.3 assumes a precise knowledge of the signal and backgrounds as systematic uncertainties are not accounted for. Assuming that the systematic uncertainties are Gaussian, nuisance parameters can be added and the test statistic modified into

$$\chi^2(\vec{\theta}) = \min_{\vec{s}}\big(\chi^2(\vec{\theta},\vec{s}) + \sum_{i}^{systs}\frac{s_i^2}{\sigma_i^2}\big), \tag{4.4}$$

where $s_i$ are the values of the individual systematic shifts, and $\sigma_i$ are the $\pm1\sigma$ ranges explored, or error, for each systematic [97]. The second term in Equation (4.4) can only be zero or positive, thus usually referred to as *penalty term*, as it can only increase or penalize the total $\chi^2$. The values of the parameters $\vec{\theta}$ that minimize Equation 4.4 such that

$$\chi^2_{min} \equiv \chi^2(\vec{\theta}_A) < \chi^2(\vec{\theta}_B)\ \ \forall\ \vec{\theta}_B \neq \vec{\theta}_A \tag{4.5}$$

are those which describe the data more accurately and are commonly referred to as *best fit* values. The $\Delta\chi^2$ test statistic defined as

$$\Delta\chi^2(\vec{\theta}) \equiv \chi^2(\vec{\theta}) - \chi^2_{min} \tag{4.6}$$

is used in this analysis with *real data* to obtain regions of confidence. For a $\Delta\chi^2$ with 1 (2) degrees of freedom, the values of the oscillation parameters for which $\Delta\chi^2 < 2.71$ (4.61), are allowed at the 90% Confidence Level (CL). The sensitivity of the analysis to measuring a particular set of oscillation parameter values is also evaluated with Equation 4.6, for which a simulated FD spectrum or FD *fake data* is constructed for a given scenario.

The oscillation model is defined by the three neutrino flavour oscillation equations in matter with $L$=810 km, and $\rho = 2.84\text{g/cm}^2$, which is the density of the earth at the average underground depth between the NOvA detectors [108]. The solar oscillation parameters $\Delta m^2_{21}$ and $\sin^2\theta_{12}$ are set from global experimental data as well as the reactor measurement of $\sin^2 2\theta_{13}$. These

three constraints are added to the statistic as a Gaussian penalty term assuming that $x = \mu \pm \sigma$. Explicitly,

$$\chi^{2\prime} = \chi^2 + \frac{(x-\mu)^2}{\sigma^2} \tag{4.7}$$

where $x \in \{\Delta m^2_{21}, \sin^2\theta_{12}, \sin^2 2\theta_{13}\}$. The solar and reactor constraints used for the fits in this thesis will be noted in the next chapters. The parameter $\delta_{CP}$ is profiled allowing it to take any value between $0\pi$ and $2\pi$.

The result of the fits are represented in the form of a bi-dimensional confidence region in the physical space of the unknown parameters $\sin^2\theta_{23}$ and $\Delta m^2_{32}$. To obtain uncertainties on the parameters $\sin^2\theta_{23}(\Delta \mathrm{m}^2_{32})$ individually, the parameter $\Delta m^2_{32}(\sin^2\theta_{23})$ is additionally profiled.

# Chapter 5

# The CPT conserved analysis

This chapter presents the results from the measurement of $\nu_\mu$ and $\bar{\nu}_\mu$ disappearance in the NOvA experiment, where the values of the neutrino and antineutrino oscillation parameters are extracted assuming CPT invariance or *conservation*. The results include data collected between February 2014 and February 2019, which corresponds to a FD exposure of $8.85 \times 10^{20}$ POT and $12.33 \times 10^{20}$ POT for the neutrino and antineutrino NuMI beam mode respectively. The chapter begins with the comparison of the ND data and simulation in § 5.1, where consistency is assessed using distributions of the energy variables relevant to the analysis. The estimated FD cosmic background spectra are presented in § 5.2. Comparisons between FD data and oscillated predictions for the relevant energy variables are presented in § 5.3. Finally, the neutrino and antineutrino beam FD data is used to constrain the values of $\sin^2\theta_{23}$ and $\Delta m^2_{32}$. The result of the fits to these data are shown in § 5.4. Hereafter, the analysis presented in this chapter will be referred to as *CPT conserved* and will be abbreviated as *CPTc*.

## 5.1 Distributions of events at the Near Detector

This section presents ND data and simulation distributions in the most relevant energy variables to the analysis. These spectra are used to asses the agreement between the data and the Monte-Carlo. Any discrepancies between the samples can be due to mis-modeling in the simulation and therefore are analyzed before proceeding to look at the FD data. As described in § 3.4.2, NOvA applies corrections to the neutrino interaction model, which are driven by theory, external experimental data and by its own ND data. As a consequence, the differences between the ND data and the base simulation are reduced by design. The corrections for this analysis are implemented as *event weights* with the `kXSecCVWgt2018` variable in the CAFAna framework.

The data presented in this section corresponds to a ND proton exposure of $8.03 \times 10^{20}$ and $3.10 \times 10^{20}$ POT for the neutrino and antineutrino beam production, respectively. Distributions of neutrino, muon and hadronic energy, as well as of hadronic energy fraction, are presented and are all POT-normalized to the ND beam exposure. The data is represented by black dots with

the statistical errors associated to the event count. The simulation is shown in purple with the corresponding 1 $\sigma$ error band from the sum in quadrature of the systematic uncertainties accounted for in the analysis. The simulated wrong sign and other beam backgrounds are shown in green and gray respectively. The arrangement of the plots is such that the distributions of the FHC and RHC datasets are presented side-by-side for a direct comparison between beam modes. Recall that the hadronic energy fraction $E_{Had}/E_{\nu}$ provides a measure of event energy resolution and thus the samples are separated in $E_{Had}/E_{\nu}$ quartiles or bins of energy resolution[1]. The total spectra are presented first and are directly followed by the breakdown in quartiles.

The **reconstructed neutrino energy** distributions in Figure 5.1 show good agreement between data and Monte Carlo in the two beam modes. Figure 5.2 shows the corresponding data distributions for individual quartiles. These distributions are also within uncertainties but the agreement is less good in the best and worst energy resolution bins. The FHC simulation is underestimated across the first quartile reconstructed energy range, and it is slightly lower (higher) at energies below (above) 2 GeV in the 4th quartile. The antineutrino beam simulation that has the worse agreement with data are quartiles 1 and 4. Quartiles 2 and 3 show a smaller discrepancy. The Monte Carlo is lower than the data in the first two RHC quartiles and higher in last two. However, the discrepancies in both beam modes are covered by the 1 $\sigma$ error bands. These offsets cancel each other in the summed quartiles thus the simulation is in good agreement with data in the combined spectra.

Figures 5.3 and 5.4 show a data-Monte Carlo comparison in terms of the **reconstructed muon energy** variable for the combined and individual $E_{Had}/E_{\nu}$ quartiles respectively. The neutrino beam predictions accurately describe the data. In the antineutrino mode, the data is below (above) the expectation at energies below (above) 2 GeV in the distributions of the sum of all quartiles. The RHC data is generally above the expectation in the first 2 quartiles, and it is below in the last 2. This pattern is similar to that observed in the neutrino energy variable. Nonetheless, all the predictions are within the 1 $\sigma$ uncertainty range.

The **hadronic energy** distributions in Figures 5.5 and 5.6, for the sum and separation of quartiles, respectively, show good agreement between the FHC data and Monte Carlo. On the other hand, the simulation of the combined quartiles in RHC underestimates the number of events in the first hadronic energy bin and overestimates those with $E_{Had}$ greater than 0.4 GeV. This RHC data-Monte Carlo discrepancy is mainly driven by the first and last two quartiles, which present this pattern of the prediction being below and above the data in the same regions, respectively. The prediction for the second quartile is in general accordance with the data. All the discrepancies are covered by the systematic uncertainties.

Figures 5.7 and 5.8 show the data and Monte Carlo **hadronic energy fraction** distributions for the combined and individual quartiles respectively. The number of events whose hadronic

[1]Events with a low hadronic component are placed in the 1st quartile, or best energy resolution bin, and highly hadronic events are placed in the 4th quartile, or worst resolution bin.

energy is less (more) than 20% of the total reconstructed neutrino energy are lower (higher) than the total RHC simulation. No evident pattern of disagreement between data and Monte Carlo is seen in the RHC plots split per quartiles. The small discrepancies are within the 1 $\sigma$ systematic band. The neutrino beam predictions are all in good agreement with data.

The hadronic energy fraction boundaries are computed from the unoscillated FD simulation, therefore the number of selected events at each ND quartile does not exactly contain 25% of the total population. Once the oscillation weights are applied, the relative proportions will also vary at the FD[2]. Table 5.1 shows the total and the fraction of selected data and Monte Carlo $\nu_\mu$ and $\bar{\nu}_\mu$ events from the neutrino and antineutrino beam and for each of the energy resolution bins. In FHC, the percentage of predicted ND selected events is about 31%, 24%, 19% and 25% in quartiles 1-4 respectively. In RHC, the percentages are about 33%, 23%, 22% and 22%. The FHC (RHC) simulation shows, from lowest to highest $E_{Had}/E_\nu$, a +2.8% (+7.9%), -0.7% (+2.5%), -1.4% (-5.3%) and +1.6% (-11.6%) offset from the observation. The total difference from the combined quartiles is of 1.3% (0.5%). These discrepancies are covered by the systematics, and they are further addressed by the extrapolation, which is done separately for each quartile. Tables 5.2 and 5.3 show the breakdown of the $\nu_\mu$ and $\bar{\nu}_\mu$ fractions of the neutrino and antineutrino beam respectively. The decrease (increase) tendency on the wrong sign fraction from quartile 1 to 4 in FHC (RHC) is expected as $\nu_\mu$ ($\bar{\nu}_\mu$) interactions are more (less) hadronic.

| | FHC | | RHC | |
|---|---|---|---|---|
| $E_{Had}/E\nu$ | Data (%) | Monte Carlo (%) | Data (%) | Monte Carlo (%) |
| Lowest | 610424(31.9) | 594634(31.3) | 137325(35.5) | 127359(32.8) |
| Second lowest | 459398(24.0) | 463576(24.4) | 93077(24.1) | 90750.5(23.3) |
| Second highest | 355715(18.6) | 361542(19.1) | 81030(21.0) | 86030.3(22.1) |
| Highest | 487103(25.5) | 477830(25.2) | 75053(19.4) | 84695.3(21.8) |
| Total | 1.91264e+06(100) | 1.89758e+06(100) | 386485(100) | 388835(100) |

**Table 5.1:** Number of selected $\nu_\mu$ and $\bar{\nu}_\mu$ CC events from data and simulation at the ND. The events are separated by beam configuration and by bins of $E_{Had}/E_\nu$. The numbers in parentheses correspond to the percentage of total selected events from data or simulation.

## 5.2 Estimation of Cosmic Induced Events at the FD

The estimation of cosmic induced events at the FD are obtained from data when the beam is not firing as described in § 4.6. The $\nu_\mu$ +$\bar{\nu}_\mu$ selection cuts presented in § 4.4 are applied to this data. Figures 5.9 and 5.10 show the reconstructed energy spectra of the FD cosmic prediction for the combination and for the separation of the sample into quartiles, respectively.

[2]Studies with simulated ND data showed that using the same quartiles in both detectors reduce the systematic uncertainties on the measurements [109].

FHC beam

| $E_{Had}/E\nu$ | Right sign: $\nu_\mu$ (%) | Wrong sign: $\bar{\nu}_\mu$ (%) | Other Bkg (%) |
|---|---|---|---|
| Lowest | 566755(95.3) | 27472(4.6) | 406(0.1) |
| Second lowest | 451993(97.5) | 11080(2.4) | 503(0.1) |
| Second highest | 352297(97.4) | 8252(2.3) | 991(0.3) |
| Highest | 467049(97.7) | 6396(1.3) | 4384(0.9) |
| Total | 1.83809e+06(96.9) | 53201(2.8) | 6286(0.3) |

**Table 5.2:** Number of selected simulated $\nu_\mu$ CC (right sign), $\bar{\nu}_\mu$ CC (wrong sign) and background events in the **FHC** beam configuration. The events are separated by bins of energy resolution. The numbers in parenthesis correspond to the percentage of the total number of events at each $E_{Had}/E_\nu$.

RHC beam

| $E_{Had}/E\nu$ | Right sign: $\bar{\nu}_\mu$ (%) | Wrong sign: $\nu_\mu$ (%) | Other Bkg (%) |
|---|---|---|---|
| Lowest | 121094(95.1) | 6218(4.9) | 46(0.0) |
| Second lowest | 81883.2(90.2) | 8804(9.7) | 62(0.1) |
| Second highest | 75039.8(87.2) | 10858(12.6) | 132(0.2) |
| Highest | 68567.8(81.0) | 15319(18.1) | 808(1.0) |
| Total | 346585(89.1) | 41200(10.6) | 1049(0.3) |

**Table 5.3:** Number of selected simulated $\bar{\nu}_\mu$ CC (right sign), $\nu_\mu$ CC (wrong sign) and background events in the **RHC** beam configuration. The events are separated by bins of energy resolution. The numbers in parenthesis correspond to the percentage of the total number of events at each $E_{Had}/E_\nu$.

The total number of predicted events from cosmic interactions is 2.07 and 0.80 for the FD livetime during the operations in FHC and RHC beam mode, with most of the events expected to happen between the 1.0-2.0 GeV range. The spectra with the split by quartiles of hadronic energy fraction show the cosmic events accumulated in the best and worse resolution bins for the neutrino beam, and only accumulating in the 4th quartile in the antineutrino case.

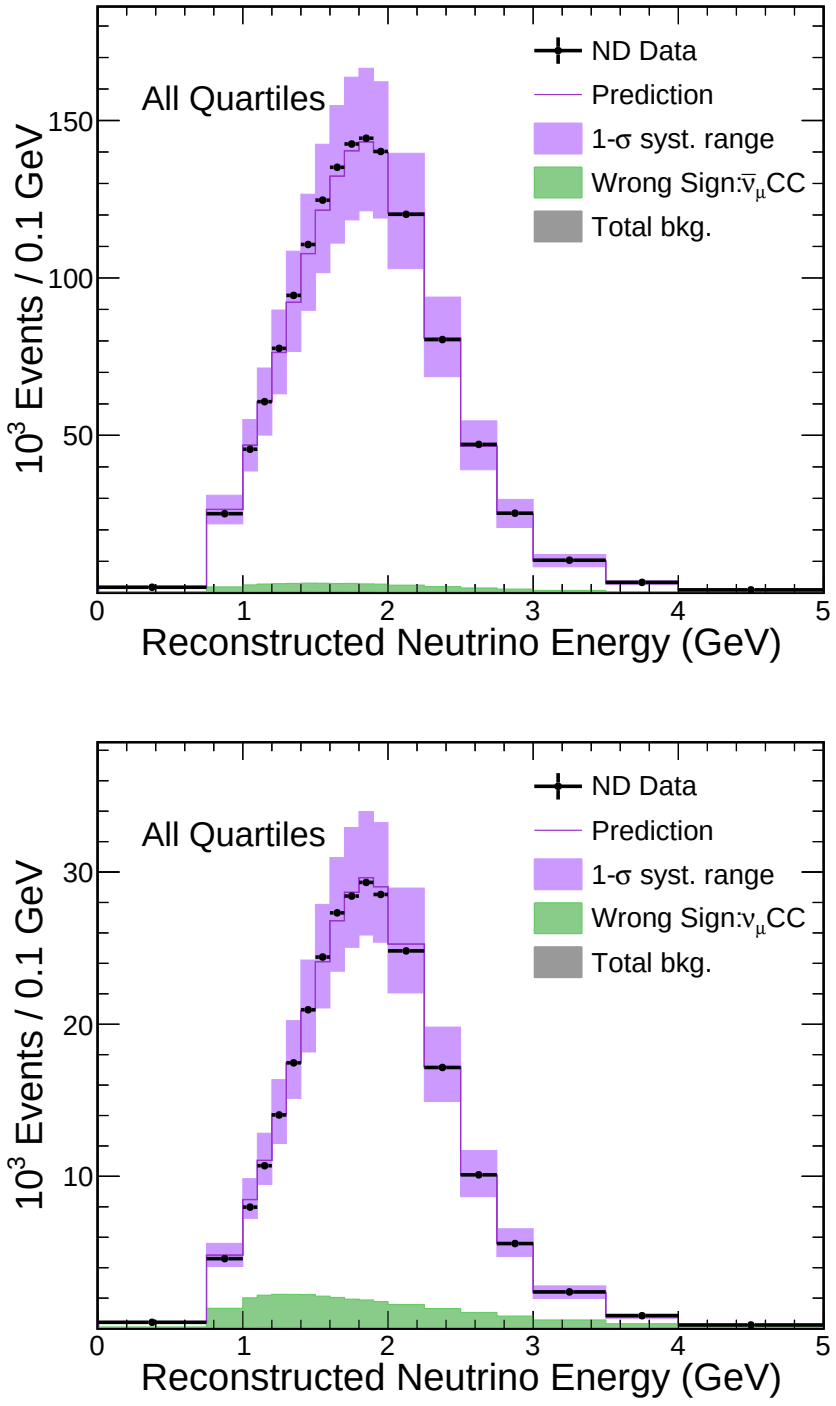


**Figure 5.1:** Distributions of selected data and simulated events in **reconstructed neutrino energy** at the **ND**. The distributions are from the neutrino (FHC) and antineutrino (RHC) beam configurations are shown at the top and bottom respectively. The data passing the $\nu_\mu$ +$\bar{\nu}_\mu$ selection criteria is shown in black dots with statistical errors. The simulation is shown in purple and the shaded region corresponds to the 1 $\sigma$ systematic uncertainty on the simulation. The simulated wrong sign component and other beam backgrounds are represented by the green and gray regions respectively.

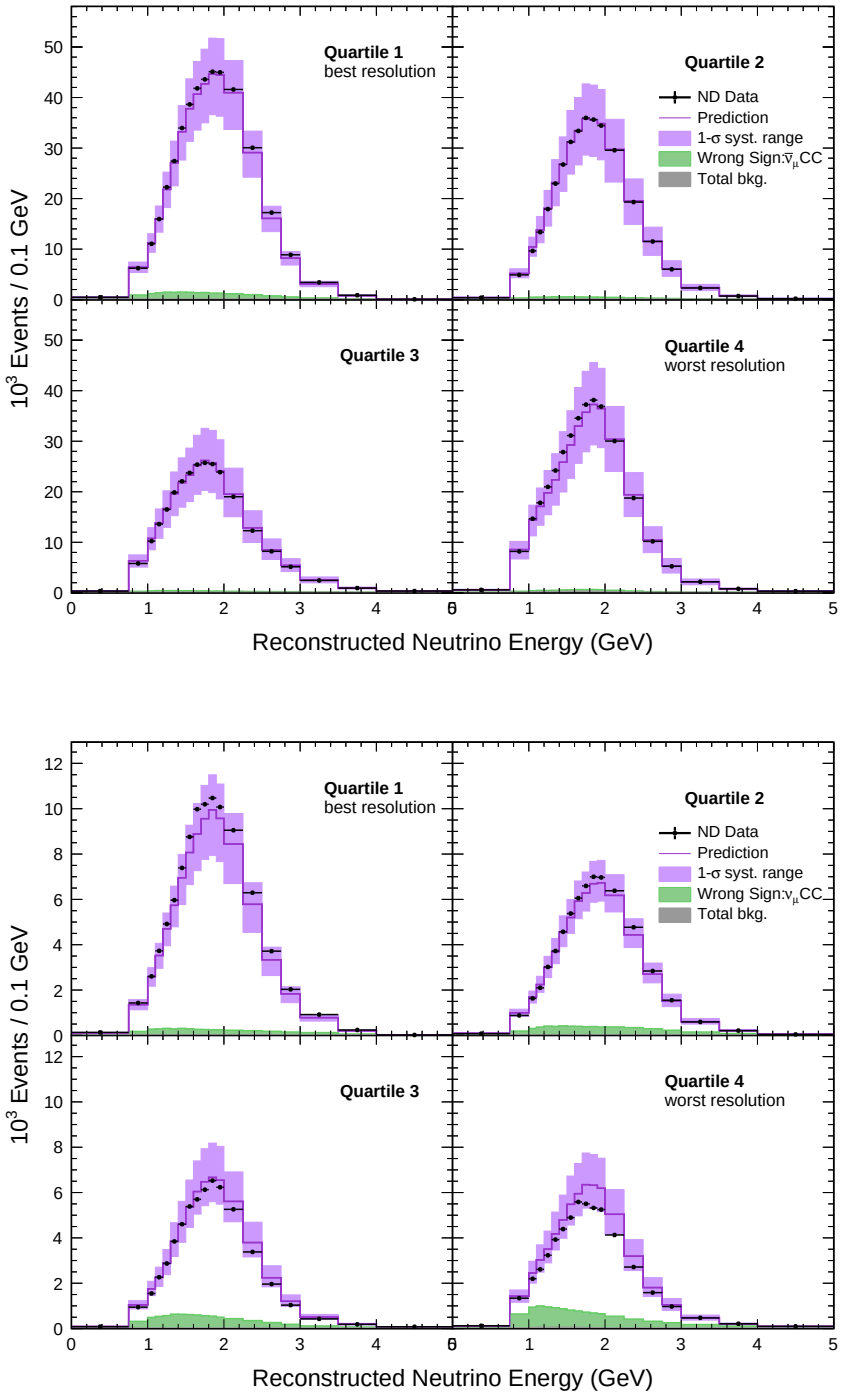


**Figure 5.2:** Distributions of selected data and simulated events in **reconstructed neutrino energy** at the **ND** for each individual $E_{Had}/E_{\nu}$ quartile. The distributions from the neutrino (FHC) and antineutrino (RHC) beam configurations are shown at the top and bottom respectively. The data passing the $\nu_{\mu}$ +$\bar{\nu}_{\mu}$ selection criteria is shown in black dots with statistical errors. The simulation is shown in purple and the shaded region corresponds to the 1 $\sigma$ systematic uncertainty on the simulation. The simulated wrong sign component and other beam backgrounds are represented by the green and gray regions respectively.

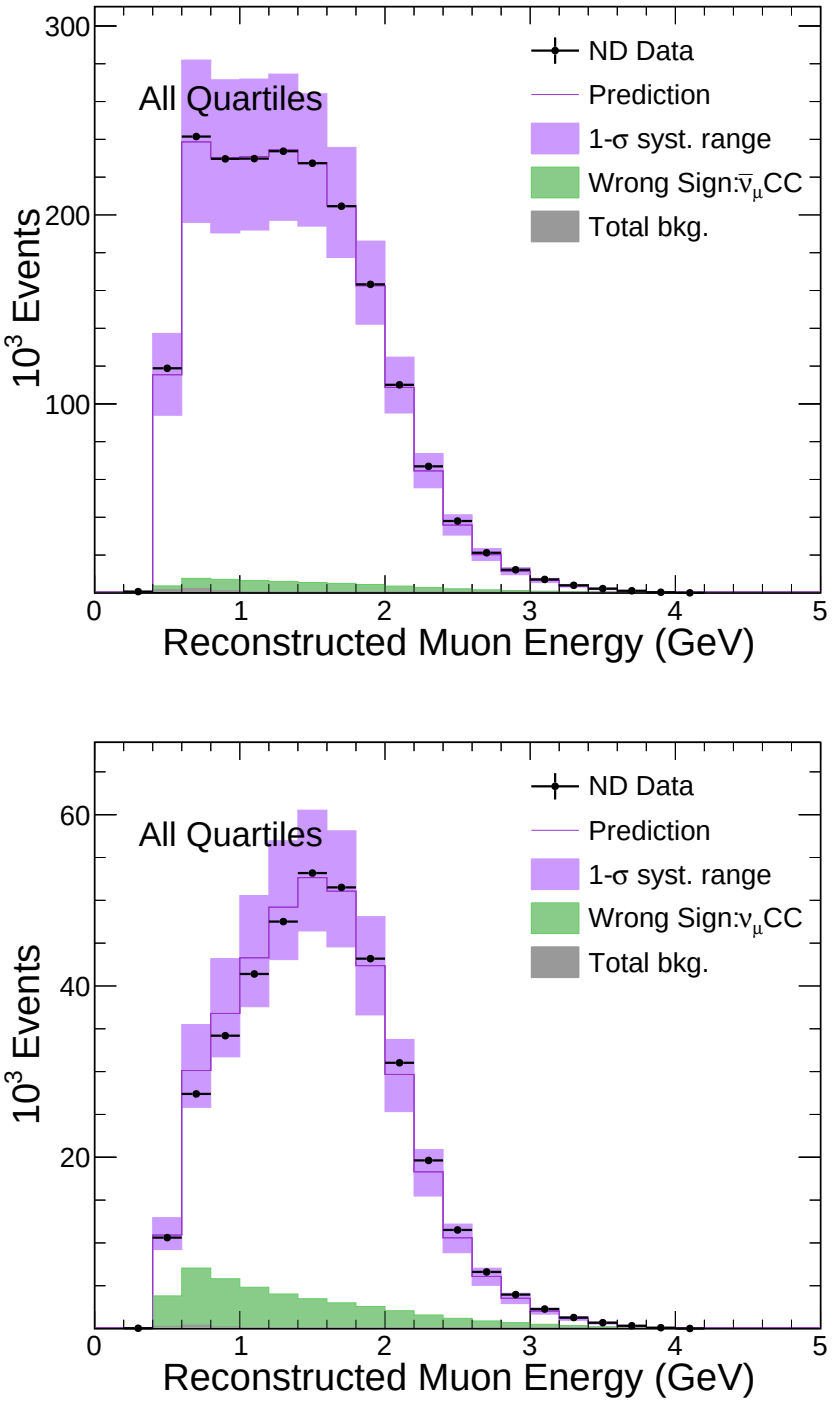


**Figure 5.3:** Distributions of selected data and simulated events in **reconstructed muon energy** at the **ND**. The distributions are from the neutrino (FHC) and antineutrino (RHC) beam configurations are shown at the top and bottom respectively. The data passing the $\nu_\mu$ +$\bar{\nu}_\mu$ selection criteria is shown in black dots with statistical errors. The simulation is shown in purple and the shaded region corresponds to the 1 $\sigma$ systematic uncertainty on the simulation. The simulated wrong sign component and other beam backgrounds are represented by the green and gray regions respectively.

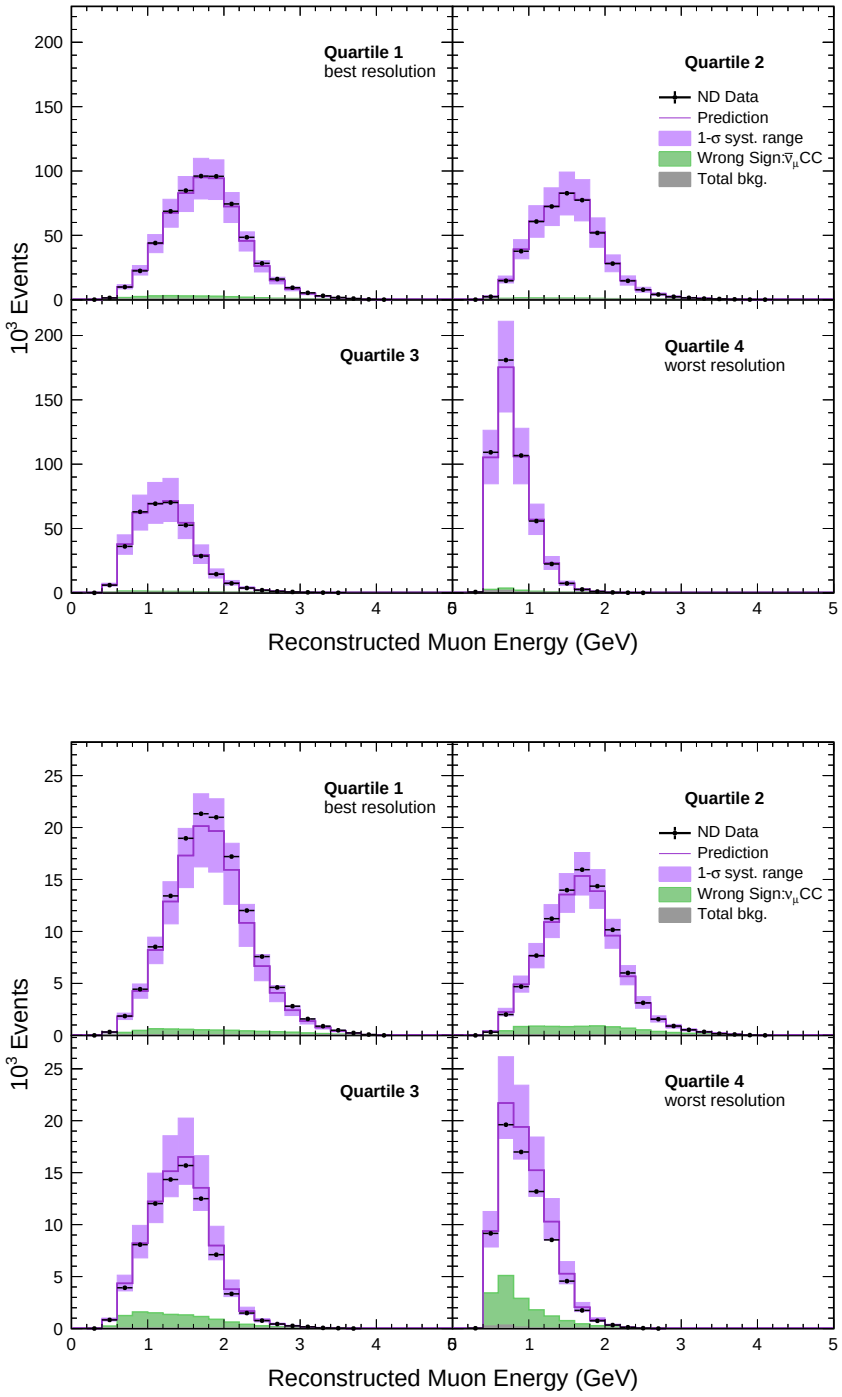


**Figure 5.4:** Distributions of selected data and simulated events in **reconstructed muon energy** at the **ND** for each individual $E_{Had}/E_{\nu}$ quartile. The distributions from the neutrino (FHC) and antineutrino (RHC) beam configurations are shown at the top and bottom respectively. The data passing the $\nu_{\mu}$ +$\bar{\nu}_{\mu}$ selection criteria is shown in black dots with statistical errors. The simulation is shown in purple and the shaded region corresponds to the 1 $\sigma$ systematic uncertainty on the simulation. The simulated wrong sign component and other beam backgrounds are represented by the green and gray regions respectively.

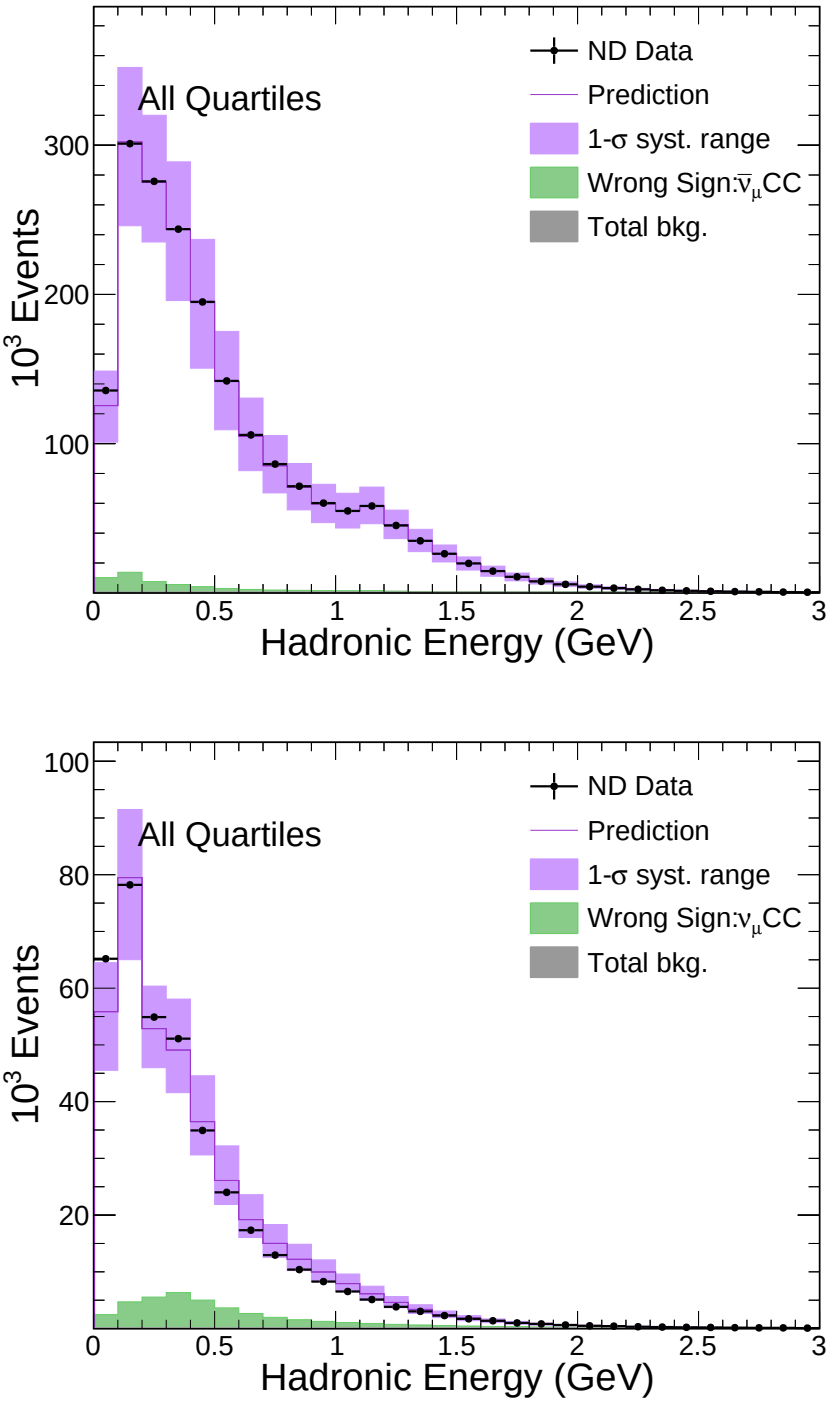


**Figure 5.5:** Distributions of selected data and simulated events in **hadronic energy** at the **ND**. The distributions are from the neutrino (FHC) and antineutrino (RHC) beam configurations are shown at the top and bottom respectively. The data passing the $\nu_\mu$ +$\bar{\nu}_\mu$ selection criteria is shown in black dots with statistical errors. The simulation is shown in purple and the shaded region corresponds to the 1 $\sigma$ systematic uncertainty on the simulation. The simulated wrong sign component and other beam backgrounds are represented by the green and gray regions respectively.

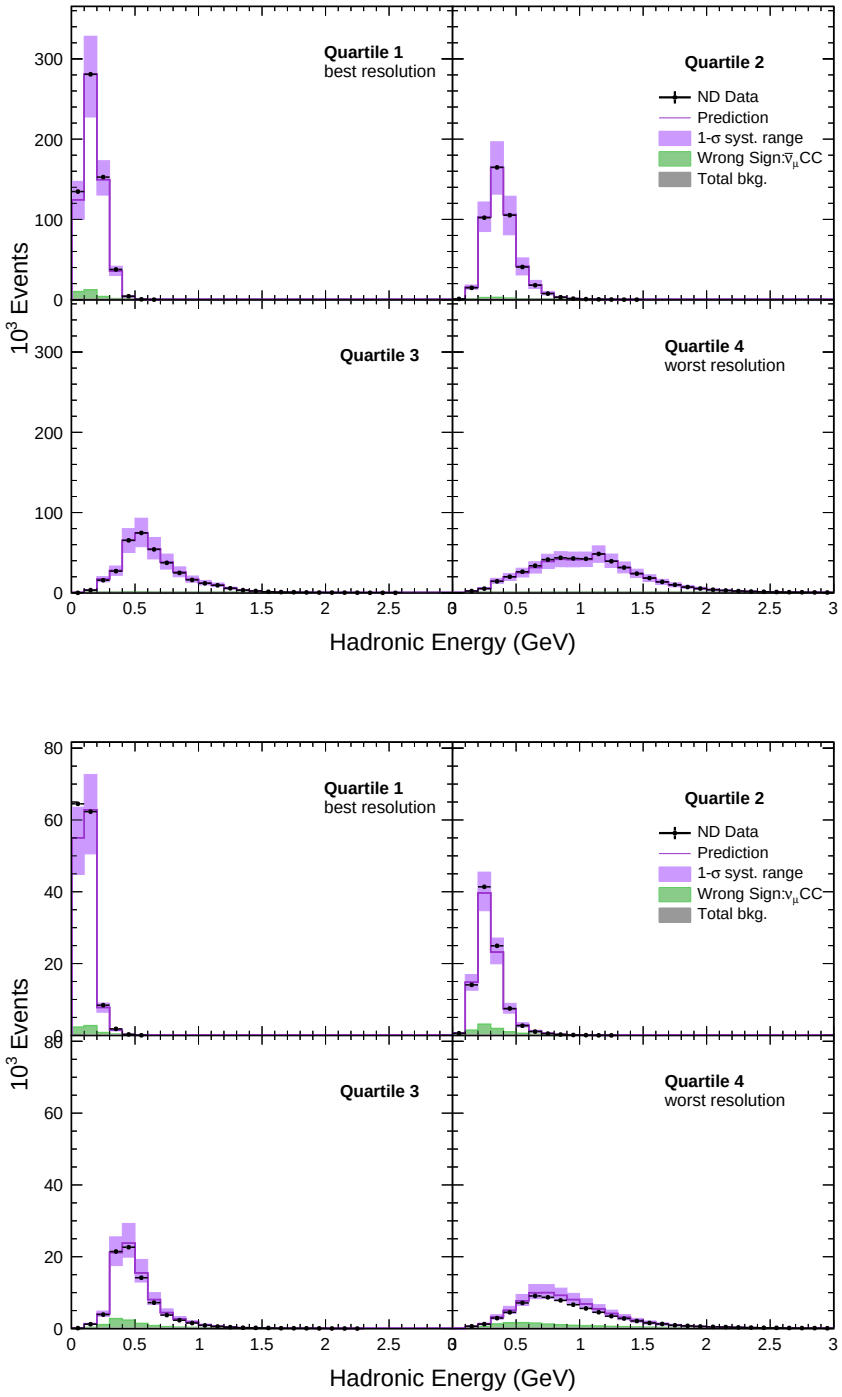


**Figure 5.6:** Distributions of selected data and simulated events in **hadronic energy** at the **ND** for each individual $E_{Had}/E_\nu$ quartile. The distributions from the neutrino (FHC) and antineutrino (RHC) beam configurations are shown at the top and bottom respectively. The data passing the $\nu_\mu + \bar{\nu}_\mu$ selection criteria is shown in black dots with statistical errors. The simulation is shown in purple and the shaded region corresponds to the 1 $\sigma$ systematic uncertainty on the simulation. The simulated wrong sign component and other beam backgrounds are represented by the green and gray regions respectively.

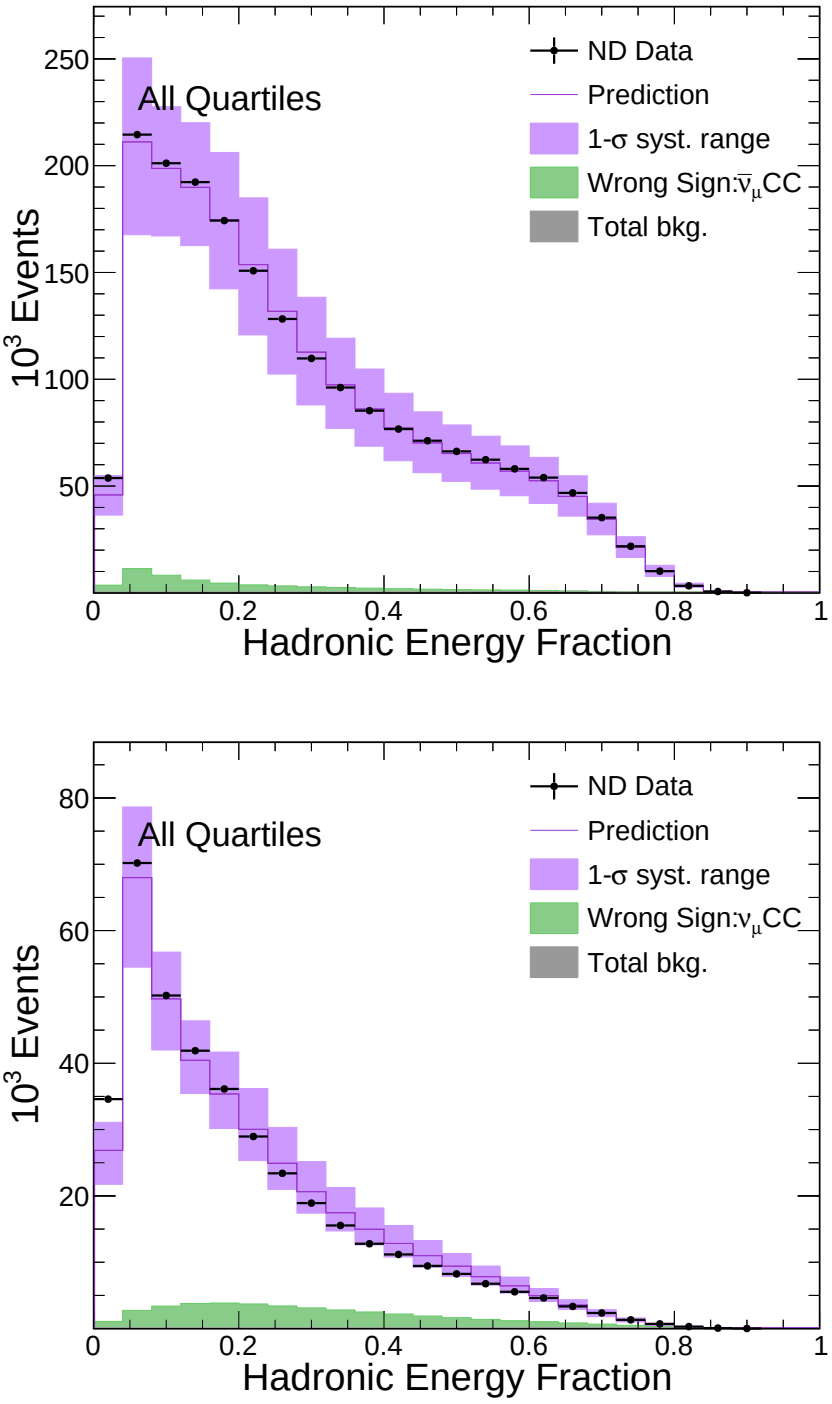


**Figure 5.7:** Distributions of selected data and simulated events in **hadronic energy fraction** at the **ND**. The distributions are from the neutrino (FHC) and antineutrino (RHC) beam configurations are shown at the top and bottom respectively. The data passing the $\nu_\mu$ $+\bar{\nu}_\mu$ selection criteria is shown in black dots with statistical errors. The simulation is shown in purple and the shaded region corresponds to the 1 $\sigma$ systematic uncertainty on the simulation. The simulated wrong sign component and other beam backgrounds are represented by the green and gray regions respectively.

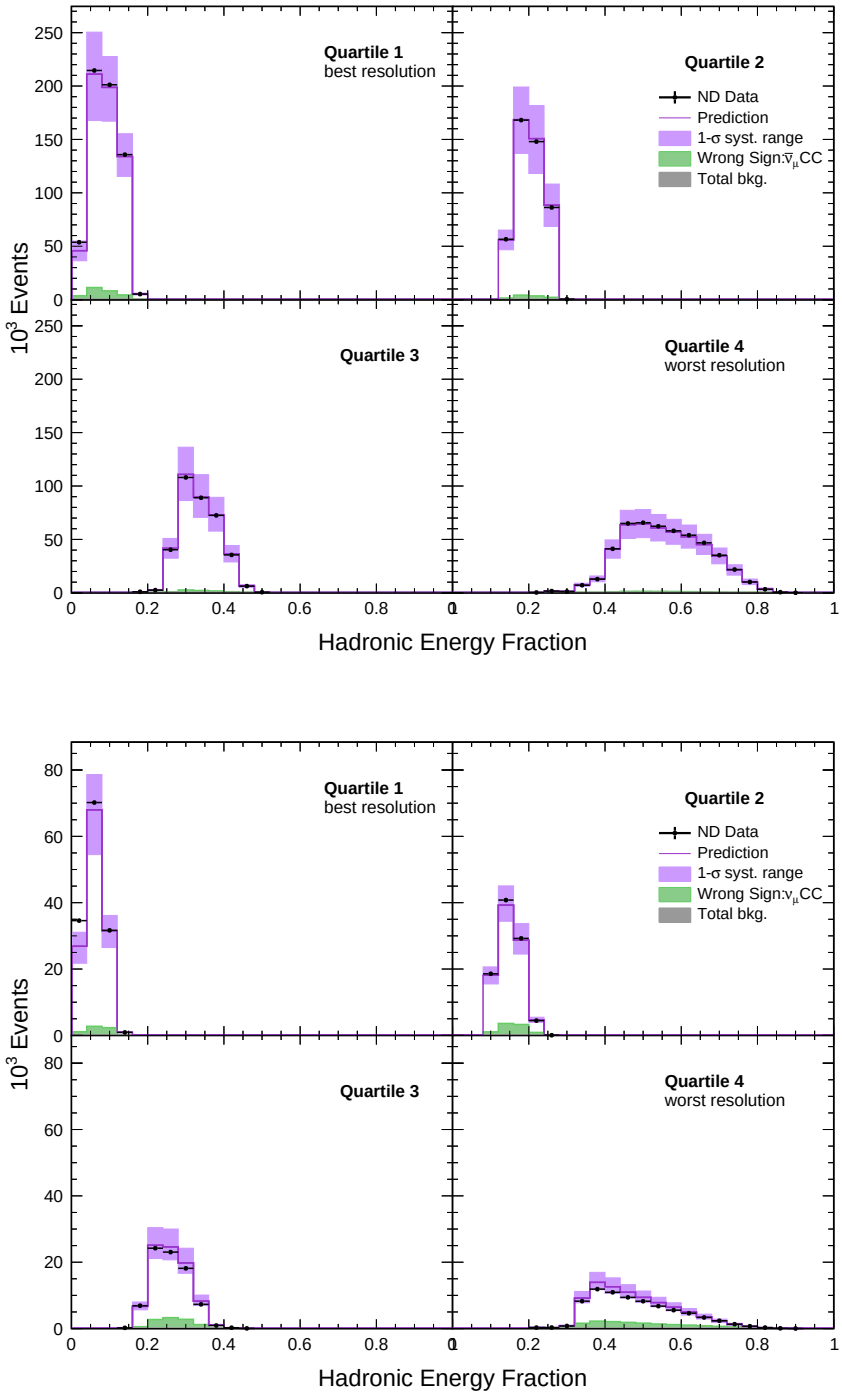


**Figure 5.8:** Distributions of selected data and simulated events in **hadronic energy fraction** at the **ND** for each individual $E_{Had}/E_{\nu}$ quartile. The distributions from the neutrino (FHC) and antineutrino (RHC) beam configurations are shown at the top and bottom respectively. The data passing the $\nu_{\mu}$ +$\bar{\nu}_{\mu}$ selection criteria is shown in black dots with statistical errors. The simulation is shown in purple and the shaded region corresponds to the 1 $\sigma$ systematic uncertainty on the simulation. The simulated wrong sign component and other beam backgrounds are represented by the green and gray regions respectively.

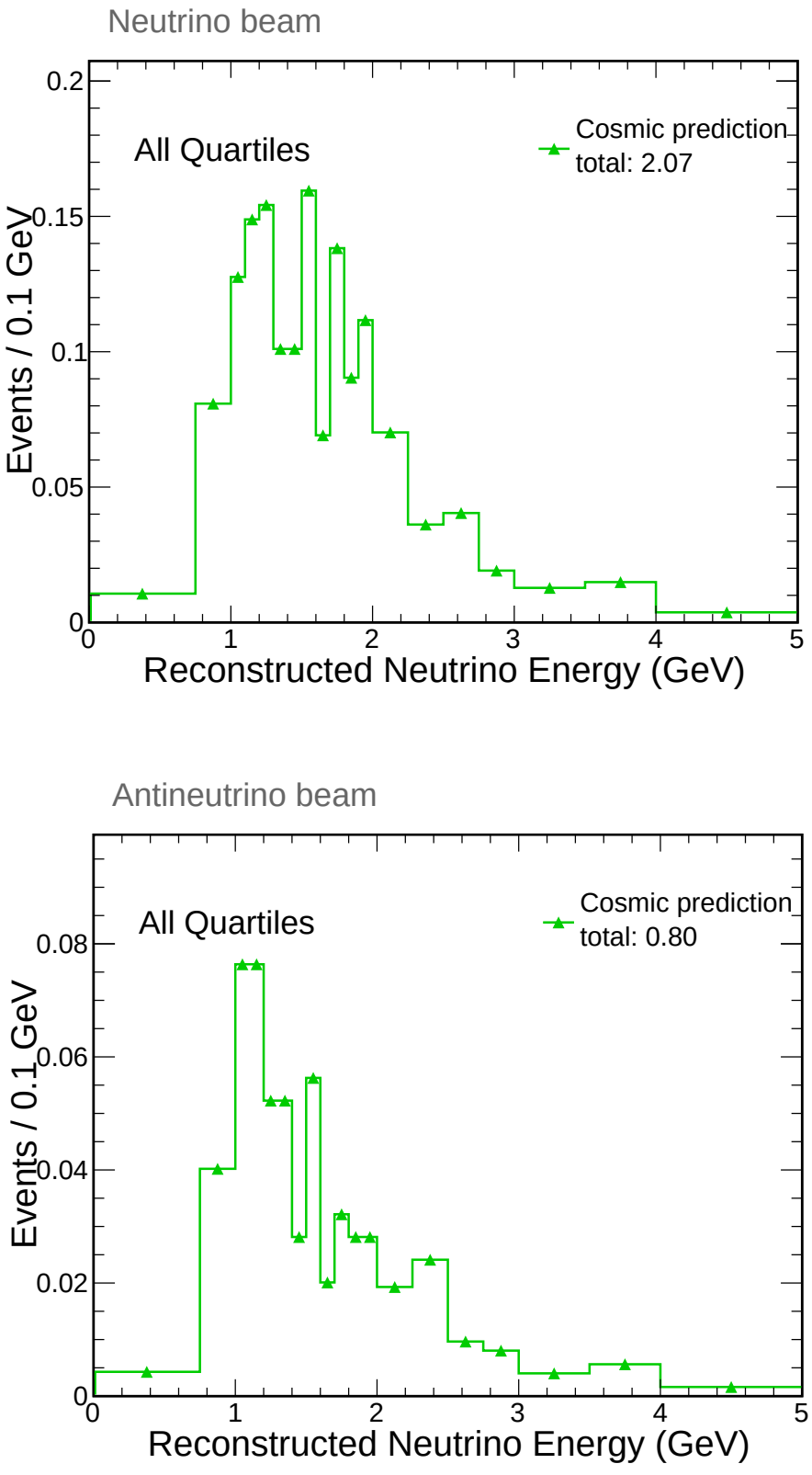


**Figure 5.9:** Estimated energy spectra of the FD cosmic background for the neutrino (top) and antineutrino (bottom) beam samples. The spectra are for all the $E_{Had}/E_{\nu}$ quartiles combined.

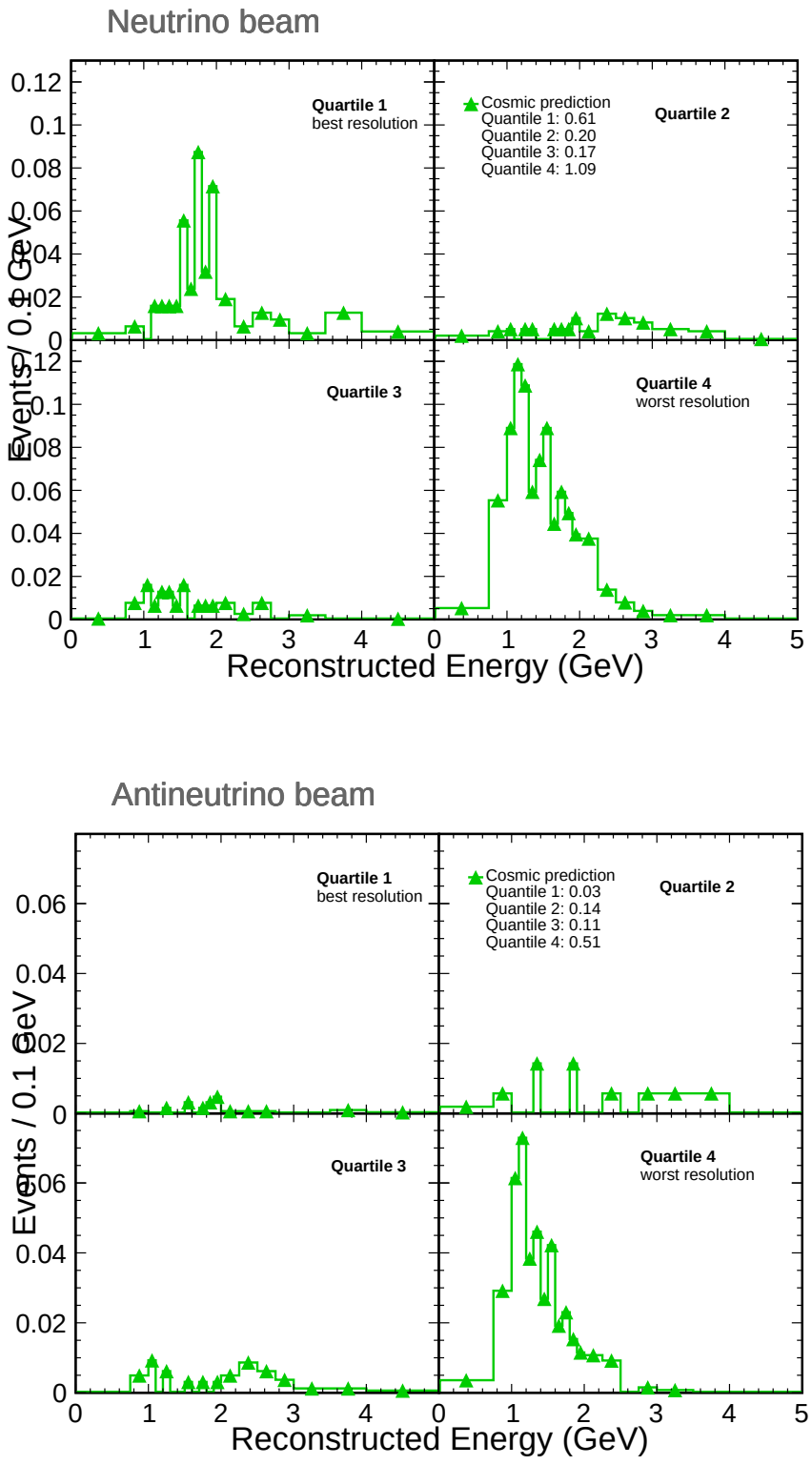


**Figure 5.10:** Estimated energy spectra of the FD cosmic background for the neutrino (top) and antineutrino (bottom) beam samples. The spectra are for each individual $E_{Had}/E_{\nu}$ quartile.

## 5.3 Selected Data and Predictions at the Far Detector

The observed reconstructed neutrino and antineutrino energy spectra at the FD are used to set the constraints on the space of oscillation parameters. A total of 113 $\nu_\mu$ CC event candidates were selected in the FHC beam mode, and 102 $\bar{\nu}_\mu$ CC event candidates in the RHC mode. Table 5.4 presents the summary of the selected number of $\nu_\mu$ and $\bar{\nu}_\mu$ CC candidate events at the FD along with the prediction at the joint neutrino+antineutrino beam disappearance best fit (see best fit values in Table 5.5) including the FD cosmic estimate and the systematic pulls from the fit. The selected events in the neutrino and antineutrino beam modes are slightly higher and lower than the prediction at the FHC+RHC best fit, respectively. However, the data is consistent with the expectation within the Poisson uncertainties.

Figures 5.11 and 5.12 show a comparison between the reconstructed energy spectrum of the selected event candidates at the FD (in black dots), the prediction at the FHC+RHC best fit (in purple) and the prediction in absence of oscillations (in green) split in bins of energy resolution and for the combination of them, respectively. Figure 5.13 shows the ratio of the oscillated to the unoscillated prediction, where the disappearance phenomena is clearly largest between 1 GeV and 2.0 GeV. This region is referred to as the *energy dip*.

In the following pages, the distribution of selected $\nu_\mu$ and $\bar{\nu}_\mu$ CC events in terms of the most relevant energy variables to the analysis are presented from the FD exposure to the neutrino and antineutrino beams. The data is shown by black dots with associated Poisson errors, and the distributions are compared to the predicted oscillated spectra at the analysis best fit. The FD Monte Carlo spectra are extrapolated predictions obtained as described in § 4.7. These predictions are represented by the purple histograms and they are displayed with the 1 $\sigma$ error band from the sum in quadrature of the systematic uncertainties accounted for in the analysis. The simulated wrong sign component, the beam background and the cosmic expectation are shown in green, gray and blue, respectively. The arrangement of the plots is such that the distributions from the FHC and RHC datasets are presented side-by-side for a direct comparison between beam modes. The total spectra are presented first and are directly followed by the breakdown in energy resolution bins.

Figures 5.14 and 5.15 show the reconstructed neutrino energy spectra of selected $\nu_\mu$ and $\bar{\nu}_\mu$ CC events at the FD and the oscillated predictions for all the hadronic energy fraction quartiles combined and for each individual quartile. The distributions show general data-Monte Carlo agreement in both beam modes. However, the FHC total data distribution presents an outlier point in the (2.75,3.0) GeV bin. The RHC data also shows a deviation from the best fit prediction in the (3.0,3,5) GeV bin. These two bins are in the energy region where the analysis is less sensitive to extracting the oscillation measurements. Moreover, the spectra for each individual quartile show that the accumulation of events in these bins could be due to statistical fluctuations. As at the ND, the FD distributions for the neutrino beam present the largest concentration of wrong sign events in the first quartile, while the inverse is true in antineutrino.

The reconstructed muon energy distributions for selected data and oscillated predictions at the FD are shown in Figures 5.16 and 5.17 for the combination and for the individual bins of energy resolution, respectively. Figures 5.18 and 5.19, and 5.20 and 5.21 show the equivalent plots in reconstructed hadronic energy and in reconstructed hadronic energy fraction respectively. These distributions also show reasonable agreement between data and the oscillated prediction.

| | FHC | | RHC | |
|---|---|---|---|---|
| $E_{Had}/E\nu$ | Data | Prediction | Data | Prediction |
| Lowest | 32 | 30.35 (186.55) | 25 | 24.82 (130.42) |
| Second lowest | 25 | 29.64 (179.74) | 25 | 24.16 (124.42) |
| Second highest | 26 | 30.64 (178.43) | 28 | 22.93 (113.58) |
| Highest | 30 | 34.41 (185.52) | 24 | 24.36 (107.20) |
| Total | 113 | 125.04 (730.23) | 102 | 96.27 (475.61) |

**Table 5.4:** Number of selected $\nu_\mu$ and $\bar{\nu}_\mu$ events from data and simulation at the FD, for the FHC and RHC beam configurations separated by bins of energy resolution. The predictions assume oscillations at the joint neutrino+antineutrino beam disappearance fit (see Table 5.5) and include the cosmic background. The predicted number of events in absence of oscillations is shown in parentheses. The numbers in this table account for the systematic pulls in the fit.

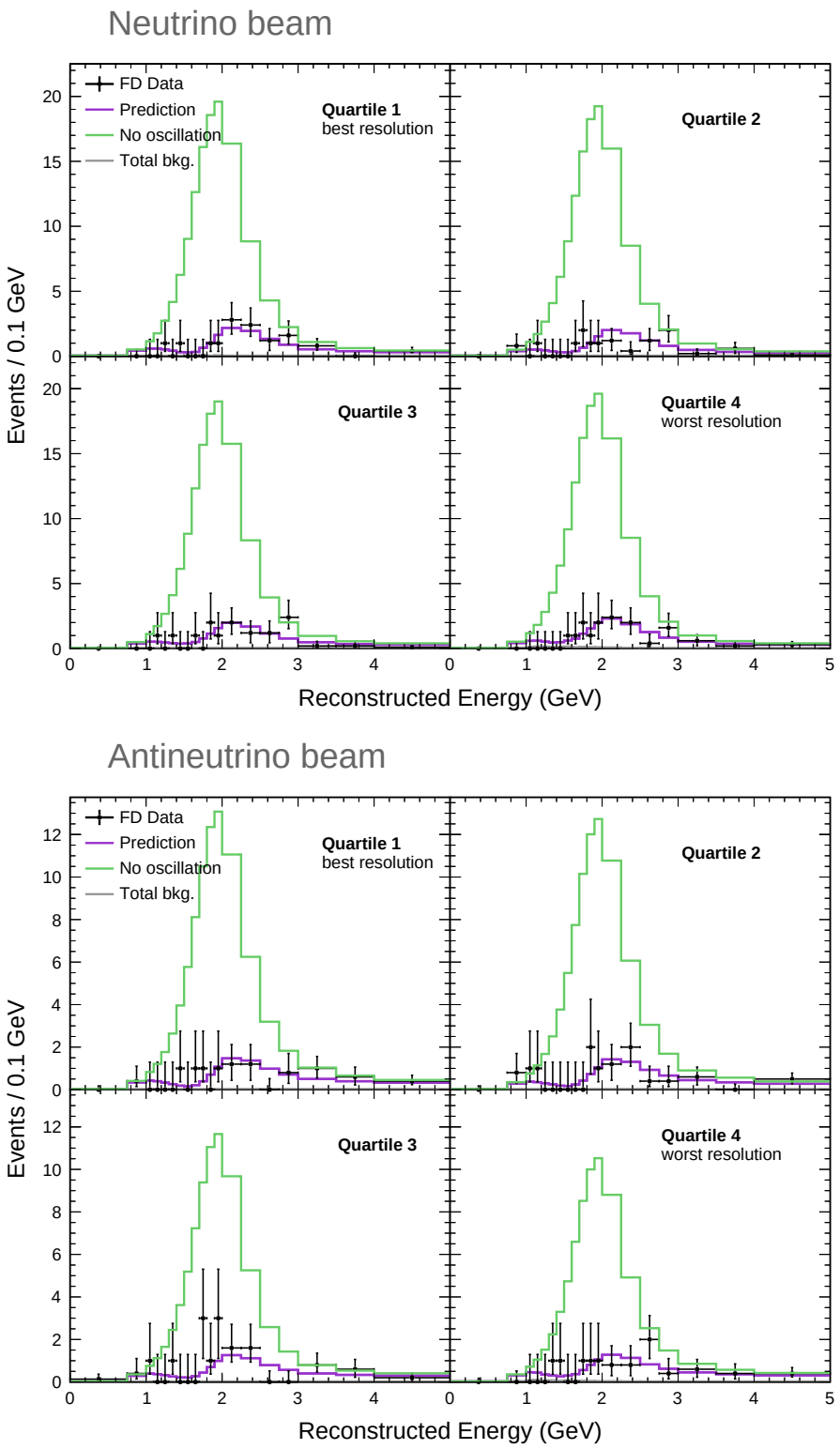


**Figure 5.11:** Reconstructed energy spectra of selected data and simulated oscillated and unoscillated neutrino events at the **FD** for the combination of each individual $E_{Had}/E_{\nu}$ quartile. The distributions are from the neutrino (FHC) and antineutrino (RHC) beam configurations are shown at the top and bottom respectively. The data passing the $\nu_{\mu}$ +$\bar{\nu}_{\mu}$ selection criteria is shown in black dots with statistical errors. The reconstructed neutrino energy spectra in absence of oscillations is shown in green. The nominal simulation oscillated with the joint neutrino+antineutrino CPTc best fit values is shown in purple. The total simulated background, which includes the wrong sign component, beam and cosmic backgrounds are represented by the gray line.

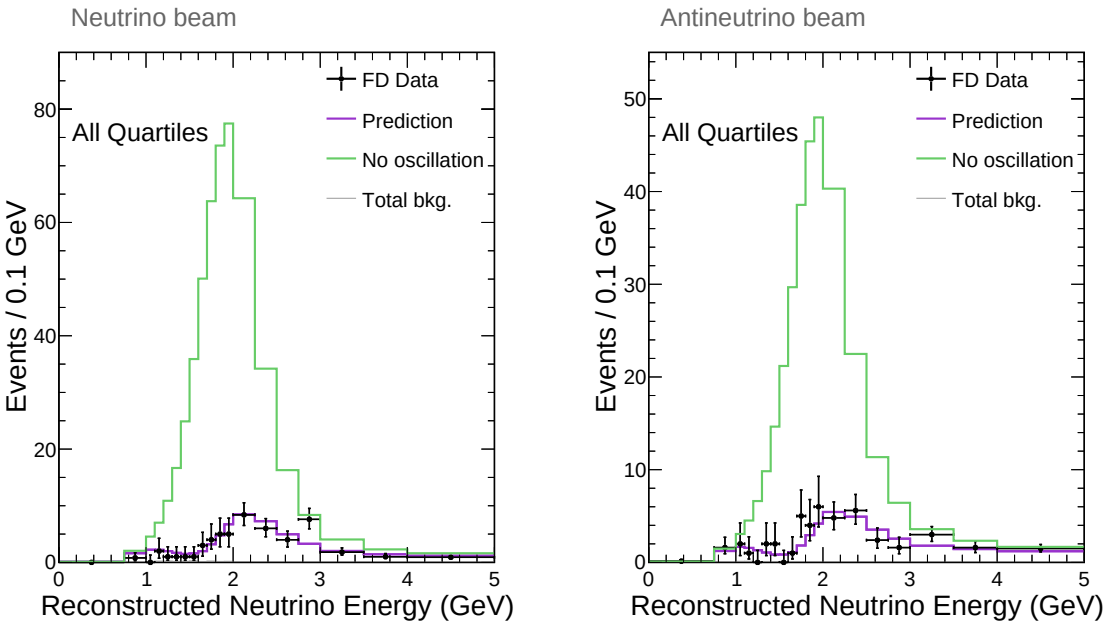


**Figure 5.12:** Reconstructed neutrino energy spectra of selected data and simulated oscillated and unoscillated neutrino events at the **FD** for the combination of all the $E_{Had}/E_{\nu}$ quartiles. The distributions are from the neutrino (FHC) and antineutrino (RHC) beam configurations are shown on the left and right respectively. The data passing the $\nu_{\mu}$ +$\bar{\nu}_{\mu}$ selection criteria is shown in black dots with statistical errors. The reconstructed neutrino energy spectra in absence of oscillations is shown in green. The nominal simulation oscillated with the joint neutrino+antineutrino CPTc best fit values is shown in purple. The total simulated background, which includes the wrong sign component, beam and cosmic backgrounds are represented by the gray line.

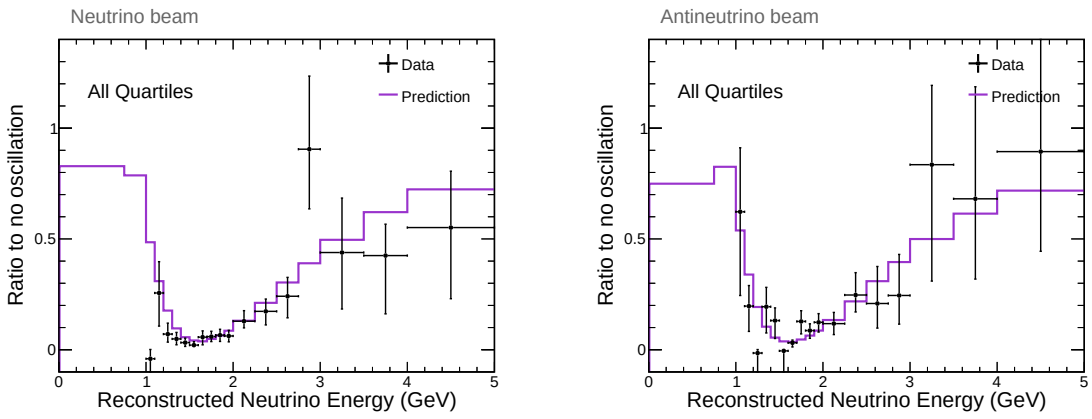


**Figure 5.13:** Reconstructed neutrino energy ratio of the FD spectra in absence of oscillations to the FD spectra at the neutrino + antineutrino best fit for the combination of $E_{Had}/E_{\nu}$ quartiles. The FHC (neutrino) and RHC (antineutrino) beam ratios are shown at the left and right respectively.

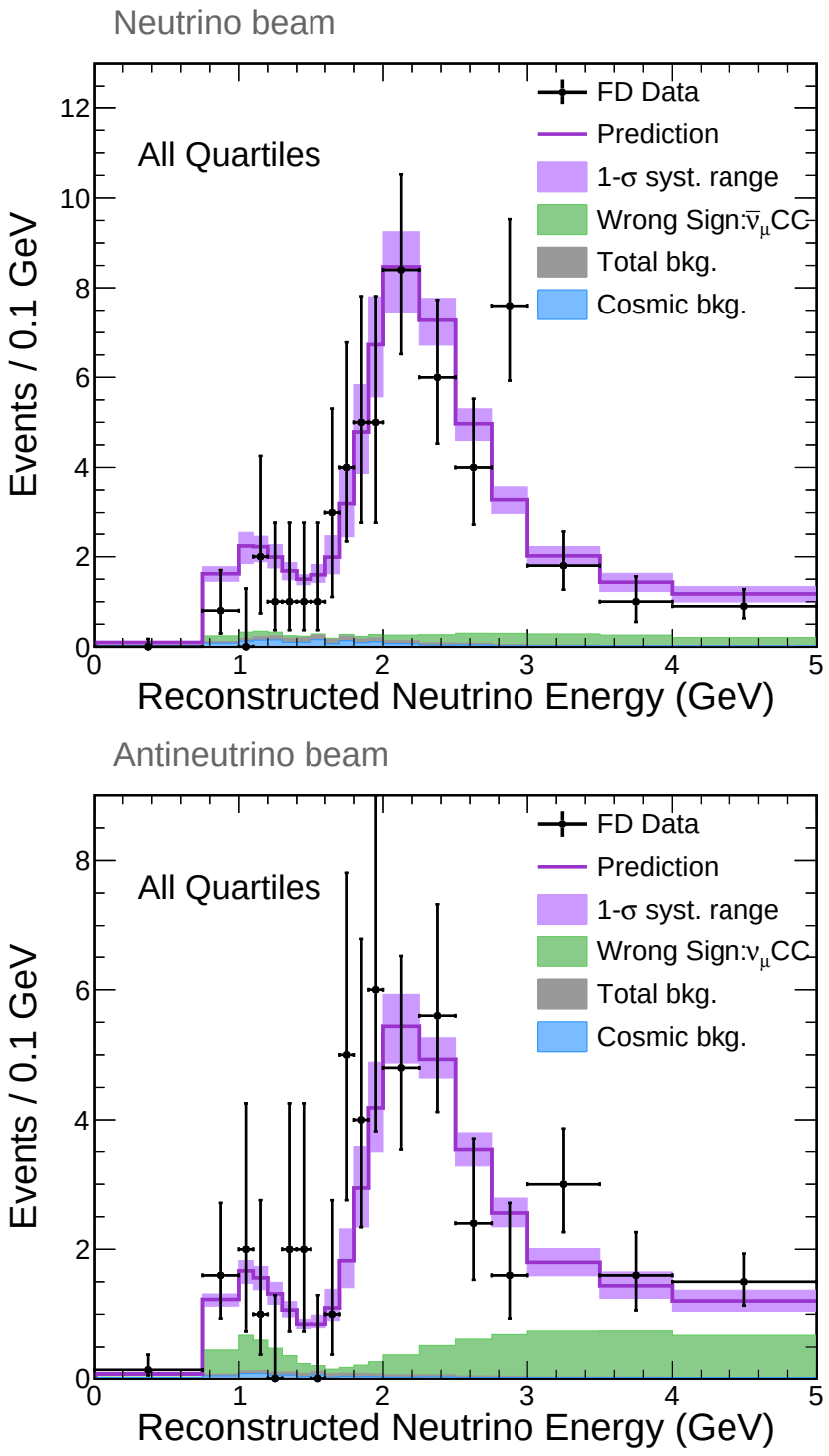


**Figure 5.14: Reconstructed neutrino energy** spectra of selected data and simulated events at the **FD** for the combination of $E_{Had}/E_\nu$ quartiles. The distributions from the neutrino (FHC) and antineutrino (RHC) beam configurations are shown at the top and bottom respectively. The data passing the $\nu_\mu$ +$\bar{\nu}_\mu$ selection criteria is shown in black dots with statistical errors. The prediction at the joint neutrino+antineutrino CPTc best fit is shown in purple and the shaded region corresponds to the 1 $\sigma$ systematic uncertainty on the simulation. The simulated wrong sign component and beam background, as well as the cosmic prediction, are represented by the green, gray and blue regions respectively.

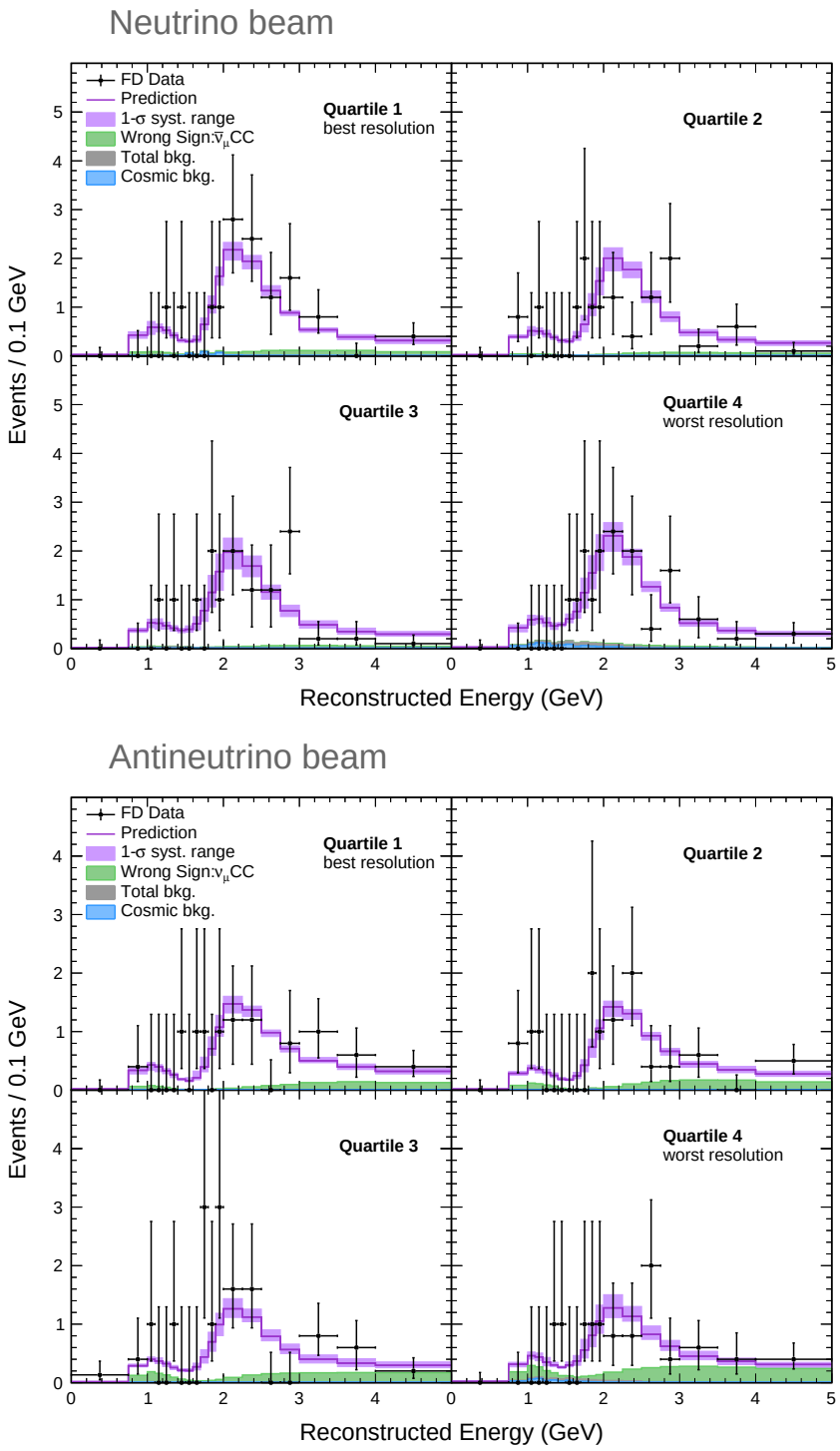


**Figure 5.15: Reconstructed neutrino energy** spectra of selected data and simulated events at the **FD** for each individual $E_{Had}/E_\nu$ quartile. The distributions from the neutrino (FHC) and antineutrino (RHC) beam configurations are shown at the top and bottom respectively. The data passing the $\nu_\mu + \bar{\nu}_\mu$ selection criteria is shown in black dots with statistical errors. The prediction at the joint neutrino+antineutrino CPTc best fit is shown in purple. The simulated wrong sign component and beam background, as well as the cosmic prediction, are represented by the green, gray and blue regions respectively.

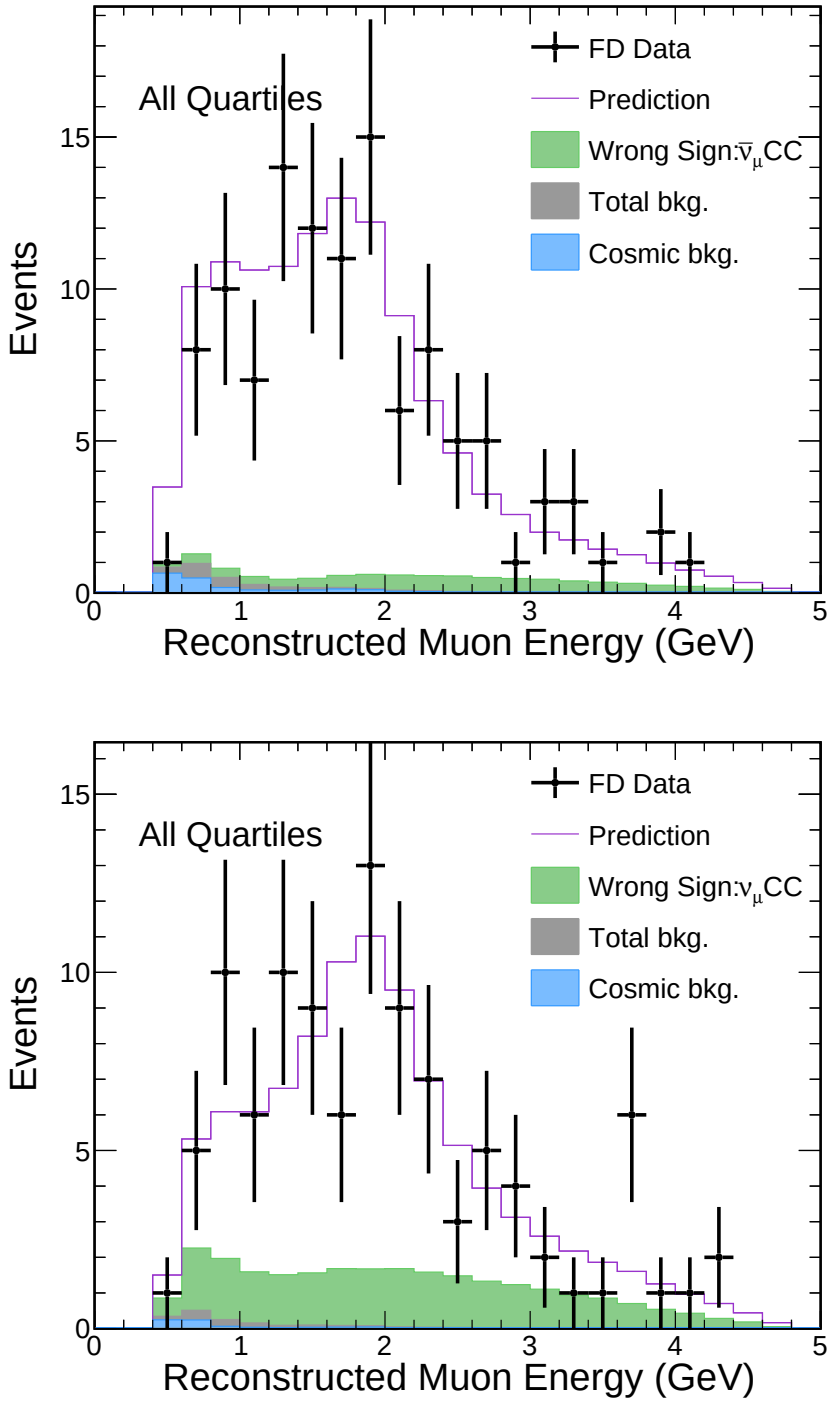


**Figure 5.16:** Distribution of selected data and simulated events at the **FD** in **reconstructed muon energy** for the combination of $E_{Had}/E_\nu$ quartiles. The distributions from the neutrino (FHC) and antineutrino (RHC) beam configurations are shown at the top and bottom respectively. The data passing the $\nu_\mu$ +$\bar{\nu}_\mu$ selection criteria is shown in black dots with statistical errors. The prediction at the joint neutrino+antineutrino CPTc best fit is shown in purple. The simulated wrong sign component and beam background, as well as the cosmic prediction, are represented by the green, gray and blue regions respectively.

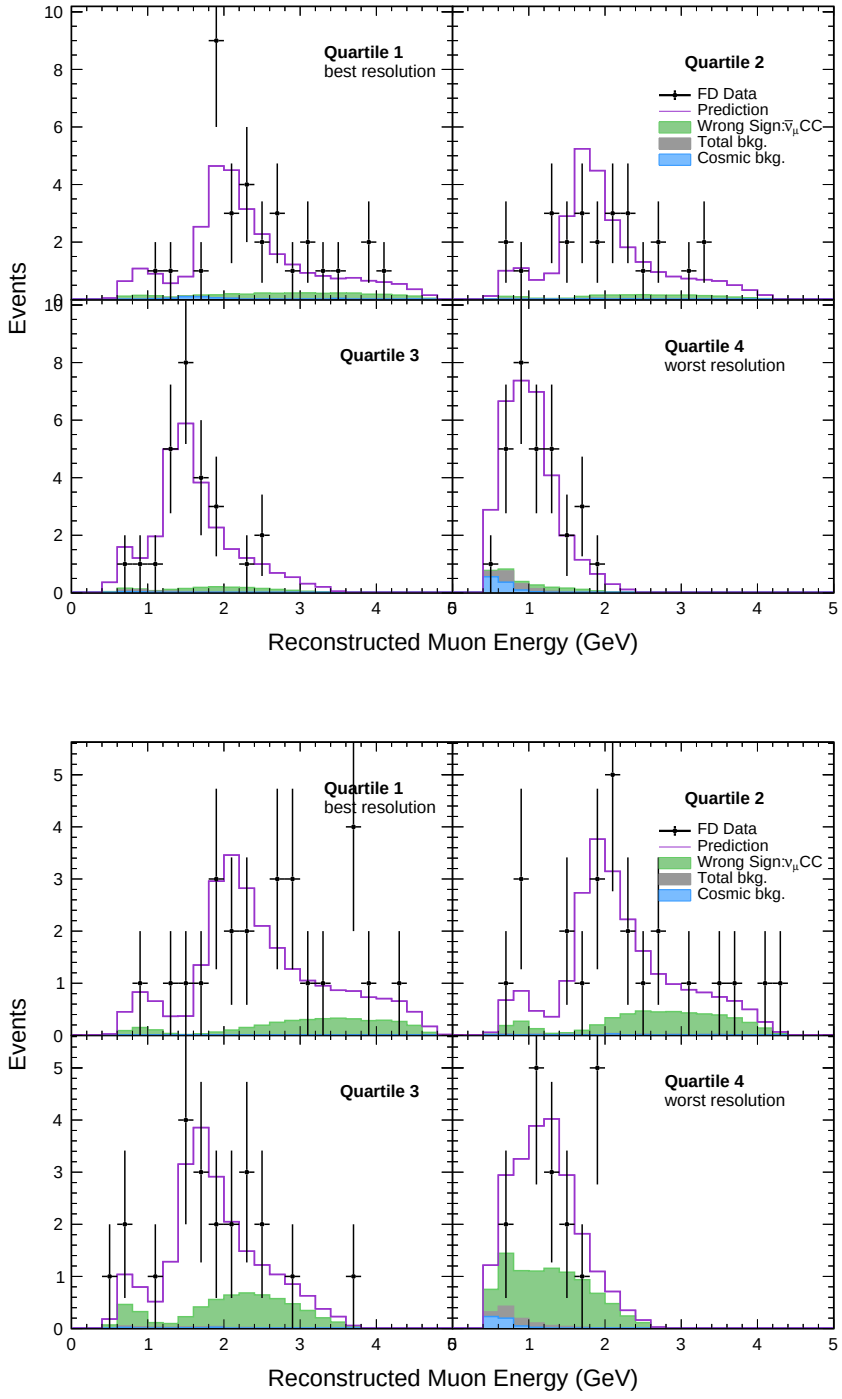


**Figure 5.17:** Distribution of selected data and simulated events at the **FD** in **reconstructed muon energy** for each individual $E_{Had}/E_\nu$ quartile. The distributions from the neutrino (FHC) and antineutrino (RHC) beam configurations are shown at the top and bottom respectively. The data passing the $\nu_\mu + \bar{\nu}_\mu$ selection criteria is shown in black dots with statistical errors. The prediction at the joint neutrino+antineutrino CPTc best fit is shown in purple and the shaded region corresponds to the 1 $\sigma$ systematic uncertainty on the simulation. The simulated wrong sign component and beam background, as well as the cosmic prediction, are represented by the green, gray and blue regions respectively.

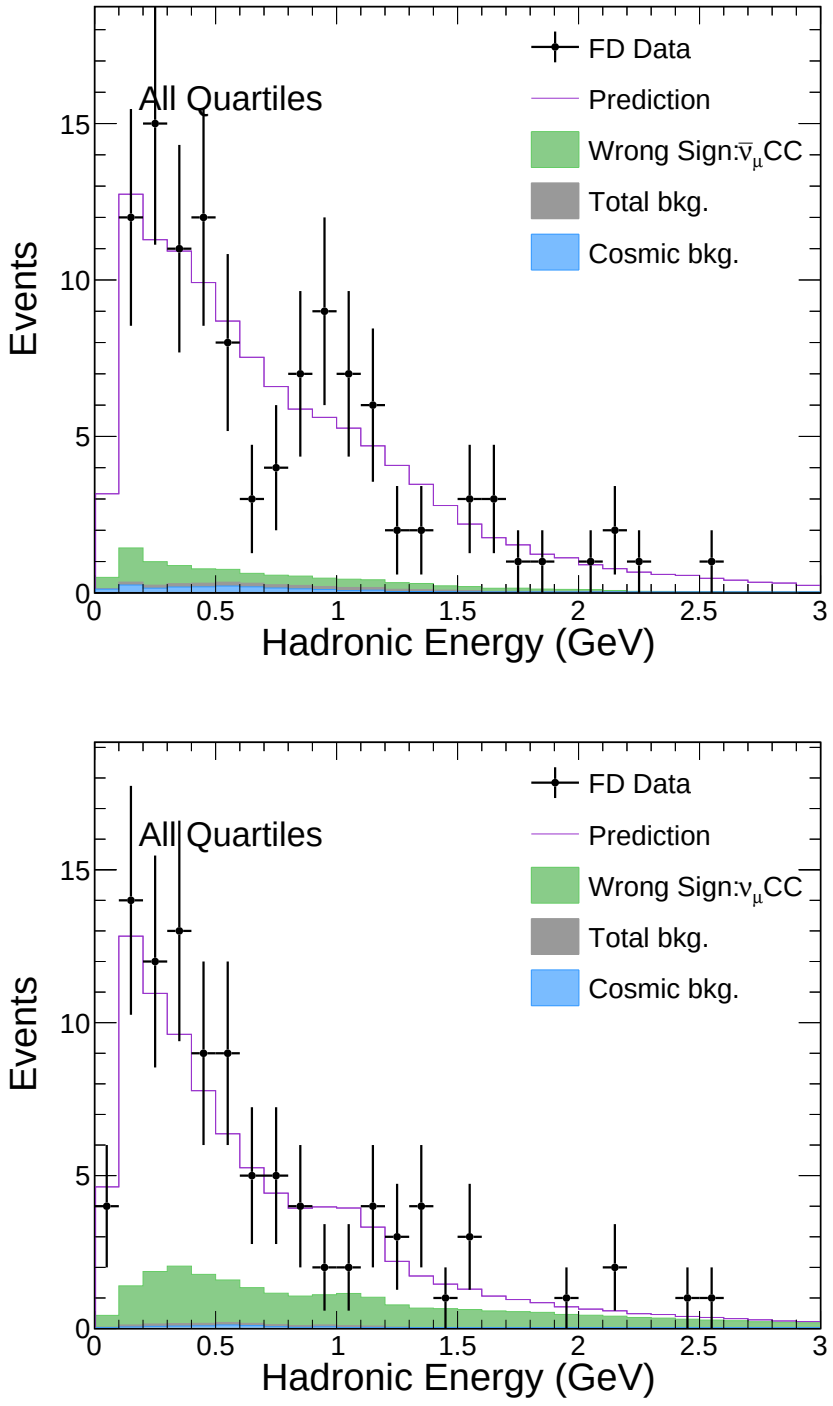


**Figure 5.18:** Distribution of selected data and simulated events at the **FD** in **hadronic energy** for the combination of $E_{Had}/E_\nu$ quartiles. The distributions from the neutrino (FHC) and antineutrino (RHC) beam configurations are shown at the top and bottom respectively. The data passing the $\nu_\mu + \bar{\nu}_\mu$ selection criteria is shown in black dots with statistical errors. The prediction at the joint neutrino+antineutrino CPTc best fit is shown in purple. The simulated wrong sign component and beam background, as well as the cosmic prediction, are represented by the green, gray and blue regions respectively.

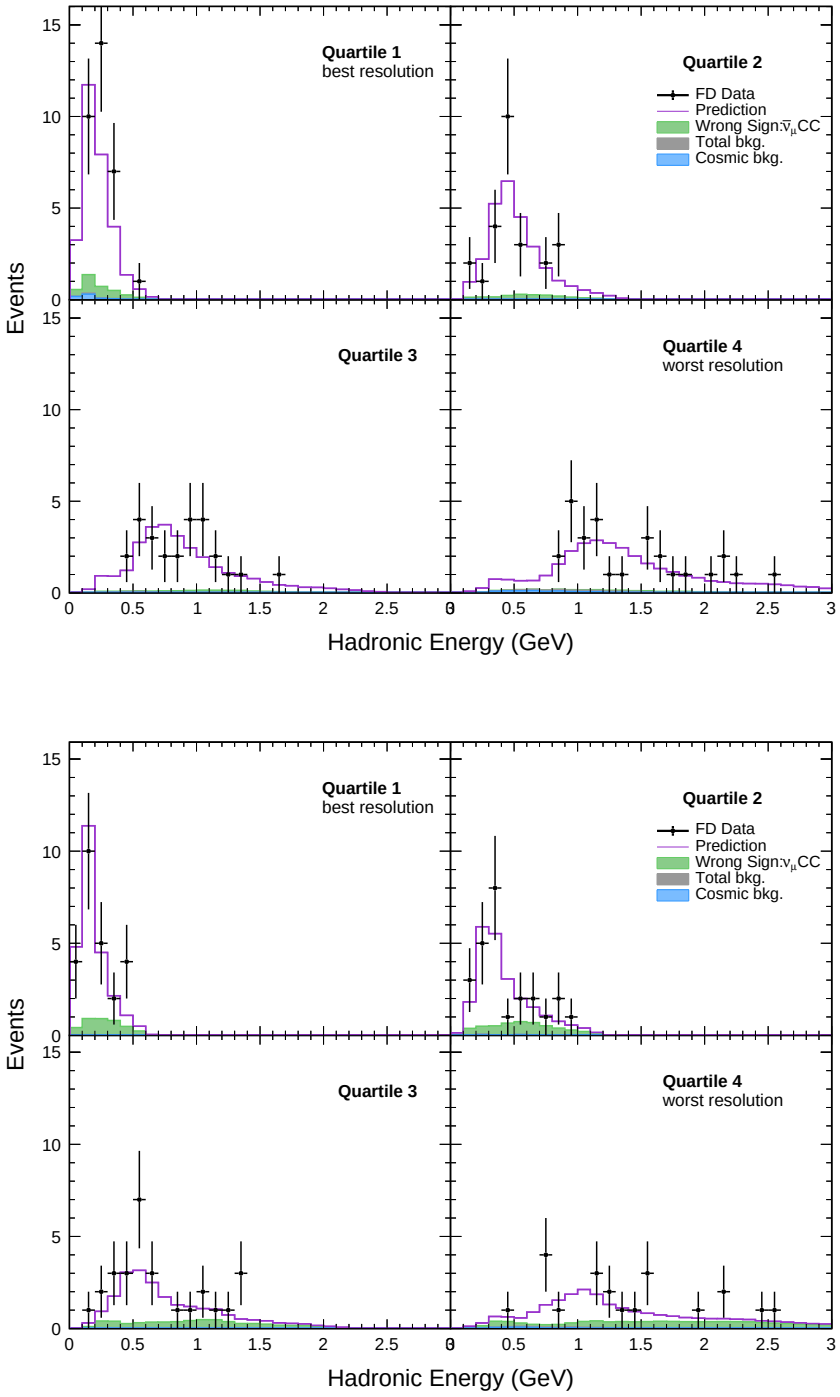


**Figure 5.19:** Distribution of selected data and simulated events at the **FD** in **hadronic energy** for each individual $E_{Had}/E_\nu$ quartile. The distributions from the neutrino (FHC) and antineutrino (RHC) beam configurations are shown at the top and bottom respectively. The data passing the $\nu_\mu + \bar{\nu}_\mu$ selection criteria is shown in black dots with statistical errors. The prediction at the joint neutrino+antineutrino CPTc best fit is shown in purple and the shaded region corresponds to the 1 $\sigma$ systematic uncertainty on the simulation. The simulated wrong sign component and beam background, as well as the cosmic prediction, are represented by the green, gray and blue regions respectively.

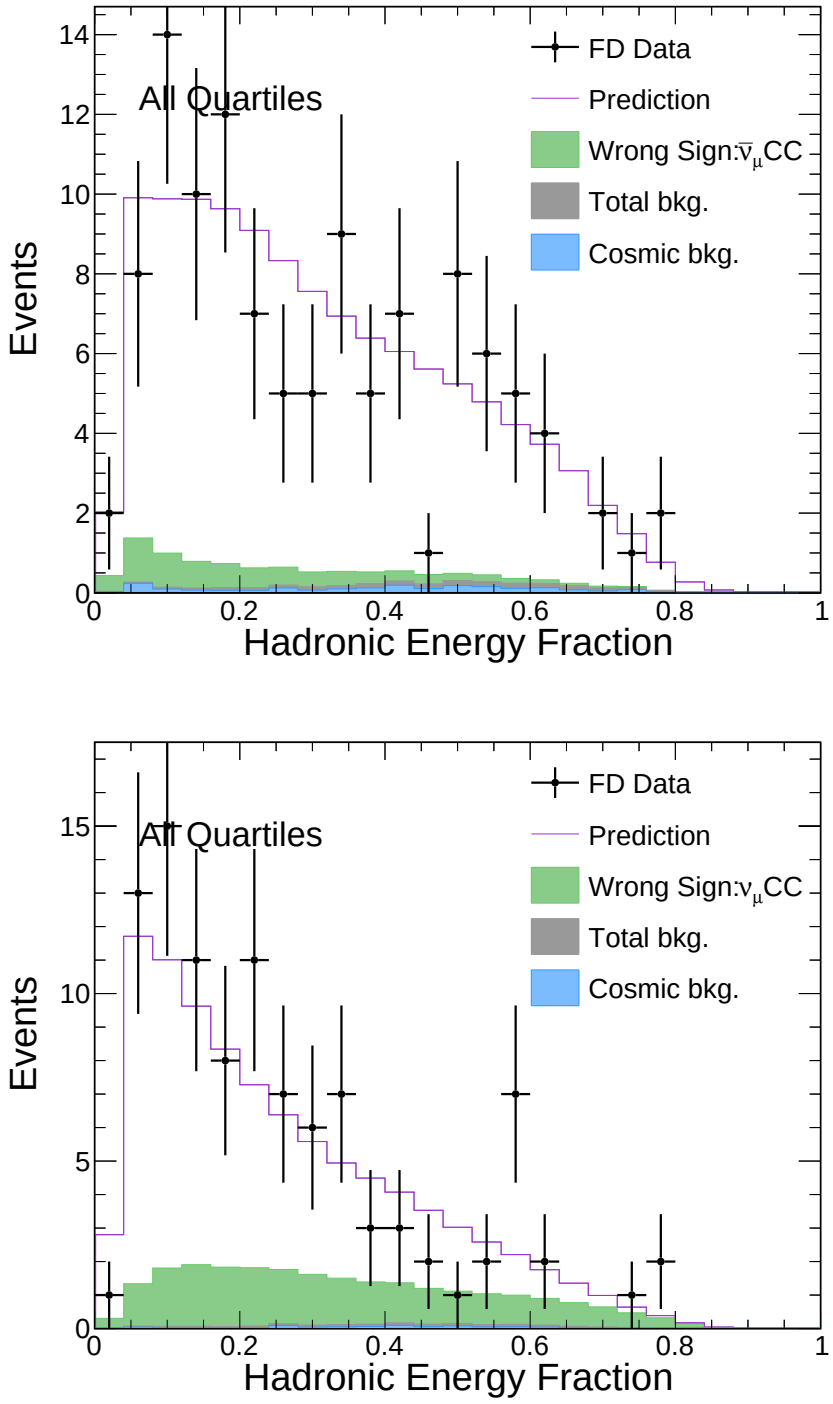


**Figure 5.20:** Distribution of selected data and simulated events at the **FD** in **hadronic energy fraction** for the combination of $E_{Had}/E_\nu$ quartiles. The distributions from the neutrino (FHC) and antineutrino (RHC) beam configurations are shown at the top and bottom respectively. The data passing the $\nu_\mu$ +$\bar{\nu}_\mu$ selection criteria is shown in black dots with statistical errors. The prediction at the joint neutrino+antineutrino CPTc best fit is shown in purple. The simulated wrong sign component and beam background, as well as the cosmic prediction, are represented by the green, gray and blue regions respectively.

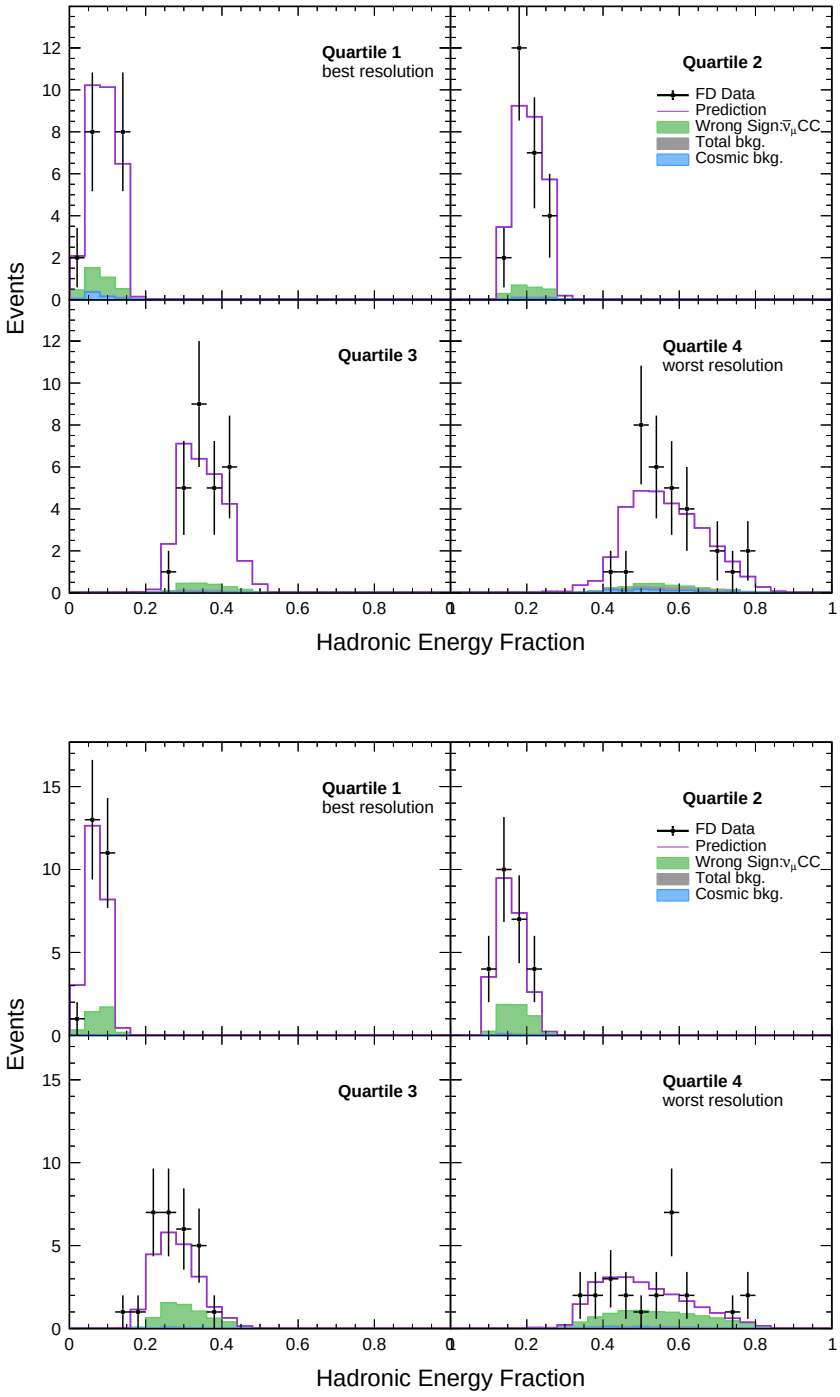


**Figure 5.21:** Distribution of selected data and simulated events at the **FD** in **hadronic energy fraction** for each individual $E_{Had}/E_\nu$ quartile. The distributions from the neutrino (FHC) and antineutrino (RHC) beam configurations are shown at the top and bottom respectively. The data passing the $\nu_\mu$ + $\bar{\nu}_\mu$ selection criteria is shown in black dots with statistical errors. The prediction at the joint neutrino+antineutrino CPTc best fit is shown in purple and the shaded region corresponds to the 1 $\sigma$ systematic uncertainty on the simulation. The simulated wrong sign component and beam background, as well as the cosmic prediction, are represented by the green, gray and blue regions respectively.

## 5.4 Results

An analysis of muon neutrino and antineutrino data is performed to constrain the values of the mass squared splitting $\Delta m^2_{32}$ and the mixing angle $\sin^2\theta_{23}$ following the method described in § 4.9. The reconstructed FD energy spectra from selected $\nu_\mu$ and $\bar{\nu}_\mu$ candidate events presented in the previous section is fit to a three neutrino oscillation model assuming CPT invariance, where the neutrinos and antineutrinos share the same values of oscillation parameters. The data collected during the exposure to the neutrino and antineutrino beams is either combined or analysed separately. Therefore, three results are presented: one is the result of a joint neutrino + antineutrino beam fit, and two are the results from using either the neutrino or the antineutrino beam data. The analysis uses an average of the global results from reactor and solar neutrino experiments, which are implemented as nuisance parameters in the fit. The values from the Particle Data Group (PDG) [26] that are used are

$$\Delta m^2_{21} = 7.39^{+0.21}_{-0.20} \times 10^{-5}\ \text{eV}^2, \tag{5.1a}$$

$$\sin^2\theta_{12} = 0.310^{+0.013}_{-0.012}, \tag{5.1b}$$

$$\sin^2\theta_{13} = 2.10 \pm 0.11 \times 10^{-2}. \tag{5.1c}$$

Separate fits are made for the normal and inverted hierarchy cases. This means that the space where the $\chi^2$ is computed is split in $\Delta m^2_{32} > 0$ and $\Delta m^2_{32} < 0$[3]. However, $\nu_\mu$ and $\bar{\nu}_\mu$ disappearance is not sensitive to the determination of the hierarchy[4] and the confidence region contours are only presented for the normal hierarchy solution. All the results account for statistical and systematic uncertainties unless otherwise stated.

### 5.4.1 Constraints on $\sin^2\theta_{23}$ and $\Delta m^2_{32}$

The results of the three independent fits to the FD data are shown in Figure 5.22. The blue and the pink contours enclose the region in the $\Delta m^2_{32}$ vs. $\sin^2\theta_{23}$ space of parameters that are allowed at the 90% confidence level when performing a fit to the data from the neutrino or the antineutrino beam only, respectively, in the normal hierarchy scenario. The 90% confidence region corresponding to the combined $\nu + \bar{\nu}$ fit is shown in green. The significance at which a particular value of $\sin^2\theta_{23}$ and $\Delta m^2_{32}$ is disfavored is shown in terms of $\sqrt{\Delta\chi^2}$. The constraints to $\Delta m^2_{32}$ vs. $\sin^2\theta_{23}$ space from the joint $\nu_\mu + \bar{\nu}_\mu$ disappearance analysis is compared in Figure 5.23 to the latest limits set by currently running (T2K, Super-Kamiokande, IceCube) and past (MINOS+) experiments, and all the results are consistent.

The best fits from a fit to the FHC beam only data in the normal hierarchy are $\sin^2\theta_{23} = 0.51^{+0.07}_{-0.07}$ and $\Delta m^2_{32} = 2.45^{+0.07}_{-0.09} \times 10^{-3}\text{eV}^2$, with a $\chi^2 = 65.6$ for 74 degrees of freedom (*d.o.f.*).

[3] A small region of $\Delta m^2_{32}$ values was used to expedite the fit: (2.0, 3.0)$\times 10^{-3}$ eV$^2$ and (-3.0, -2.0)$\times 10^{-3}$ eV$^2$ for normal and inverted hierarchy respectively.

[4] The minimum $\chi^2$ has almost exactly the same value at the inverted and normal hierarchy best fits.

The RHC beam only data best fit in normal hierarchy for $\Delta m^2_{32}$ is at $2.53^{+0.10}_{-0.12} \times 10^{-3}$ eV$^2$, and two statistically degenerated best fits for $\sin^2\theta_{23}$ in 0.42 and 0.60, with a $\chi^2/d.o.f = 67.7/74$. The RHC-only $1\sigma$ confidence intervals for $\sin^2\theta_{23}$ are $[0.39, 0.46]$ and $[0.56, 0.63]$. The neutrino and antineutrino beam only results are consistent at 47%. The best fit point from the combined fit to neutrino and antineutrino beam data is found at $\Delta m^2_{32} = 2.48^{+0.08}_{-0.06}$, and $\sin^2\theta_{23} = 0.57$ in the range $[0.53, 0.59]$ and $[0.44, 0.48]$ allowed at 1 $\sigma$ in the normal hierarchy with $\chi^2/d.o.f. = 134.8/150$. The quoted 1 $\sigma$ bounds are the combined statistical and systematic uncertainty bounds. Table 5.5 summarizes the results of the measurements of the mixing angle $\sin^2\theta_{23}$ and the mass splitting $\Delta m^2_{32}$, and include the inverted hierarchy measurements.

The systematic uncertainties can distort the normalisation and/or the shape of the predicted spectra, which reduce the experiment's sensitivity. Figure 5.24 shows the comparison between the 90% confidence regions from the joint neutrino + antineutrino beam fit to data when including only statistical fluctuations, and the results from the fit where both statistical and systematic uncertainties are accounted for. The systematic uncertainties have a larger effect on the measurement of $\Delta m^2_{32}$. NOvA's previous neutrino beam only disappearance results are shown by the gray dashed line. Figure 5.25 show the systematic shifts, quoted as fractions of $\sigma$, that contribute to the $\chi^2$ in the neutrino-only, antineutrino-only and neutrino + antineutrino beam joint fits. These plots represent the extent to which a prediction has to be shifted to improve the $\chi^2$ between the data and the oscillation model due to a systematic uncertainty and are referred to as pull terms. The largest pulls arise from the calibration and light model systematics and both are less than 1 $\sigma$.

The uncertainties are evaluated by comparing the statistical only fit against a fit that also includes a systematic uncertainty. The impact of an individual or a group of systematics on the measurement is assessed by subtracting in quadrature the $1\sigma$ boundaries from these two fits. Figures 5.26 and 5.27 graphically show the impact of uncertainty sets on the mixing angle and mass square splitting, respectively, arranged from largest to smallest for the neutrino and antineutrino measurements. A mapping between the individual uncertainties as displayed in Figure 5.25 and the groups of uncertainties in Figures 5.26 and 5.27 is shown in Table 5.6. The dominant systematic uncertainty for both the mixing angle and the mass-squared difference is the absolute and relative hadronic energy scales and the neutron uncertainty.

| | Normal Hierarchy | | Inverted Hierarchy | |
|---|---|---|---|---|
| Beam mode | $\sin^2\theta_{23}$ | $\Delta m^2_{32}(\times 10^{-3}$ eV$^2)$ | $\sin^2\theta_{23}$ | $\Delta m^2_{32}(\times 10^{-3}$ eV$^2)$ |
| FHC | $0.51^{+0.07}_{-0.07}$ | $2.45^{+0.08}_{-0.09}$ | $0.51^{+0.07}_{-0.06}$ | $-2.48^{+0.07}_{-0.09}$ |
| RHC | $0.42 \in [0.39, 0.46] \cup 0.60 \in [0.56, 0.63]$ | $2.53^{+0.10}_{-0.12}$ | $0.43 \in [0.40, 0.47] \cup 0.60 \in [0.56, 0.63]$ | $-2.57^{+0.10}_{-0.12}$ |
| FHC+RHC | $0.57 \in [0.53, 0.59], [0.44, 0.48]$ | $2.48^{+0.08}_{-0.06}$ | $0.46 \in [0.43, 0.51], [0.52, 0.58]$ | $-2.53^{+0.07}_{-0.07}$ |

**Table 5.5:** Best fit values of the $\sin^2\theta_{23}$ and $\Delta m^2_{32}$ oscillation parameters from a CPT invariance $\nu_\mu$ and $\bar{\nu}_\mu$ disappearance analysis with an exposure to $8.85 \times 10^{20}$ and $12.33 \times 10^{20}$ POT in the FHC and RHC beam configuration, respectively. The data from either one or the two beams was used for the fits. The quoted 1 $\sigma$ bounds are the combined statistical and systematic uncertainty bounds

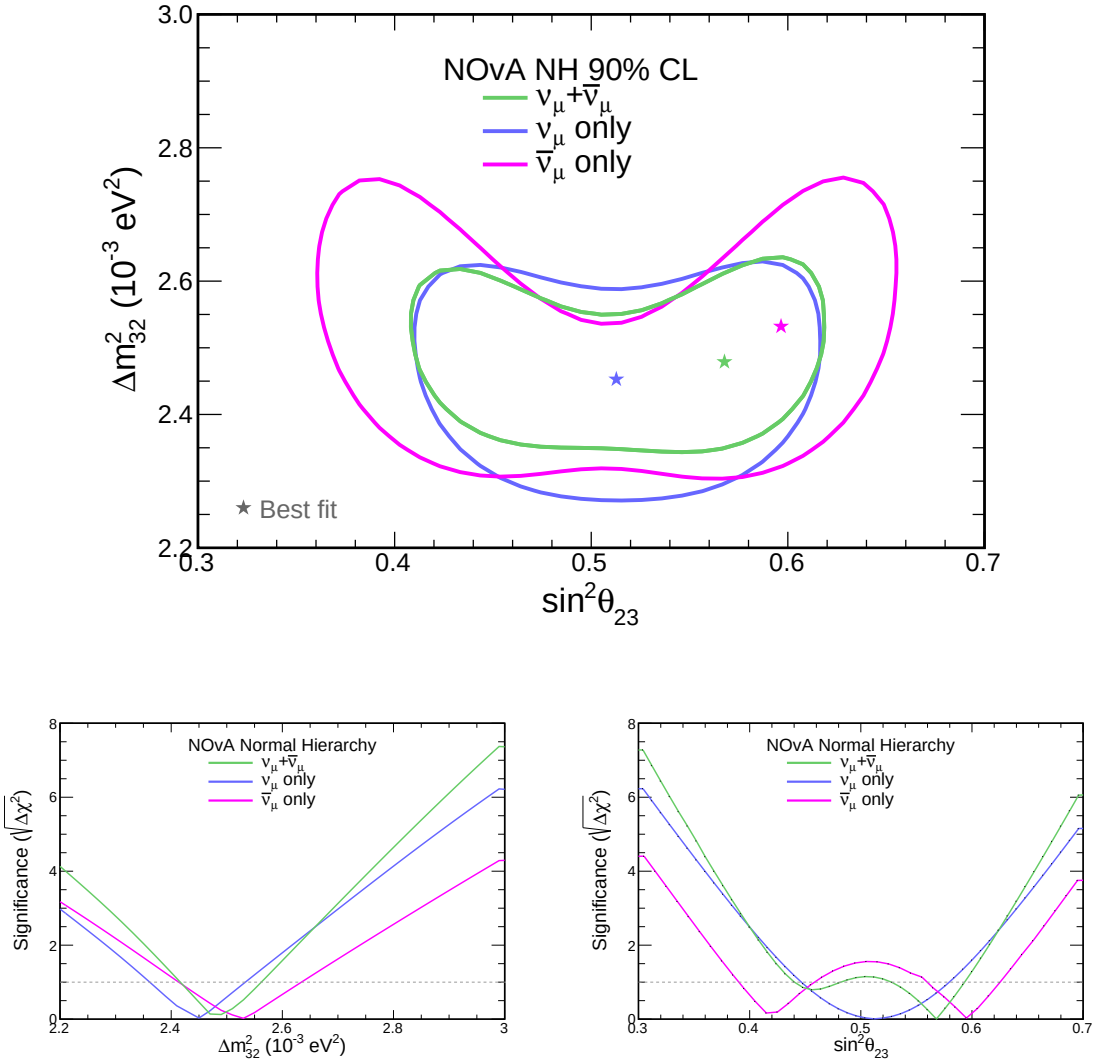


**Figure 5.22:** Constraints on $\sin^2\theta_{23}$ and $\Delta m^2_{32}$ from a $\nu_\mu$ and $\bar{\nu}_\mu$ disappearance analysis assuming CPT invariance, with an exposure to $8.85\times10^{20}$ and $12.33\times10^{20}$ POT in the FHC and RHC beam configuration, respectively. The top plot shows the 90% confidence regions of the mixing angle $\sin^2\theta_{23}$ and the mass squared difference $\Delta m^2_{32}$. The results are displayed in blue, pink and green for a FHC-only, RHC-only or the combined FHC+RHC data fit respectively. The best fit points are represented by a star for each case. The bottom plots show the significance on the measurement for each individual parameter. These results are for the normal neutrino mass ordering.

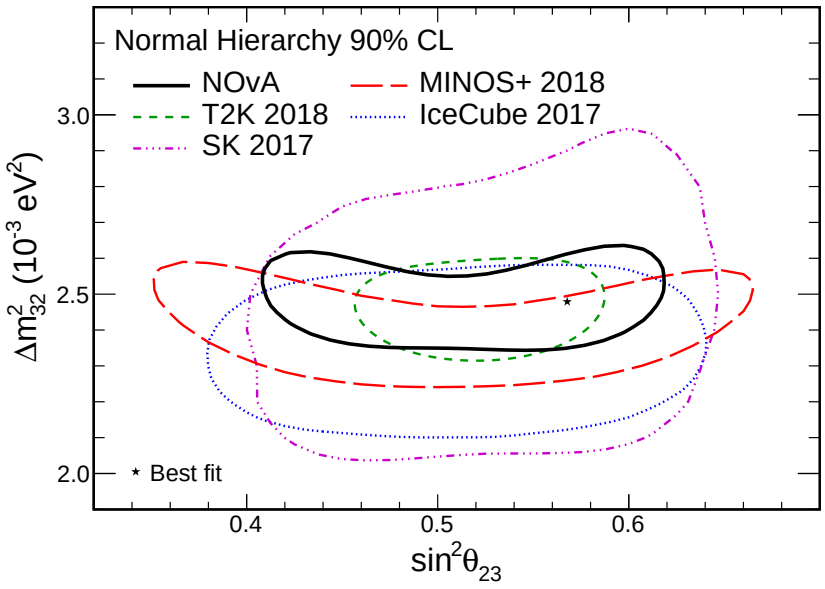


**Figure 5.23:** Comparison between NOvA $\nu_\mu + \bar{\nu}_\mu$ disappearance fit assuming CPT invariance and the world constraints on $\sin^2\theta_{23}$ and $\Delta m^2_{32}$. The 90% confidence level contour from a disappearance only fit with NOvA neutrino + antineutrino data from an exposure to $8.85 \times 10^{20}$ $+12.33 \times 10^{20}$ POT is shown in solid black. The best fit from this result is shown by the black star. The latest results from MINOS+ [50], T2K [47], SuperKamiokande [51] and Ice-Cube [49] are plotted for reference.

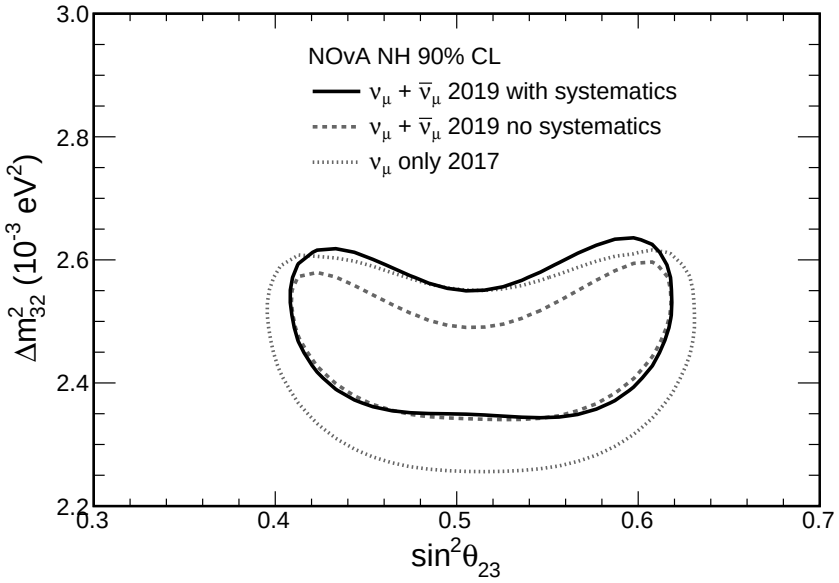


**Figure 5.24:** Comparison between NOvA $\nu_\mu + \bar{\nu}_\mu$ disappearance constraints on $\sin^2\theta_{23}$ and $\Delta m^2_{32}$ and NOvA's previous $\nu_\mu$ disappearance only result. The 90% confidence level contour in solid black is the result of the joint neutrino+antineutrino fit from a FD exposure to $8.85 \times 10^{20}$ $+12.33 \times 10^{20}$ POT. The result of a fit where only statistical errors are accounted for is shown by the dashed gray line. NOvA's previous $\nu_\mu$ only disappearance result is displayed for reference.

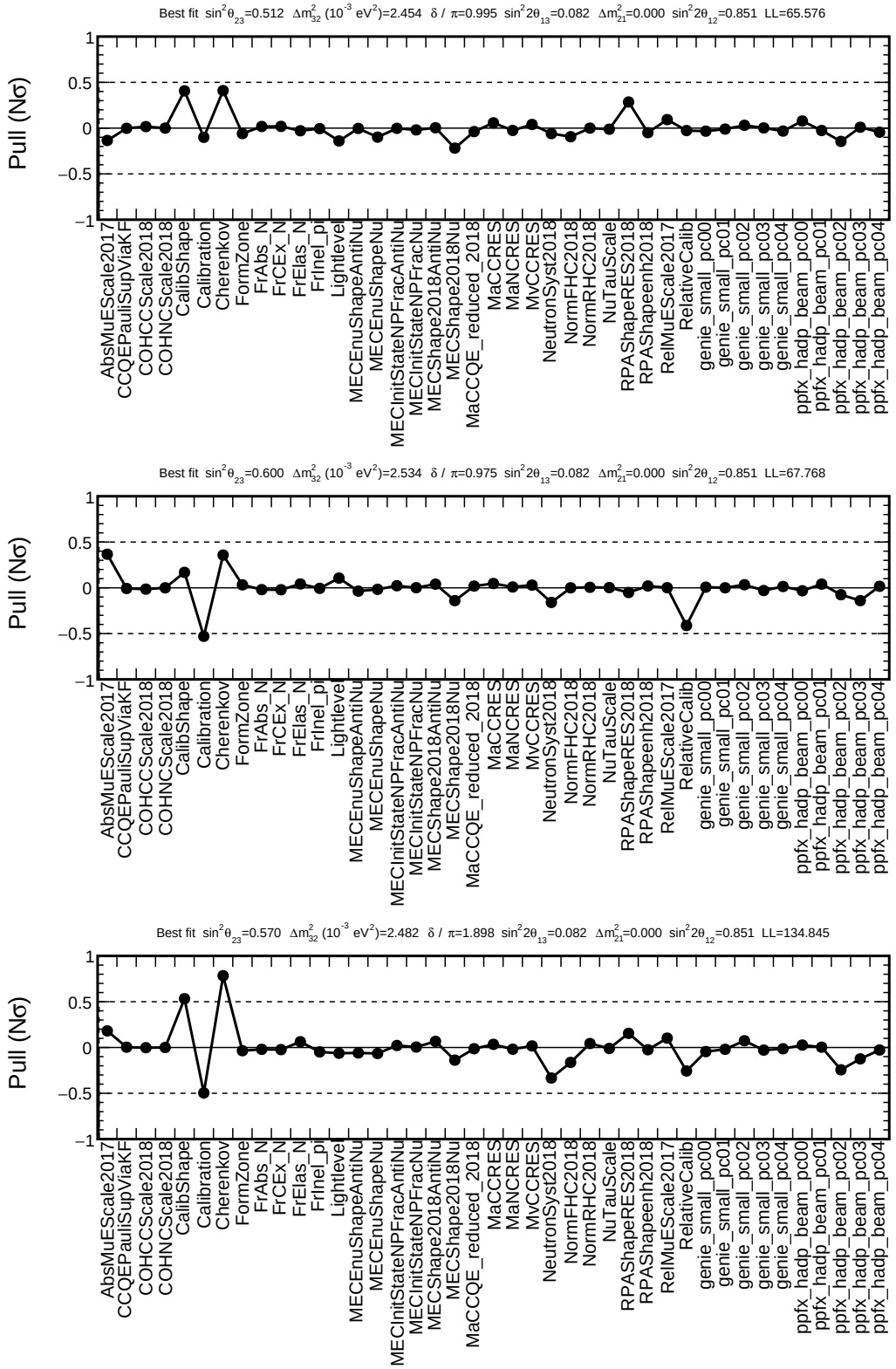


**Figure 5.25:** Systematic pulls for each of the uncertainties included in the CPT-conserved $\nu_\mu$ and/or $\bar{\nu}_\mu$ disappearance fit. The pulls are displayed in units of $\sigma$ for the FHC-only (top), RHC-only (middle), and FHC+RHC (bottom) analysis.

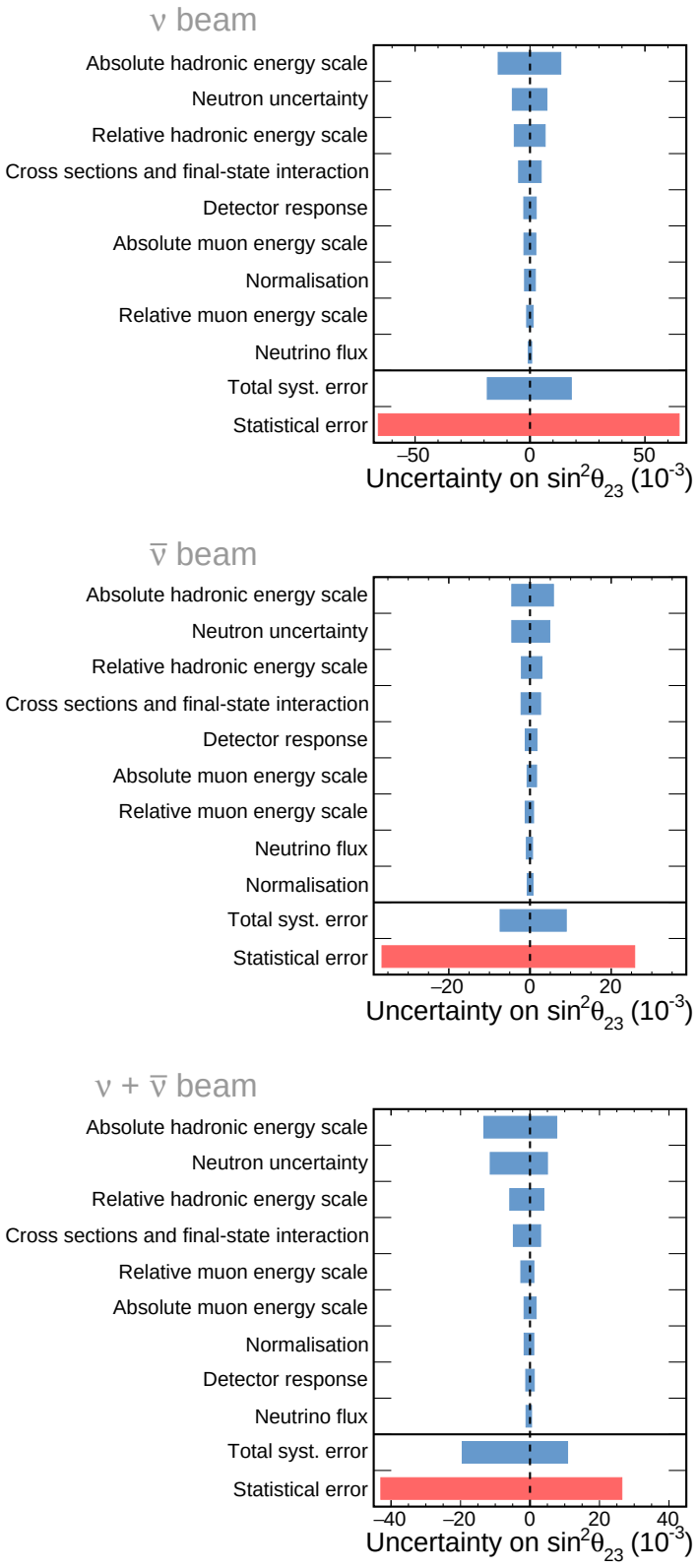


**Figure 5.26:** Illustration of the analysis uncertainty sources and the size of their impact in the measurement of the atmospheric mixing angle $\sin^2\theta_{23}$ for the FHC-only (top), RHC-only (middle), and FHC+RHC (bottom) analysis respectively. The bars correspond to the 1 $\sigma$ uncertainties on the parameter due to a single group of uncertainties and are arranged in decreasing size from top to bottom.

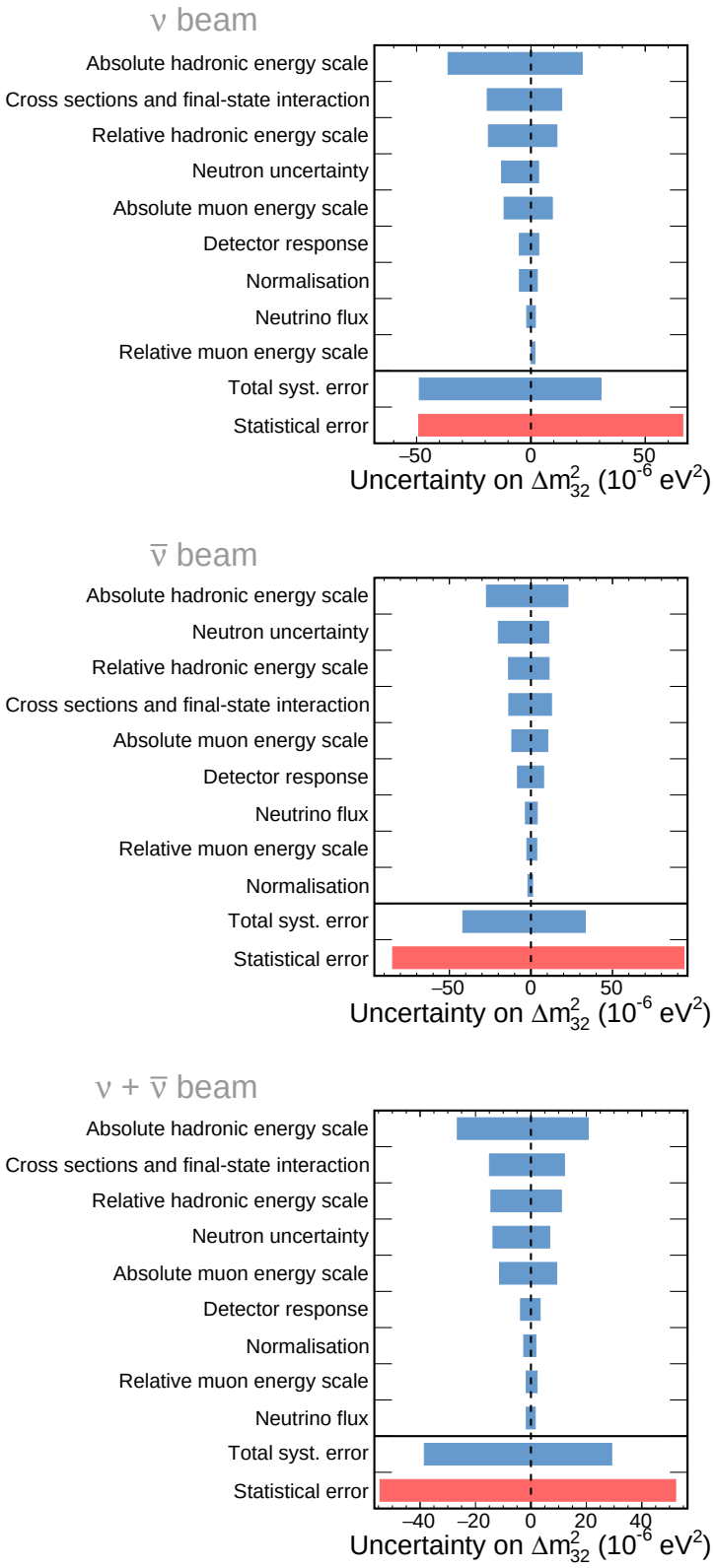


**Figure 5.27:** Illustration of the analysis uncertainty sources and the size of their impact in the measurement of the atmospheric mass splitting $\Delta m^2_{32}$ for the FHC-only (top), RHC-only (middle), and FHC+RHC (bottom) analysis respectively. The bars correspond to the 1 $\sigma$ uncertainties on the parameter due to a single group of uncertainties and are arranged in decreasing size from top to bottom.

| **Systematic uncertainty in Figures 5.26 and 5.27** | **Systematic uncertainty in Figure 5.25** |
|---|---|
| Absolute muon energy scale | AbsMuEScale2017 |
| Relative muon energy scale | RelMuEScale2017 |
| Absolute hadronic energy scale | Calibration<br>CalibShape |
| Relative hadronic energy scale | RelativeCalib |
| Detector response | Lightlevel<br>Cherenkov |
| Normalisation | Norm{FHC,RHC}2018 |
| Neutron uncertainty | NeutronSyst2018 |
| Neutrino flux | ppfx_hadp_beam_pc{00,01,02,03,04} |
| Cross sections and final-state interaction | MECEnuShape{Nu,AntiNu}<br>MECShape2018{Nu,Antinu}<br>MECInitStateNPFrac{Nu,AntiNu}<br>MaCCQE_reduced_2018<br>RPARESSyst2018<br>MECEnuShape{Nu,AntiNu}<br>MECShape2018{Nu,AntiNu}<br>MECInitStateNPFrac{Nu,AntiNu}<br>MaCCQE_reduced_2018<br>RPARESSyst2018<br>RPACCQEEnhSyst2018<br>COHCCScaleSyst2018<br>COHNCScaleSyst2018<br>MaCCRES<br>MaNCRES<br>MvCCRES<br>CCQEPauliSupViaKF<br>FrElas_N<br>FrCEx_N<br>FrAbs_N<br>FrInel_pi<br>FormZone<br>genie_small_pc{00,01,02,03,04} |

**Table 5.6:** Mapping between systematic uncertainty definitions. The individual systematic uncertainties displayed in Figure 5.25, shown in the right column, are grouped into nine systematic uncertainty sets, shown at the left, for the results presented Figures 5.26 and 5.27.

### 5.4.2 Matter effect and octant-hierarchy preference

The neutrino beam only result is consistent with $\sin^2\theta_{23} = 0.5$ whereas the antineutrino beam only fit disfavours maximal mixing at 1.5 $\sigma$. This is because there are more events in the maximal disappearance region in RHC than in FHC and so the RHC-only result prefers less disappearance. When combined, the neutrino and antineutrino beam data slightly disfavours 2 out of 4 octant-hierarchy combinations. Figure 5.28 shows the significance of the measurement of $\sin^2\theta_{23}$ for a $\nu_\mu + \bar{\nu}_\mu$ joint disappearance fit in the normal and inverted hierarchy. In the normal hierarchy, the result disfavours maximal mixing at 1.13 $\sigma$ and favours $\theta_{23}$ in the upper octant. The opposite occurs for the inverted mass hierarchy, where the lower octant is preferred. This octant-hierarchy preference when combining data from FHC+RHC occurs because of the different neutrino-antineutrino interactions with matter.

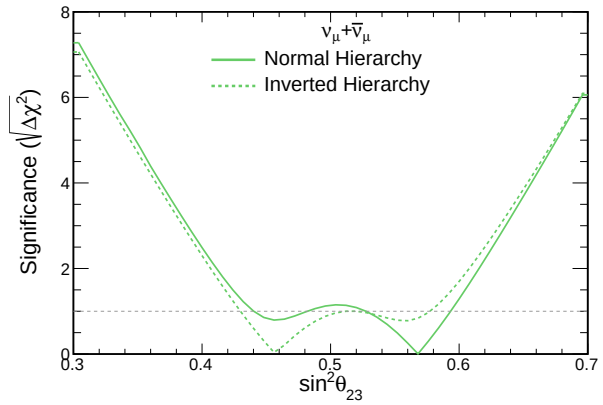


**Figure 5.28:** Significance on the measurement of $\sin^2\theta_{23}$ in the normal and inverted hierarchy scenarios, when performing a joint $\nu_\mu + \bar{\nu}_\mu$ disappearance analysis assuming CPT invariance.

There is no CP violation in a two neutrino flavour model. However, the existence of a third neutrino introduces the possibility of CP violation via the $\delta_{CP}$ phase. In vacuum, $\nu_\mu$ and $\bar{\nu}_\mu$ disappearance are the same, but the $\nu_e$ vs. $\bar{\nu}_e$ appearance, and $\nu_\tau$ vs. $\bar{\nu}_\tau$ appearance can differ depending on the values of $\delta_{CP}$ and if the neutrino mass ordering is normal or inverted. Figure 5.29 shows plots of the appearance probability of $\bar{\nu}_e$ vs. $\nu_e$ to exemplify the oscillation effects with different values of $\delta_{CP}$ in vacuum and in matter. In matter and normal hierarchy $\nu_\mu \rightarrow \nu_e$ is enhanced, which can occur because $\nu_\tau$ appearance is suppressed or because there is more $\nu_\mu$ disappearance. The opposite occurs for $\bar{\nu}_\mu \rightarrow \bar{\nu}_e$, which is suppressed. In inverted hierarchy, $\nu_\mu \rightarrow \nu_e$ is suppressed and $\bar{\nu}_\mu \rightarrow \bar{\nu}_e$ is enhanced. The disappearance of $\nu_\mu$ and $\bar{\nu}_\mu$ differs in matter when it does not in vacuum.

Another interesting aspect of the way matter affects the disappearance probabilities of $\nu_\mu$ and $\bar{\nu}_\mu$ relates to the point of maximal disappearance. Maximal disappearance in matter occurs above or below the maximum disappearance point in vacuum ($\sin^2\theta_{23} = 0.511$). The value at which maximal disappearance occurs changes with baseline and matter density therefore it is not

necessarily the same for all the experiments. For NOvA, the $\sin^2\theta_{23}$ values at which the $\nu_\mu$ and $\bar{\nu}_\mu$ disappearance is maximal are:

- Normal hierarchy: 0.514 for $\nu_\mu$ and 0.507 for $\bar{\nu}_\mu$
- Inverted hierarchy: 0.507 for $\nu_\mu$ and 0.514 for $\bar{\nu}_\mu$

Figure 5.30 shows the $\nu_\mu \to \nu_\mu$ and $\bar{\nu}_\mu \to \bar{\nu}_\mu$ oscillation probabilities as a function of $\sin^2\theta_{23}$ for the normal and inverted hierarchy case, and for different values of $\delta_{CP}$. The $\nu_\mu \to \nu_\mu$ and $\bar{\nu}_\mu \to \bar{\nu}_\mu$ probability functions lie either side of the maximal disappearance point in vacuum. The point where the $\nu_\mu$ and $\bar{\nu}_\mu$ survival is lowest can be seen in these plots. The flip in the maximum disappearance point between the $\nu_\mu$ and $\bar{\nu}_\mu$ can be seen by comparing the left and right plots. The value of $\delta_{CP}$ slightly changes the amount of disappearance but it has a small effect on the value of $\sin^2\theta_{23}$ at which it is maximal.

Figure 5.31 shows the $\nu_\mu$ and $\bar{\nu}_\mu$ survival probability difference as a function of neutrino energy for specific values of $\sin^2\theta_{23}$ in the normal and inverted hierarchy. The oscillation probability difference is stronger at higher energies as $\theta_{23}$ goes away from maximal mixing and it is more pronounced with increased earth crust density. Consider the scenario where a 97% and 96% $\nu_\mu$ and $\bar{\nu}_\mu$ disappearance is observed, respectively. In this case, $P(\nu_\mu \to \nu_\mu) = 0.03$ and $P(\bar{\nu}_\mu \to \bar{\nu}_\mu) = 0.04$ thus the survival probability difference between $\nu_\mu$ and $\bar{\nu}_\mu$ would be negative. As suggested by the functions in Figure 5.31, the lower octant values for $\theta_{23}$, e.g. blue curve, would be preferred in the energy dip region (1-2 GeV) for the normal hierarchy. For the inverted hierarchy, the upper octant values, e.g. pink curve, would be preferred. This is the reason that NOvA's combined neutrino + antineutrino measurements prefer two out of the four octant-hierarchy combinations.

Neutrino and antineutrino interactions in matter could fake CPT violation, but this effect is small at NOvA's baseline, energies and earth crust density, and is included in NOvA's simulation. In the next chapters, a measurement of the oscillation parameters is performed as a test of CPT conservation, using just the information from the neutrinos and just the information from antineutrinos.

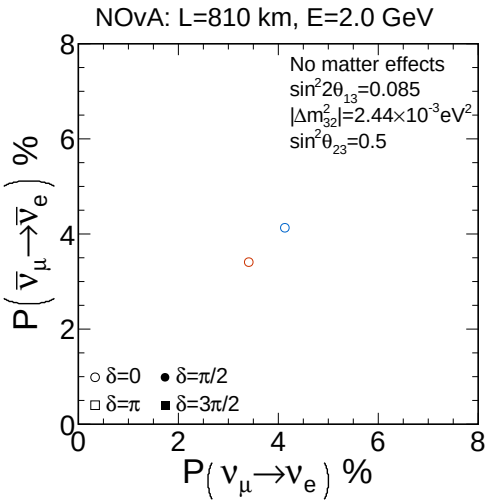


**(a)** Oscillations in vacuum, no CP violation ($\delta_{CP} = 0$).

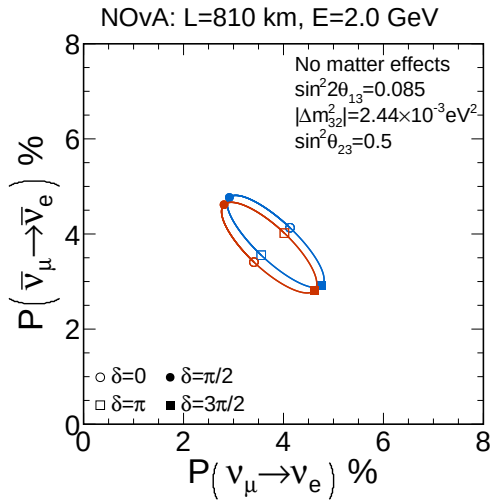


**(b)** Oscillations in vacuum, possible CP violation ($\delta_{CP} \neq 0, \pi$).

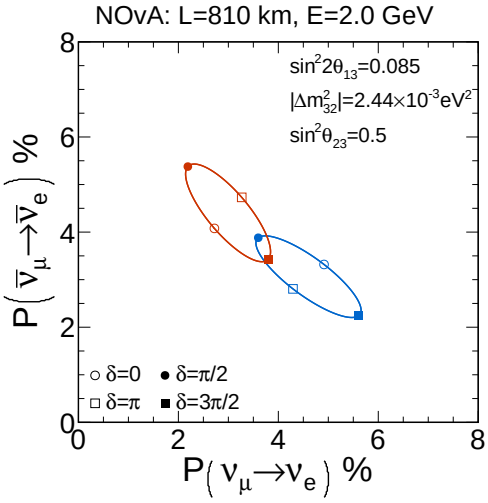


**(c)** Oscillations in matter, maximal mixing ($\theta_{23} = \pi/4$).

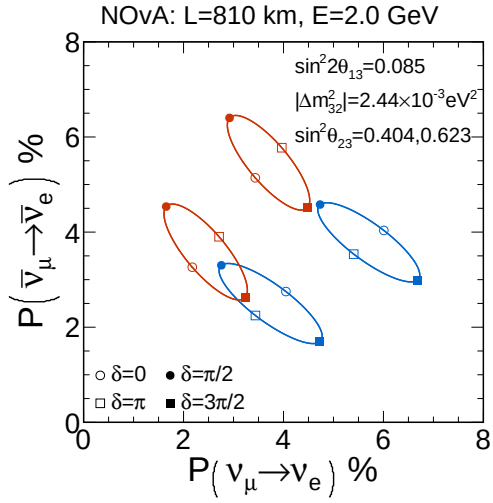


**(d)** Oscillations in matter, upper and lower octant ($\theta_{23} < \pi/4$ or $> \pi/4$).

**Figure 5.29:** Appearance probability of $\bar{\nu}_e$ vs. $\nu_e$ at NOvA's 810 km baseline, earth crust density of 2.8 gr/cm$^3$ and neutrino energy of 2.0 GeV. Ellipses are formed in the bi-probability space as the value of $\delta_{CP}$ changes and according to the normal (blue markers and lines) or the inverted (red markers and lines) hierarchy hypothesis. The top plots are shown for oscillations in vacuum, for no (left) and possible (right) CP violation. The bi-probability plots for oscillations in matter are shown at the bottom, for $\sin^2\theta_{23} = 0.5$ (left) and $\theta_{23}$ in the upper octant (right plot, top right ellipses) or in the lower octant (right plot, bottom left ellipses).

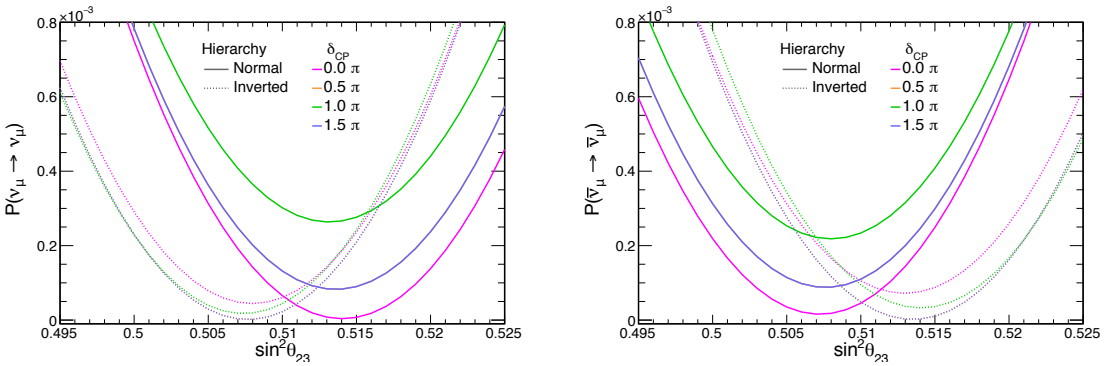


**Figure 5.30:** Muon neutrino (left) and antineutrino (right) disappearance probability as a function of $\sin^2\theta_{23}$. Oscillations are assumed for the normal (solid lines) and inverted (dashed lines) neutrino mass hierarchy at NOvA's 810 km baseline, earth crust density of 2.8 gr/cm$^3$ and neutrino energy of 1.6 GeV, for which four $\delta_{CP}$ values are considered. The survival probability for $\delta_{CP}$ equal to $1/2\pi$ and $3/2\pi$ are the same and are therefore overlapped.

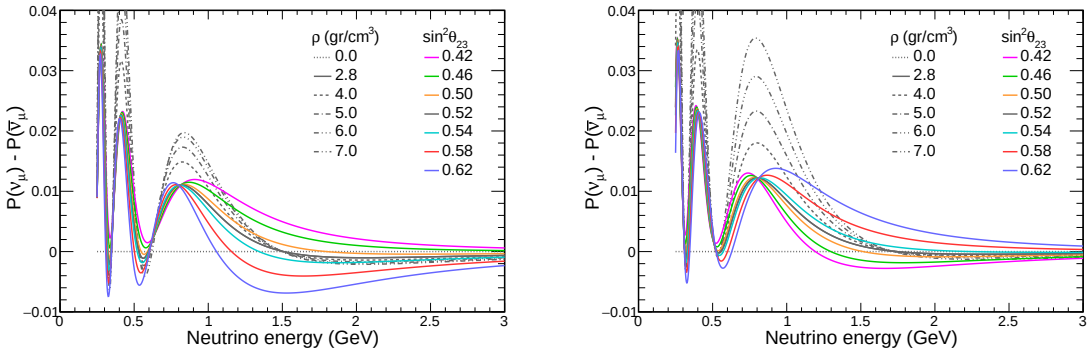


**Figure 5.31:** Disappearance probability difference between muon neutrinos and antineutrinos as a function of energy. Oscillations are assumed for the normal (left) and inverted (right) neutrino mass hierarchy at NOvA's baseline (810 km) with an average earth crust density $\rho = 2.8$gr/cm$^3$ for which a set of $\sin^2\theta_{23}$ values are used. A particular case, $\sin^2\theta_{23} = 0.52$, is considered for which $\rho$ is varied to illustrate the matter effect on the oscillations.

# Chapter 6

# The CPT violation analysis

NOvA's beam is a highly intense and pure source of $\nu_\mu$ and $\bar{\nu}_\mu$. The FHC and RHC configuration provide a 97% pure $\nu_\mu$ and 90% pure $\bar{\nu}_\mu$ beam, respectively. The *wrong sign* parts of the beam, which is the antineutrinos in the FHC beam and the neutrinos in the RHC beam, are the second largest beam component. The NOvA detectors have limited capability to separate positive and negatively charged particles on an event-by-event basis. The presence of the wrong sign component does not have a significant impact in the standard disappearance analysis, as both $\nu_\mu$ and $\bar{\nu}_\mu$ oscillate in the same way except for small differences in matter. However, if $\nu$ and $\bar{\nu}$ oscillations do not occur with the same parameter values, the beam contamination reduces the sensitivity of the oscillation parameter extraction from the analysis presented next.

A $\nu_\mu$ and $\bar{\nu}_\mu$ disappearance analysis is developed in this chapter to extract the oscillation parameters using just the information from neutrinos and also just the information from antineutrinos. The analysis uses the FHC and RHC samples in combination. A difference between the preferred parameter values for $\nu$ and $\bar{\nu}$ could be the indication of CPT not being conserved or something else, such as a non-standard interaction with matter. For simplicity, this analysis will be referred to as *CPT violation* analysis and will be abbreviated as *CPTv*. The parameters measured using just the information from antineutrinos are referred to as $\Delta\bar{m}^2_{32}$ and $\sin^2\bar{\theta}_{23}$. The analysis presented in the previous chapter will be referred to as *CPT conserved* or *CPTc*.

This chapter describes the CPTv analysis approach and builds on the results presented in Chapter 5 in that the same ND and FD samples are used and its best fit values are used for the sensitivities. Section § 6.1 shows a comparison between predicted FD energy spectra assuming the same or different neutrino and antineutrino oscillations. The fitting procedure for the CPTv analysis and NOvA's sensitivities are presented in § 6.2. The implementation of a wrong sign uncertainty and its impact on the CPTv analysis is assessed in § 6.3.

## 6.1 Predictions

This section presents the predictions of selected $\nu_\mu$ and $\bar{\nu}_\mu$ CC events at the FD for an exposure of $8.85 \times 10^{20}$ and $12.33 \times 10^{20}$ POT to the neutrino and antineutrino beams, respectively, which is the same exposure as for the CPTc analysis. Figures 6.1 and 6.2 show the reconstructed neutrino and antineutrino predicted energy spectra of $\nu_\mu$ and $\bar{\nu}_\mu$ CC events at the FD, for the combined and individual $E_{Had}/E_\nu$ quartiles. These spectra are extrapolated predictions as described in § 4.7 and for which the ND spectra presented in § 5.1 are used. The predictions shown by the solid lines assume the scenario where neutrino and antineutrino oscillations are governed by different parameter values. In this case, the $\nu$ and $\bar{\nu}$ are oscillated with the normal hierarchy best fit from the FHC-only and RHC-only CPTc analysis, respectively (see Table 5.5). The total oscillated prediction at the FD is shown in purple and the displayed 1 $\sigma$ error band corresponds to the sum in quadrature of the systematic uncertainties. The simulated wrong sign component, beam background and cosmic expectation are shown in green, gray and blue, respectively. The total FD prediction where both $\nu$ and $\bar{\nu}$ are oscillated with the normal hierarchy best fit from the combined FHC+RHC CPTc analysis is shown by the dashed purple line.

The FHC spectra for the CPTv scenario is below the CPTc prediction for events with less than 2.25 GeV of reconstructed neutrino or antineutrino energy. In the RHC case, the CPTv spectra is above the CPTc prediction at energies below 2 GeV and is slightly above for higher energies. The total event difference in the FHC configuration is of about 3 events less for the CPTv prediction than for the CPTc. The difference in RHC is about 1.5 more events in the CPTv than in CPTc case. Most of these differences can be attributed to events around the energy dip region. Tables 6.1 and 6.2 show the number of predicted events at the FD from the FHC and RHC beam, respectively, and for the CPTv and CPTc scenarios described above. The expectations are displayed for different $\nu$ and $\bar{\nu}$ oscillation channels as well as for the simulated and estimated backgrounds and for the prediction in absence of oscillations.

## 6.2 Fit to oscillation model

A $\nu_\mu$ and $\bar{\nu}_\mu$ disappearance analysis is performed to extract the values of the neutrino and antineutrino oscillation parameters, following the method described in § 4.9. For the *CPTv* analysis presented in this section and in the next chapter, the $\nu$ and $\bar{\nu}$ parameters are allowed to vary independently. This means that the value of $\sin^2\theta_{23}$ can differ from $\sin^2\bar{\theta}_{23}$. Similarly, the mass squared differences are allowed to vary such that $\Delta m^2_{23} \neq \Delta\bar{m}^2_{23}$ is possible.

The data collected from the beam in FHC and RHC mode is simultaneously used for the measurements. The CPTv analysis uses an average of the most recent global results from reactor and solar neutrino experiments available at the time of the analysis, and implements them as

| Channel | CPTc | | | | | CPTv | | | | |
|---|---|---|---|---|---|---|---|---|---|---|
| | All Q | Q1 | Q2 | Q3 | Q4 | All Q | Q1 | Q2 | Q3 | Q4 |
| $\nu_\mu \to \nu_\mu$ | 110.37 | 27.27 | 26.16 | 26.80 | 30.14 | 107.40 | 26.50 | 25.40 | 26.04 | 29.47 |
| $\bar{\nu}_\mu \to \bar{\nu}_\mu$ | 7.26 | 3.16 | 1.76 | 1.50 | 0.83 | 7.31 | 3.20 | 1.77 | 1.50 | 0.83 |
| $\nu_\mu \to \nu_e$ | 0.09 | 0.00 | 0.00 | 0.01 | 0.08 | 0.08 | 0.00 | 0.00 | 0.01 | 0.07 |
| $\bar{\nu}_\mu \to \bar{\nu}_e$ | 0.00 | 0.00 | 0.00 | 0.00 | 0.00 | 0.00 | 0.00 | 0.00 | 0.00 | 0.00 |
| $\nu_\mu \to \nu_\tau$ | 0.35 | 0.07 | 0.09 | 0.10 | 0.09 | 0.35 | 0.07 | 0.09 | 0.10 | 0.09 |
| $\bar{\nu}_\mu \to \bar{\nu}_\tau$ | 0.05 | 0.01 | 0.01 | 0.01 | 0.01 | 0.05 | 0.01 | 0.01 | 0.01 | 0.01 |
| $\nu_e \to \nu_\mu$ | 0.27 | 0.06 | 0.06 | 0.07 | 0.07 | 0.24 | 0.06 | 0.06 | 0.06 | 0.06 |
| $\bar{\nu}_e \to \bar{\nu}_\mu$ | 0.01 | 0.01 | 0.00 | 0.00 | 0.00 | 0.01 | 0.01 | 0.00 | 0.00 | 0.00 |
| $\nu_e \to \nu_e$ | 0.02 | 0.00 | 0.00 | 0.00 | 0.02 | 0.02 | 0.00 | 0.00 | 0.00 | 0.02 |
| $\bar{\nu}_e \to \bar{\nu}_e$ | 0.00 | 0.00 | 0.00 | 0.00 | 0.00 | 0.00 | 0.00 | 0.00 | 0.00 | 0.00 |
| $\nu_e \to \nu_\tau$ | 0.00 | 0.00 | 0.00 | 0.00 | 0.00 | 0.00 | 0.00 | 0.00 | 0.00 | 0.00 |
| $\bar{\nu}_e \to \bar{\nu}_\tau$ | 0.00 | 0.00 | 0.00 | 0.00 | 0.00 | 0.00 | 0.00 | 0.00 | 0.00 | 0.00 |
| $\nu_\mu + \bar{\nu}_\mu$ signal | 117.90 | 30.50 | 27.99 | 28.37 | 31.04 | 114.96 | 29.76 | 27.23 | 27.61 | 30.37 |
| NC | 1.19 | 0.05 | 0.10 | 0.22 | 0.81 | 1.19 | 0.05 | 0.10 | 0.22 | 0.81 |
| Other beam bkg | 0.51 | 0.08 | 0.10 | 0.13 | 0.20 | 0.50 | 0.08 | 0.10 | 0.12 | 0.20 |
| Cosmics | 2.07 | 0.61 | 0.20 | 0.17 | 1.09 | 2.07 | 0.61 | 0.20 | 0.17 | 1.09 |
| Tot. Osc. Pred. | 121.68 | 31.25 | 28.40 | 28.89 | 33.15 | 118.73 | 30.50 | 27.63 | 28.13 | 32.47 |
| Unosc. Pred. | 730.23 | 186.55 | 179.74 | 178.43 | 185.52 | 730.23 | 186.55 | 179.74 | 178.43 | 185.52 |

**Table 6.1:** Expected number of events at the FD nominal prediction, with extrapolation, with $8.85\times10^{20}$ POT for the production of the **neutrino beam**. These numbers assume $\sin^2\theta_{23} = 0.51$ and $\sin^2\bar{\theta}_{23} = 0.60$, and $\Delta m^2_{32} = 2.45$ and $\Delta\bar{m}^2_{32} = 2.53$ for the CPTv scenario, and $\sin^2\theta_{23} = 0.57$ and $\Delta m^2_{32} = 2.48$ in the CPT conservation case. The numbers in this table do not account for the systematic pulls in the fit.

nuisance parameters in the fit. The values used are those reported in [31] by the NuFIT collaboration.

$$\Delta m^2_{21}, \Delta\bar{m}^2_{21} = 7.39^{+0.21}_{-0.20} \times 10^{-5}\ \text{eV}^2, \tag{6.1a}$$

$$\sin^2\theta_{12}, \sin^2\bar{\theta}_{12} = 0.310^{+0.013}_{-0.012}, \tag{6.1b}$$

$$\sin^2\theta_{13}, \sin^2\bar{\theta}_{13} = 2.20 \pm 0.07 \times 10^{-2}. \tag{6.1c}$$

The solar data was used to sets limits on $\Delta m^2_{21}$ and $\sin^2\theta_{12}$ and the KamLAND experiment constrains $\Delta\bar{m}^2_{21}$ and $\bar{\theta}_{12}$. The reactor experiments constrain the value of $\bar{\theta}_{13}$. The magnitude of the reactor mixing angle is such that it has a negligible effect on the disappearance and any difference between the neutrino and antineutrino values does not significantly change the results. NOvA's disappearance analysis can not constrain the solar nor the reactor parameters and these are assumed to be the same for neutrinos and antineutrinos. The neutrinos and antineutrinos are also assumed to have the same mass ordering.

| Channel | CPTc | | | | | CPTv | | | | |
|---|---|---|---|---|---|---|---|---|---|---|
| | All Q | Q1 | Q2 | Q3 | Q4 | All Q | Q1 | Q2 | Q3 | Q4 |
| $\nu_\mu \to \nu_\mu$ | 22.51 | 3.69 | 4.79 | 5.59 | 8.45 | 22.32 | 3.66 | 4.75 | 5.52 | 8.39 |
| $\bar{\nu}_\mu \to \bar{\nu}_\mu$ | 65.79 | 20.36 | 17.37 | 15.04 | 13.00 | 67.55 | 20.91 | 17.85 | 15.48 | 13.31 |
| $\nu_\mu \to \nu_e$ | 0.01 | 0.00 | 0.00 | 0.00 | 0.01 | 0.01 | 0.00 | 0.00 | 0.00 | 0.01 |
| $\bar{\nu}_\mu \to \bar{\nu}_e$ | 0.01 | 0.00 | 0.00 | 0.00 | 0.01 | 0.01 | 0.00 | 0.00 | 0.00 | 0.01 |
| $\nu_\mu \to \nu_\tau$ | 0.19 | 0.02 | 0.04 | 0.06 | 0.07 | 0.19 | 0.02 | 0.04 | 0.06 | 0.07 |
| $\bar{\nu}_\mu \to \bar{\nu}_\tau$ | 0.18 | 0.04 | 0.04 | 0.05 | 0.05 | 0.19 | 0.04 | 0.04 | 0.05 | 0.06 |
| $\nu_e \to \nu_\mu$ | 0.06 | 0.01 | 0.01 | 0.01 | 0.02 | 0.05 | 0.01 | 0.01 | 0.01 | 0.02 |
| $\bar{\nu}_e \to \bar{\nu}_\mu$ | 0.11 | 0.03 | 0.03 | 0.03 | 0.02 | 0.11 | 0.03 | 0.03 | 0.03 | 0.02 |
| $\nu_e \to \nu_e$ | 0.01 | 0.00 | 0.00 | 0.00 | 0.01 | 0.01 | 0.00 | 0.00 | 0.00 | 0.01 |
| $\bar{\nu}_e \to \bar{\nu}_e$ | 0.00 | 0.00 | 0.00 | 0.00 | 0.00 | 0.00 | 0.00 | 0.00 | 0.00 | 0.00 |
| $\nu_e \to \nu_\tau$ | 0.00 | 0.00 | 0.00 | 0.00 | 0.00 | 0.00 | 0.00 | 0.00 | 0.00 | 0.00 |
| $\bar{\nu}_e \to \bar{\nu}_\tau$ | 0.00 | 0.00 | 0.00 | 0.00 | 0.00 | 0.00 | 0.00 | 0.00 | 0.00 | 0.00 |
| $\nu_\mu + \bar{\nu}_\mu$ signal | 88.45 | 24.09 | 22.20 | 20.67 | 21.49 | 90.03 | 24.61 | 22.64 | 21.04 | 21.74 |
| NC | 0.69 | 0.02 | 0.04 | 0.10 | 0.53 | 0.69 | 0.02 | 0.04 | 0.10 | 0.53 |
| Other beam bkg | 0.41 | 0.06 | 0.08 | 0.11 | 0.15 | 0.41 | 0.06 | 0.08 | 0.11 | 0.15 |
| Cosmics | 0.80 | 0.03 | 0.14 | 0.11 | 0.51 | 0.80 | 0.03 | 0.14 | 0.11 | 0.51 |
| Tot. Osc. Pred. | 90.35 | 24.19 | 22.46 | 21.00 | 22.69 | 91.93 | 24.71 | 22.90 | 21.37 | 22.94 |
| Unosc. Pred. | 475.61 | 130.42 | 124.42 | 113.58 | 107.20 | 475.61 | 130.42 | 124.42 | 113.58 | 107.20 |

**Table 6.2:** Expected number of events at the FD nominal prediction, with extrapolation, with $12.33\times10^{20}$ POT for the production of the **antineutrino beam**. These numbers assume $\sin^2\theta_{23} = 0.51$ and $\sin^2\bar{\theta}_{23} = 0.60$, and $\Delta m^2_{32} = 2.45$ and $\Delta\bar{m}^2_{32} = 2.53$ for the CPTv scenario, and $\sin^2\theta_{23} = 0.57$ and $\Delta m^2_{32} = 2.48$ in the CPT conservation case. The numbers in this table do not account for the systematic pulls in the fit.

### 6.2.1 Sensitivity

Sensitivity contours are obtained to assess the potential of the experiment to constrain the space of parameters under a given hypothesis. The construction of the sensitivity contours presented in this section follow the procedure described in § 4.9 but instead of real data, a simulated FD oscillated prediction or *fake data* is used. The simulated spectrum is an Asimov prediction constructed with known values of the oscillation parameters. This prediction can have a non-integer number of events per bin, which are assigned the statistical errors expected from the assumed beam exposure.

The FHC-only and RHC-only CPTc best fits in normal hierarchy are used for the CPTv analysis sensitivities presented in this section. The values of $(\Delta m^2_{32}, \sin^2\theta_{23}) = (2.45\times10^{-3}\ \text{eV}^2, 0.51)$ and $(\Delta\bar{m}^2_{32}, \sin^2\bar{\theta}_{23}) = (2.53\times10^{-3}\ \text{eV}^2, 0.60)$ are used to oscillate $\nu$ and $\bar{\nu}$ respectively, and use the FHC+RHC exposure to extract the $\nu$ and $\bar{\nu}$ parameters. The CPTv 90% sensitivity contours are shown in Figure 6.3 and are presented with the CPTc sensitivity contours for comparison. The CPTc sensitivities use the FHC-only best fit or the RHC-only best fits to oscillate neutrinos or antineutrinos, respectively, and use the information from only one beam exposure. The difference

between the CPTv sensitivity to the measurement of the $\nu$ parameters and the CPTc FHC-only sensitivity is not significant. However, the CPTv sensitivity to the $\bar{\nu}$ parameters is reduced compared to the CPTc RHC-only sensitivity. This is because the wrong sign fraction in the RHC beam is larger than in FHC.

Figure 6.4 shows NOvA's sensitivities for the scenario where NOvA CPTc best fits are the truth values of the oscillation parameters. The 90% confidence regions are presented for the constraints in $\sin^2\theta_{23}$ vs. $\Delta m^2_{32}$ and $\sin^2\bar{\theta}_{23}$ vs. $\Delta\bar{m}^2_{32}$, when only statistical or statistical and systematic uncertainties are accounted for. The significance at which a particular value of the mixing angle or the mass splitting would be excluded is shown in units of $\sqrt{\Delta\chi^2}$. The systematic uncertainties have a bigger impact on the measurement of the mass squared difference than on the mixing angle. A larger systematic effect is seen on the $\Delta m^2_{23}$ constraint than on $\Delta\bar{m}^2_{23}$. However, the measuring precision for $\Delta\bar{m}^2_{23}$ is less than that for $\Delta m^2_{23}$, meaning that larger uncertainties are expected for the antineutrino parameter. The $\sin^2\theta_{23}$ and $\sin^2\bar{\theta}_{23}$ sensitivities are mostly only affected for $\theta_{23}$ values away from maximal mixing.

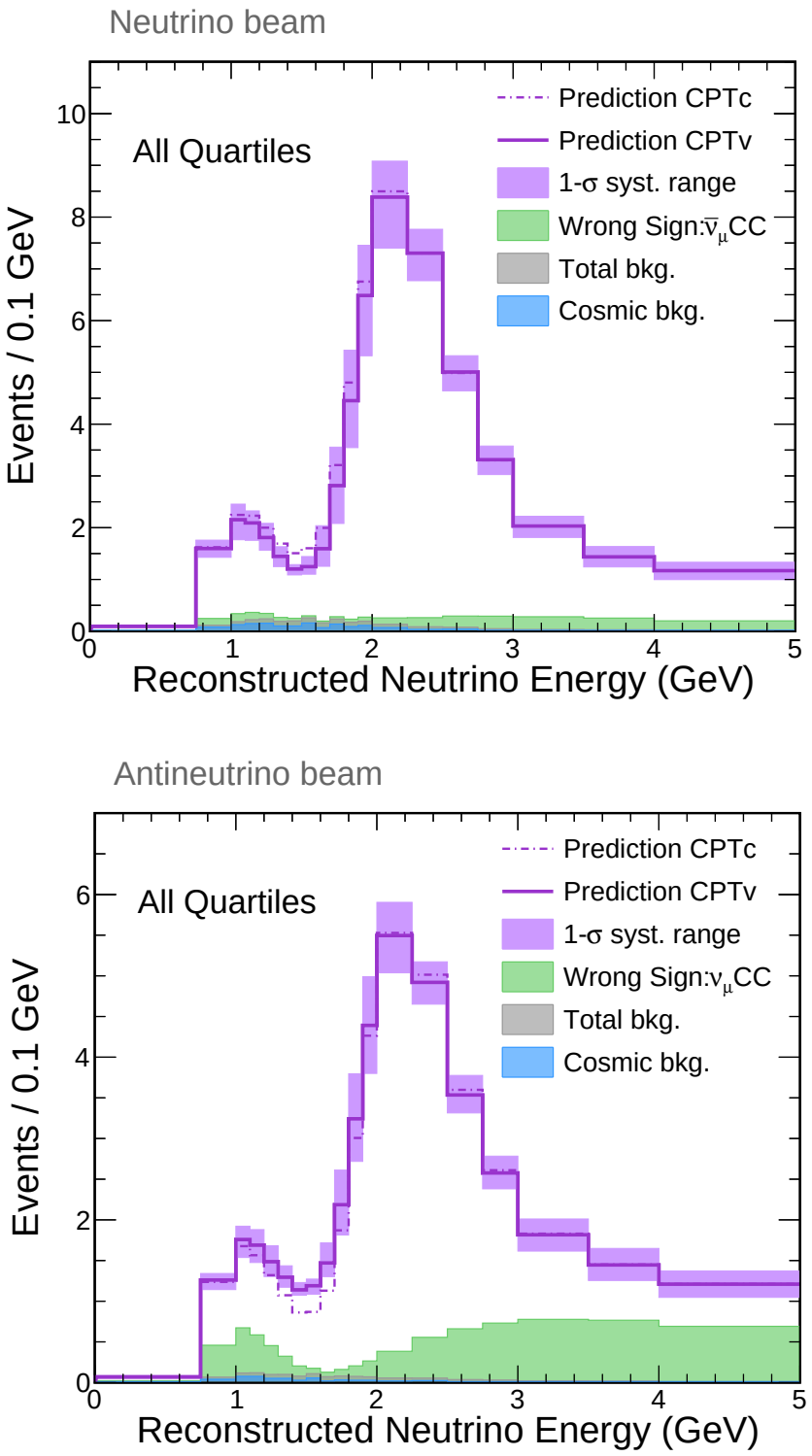


**Figure 6.1:** Reconstructed neutrino energy spectra of selected data and simulated events at the **FD** for the combination of $E_{Had}/E_\nu$ quartiles and ND constraints. The distributions from the neutrino (FHC) and antineutrino (RHC) beam configurations are shown at the top and bottom respectively. The FD prediction where $\nu$ and $\bar{\nu}$ have been oscillated with the FHC-only and RHC-only CPTc best fit values, respectively, is shown by the solid purple line and the shadowed region corresponds to the 1 $\sigma$ error band on the simulation. The simulated wrong sign component and beam background, as well as the cosmic prediction, are represented by the green, gray and blue regions respectively. The dashed purple line represents the prediction where $\nu$ and $\bar{\nu}$ have both been oscillated with the FHC+RHC CPTc best fit.

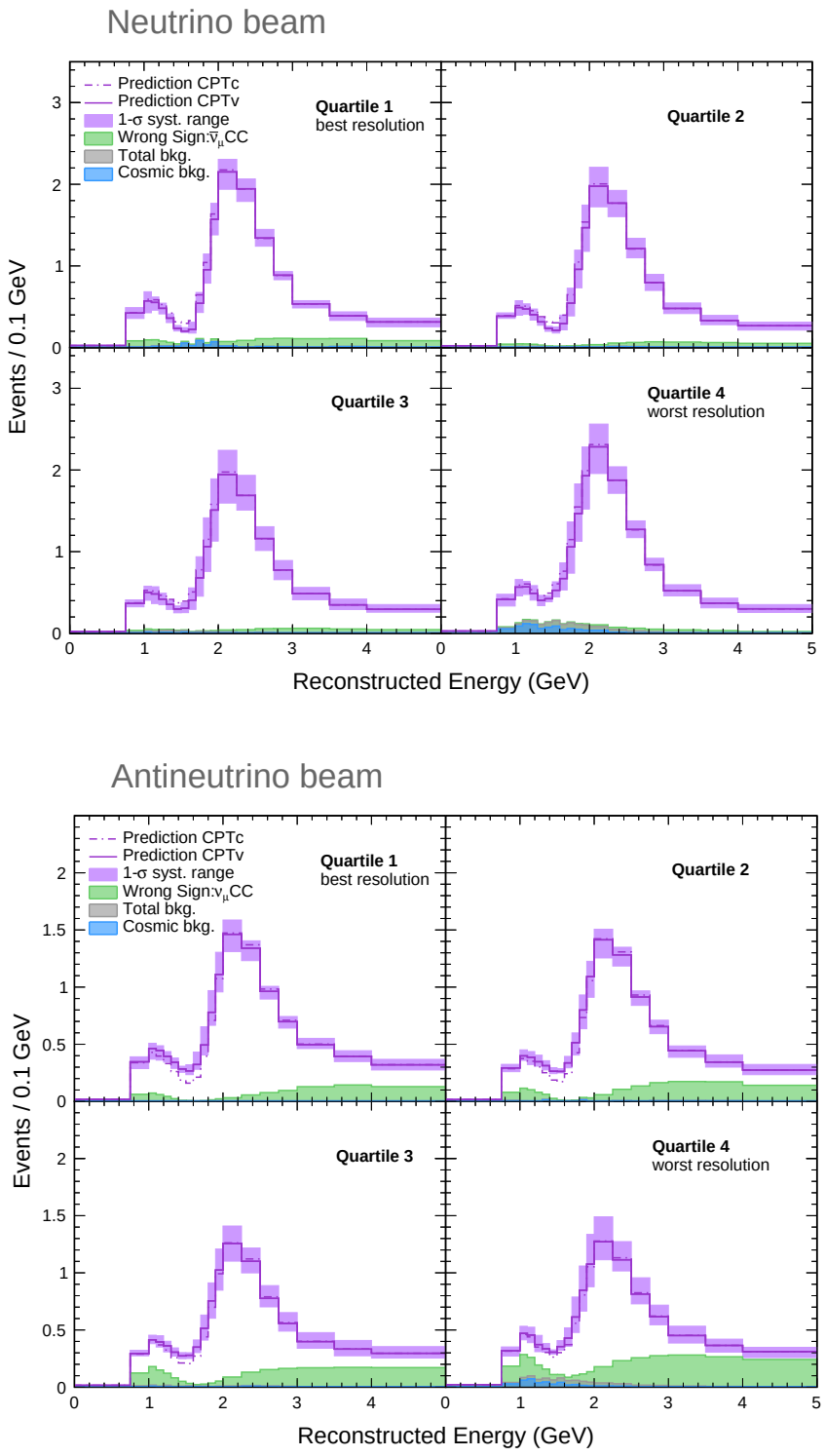


**Figure 6.2:** Reconstructed neutrino energy spectra of selected data and simulated events at the **FD** for each individual $E_{Had}/E_{\nu}$ quartile and ND constraints. The distributions from the neutrino (FHC) and antineutrino (RHC) beam configurations are shown at the top and bottom respectively. The FD prediction where $\nu$ and $\bar{\nu}$ have been oscillated with the FHC-only and RHC-only CPTc best fit values, respectively, is shown by the solid purple line and the shadowed region corresponds to the 1 $\sigma$ error band on the simulation. The simulated wrong sign component and beam background, as well as the cosmic prediction, are represented by the green, gray and blue regions respectively. The dashed purple line represents the prediction where $\nu$ and $\bar{\nu}$ have both been oscillated with the FHC+RHC CPTc best fit.

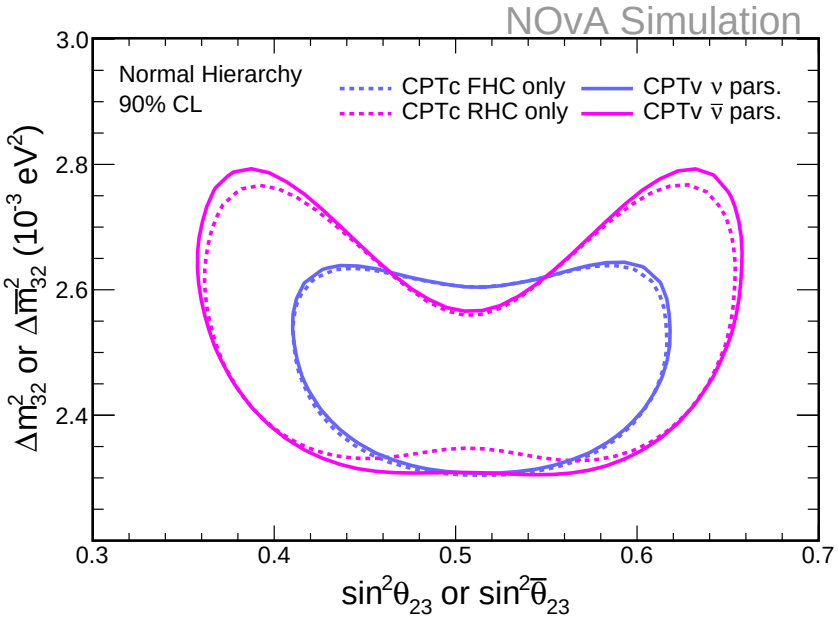


**Figure 6.3:** Projected sensitivities of the CPTv analysis (solid lines) to the measurement of the neutrino and antineutrino oscillation parameters compared to the CPTc analysis sensitivities (dashed lines). The assumed exposure is $8.85 \times 10^{20}$ POT for the beam in FHC configuration and $12.33 \times 10^{20}$ POT for RHC. The FHC-only and RHC-only CPTc normal hierarchy best fits are assumed to oscillate $\nu$ and $\bar{\nu}$ , respectively. The plot shows the 90% confidence regions of the mixing angle and mass squared difference for neutrinos (in solid blue) and antineutrinos (in solid pink).

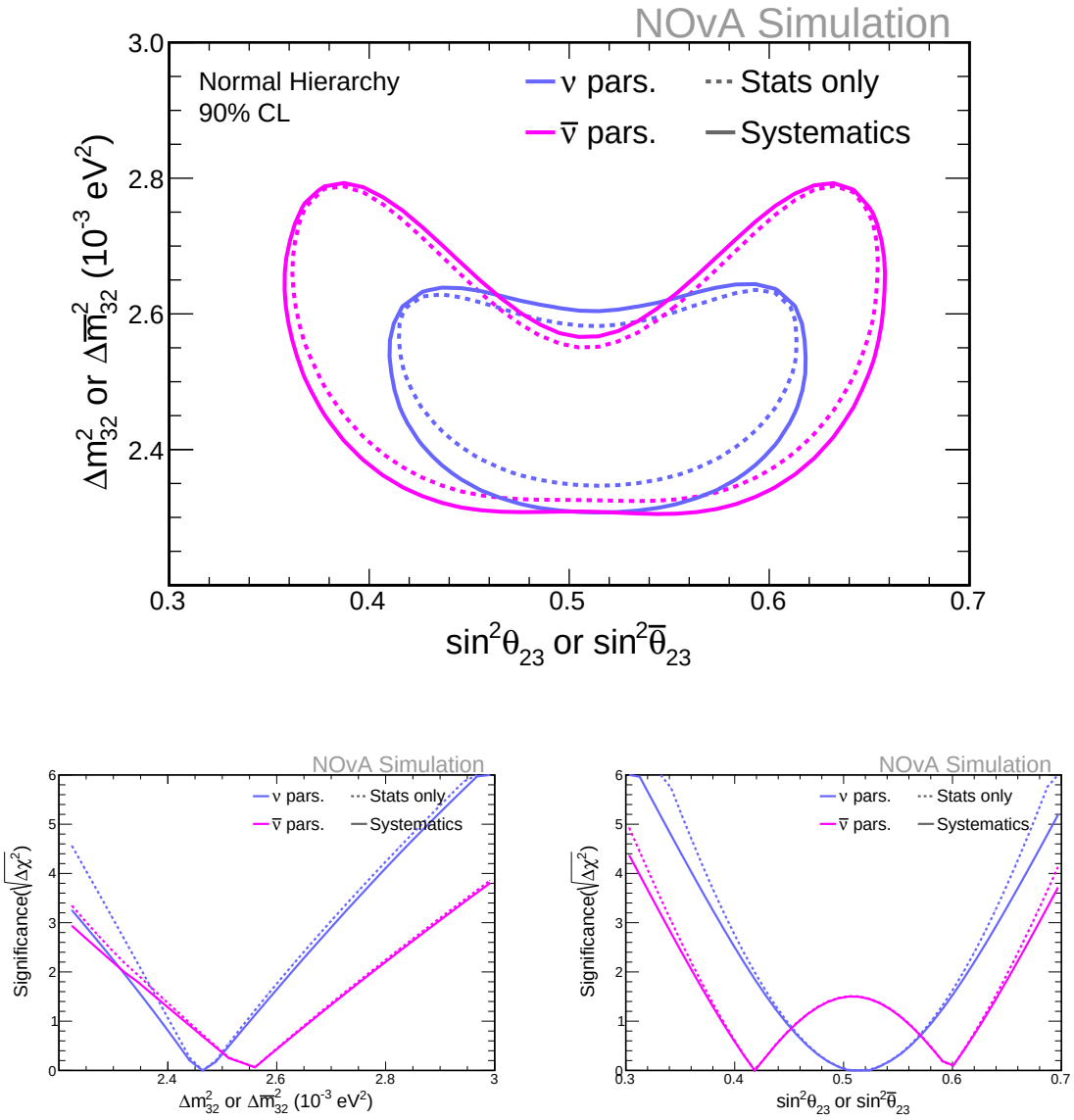


**Figure 6.4:** Projected sensitivities to the measurement of the neutrino and antineutrino oscillation parameters, $\sin^2\theta_{23}$ and $\Delta m^2_{32}$, and $\sin^2\bar{\theta}_{23}$ and $\Delta\bar{m}^2_{32}$ respectively, with an exposure to $8.85 \times 10^{20}$ in the FHC configuration and $12.33 \times 10^{20}$ POT in RHC. The FHC-only and RHC-only CPTc normal hierarchy best fits in table 5.5 are assumed to oscillate $\nu$ and $\bar{\nu}$ , respectively. The top plot shows the 90% confidence regions of the mixing angle and mass squared difference for neutrinos (in blue line) and antineutrinos (in pink line). The bottom plots show the significance on the measurement of each individual parameter.

## 6.3 Effect of the wrong sign on the analysis

The presence of the wrong sign beam component, the $\bar{\nu}_\mu$ in the beam of $\nu_\mu$ and vice versa, does not allow for a pure and unbiased extraction of the neutrino and antineutrino oscillation parameters when performing the FHC-only and RHC-only analyses presented in Chapter 5. The fact that the wrong sign component exists and that it can statistically fluctuate could significantly reduce the sensitivity of the analysis developed in this chapter, more so for the measurement of the antineutrino parameters. The wrong sign amount is estimated to account for less than 11%(3%) of selected antineutrino (neutrino) beam events. However, this number can statistically fluctuate and the exact amount of beam wrong sign is not precisely known on average.

A 100% scaling of the beam wrong sign component is chosen as an extreme scenario to illustrate the impact that a large uncertainty in the wrong sign could have on the CPTv analysis. The 100% uncertainty on the wrong sign is defined as the 1 $\sigma$ uncertainty in this component and is implemented by weighting $\bar{\nu}$ and $\nu$ events in the FHC and RHC beam respectively, and at both detectors. This means that the number of antineutrinos (neutrinos) in the beam of mostly neutrinos (antineutrinos) will be doubled or will be completely removed. This section presents the results of such implementation to the CPTv analysis.

Figures 6.5 and 6.6 show the reconstructed neutrino and antineutrino energy spectra of simulated selected $\nu_\mu$ and $\bar{\nu}_\mu$ CC events at the ND for the combined and individual $E_{Had}/E_\nu$ quartiles. The data is represented by black dots with the statistical errors associated to the event count. The base total simulation is shown by the purple solid lines and the simulated wrong sign is shown in solid green lines. The right sign component and other beam backgrounds are shown in solid blue and gray lines respectively. The 100% increase or decrease in the wrong sign component due to the implemented $\pm 1$ $\sigma$ shifts is shown by the dashed and dotted distributions, respectively. The shaded region corresponds to the 1 $\sigma$ error band from this tested systematic. The consequent change on the total simulation is also shown as a shaded region.

A 100% uncertainty in the estimation of the wrong sign does not fully cover the small discrepancies between data and simulation at 1 $\sigma$ in the individual quartiles. It is likely that the discrepancies between data and simulation are somewhere else in the interaction model described in § 3.4. In the FHC fourth quartile, the upper 1 $\sigma$ bound does not cover the discrepancy with data for events with reconstructed energy between 1.2 GeV and 2.0 GeV. In the first RHC quartile, data events with reconstructed energy between 1.5 GeV and 3.0 GeV remain outside of the 1 $\sigma$ bound. In the fourth RHC quartile, the 1 $\sigma$ bound remains above the data for events with reconstructed energy between 1.8 GeV and 2.2 GeV. However, all the other quartiles, as well as the combination of the four in FHC and RHC are in good agreement with the data.

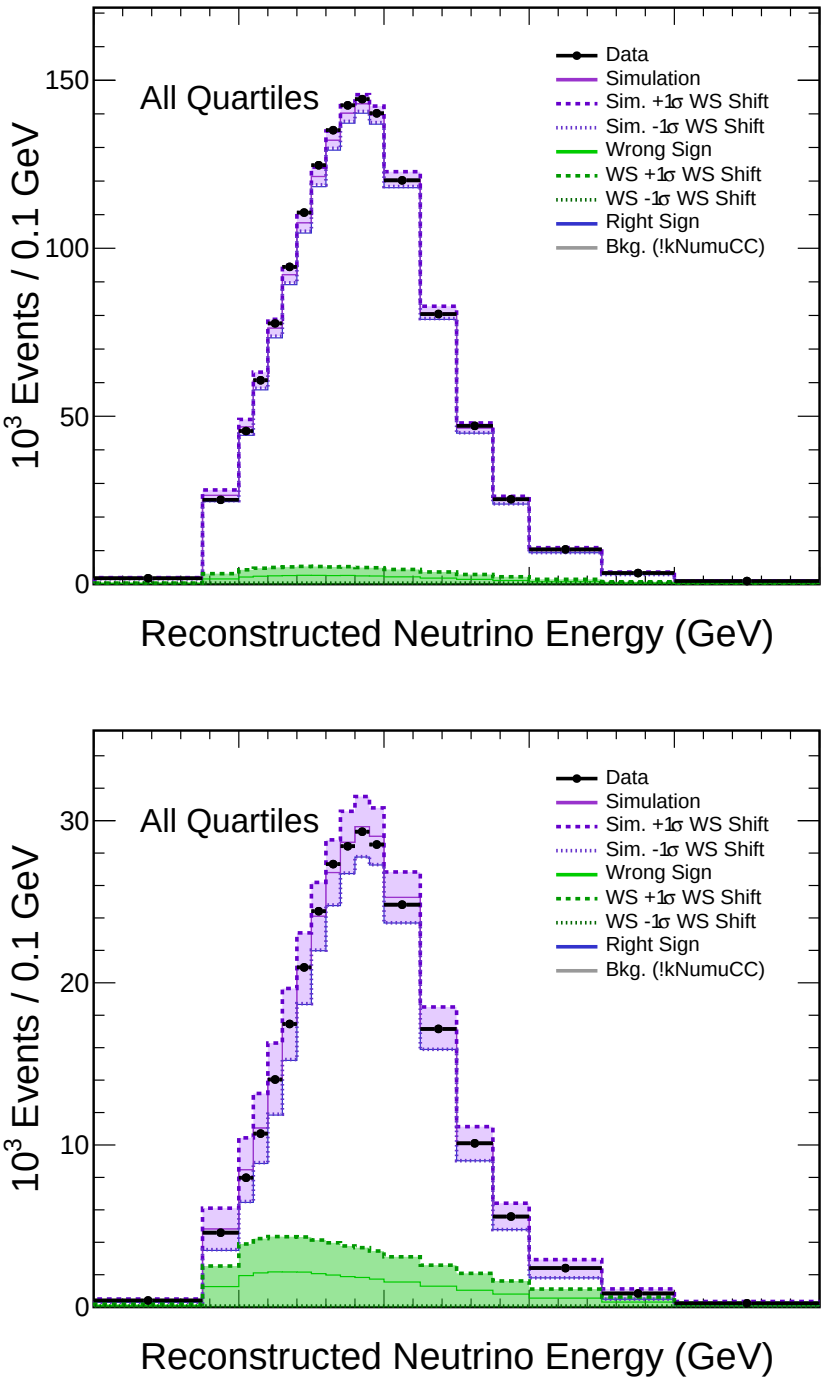


**Figure 6.5:** ND reconstructed energy spectra from selected $\nu_\mu$ CC events in the FHC(top) and RHC(bottom) beam modes. The events passing this selection for data and simulation are shown in black points and by lines, respectively. The total base simulation is shown by the solid purple line. The right sign, wrong sign and other beam backgrounds are represented by the blue, green and gray lines, respectively. The shadowed regions around the prediction are the 1 $\sigma$ wrong sign only error band, where the dashed and dotted lines represent the upper and lower limits, respectively.

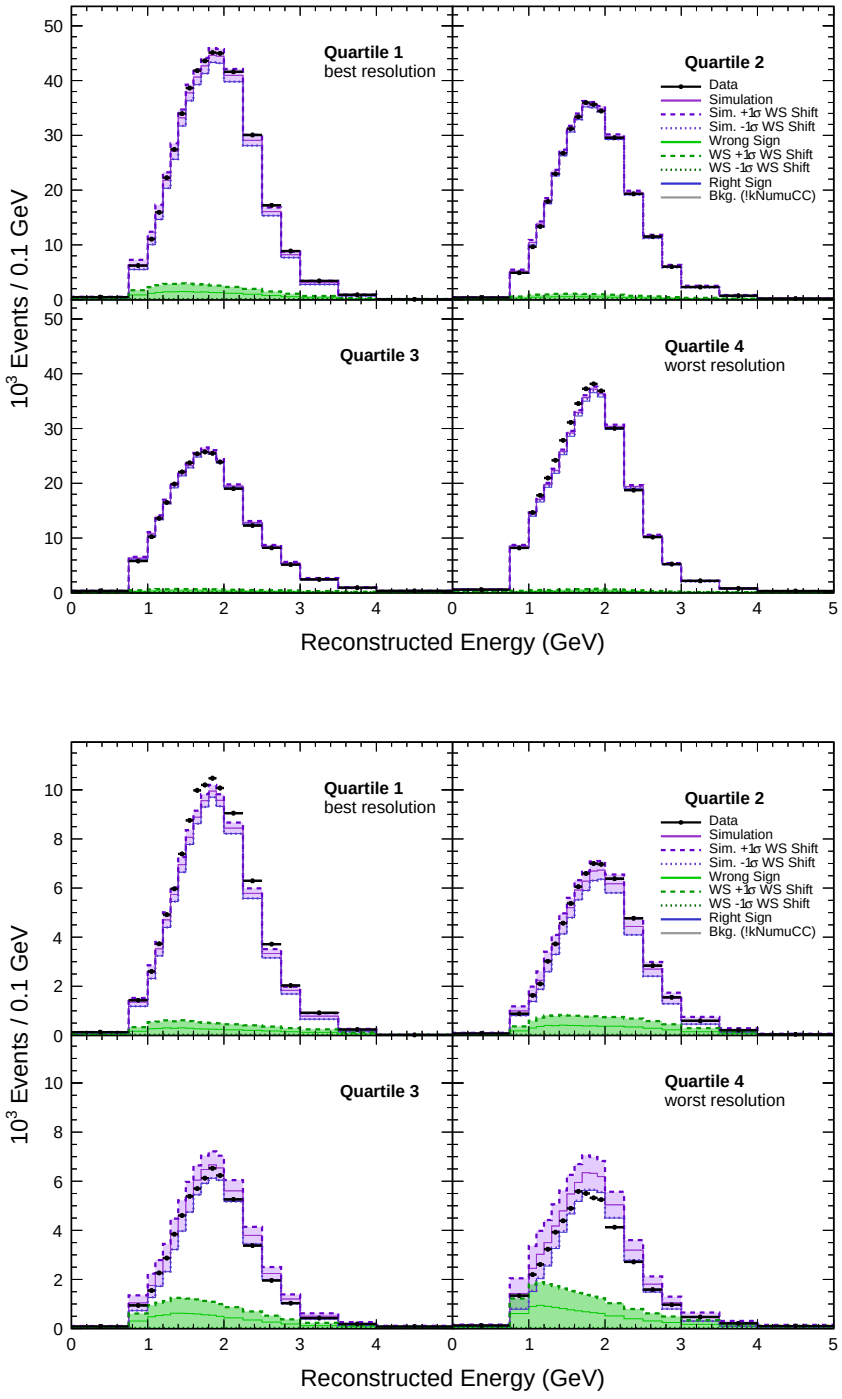


**Figure 6.6:** ND reconstructed energy spectra from selected $\nu_\mu$ CC events in the FHC(top) and RHC(bottom) beam modes, for each individual $E_{Had}/E_\nu$ quartile. The events passing this selection for data and simulation are shown in black points and by lines, respectively. The total base simulation is shown by the solid purple line. The right sign, wrong sign and other beam backgrounds are represented by the blue, green and gray lines, respectively. The shadowed regions around the prediction are the 1 $\sigma$ wrong sign only error band, where the dashed and dotted lines represent the upper and lower limits, respectively.

### 6.3.1 Effect on the FD predictions

This subsection explores the predicted FD reconstructed energy spectra and their uncertainty bounds given the 100% wrong sign scale previously discussed. These bounds are compared to different oscillation hypotheses. The aim of this is to determine if a 1 $\sigma$ pull of the 100% scale uncertainty would allow those scenarios during the fit. Special attention is paid to the reconstructed neutrino and antineutrino energy dip as this region provides most of the sensitivity to the oscillation parameters measurement. The 100% wrong sign scale is compared to the calibration systematic, which has one of the largest effects on the oscillation parameter measurements.

Three different sets of parameter values were chosen for the above purpose, with two of them representing a large $\nu - \bar{\nu}$ oscillation difference. Combinations of $\sin^2\theta_{23}$, $\sin^2\bar{\theta}_{23}$, $\Delta\bar{m}^2_{32}$ and $\Delta m^2_{32}$ use the CPTc normal hierarchy best fits (summarised in Table 5.5) to oscillate the $\nu$ and $\bar{\nu}$ either with the same or with different values as follows:

- $\nu$ and $\bar{\nu}$ oscillate with the FHC+RHC best fit,
- $\nu$ oscillate with the FHC only best fit, $\bar{\nu}$ oscillate with the RHC only best fit,
- $\nu$ oscillate with the RHC only best fit, $\bar{\nu}$ oscillate with the FHC only best fit.

Recall that the FHC-only best fit prefers maximal mixing, RHC-only prefers a non-maximal fit and the joint FHC+RHC fit prefers a point in-between. Therefore, this choice of values should represent a middle disappearance case, and two extreme opposites around it, which are the first and last scenarios from the list, respectively.

Figures 6.7 and 6.8 show the simulated reconstructed energy spectra at the FD, of selected $\nu_\mu$ and $\bar{\nu}_\mu$ CC events from the FHC and RHC beam modes, with ND constraints and assuming the above oscillation scenarios. The 1 $\sigma$ systematic range around the total simulation corresponds to the 1 $\sigma$ uncertainty from the calibration systematic. Figures 6.9 and 6.10 contain the analogous plots with the 1 $\sigma$ uncertainty band from the wrong sign systematic. The $-1\sigma$ uncertainty bound on the wrong sign does not correspond to a full disappearance of this component as uncertainties are reduced due to the extrapolation technique for the computation of the FD predictions (see § 4.7). The predicted FD reconstructed energy spectra without constraints from the ND, *without extrapolation*, are found in appendix B.

The calibration systematic has a significant effect in the energy dip region in both FHC and RHC beam modes. The wrong sign scale systematic has the completely opposite effect for two reasons. The FHC wrong sign background is small all across the reconstructed energy range so the uncertainty band is barely perceived. The amount of RHC wrong sign relative to the right sign component is large at high energies and small in the energy dip so the uncertainty band is large everywhere except at the region of most disappearance. Additionally, the extrapolation procedure described in § 4.7 reduces the common detector systematic uncertainties. The dashed and dotted lines, for the cases where the $\nu$ and $\bar{\nu}$ parameter values differ widely, provide a sense of whether or

not the uncertainty pulls could allow the oscillation hypothesis represented by those lines. A 100% uncertainty in the wrong sign component is not significant enough to cover those extreme scenarios, whereas the calibration uncertainty is. This will be reflected in the sensitivity fits presented next.

### 6.3.2 Sensitivities with 100% wrong sign scale

Sensitivity fits were produced considering either only the calibration or wrong sign scale systematic with the procedure as described in § 6.2. This only-one systematic approach allows to isolate the individual effect of each systematic on the measurement of the neutrino and antineutrino parameters. The following results consider an exposure of $8.85\times10^{20}$ POT in FHC and $12.33\times10^{20}$ POT in RHC beam mode, and assume $\nu$ and $\bar{\nu}$ oscillations with the normal hierarchy FHC-only and RHC-only CPTc best fits, respectively.

Figures 6.11 and 6.12 show the 90% confidence regions for the determination of the $\nu$ and $\bar{\nu}$ oscillation parameters. The significance of the measurements is shown in the same figure. A comparison between the results obtained without systematic uncertainties, *statistics only*, and the application of the wrong sign scale systematic demonstrates that the later case has little to no effect on the $\nu$ and $\bar{\nu}$ parameter constraints. This is especially the case in the region around maximal mixing, where $\sin^2\theta_{23}$ and $\sin^2\bar{\theta}_{23}$ are in the (0.4, 0.6) range. The wrong sign uncertainty only becomes slightly relevant outside of that range. The measurement of $\Delta m^2_{32}$ and $\Delta\bar{m}^2_{32}$ is susceptible to the 100% wrong sign systematic at values above $2.8\times10^{-3}$ eV$^2$ but the effect is still negligible elsewhere. On the contrary, the calibration systematic impacts the constrains on the neutrino and antineutrino measurements across the space of parameters.

## 6.4 Summary

A $\nu_\mu$ and $\bar{\nu}_\mu$ disappearance analysis has been developed to extract neutrino and antineutrino oscillation parameters. The analysis uses data from NOvA's FHC and RHC beams but only the $\nu$ and only the $\bar{\nu}$ information is used to set constraints in the $\Delta m^2_{32}$ vs. $\sin^2\theta_{23}$ and $\Delta\bar{m}^2_{32}$ vs. $\sin^2\bar{\theta}_{23}$ space, respectively.

The amount of wrong sign contamination and its uncertainty could reduce the sensitivity of the analysis. As an extreme example, a 100% uncertainty in the wrong sign component was evaluated in the analysis. The results showed that a 100% scale on the wrong sign background, applied to the FHC and RHC beam modes, has a negligible effect on the sensitivity to the measurement of the mixing angle and mass squared splitting. The systematics that affect the wrong sign component are presented in the next chapter.

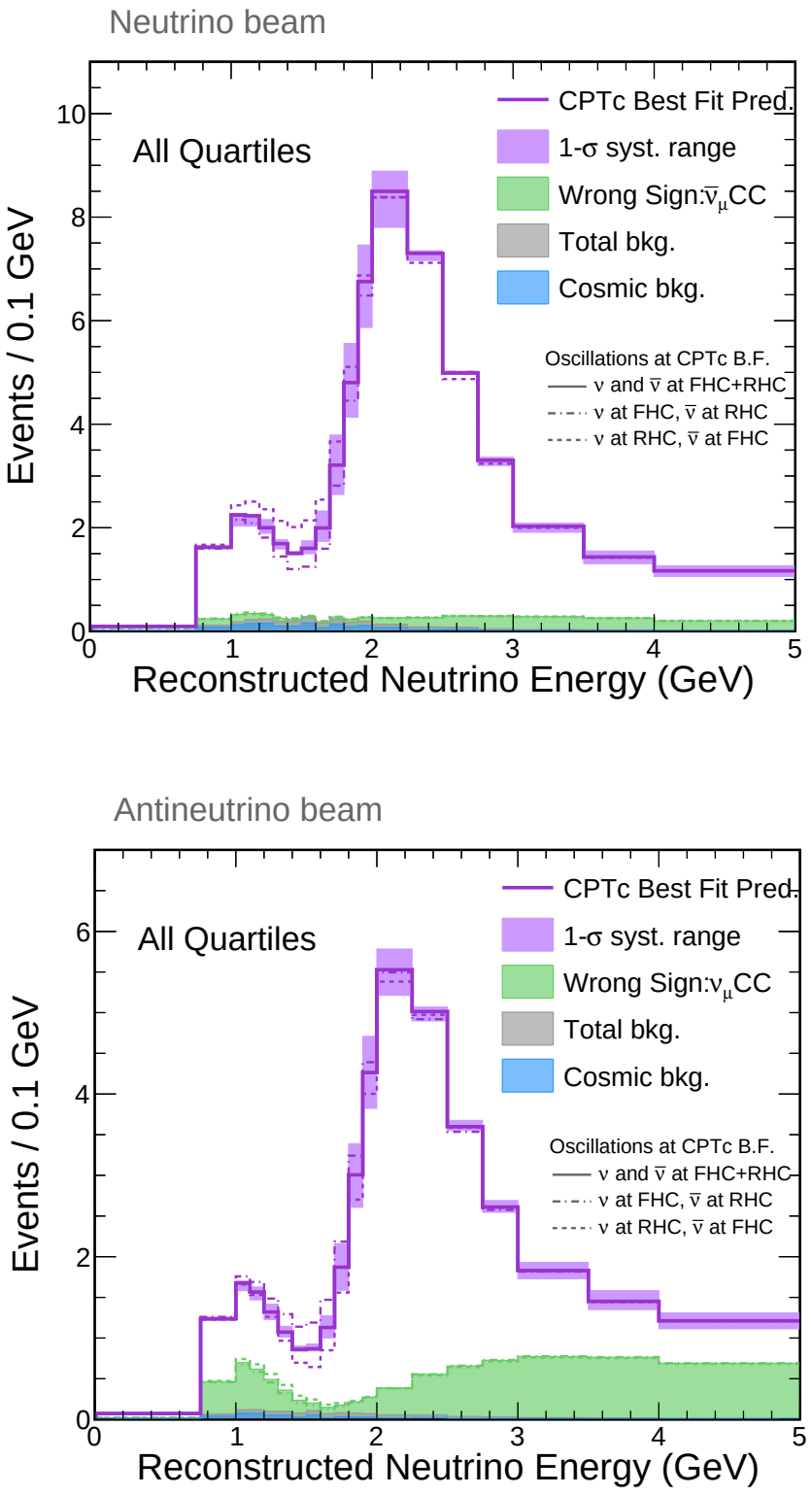


**Figure 6.7:** Simulated FD reconstructed energy spectra, with ND data constraints, from selected $\nu_\mu$ and $\bar{\nu}_\mu$ CC events in the FHC (top) and RHC (bottom) beam modes, for the combination of all energy resolution bins. The total number of predicted events passing this selection are represented in the purple histogram, where the shadowed regions is the 1 $\sigma$ **calibration only error band**. The solid distributions assume that both $\nu$ and $\bar{\nu}$ oscillate with the FHC+RHC CPTc best fit values. The dashed lines corresponds to $\nu$ oscillations with the FHC best fit and $\bar{\nu}$ oscillations with the RHC best fit, and the inverse case for the dotted lines.

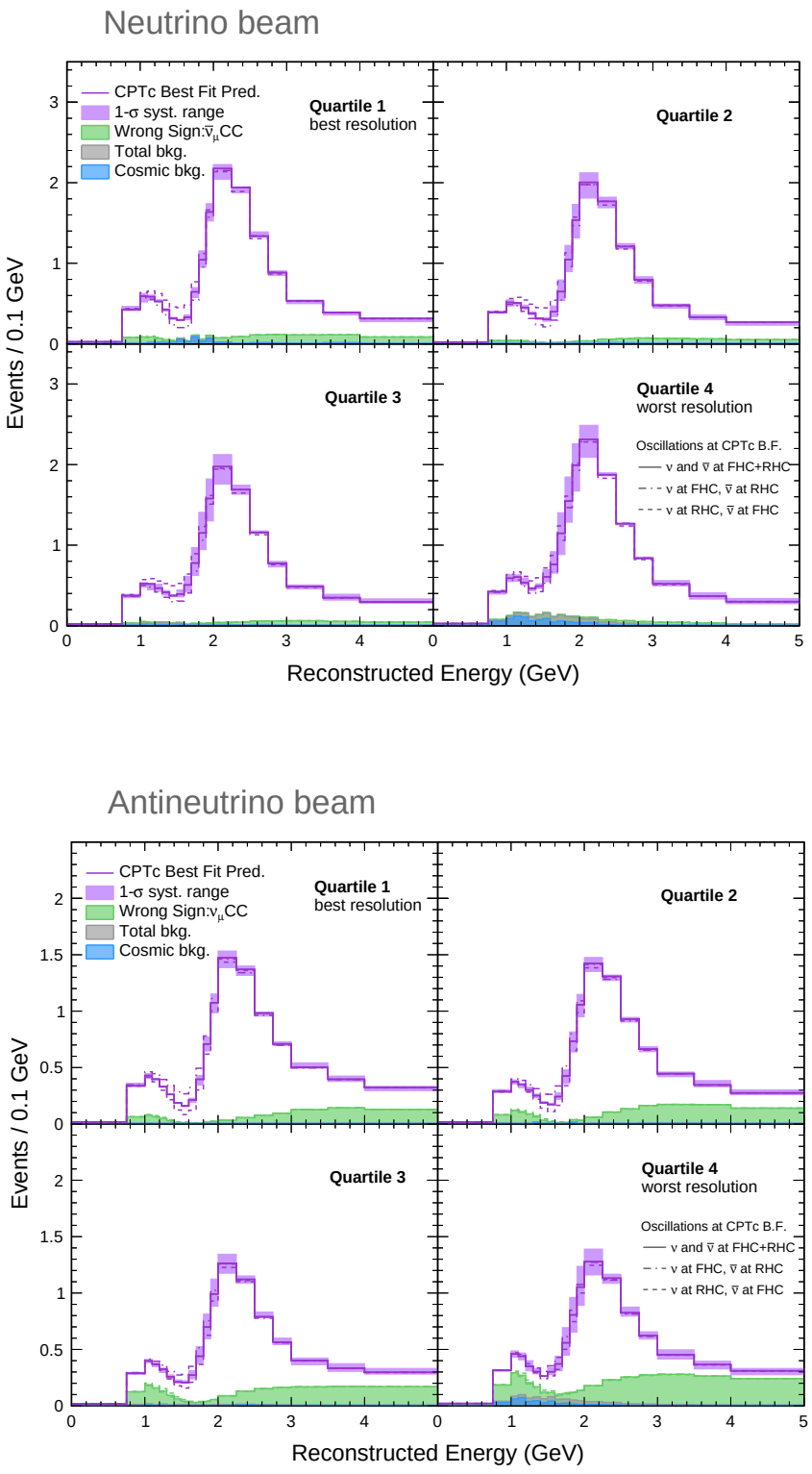


**Figure 6.8:** Simulated FD reconstructed energy spectra, with ND data constraints, from selected $\nu_\mu$ and $\bar{\nu}_\mu$ CC events in the FHC (top) and RHC (bottom) beam modes per energy resolution bins. The total number of predicted events passing this selection are represented in the purple histogram, where the shadowed regions is the 1 $\sigma$ **calibration only error band**. The solid distributions assume that both $\nu$ and $\bar{\nu}$ oscillate with the FHC+RHC CPTc best fit values. The dashed lines corresponds to $\nu$ oscillations with the FHC best fit and $\bar{\nu}$ oscillations with the RHC best fit, and the inverse case for the dotted lines.

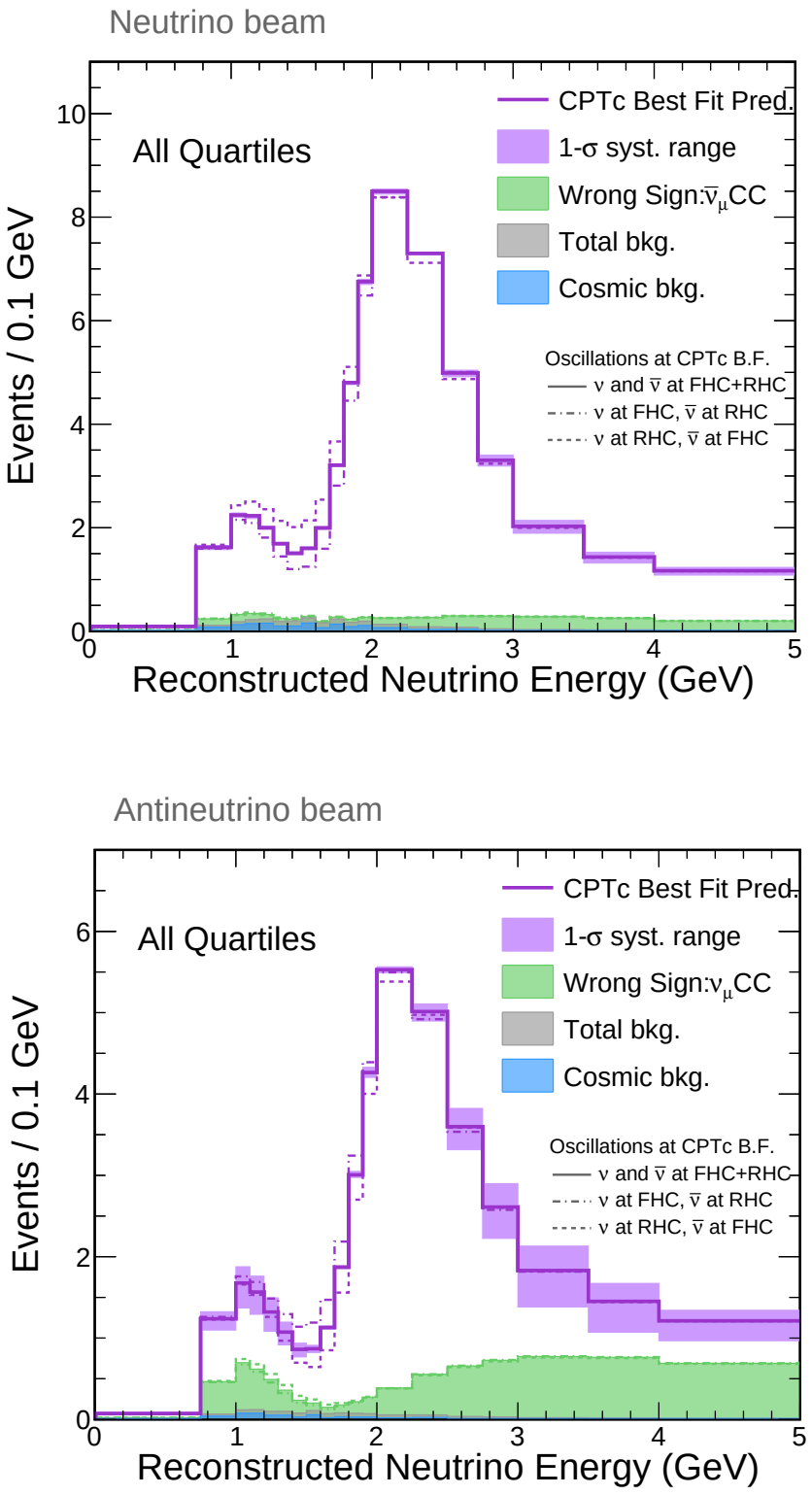


**Figure 6.9:** Simulated FD reconstructed energy spectra, with ND data constraints, from selected $\nu_\mu$ and $\bar{\nu}_\mu$ CC events in the FHC (top) and RHC (bottom) beam modes, for the combination of all energy resolution bins. The total number of predicted events passing this selection are represented in the purple histogram, where the shadowed regions is the 1 $\sigma$ **100% wrong sign scale only error band**. The solid distributions assume that both $\nu$ and $\bar{\nu}$ oscillate with the FHC+RHC CPTc best fit values. The dashed lines corresponds to $\nu$ oscillations with the FHC best fit and $\bar{\nu}$ oscillations with the RHC best fit, and the inverse case for the dotted lines.

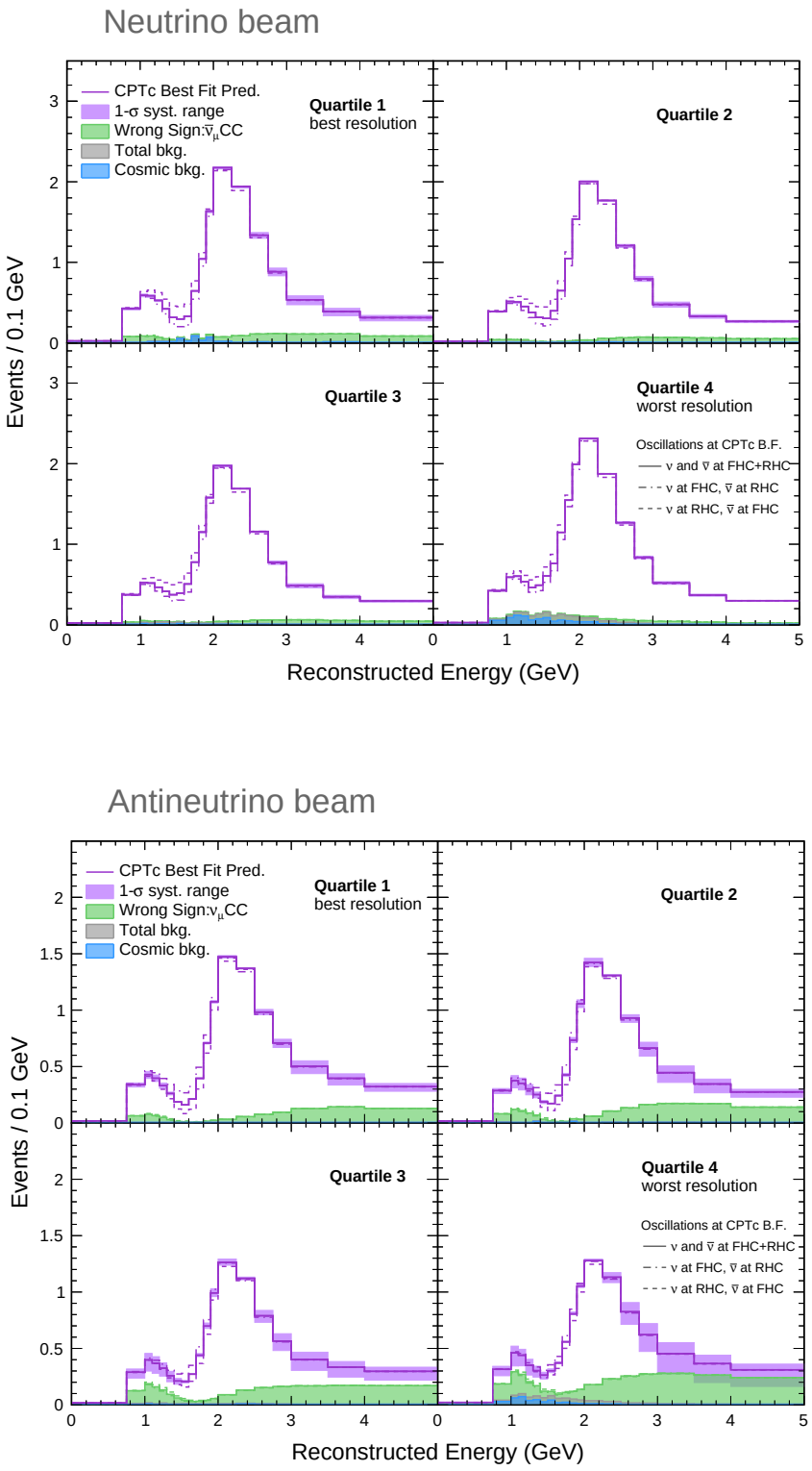


**Figure 6.10:** Simulated FD reconstructed energy spectra, with ND data constraints, from selected $\nu_\mu$ and $\bar{\nu}_\mu$ CC events in the FHC (top) and RHC (bottom) beam modes per energy resolution bins. The total number of predicted events passing this selection are represented in the purple histogram, where the shadowed regions is the 1 $\sigma$ **100% wrong sign scale only error band**. The solid distributions assume that both $\nu$ and $\bar{\nu}$ oscillate with the FHC+RHC CPTc best fit values. The dashed lines corresponds to $\nu$ oscillations with the FHC best fit and $\bar{\nu}$ oscillations with the RHC best fit, and the inverse case for the dotted lines.

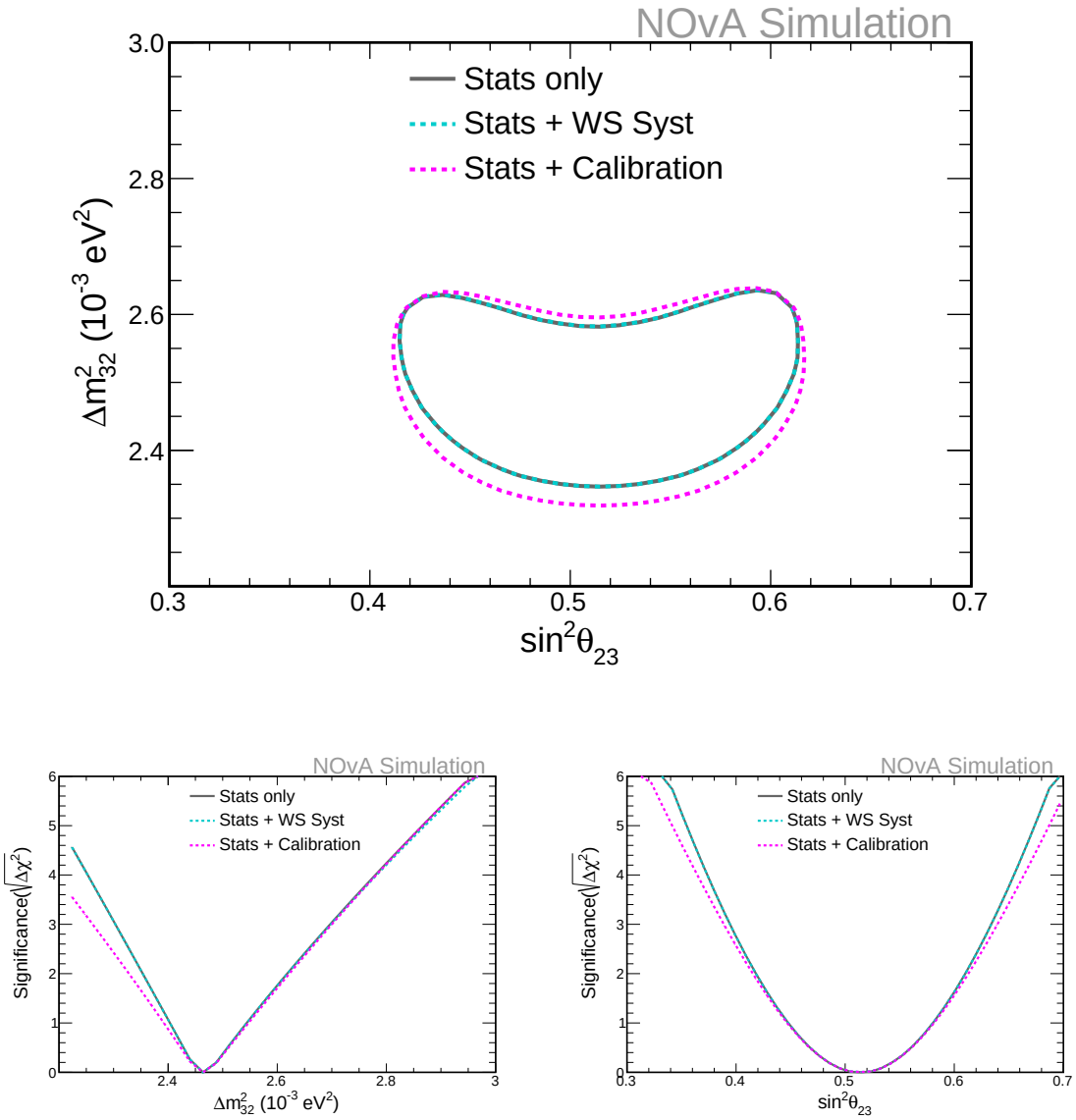


**Figure 6.11:** Projected sensitivities to the measurement of the **neutrino oscillation parameters** $\sin^2\theta_{23}$ and $\Delta m^2_{32}$, with an exposure to $8.85 \times 10^{20}$ and $12.33 \times 10^{20}$ POT in the FHC and RHC configuration, respectively, when applying the calibration and 100% wrong sign systematic individually. The FHC-only and RHC-only CPTc normal hierarchy best fits from table 5.5 are assumed to oscillate $\nu$ and $\bar{\nu}$ , respectively. The top plot shows the 90% confidence region for the 2D parameter space of the mixing angle and mass squared difference; the bottom plots show the significance of the measurement for each individual parameter.

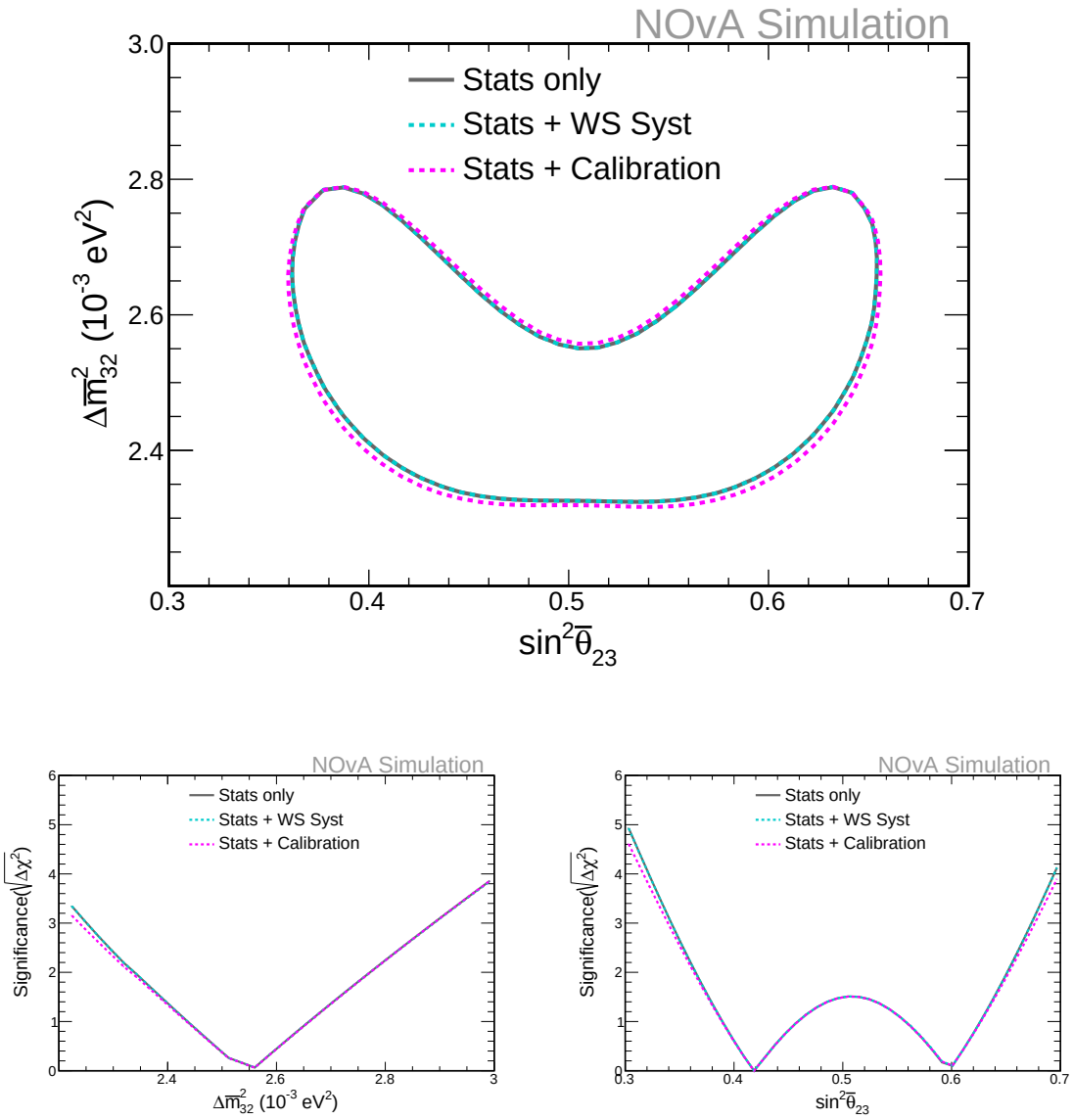


**Figure 6.12:** Projected sensitivities to the **antineutrino oscillation parameters** $\sin^2\bar{\theta}_{23}$ and $\Delta\bar{m}^2_{32}$, with an exposure to $8.85 \times 10^{20}$ and $12.33 \times 10^{20}$ POT in the FHC and RHC configuration, respectively, when applying the calibration and 100% wrong sign systematic individually. The FHC only and RHC only disappearance best fits from table 5.5, are assumed to oscillate $\nu$ and $\bar{\nu}$ , respectively. The top plot shows the 90% confidence region for the 2D parameter space of the mixing angle and mass squared difference; the bottom plots show the significance of the measurement for each individual parameter.

# Chapter 7

# Results

This chapter presents the results from the $\nu_\mu$ and $\bar{\nu}_\mu$ disappearance analysis introduced in Chapter 6. In this analysis the $\nu$ and $\bar{\nu}$ atmospheric mass splitting and mixing angle are extracted using only the information from neutrinos or only the information from antineutrinos. This approach is used to test one of the CPT conservation predictions, which tells that the neutrinos and antineutrinos have the same mass splitting and mixing parameters. For simplicity, this analysis is referred to as *CPT violation* or *CPTv*. The data used for this analysis was collected between February 2014 and February 2019, which corresponds to a FD exposure of $8.85 \times 10^{20}$ POT and $12.33 \times 10^{20}$ POT for the neutrino and antineutrino beam mode respectively.

This chapter begins with the comparison of the ND data and simulation in Section § 7.1, with particular focus on the wrong sign component. The neutrino and antineutrino FD data is used in a fit to a three neutrino flavour oscillation model where the $\nu$ and $\bar{\nu}$ parameters are allowed to vary independently and § 7.2 presents the results of the constraints on $\sin^2\theta_{23}, \sin^2\bar{\theta}_{23}, \Delta m^2_{32}$ and $\Delta\bar{m}^2_{32}$.

## 7.1 Evaluation of the wrong sign background at the near detector

NOvA's neutrino and antineutrino source has a component of $\bar{\nu}_\mu$ in the $\nu_\mu$ beam and vice versa. This wrong sign component is estimated to be 2.8±0.3%(10.6±1.1%) of the selected events from the antineutrino (neutrino) beam [110]. However, NOvA's detectors are not capable of distinguishing $\nu_\mu$ from $\bar{\nu}_\mu$ on an event by event basis. In this section, NOvA's own ND data is presented in a way that allows comparison of the wrong sign component in data and Monte Carlo.

Figures 7.1 and 7.2 show distributions in $\nu$ and $\bar{\nu}$ energy of selected data and simulated events at the ND from the FHC and RHC beam, respectively. The top panel shows the data in black dots with associated statistical errors. The simulated total and wrong sign component spectra are shown in purple and green, respectively. The nominal simulations are represented by the solid lines and the

simulation without the corrections to the interaction model (see Section § 3.4) are shown in dashed lines. The nominal simulations are displayed with a 1 $\sigma$ error band, which is calculated from the sum in quadrature of the systematic uncertainties accounted for in the analysis. The middle panel shows the wrong sign fraction in solid green for the nominal simulation and in dashed green for the simulation without cross-section tuning. The systematic error band on the wrong sign fraction is computed from the effect that the systematic uncertainties have on the total simulation and wrong sign component. The way the total and the wrong sign systematically shifted simulations correlate reduces or enlarges the error in the wrong sign fraction. Systematic uncertainties that change the number of total and wrong sign events at about the same level contribute in a small amount to the uncertainty in the wrong sign fraction. The opposite occurs with systematic uncertainties that are negatively correlated. The uncertainties that largely contribute to the wrong sign fraction error include the calibration, neutron, flux and MEC systematics. See Appendix C for a full set of ND tables showing the effect of individual systematic shifts. The bottom panel of Figures 7.1 and 7.2 shows the ratio of data over simulation in solid purple and in dashed purple for the nominal and for the simulation without cross-section tuning, respectively. The error band around the data to nominal Monte Carlo ratio is computed as the ratio between the data and the 1 $\sigma$ bounds of the nominal simulation. Appendix D has further details about how the uncertainty bands in these plots are calculated.

The FHC energy spectra show that the wrong sign fractions are the lowest between 1 and 3 GeV. These fractions are below 5% in the 1-3 GeV range, and are not higher than 11% outside this region. In the RHC beam, the wrong sign component is less than 20% at energies below 3 GeV but it can contribute with up to 50% at energies above 3 GeV. In both beams, the wrong sign fraction is lowest around the 2 GeV energy peak. These statements are not significantly different between the simulation with and without the cross-section tuning, which means that the interaction model does not significantly change the wrong sign fraction. However, the cross-section model improves the data-simulation agreement especially at energies below 4 GeV where the simulation can go from being 20% lower than data to being only 5% low in both beam configurations. The improvement is largely expected, as the cross-section model was fit to NOvA's own data. The data-simulation agreement is already within 5% in the highest energy bin, which ranges between 4 and 5 GeV.

In the following subsection, ND data and Monte Carlo samples are analysed to investigate the RHC wrong sign component. Similarly to the plots shown in Figures 7.1 and 7.2, two base simulations are considered to asses the cross-section model dependency on the wrong sign component and on the discrepancies between data and Monte Carlo: one is the simulation with corrections to the interaction model, which is the nominal analysis simulation, and a second is the simulation without the cross-section tuning.

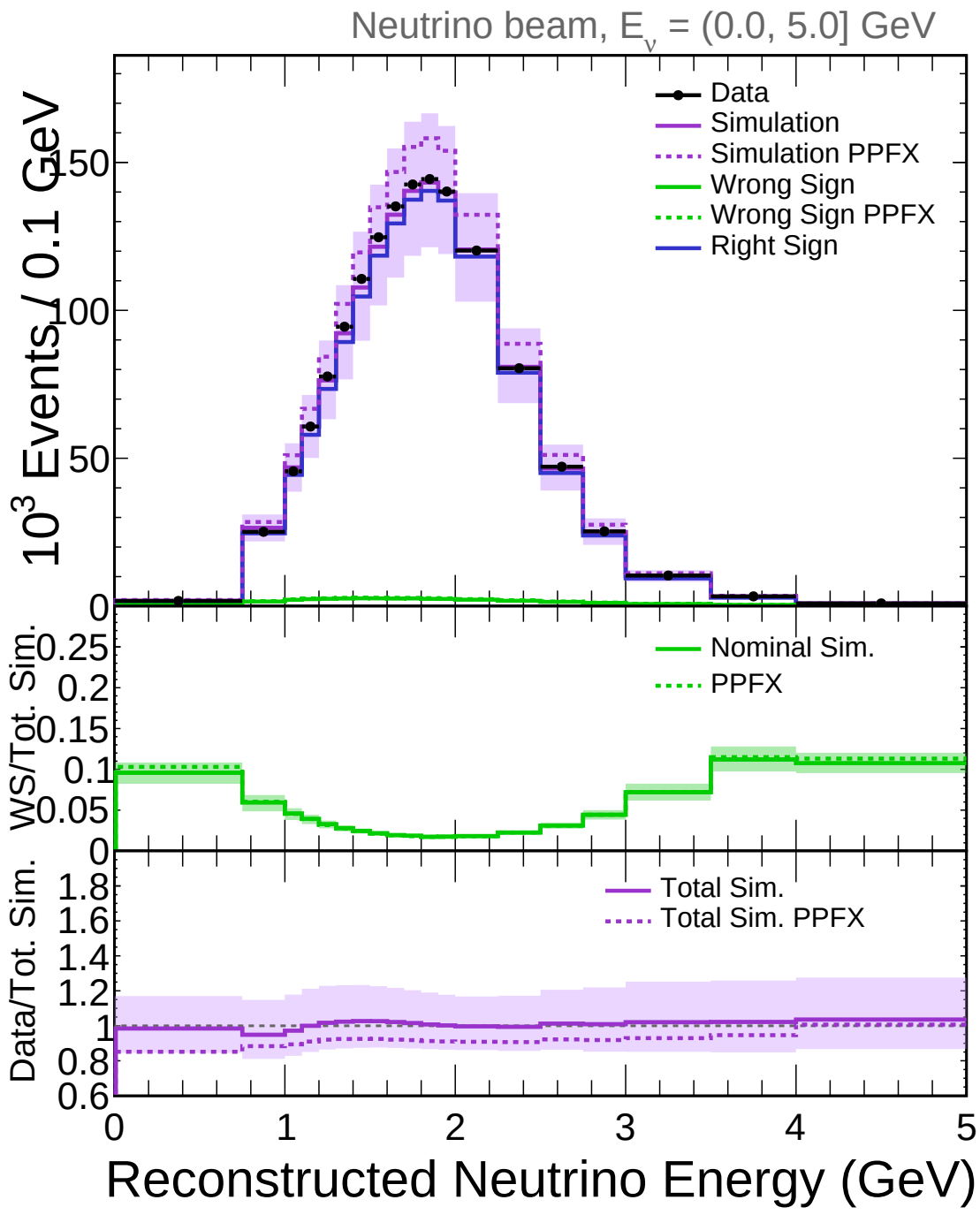


**Figure 7.1:** Distributions of selected **ND** data and simulated events in reconstructed energy from the **FHC** beam. The top panel shows the data passing the $\nu_\mu$ and $\bar{\nu}_\mu$ CC selection criteria in black dots with statistical errors. The total, right sign, wrong sign and other beam backgrounds are shown in purple, blue, green and gray lines respectively. The nominal simulation is represented by solid lines and the simulation without cross-section tuning is shown by the dotted lines. The middle panel shows the simulated wrong sign fraction. The bottom panel displays the ratio of the data to the total simulation. The shaded regions correspond to the $1\sigma$ uncertainty bounds with respect to the nominal predictions. In the three panels, the distributions corresponding to the simulation without cross-section tuning are labeled as *PPFX*. All the spectra are normalised by POT.

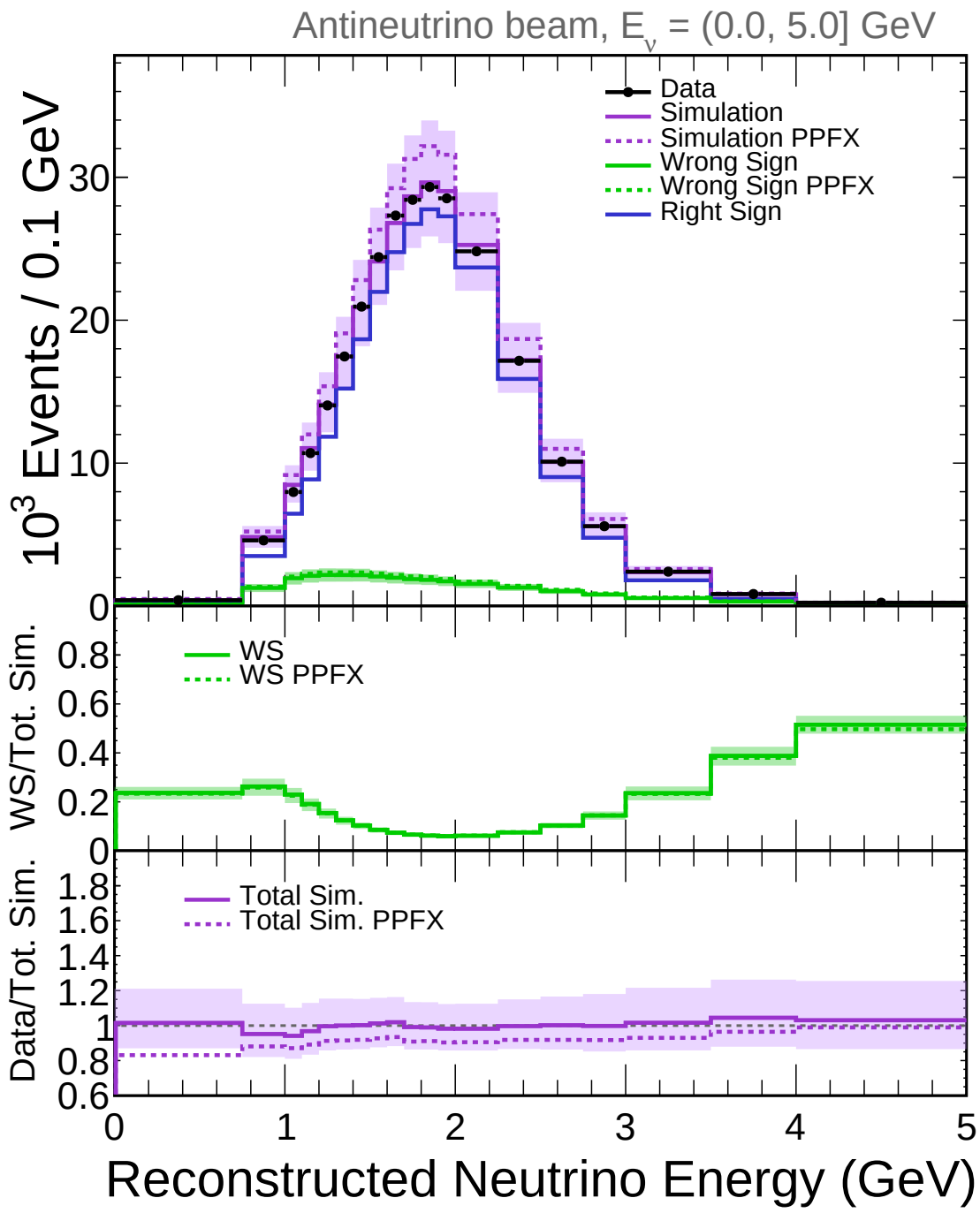


**Figure 7.2:** Distributions of selected **ND** data and simulated events in reconstructed energy from the **RHC** beam. The top panel shows the data passing the $\nu_\mu$ and $\bar{\nu}_\mu$ CC selection criteria in black dots with statistical errors. The total, right sign, wrong sign and other beam backgrounds are shown in purple, blue, green and gray lines respectively. The nominal simulation is represented by solid lines and the simulation without cross-section tuning is shown by the dotted lines. The middle panel shows the simulated wrong sign fraction. The bottom panel displays the ratio of the data to the total simulation. The shaded regions correspond to the $1\sigma$ uncertainty bounds with respect to the nominal predictions. In the three panels, the distributions corresponding to the simulation without cross-section tuning are labeled as *PPFX*. All the spectra are normalised by POT.

### 7.1.1 Hadronic fraction distributions at the ND

Figures 7.3 and 7.4 show FHC and RHC distributions in hadronic energy fraction of selected data and simulated $\nu_\mu$ and $\bar{\nu}_\mu$ CC events at NOvA's ND. These figures show an analogous set of plots to those previously described Figures 7.1 and 7.2. The solid and dashed lines correspond to the simulations with and without the cross-section tuning, respectively. It can be seen from these plots that the RHC(FHC) wrong sign component is highest at high(low) hadronic energy fraction and the simulation agrees with the data to about $\pm 20\%$ either with or without the cross-section tuning. The wrong sign fraction error band in Figure 7.4 includes all the systematic uncertainties accounted for in the CPTv analysis. Given the correlation between systematic uncertainties, the wrong sign fraction in an specific hadronic energy fraction region can not be changed without changing another. In particular, even a 1 $\sigma$ change in high hadronic energy region, which has the largest uncertainty and which would result on a change of about 10% in the wrong sign fraction, would modify the low hadronic energy fraction region by less than 5%. A similar conclusion is obtained for the energy spectrum wrong sign fraction plots shown in Figures 7.1 and 7.2. Further information can be extracted from combining the trends seen in these plots. It can be seen from Figure 7.4 that a sample with high wrong sign purity in the RHC beam is obtained by focusing on the region above 0.8. In addition, Figure 7.2 shows that the RHC wrong sign fraction is largest in the highest reconstructed energy bin. Thus the large hadronic energy fraction region in the highest bin of reconstructed energy allows a more direct data to Monte Carlo comparison of the RHC wrong sign component.

Two regions are presented in what follows to illustrate the wrong sign fraction. One is a region around the energy peak, which is especially relevant for the analysis. The other is the region with high RHC wrong sign purity. Figures 7.5 and 7.6 show the hadronic energy fraction of selected data and simulated $\nu_\mu$ and $\bar{\nu}_\mu$ CC events at NOvA's ND between 2 and 2.25 GeV, around the energy peak. These distributions show that the wrong sign fraction is about the same size or smaller than the uncertainty on the simulation. The wrong sign component is less than 5% and 20% in the FHC and RHC beam, respectively. The data-simulation differences in the RHC beam could be accounted for with relatively small changes to the simulated right sign component ($\bar{\nu}_\mu$) or rather large changes to the wrong sign ($\nu_\mu$). This is simply a reflection of the high purity in the peak of the beam. Figures 7.7 and 7.8 show the analogous distributions for events with energies between 4 and 5 GeV, which is the highest reconstructed energy in the analysis. In these plots and for events with hadronic energy fraction in the range 0.6-0.9, the RHC data is mostly comprised by $\nu_\mu$ events and the simulation agrees with data within 20% with or without cross-section tuning. In the FHC case, the analogous region is also mostly comprised by $\nu_\mu$ events and the simulation describes the data to about 10 or 20% with and without cross-section tuning, respectively. This provides evidence that the hadronic energy fraction distribution for $\nu_\mu$ events of 4-5 GeV is reasonably well modeled. In both beams, the simulated wrong sign and the fraction prior to the cross-section tuning are within the $1\sigma$ uncertainty in the highest energy bin and high hadronic energy fraction.

The plots for the other reconstructed energy bins are found in Appendix E.

Based on the plots in Figures 7.7 and 7.8, even if the difference between data and simulation was entirely due to the wrong sign component, it would only be a 20% change. The Monte Carlo agreement with data in the high wrong sign fraction regions is in the 10% or 20% level and so provides some evidence that the wrong sign component is at least modeled to around the 20% level. Moreover, a previous study has estimated that the scale of the $\nu_\mu$ component in the RHC beam is $1.05 \pm 0.12$ [106] (see also § 4.8). At this level the systematic uncertainty on the WS component has a completely negligible effect on the analysis, since it was shown in § 6.3 that even a 100% uncertainty on the wrong sign component has a negligible effect on the CPTv analysis.

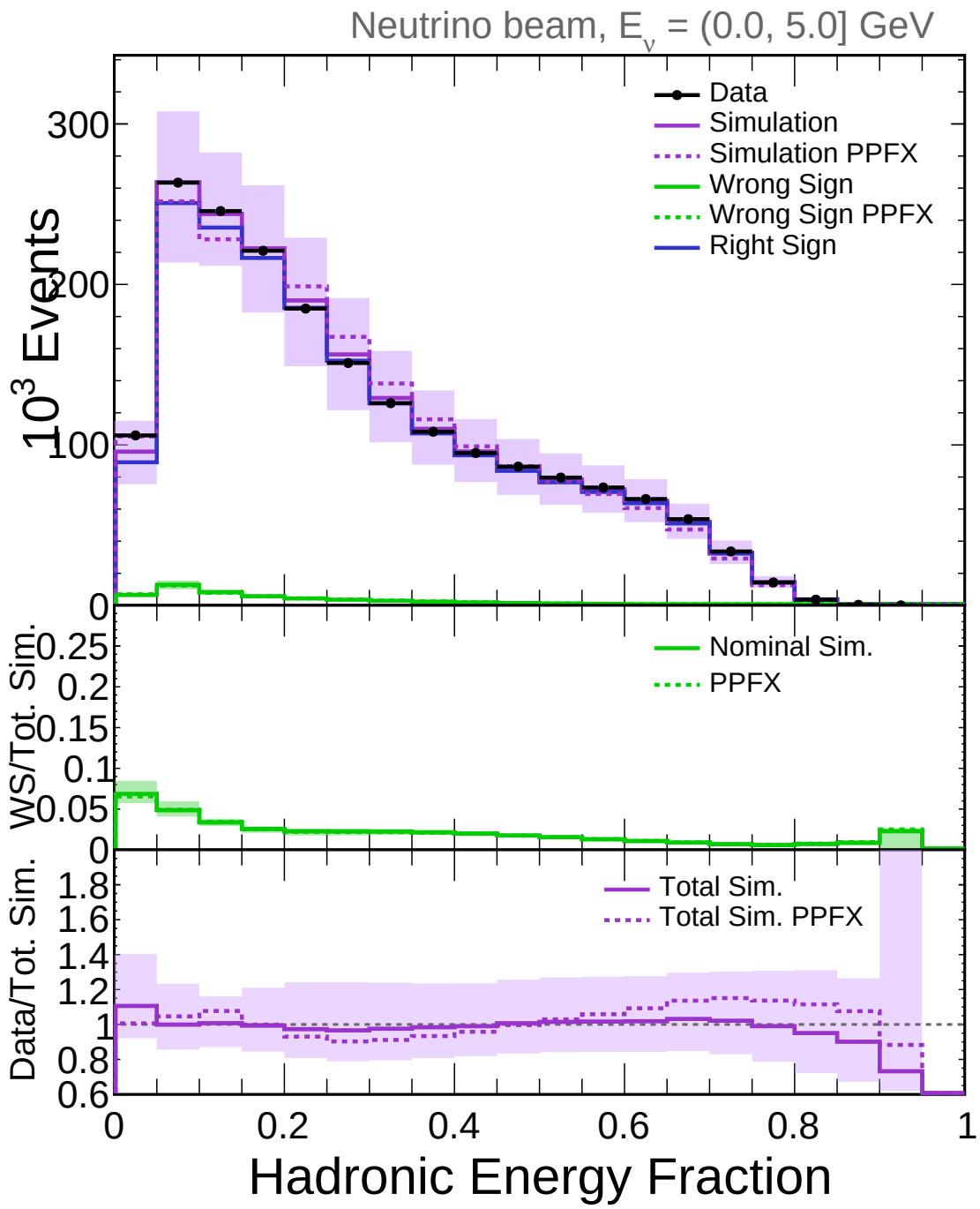


**Figure 7.3:** Distributions of selected **ND** data and simulated events in hadronic energy fraction from the **FHC** beam. The top panel shows the data in black dots and with statistical errors. The simulated total, right sign, wrong sign and other beam backgrounds are shown by the purple, blue, green and gray lines respectively. The nominal simulation and the simulation without cross-section tuning are shown by the solid and dotted lines respectively. The middle panel shows the simulated wrong sign fraction. The bottom panel displays the ratio of the data to the total simulation. The shaded regions correspond to the $1\sigma$ uncertainty bounds computed with respect to the nominal predictions. In the three panels, the distributions corresponding to the simulation without cross-section tuning are labeled as *PPFX*. All the spectra are normalised by POT.

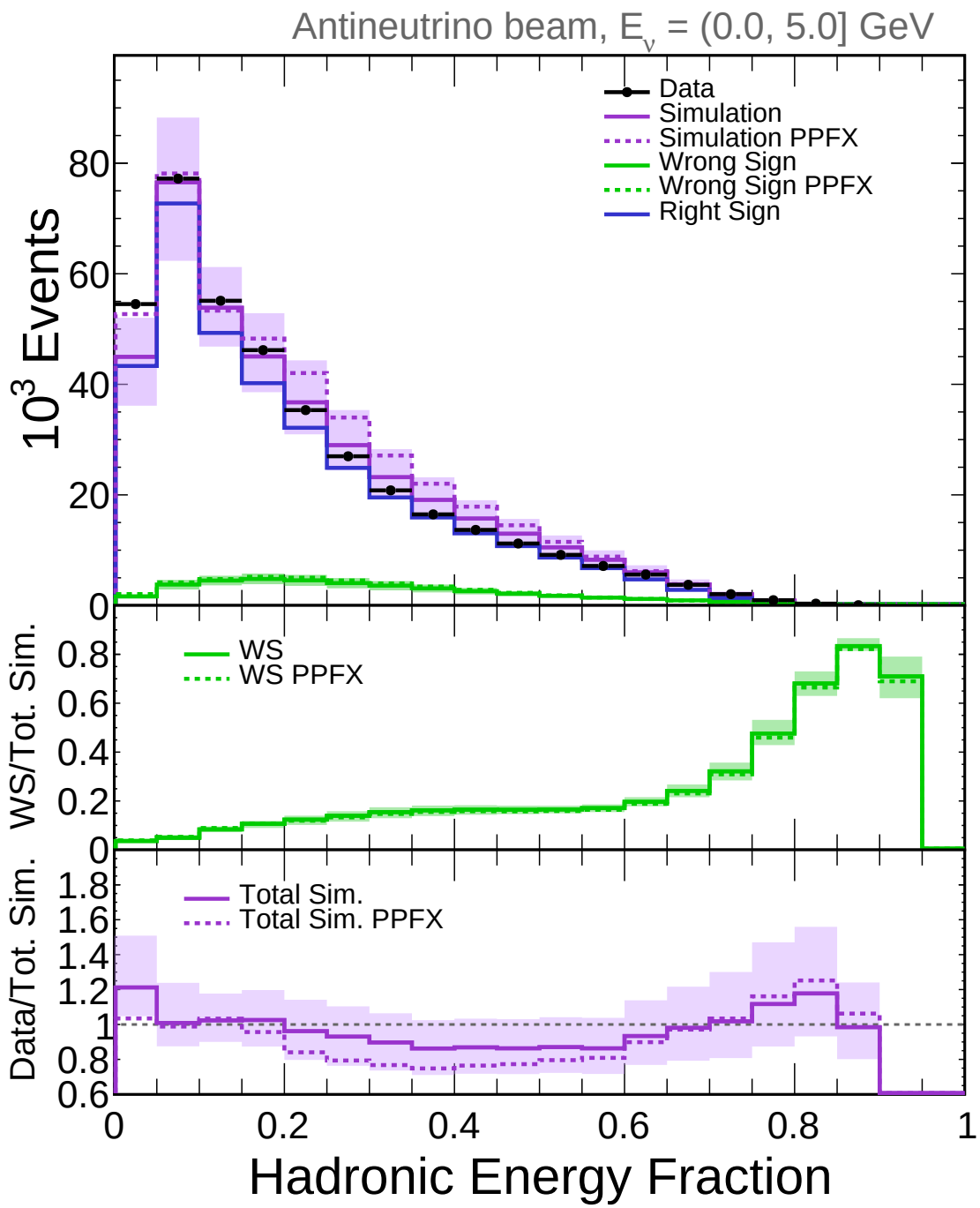


**Figure 7.4:** Distributions of selected **ND** data and simulated events in hadronic energy fraction from the **RHC** beam. The top panel shows the data in black dots and with statistical errors. The simulated total, right sign, wrong sign and other beam backgrounds are shown by the purple, blue, green and gray lines respectively. The darker dashed and dotted distributions correspond to the corrected Monte Carlo using the FHC simulation with or without cross-section tuning, respectively. The nominal simulation and the simulation without cross-section tuning are shown by the solid and dotted lines respectively. The middle panel shows the simulated wrong sign fraction. The bottom panel displays the ratio of the data to the total simulation. The shaded regions correspond to the $1\sigma$ uncertainty bounds computed with respect to the nominal predictions. In the three panels, the distributions corresponding to the simulation without cross-section tuning are labeled as *PPFX*. All the spectra are normalised by POT.

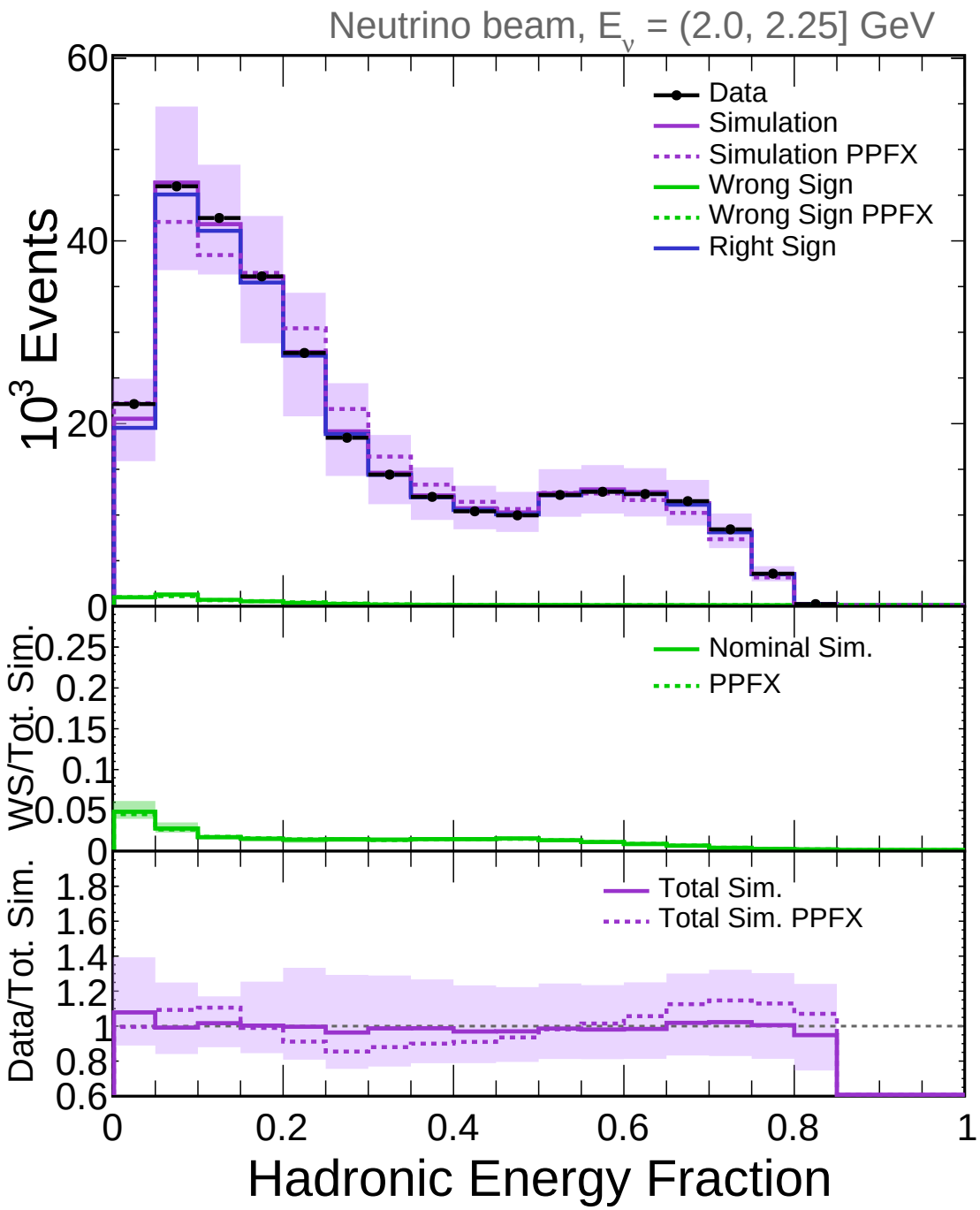


**Figure 7.5:** Distributions of selected **ND** data and simulated events in hadronic energy fraction from the **FHC** beam, for interactions with reconstructed neutrino energy between **2 and 2.25 GeV**. The top panel shows the data in black dots and with statistical errors. The simulated total, right sign, wrong sign and other beam backgrounds are shown by the purple, blue, green and gray lines respectively. The nominal simulation and the simulation without cross-section tuning are shown by the solid and dotted lines respectively. The middle panel shows the simulated wrong sign fraction. The bottom panel displays the ratio of the data to the total simulation. The shaded regions correspond to the $1\sigma$ uncertainty bounds computed with respect to the nominal predictions. In the three panels, the distributions corresponding to the simulation without cross-section tuning are labeled as *PPFX*. All the spectra are normalised by POT.

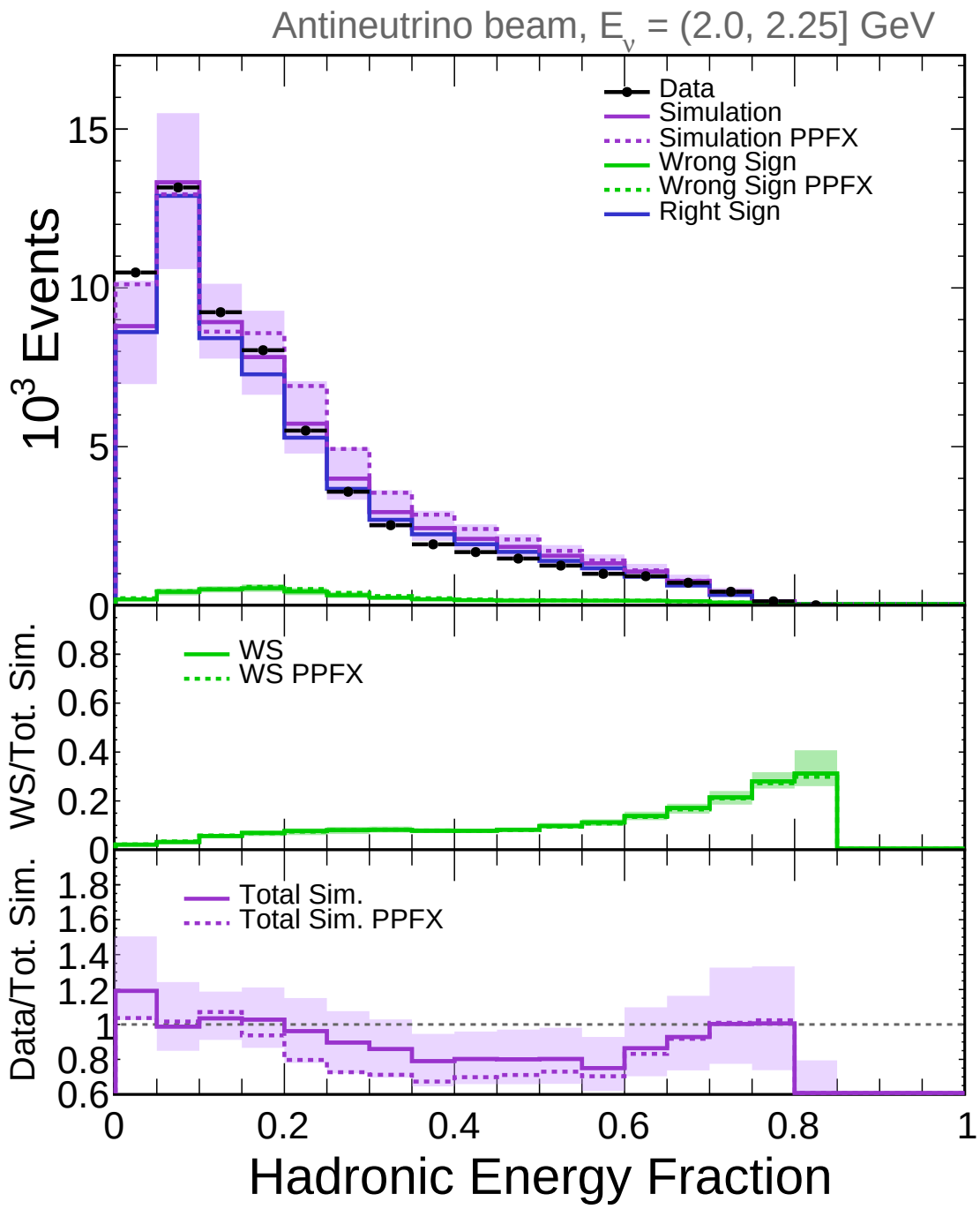


**Figure 7.6:** Distributions of selected **ND** data and simulated events in hadronic energy fraction from the **RHC** beam, for interactions with reconstructed neutrino energy between **2 and 2.25 GeV**. The top panel shows the data in black dots and with statistical errors. The simulated total, right sign, wrong sign and other beam backgrounds are shown by the purple, blue, green and gray lines respectively. The darker dashed and dotted distributions correspond to the corrected Monte Carlo using the FHC simulation with or without cross-section tuning, respectively. The nominal simulation and the simulation without cross-section tuning are shown by the solid and dotted lines respectively. The middle panel shows the simulated wrong sign fraction. The bottom panel displays the ratio of the data to the total simulation. The shaded regions correspond to the $1\sigma$ uncertainty bounds computed with respect to the nominal predictions. In the three panels, the distributions corresponding to the simulation without cross-section tuning are labeled as *PPFX*. All the spectra are normalised by POT.

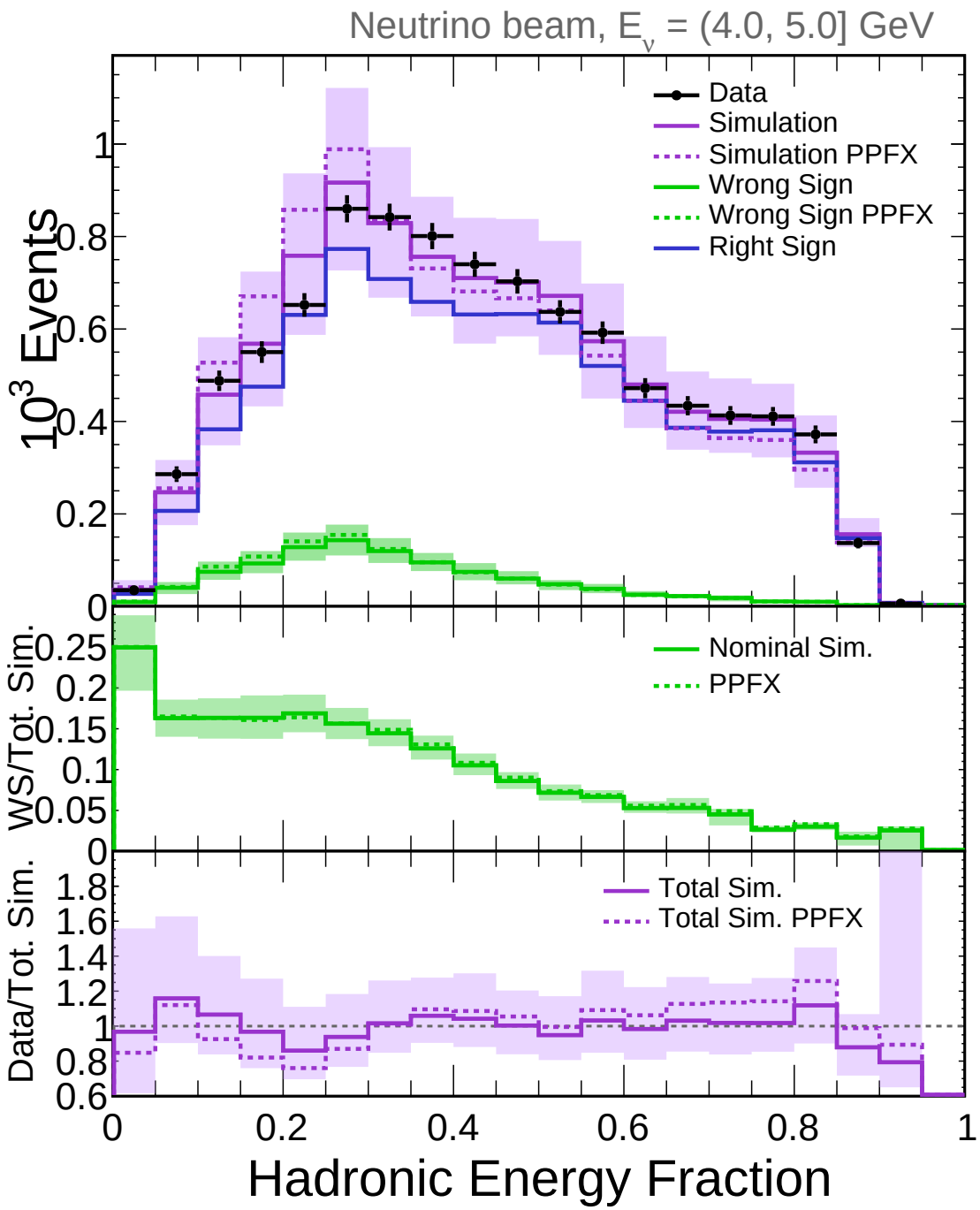


**Figure 7.7:** Distributions of selected **ND** data and simulated events in hadronic energy fraction from the **FHC** beam, for interactions with reconstructed neutrino energy between **4 and 5 GeV**. The top panel shows the data in black dots and with statistical errors. The simulated total, right sign, wrong sign and other beam backgrounds are shown by the purple, blue, green and gray lines respectively. The nominal simulation and the simulation without cross-section tuning are shown by the solid and dotted lines respectively. The middle panel shows the simulated wrong sign fraction. The bottom panel displays the ratio of the data to the total simulation. The shaded regions correspond to the $1\sigma$ uncertainty bounds computed with respect to the nominal predictions. In the three panels, the distributions corresponding to the simulation without cross-section tuning are labeled as *PPFX*. All the spectra are normalised by POT.

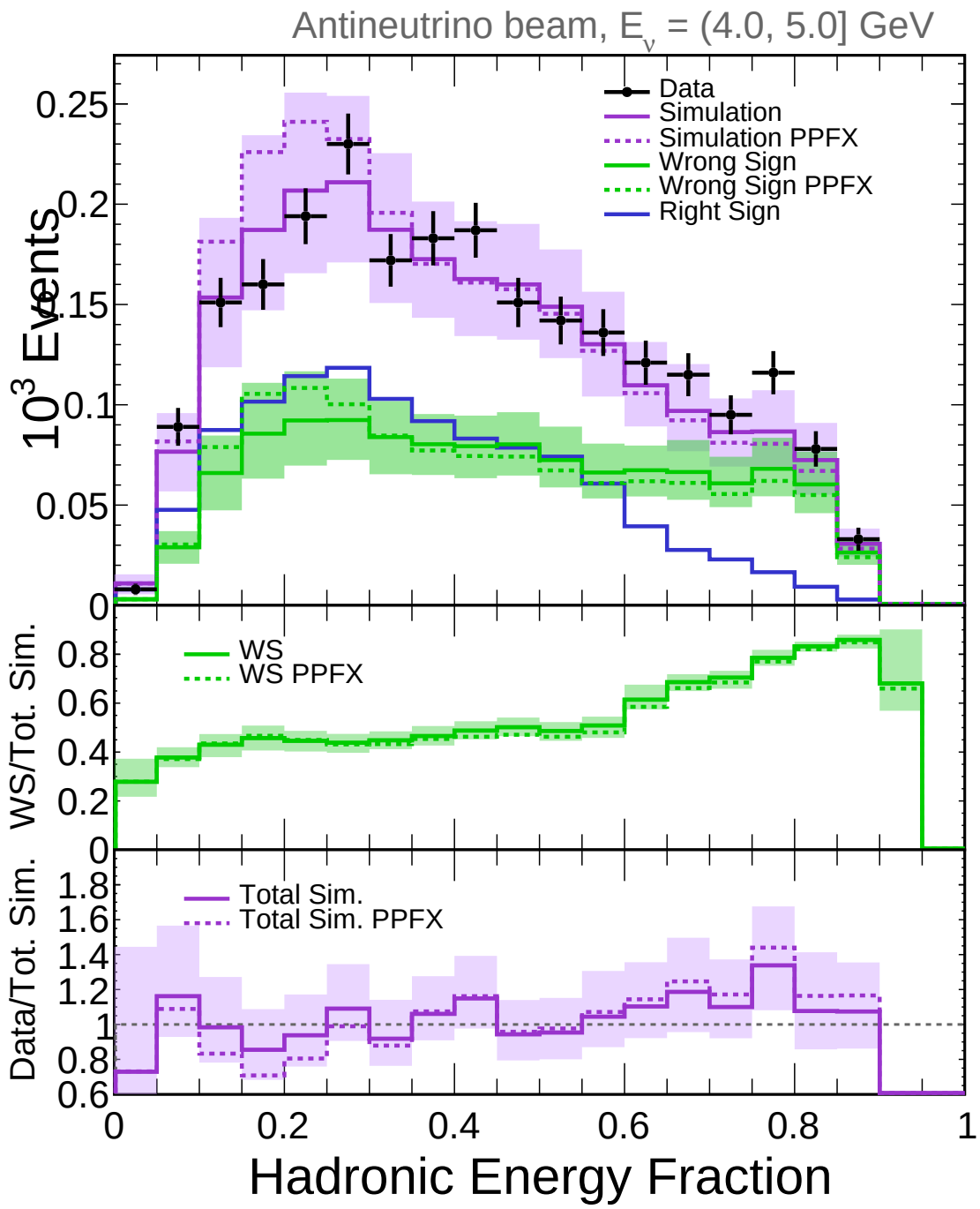


**Figure 7.8:** Distributions of selected **ND** data and simulated events in hadronic energy fraction from the **RHC** beam, for interactions with reconstructed neutrino energy between **4 and 5 GeV**. The top panel shows the data in black dots and with statistical errors. The simulated total, right sign, wrong sign and other beam backgrounds are shown by the purple, blue, green and gray lines respectively. The darker dashed and dotted distributions correspond to the corrected Monte Carlo using the FHC simulation with or without cross-section tuning, respectively. The nominal simulation and the simulation without cross-section tuning are shown by the solid and dotted lines respectively. The middle panel shows the simulated wrong sign fraction. The bottom panel displays the ratio of the data to the total simulation. The shaded regions correspond to the $1\sigma$ uncertainty bounds computed with respect to the nominal predictions. In the three panels, the distributions corresponding to the simulation without cross-section tuning are labeled as *PPFX*. All the spectra are normalised by POT.

## 7.2 Constraints on the $\nu$ and $\bar{\nu}$ parameters

This section presents the results of the CPTv analysis performed to constrain both the $\nu$ and $\bar{\nu}$ oscillation parameters. The analysis uses NOvA's data from $8.85 \times 10^{20}$ and $12.33 \times 10^{20}$ POT for the FHC and RHC beams, respectively, but only the information from the neutrinos or only the information from the antineutrinos is used to extract the neutrino or the antineutrino measurements, respectively. In this analysis, the $\nu$ and $\bar{\nu}$ parameters are allowed to vary independently. Constraints are set on the mixing angles $\theta_{23}$ and $\bar{\theta}_{23}$, and on the mass squared difference $\Delta m^2_{32}$ and $\Delta \bar{m}^2_{32}$. Figure 7.9 shows the CPTv results in normal hierarchy. In the top sub-figure, the blue and pink contours enclose the $\Delta m^2_{32}$ vs. $\sin^2\theta_{23}$ and $\Delta \bar{m}^2_{32}$ vs. $\sin^2\bar{\theta}_{23}$ space of parameters, respectively, that are allowed at the 90% confidence level. The significance at which a particular value of individual parameters is disfavored is shown by the bottom sub-figures in terms of $\sqrt{\Delta\chi^2}$. The results in this section account for statistical and systematic uncertainties unless otherwise stated.

The best fits in the normal hierarchy for neutrinos are $\Delta m^2_{32} = 2.48^{+0.07}_{-0.09} \times 10^{-3}$ eV$^2$ and $\sin^2\theta_{23} = 0.51^{+0.06}_{-0.06}$. The antineutrino best fits are $\Delta \bar{m}^2_{32} = 2.55^{+0.12}_{-0.13} \times 10^{-3}$ eV$^2$ and $\sin^2\bar{\theta}_{23} = 0.41, 0.61$, with the $1\sigma$ confidence intervals $[0.38, 0.45]$ and $[0.57, 0.64]$, with a $\chi^2 = 133.0$ for 150 degrees of freedom (*d.o.f.*). The quoted bounds are the combined statistical and systematic 1 $\sigma$ uncertainty bounds. Table 7.1 summarizes the results of the measurements of the $\nu$ and $\bar{\nu}$ mixing angle and mass splitting, and include the inverted hierarchy measurements. In normal hierarchy, the neutrino mass splitting prefers a lower best fit than the antineutrinos. The $\sin^2\theta_{23}$ best fit are the same in both hierarchies and the allowed 1 $\sigma$ ranges are almost identical. In the normal hierarchy, the antineutrino result disfavours maximal mixing at 1.7 $\sigma$ and maximal mixing is disfavoured at 1.6 $\sigma$ in the inverted hierarchy. The best fit values of $\sin^2\theta_{23}$ in each octant are degenerate. The normal and inverted hierarchy allowed 1 $\sigma$ ranges of $\sin^2\bar{\theta}_{23}$ are the same. The neutrino and antineutrino results for the measurement of the atmospheric-scale mass splitting are consistent at the 90% confidence level under both hierarchy assumptions. No significant evidence of a difference between the neutrino mixing angle was found.

| | Parameter | | | |
|---|---|---|---|---|
| Hierarchy | $\sin^2\theta_{23}$ | $\sin^2\bar{\theta}_{23}$ | $\Delta m^2_{32}(\times 10^{-3}$ eV$^2)$ | $\Delta \bar{m}^2_{32}(\times 10^{-3}$ eV$^2)$ |
| Normal | $0.51 \in [0.45, 0.57]$ | $0.41 \in [0.38, 0.45] \cup 0.61 \in [0.57, 0.64]$ | $2.48^{+0.07}_{-0.09}$ | $2.55^{+0.12}_{-0.13}$ |
| Inverted | $0.51 \in [0.46, 0.57]$ | $0.42 \in [0.38, 0.45] \cup 0.61 \in [0.57, 0.64]$ | $-2.51^{+0.06}_{-0.08}$ | $-2.57^{+0.11}_{-0.14}$ |

**Table 7.1:** Best fit values of the $\sin^2\theta_{23}, \sin^2\bar{\theta}_{23}, \Delta m^2_{32}$ and $\Delta \bar{m}^2_{32}$ oscillation parameters from a CPT invariance $\nu_\mu$ and $\bar{\nu}_\mu$ disappearance analysis with an exposure to $8.85 \times 10^{20}$ and $12.33 \times 10^{20}$ POT in the FHC and RHC beam configuration, respectively. The quoted 1 $\sigma$ bounds are the combined statistical and systematic uncertainty bounds.

The CPTv and the CPTc results are overlaid in Figure 7.10. The 90% confidence regions from the CPTv analysis for the neutrino and antineutrino parameters are enclosed by the solid

blue and solid pink contours respectively. The three CPTc contours, FHC-only, RHC-only and FHC+RHC beam, are shown by the dashed lines for the measurement of $\Delta m^2_{32}$ and $\sin^2\theta_{23}$, which are assumed to be the same for neutrinos and antineutrinos. Although the CPTv analysis uses both FHC and RHC data, it is interesting to compare the CPTv neutrino (antineutrino) result to the CPTc FHC-only (RHC-only) result. If the FHC (RHC) was a 100% pure beam of $\nu_\mu$ ($\bar{\nu}_\mu$), the CPTc analysis would directly measure the neutrino (antineutrino) oscillation parameters. In reality, that is not the case and is the main reason for developing the CPTv analysis. As can be seen in Figure 7.10, the precision in the antineutrino measurements is slightly reduced if comparing the CPTv vs. CPTc results as outlined above. This is because of the wrong sign component in RHC beam.

Table 7.2 presents the summary of the selected number of $\nu_\mu$ and $\bar{\nu}_\mu$ CC candidate events at the FD along with the prediction at the CPTv best fit which includes the FD cosmic estimate and the effect of the systematic pulls from the fit. The number of predicted events for the FHC exposure is about 4 events less than the prediction at the FHC+RHC CPTc best fit, and is about 4 events more for RHC (see Table 5.4 for the CPTc numbers). The CPTv predictions are in better agreement with the observations than the CPTc result. The CPTv $\chi^2$ at the CPTv best fit is 1.8 units less than the equivalent from the CPTc FHC+RHC result although the number of d.o.f. is larger by two.

| | FHC | | RHC | |
|---|---|---|---|---|
| $E_{Had}/E\nu$ | Data | Prediction | Data | Prediction |
| Lowest | 32 | 29.30 (186.55) | 25 | 25.95 (130.42) |
| Second lowest | 25 | 28.76 (179.74) | 25 | 25.20 (124.42) |
| Second highest | 26 | 29.83 (178.43) | 28 | 23.89 (113.58) |
| Highest | 30 | 33.53 (185.52) | 24 | 25.13 (107.20) |
| Total | 113 | 121.42 (730.23) | 102 | 100.17 (475.61) |

**Table 7.2:** Number of selected $\nu_\mu$ and $\bar{\nu}_\mu$ events from data and simulation at the FD, for the FHC and RHC beam configurations separated by bins of energy resolution. The predictions assume oscillations at the CPTv best fit and include the cosmic background. The predicted number of events in absence of oscillations is shown in parentheses. The numbers account for the systematic pulls in the fit.

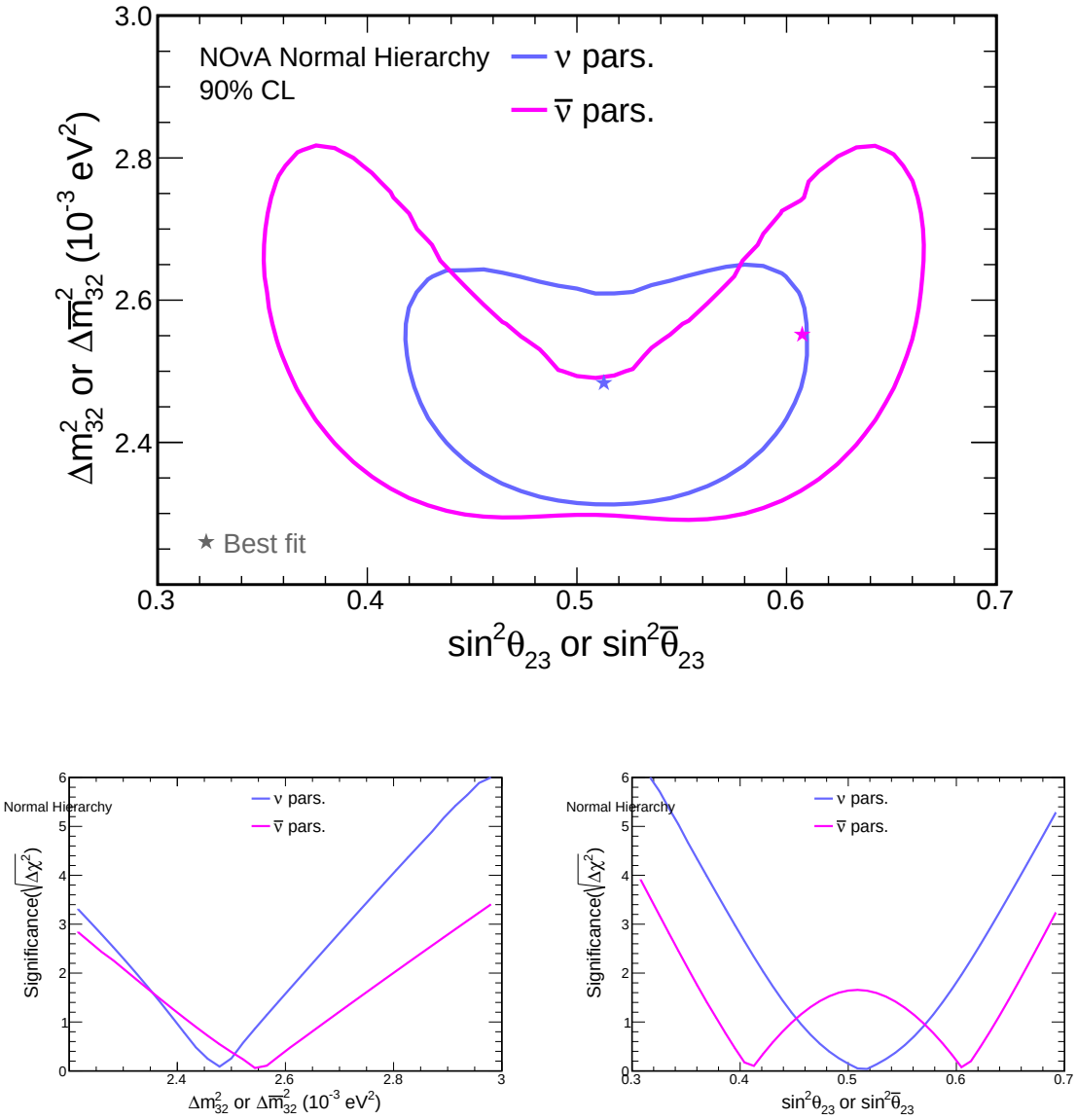


**Figure 7.9:** Constraints on the $\nu$ and $\bar{\nu}$ oscillation parameters from a $\nu_\mu$ and $\bar{\nu}_\mu$ disappearance analysis assuming CPT violation. The analysis uses a combined FD exposure of $8.85 \times 10^{20}$ and $12.33 \times 10^{20}$ POT in the FHC and RHC beam configuration respectively. The results are shown in blue for the neutrinos and in pink for the antineutrino measurements. The 90% confidence regions of the mixing angle and the mass squared difference are shown at the top and best fit points are represented by a star for each case. The bottom plots show the significance of the measurement for each individual parameter.

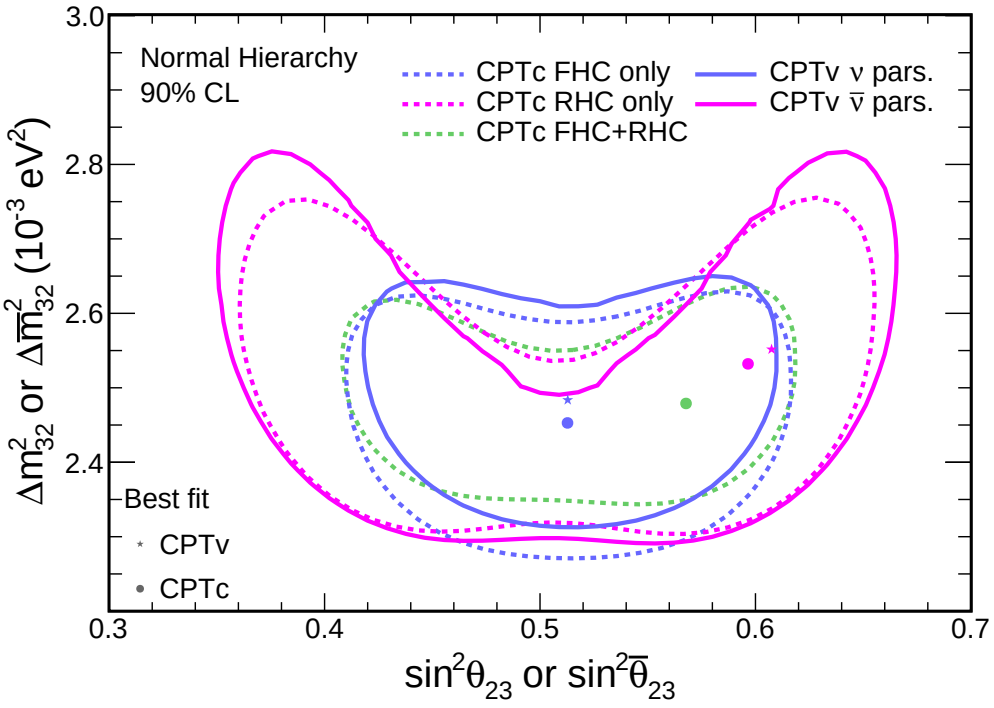


**Figure 7.10:** 90% confidence level contours from the the CPTv (solid lines) and CPTc (dashed lines) $\nu_\mu$ and $\bar{\nu}_\mu$ disappearance analyses, with an exposure to $8.85 \times 10^{20}$ POT for the beam in FHC configuration and/or $12.33 \times 10^{20}$ POT for RHC. The best fit points are represented by the stars and dots for the CPTv and CPTc analysis, respectively.

### 7.2.1 Measurement uncertainties

Figure 7.11 shows a comparison between the 90% confidence regions from the fit to data when including only statistical uncertainties, and where both statistical and systematic uncertainties are accounted for. The CPTv sensitivities for the analysis best fits are shown in the same figure and are consistent with the results. The systematic uncertainties move the $\Delta m^2_{32}$ and $\Delta \bar{m}^2_{32}$ best fit to higher values but do not change the $\sin^2\theta_{32}$ nor $\sin^2\bar{\theta}_{23}$ best fit. Figure 7.12 shows the pulls on the systematic uncertainties, quoted as fractions of $\sigma$, that contribute to the $\chi^2$. The largest pulls are due to the calibration and light model systematics and both are less than 1 $\sigma$.

Table 7.3 summarises the uncertainty sources accounted for in the analysis and their impact on the neutrino and antineutrino parameter measurements. The impact that each systematic uncertainty in Table 7.3 has on the measurements is estimated in terms of its contribution to the total uncertainty. The procedure uses FD predictions made with the extrapolation procedure described in § 4.7 but using the ND base simulation instead of ND data. These FD predictions are used in a fit to FD spectra oscillated with the CPTv analysis best fits. This approach separates the systematic effect from that of the extrapolation [95, 104]. The uncertainties are evaluated by comparing the statistical only fit against a fit that also includes a systematic uncertainty. The impact of an individual or group of systematic uncertainties on the measurement is assessed by subtracting in quadrature the $1\sigma$ boundaries from these two fits. The total systematic uncertainty is calculated from the subtraction in quadrature of the 1 $\sigma$ boundaries from the statistical only fit and the fit accounting for both statistical and systematic uncertainties. The upper octant boundaries are considered for the calculation of the $\bar{\theta}_{23}$ uncertainties. Figures 7.13 and 7.14 graphically show the impact of the individual uncertainties on the mixing angle and mass square splitting, respectively, arranged from largest to smallest for the neutrino and antineutrino measurements. A mapping table between the uncertainties in Figure 7.12 and Table 7.3, Figures 7.13 and 7.14 is shown in Table 5.6.

The mixing disappearance is proportional to $\sin^2 2\theta_{23}$ and reported as $\sin^2\theta_{23}$, so the errors on $\sin^2\theta_{23}$ are larger and almost symmetrical around maximal mixing (see significance of the mixing angle measurement in Figure 7.9). Thus the uncertainty on $\sin^2\theta_{23}$ is larger than for $\sin^2\bar{\theta}_{23}$. The -1$\sigma$ uncertainties on $\sin^2\bar{\theta}_{23}$ are overall larger than the +1$\sigma$ uncertainties because the uncertainty is calculated in the upper octant. The opposite occurs for the best fit in the lower octant. The total uncertainty on $\Delta \bar{m}^2_{32}$ is about twice of the uncertainty on $\Delta m^2_{32}$ due to the best fit being away from maximal mixing and results in the bean-shaped contour. The dominant systematic uncertainties for both the mixing angle and the mass-squared difference are the absolute and relative hadronic energy, and the neutron uncertainty. This can be explained by the energy systematics being able to move events between bins of reconstructed energy thus moving events in or out the energy dip region around 1.6 GeV. Similarly, the neutron uncertainty can lead to underestimating the hadron system energy as the neutral particles could go undetected. The cross-section uncertainties impact the measurements at a lower level.

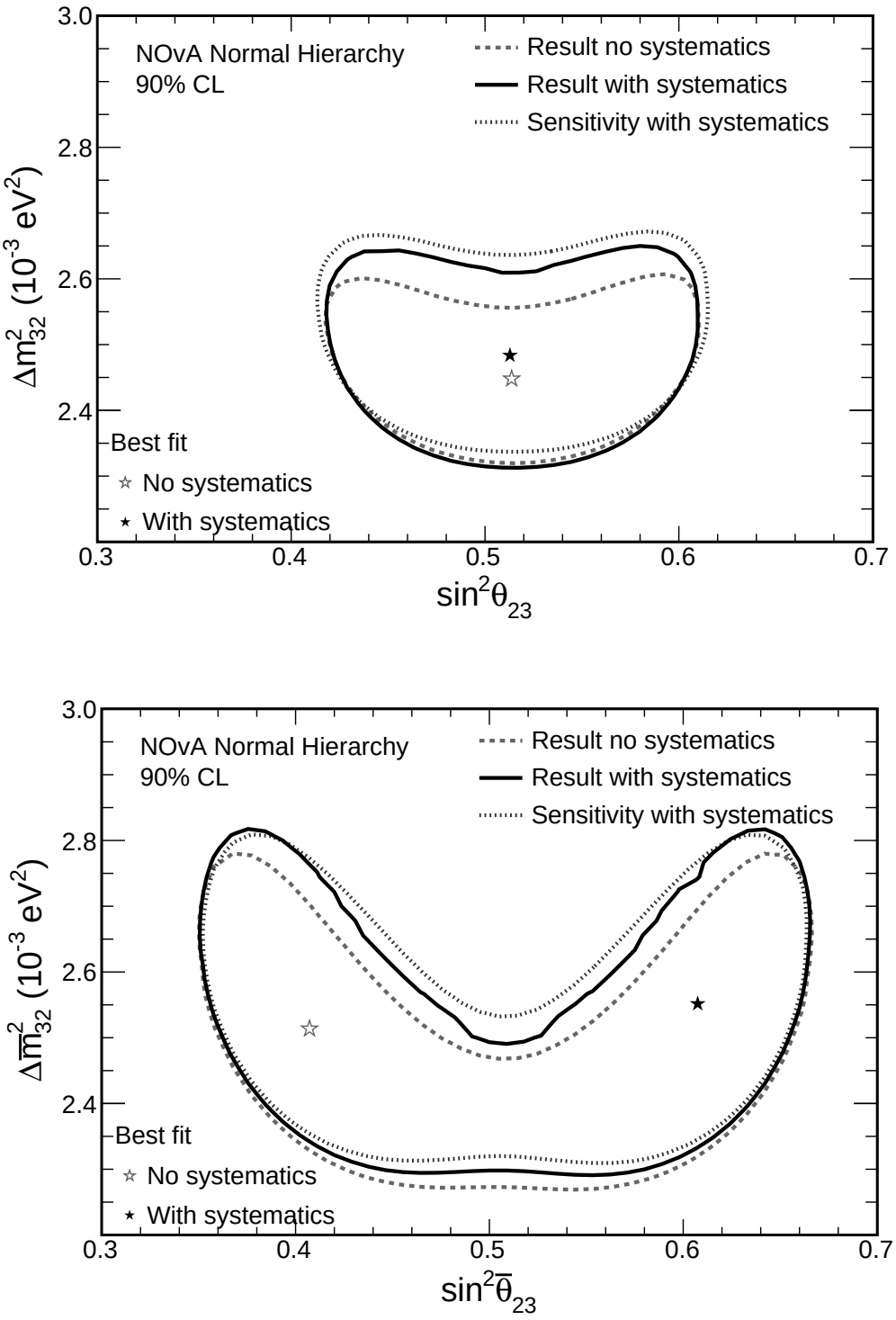


**Figure 7.11:** 90% confidence regions from the CPTv analysis. The results of the fit accounting for systematic uncertainties or only for statistical uncertainties are displayed in solid and dashed lines, respectively, for the neutrino (top) and antineutrino (bottom) parameters. The CPTv sensitivities with the analysis best fits are displayed in dotted lines.

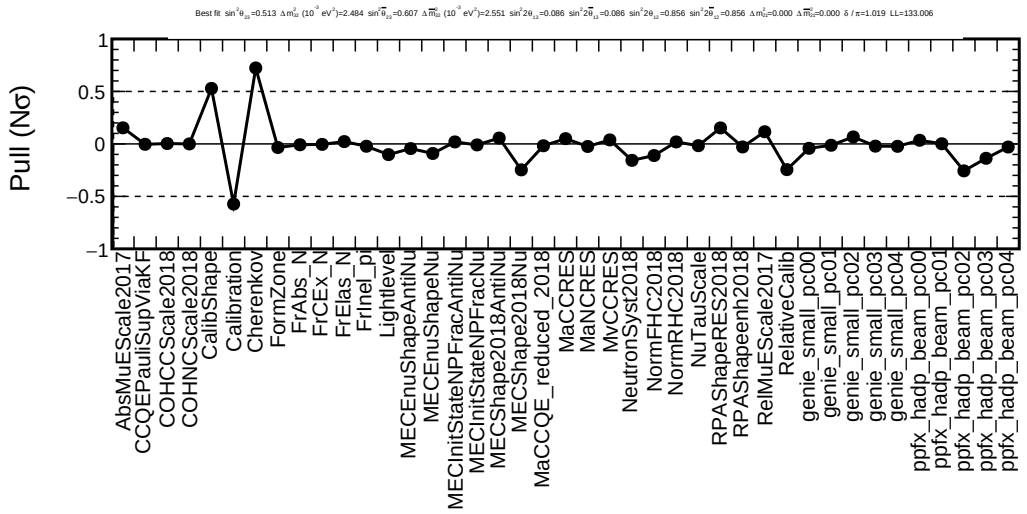


**Figure 7.12:** Systematic pulls for each of the uncertainties included in the CPT-violation $\nu_\mu$ and $\bar{\nu}_\mu$ disappearance fit. The pulls are displayed in units of $\sigma$ at the analysis best fit.

| Source of uncertainty | Uncertainty in | | | |
|---|---|---|---|---|
| | $\sin^2\theta_{23}$ $(10^{-3})$ | $\sin^2\bar{\theta}_{23}$ $(10^{-3})$ | $\Delta m^2_{32}$ $(10^{-6}\text{eV}^2)$ | $\Delta\bar{m}^2_{32}$ $(10^{-6}\text{eV}^2)$ |
| Absolute hadronic energy scale | +12 / -12 | +5.9 / -4 | +22 / -35 | +15 / -22 |
| Absolute muon energy scale | +2.3 / -2.4 | +1.8 / -0.76 | +9.4 / -12 | +8.2 / -11 |
| Cross sections and final-state interaction | +4.9 / -4.9 | +2.6 / -1.8 | +14 / -19 | +10 / -12 |
| Detector response | +2.8 / -2.8 | +1.8 / -1.3 | +3.5 / -5 | +8.1 / -8.5 |
| Neutrino Flux | +0.78 / -0.78 | +0.71 / -1 | +2.3 / -2.2 | +4.8 / -4.3 |
| Neutron Uncertainty | +6.6 / -6.9 | +5.1 / -3.5 | +3.9 / -13 | +8 / -20 |
| Normalisation | +2.4 / -2.5 | +0.73 / -0.61 | +2.6 / -5.1 | +1.4 / -1.8 |
| Relative Hadronic Energy Scale | +6.2 / -6.3 | +3.3 / -2.1 | +12 / -19 | +6.7 / -12 |
| Relative Muon Energy Scale | +1.3 / -1.3 | +0.93 / -1.1 | +1.7 / -0 | +4.6 / -2.8 |
| Statistical Uncertainty | +64 / -65 | +27 / -35 | +71 / -50 | +1.1e+02 / -1.1e+02 |
| Systematic Uncertainty | +15 / -16 | 8.6 / -6.1 | +28 / -42 | +23 / -34 |
| Total Uncertainty | +66 / -67 | +29 / -36 | +76 / -65 | +1.1e+02 / -1.1e+02 |

**Table 7.3:** Uncertainty sources and their impact in the measurement of the neutrino oscillation parameters $\sin^2\theta_{23}, \sin^2\bar{\theta}_{23}, \Delta m^2_{32}$ and $\Delta\bar{m}^2_{32}$. The quoted numbers correspond to the $1\sigma$ uncertainties on the parameter due to a single group of uncertainties.

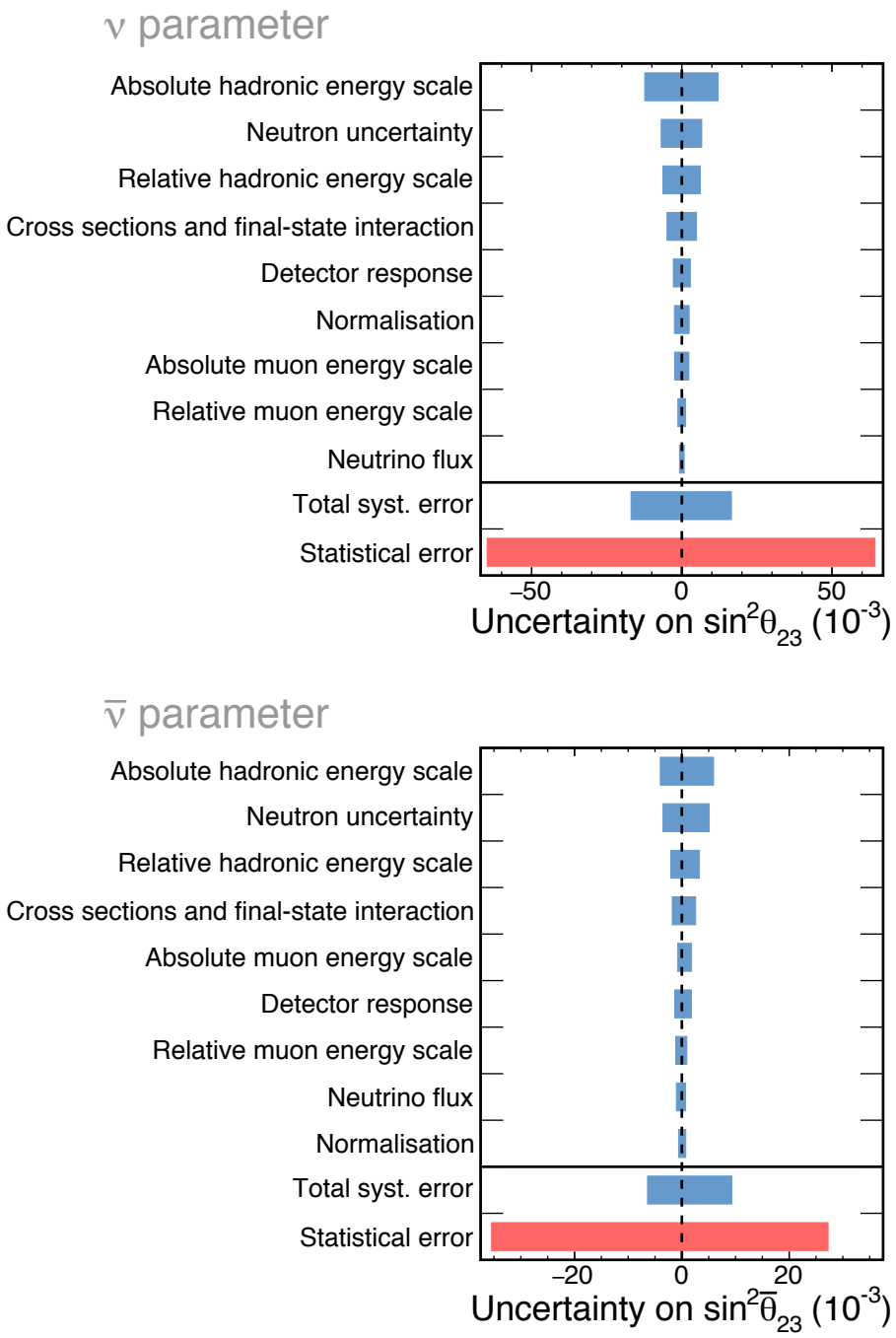


**Figure 7.13:** Illustration of the analysis uncertainty sources and the size of their impact in the measurement of the neutrino (top) and antineutrino (bottom) atmospheric mixing angle, $\sin^2\theta_{23}$ and $\sin^2\bar{\theta}_{23}$ respectively. The bars correspond to the 1 $\sigma$ uncertainties on the parameter due to a single group of uncertainties and are arranged in decreasing size from top to bottom.

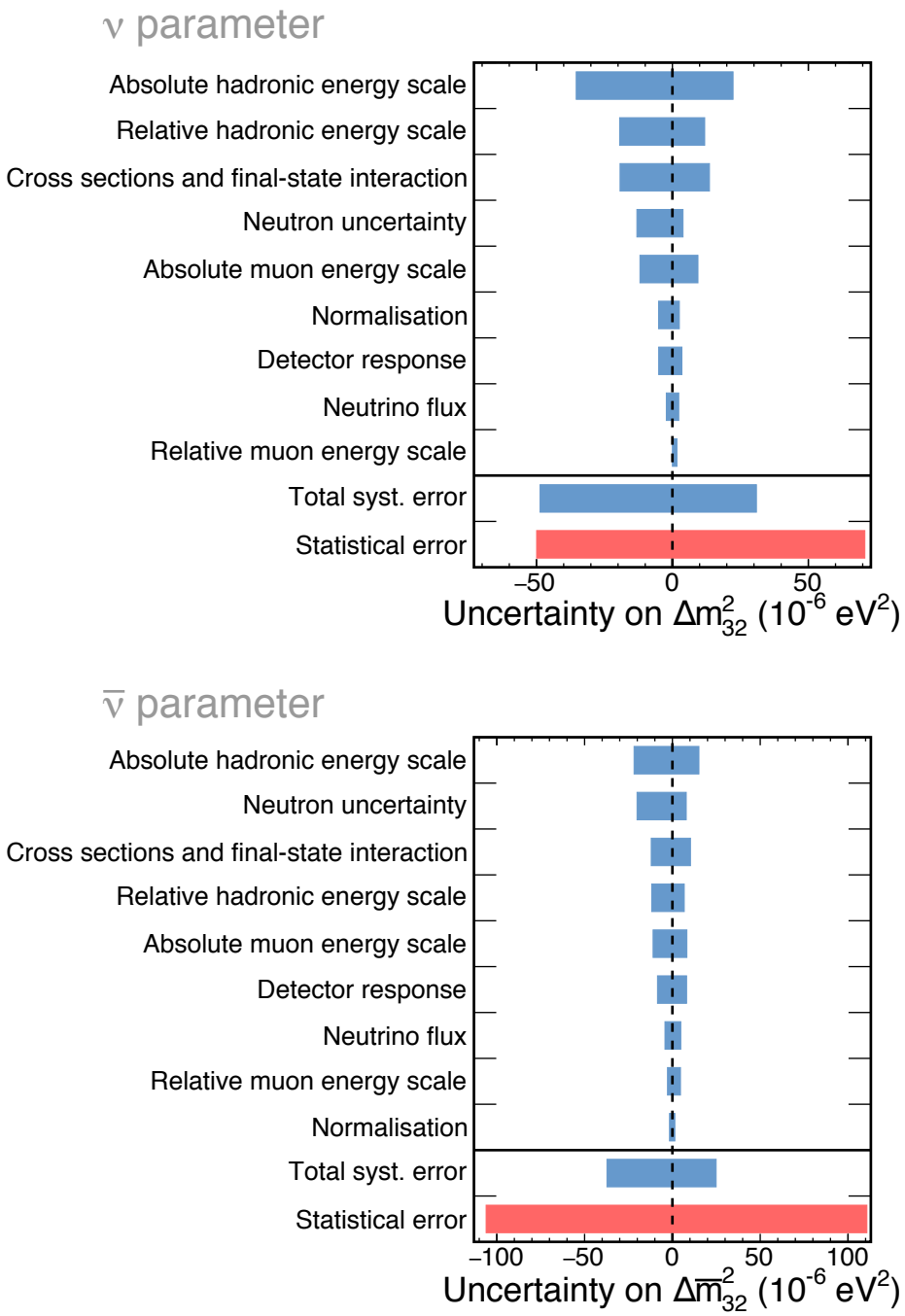


**Figure 7.14:** Illustration of the analysis uncertainty sources and the size of their impact in the measurement of the neutrino (top) and antineutrino (bottom) atmospheric mass splitting, $\Delta m^2_{32}$ and $\Delta \bar{m}^2_{32}$ respectively. The bars correspond to the 1 $\sigma$ uncertainties on the parameter due to a single group of uncertainties and are arranged in decreasing size from top to bottom.

## 7.3 Comparison with other experiments

Figure 7.15 shows a comparison between the normal hierarchy CPTv results from this thesis and an equivalent analysis from the T2K experiment [57]. T2K's best fit values are $\Delta m^2_{32} = 2.53^{+0.15}_{-0.13} \times 10^{-3}$ eV$^2$ and $\sin^2\theta_{23} = 0.51^{+0.08}_{-0.07}$ for neutrinos and $\Delta\bar{m}^2_{32} = 2.55^{+0.33}_{-0.27} \times 10^{-3}$ eV$^2$ and $\sin^2\bar{\theta}_{23} = 0.42^{+0.25}_{-0.07}$ for antineutrinos. The neutrino results from NOvA and T2K have the same $\sin^2\theta_{23}$ best fit and are consistent with maximal mixing. The CPTv antineutrino results both have a degenerate best fit for $\bar{\theta}_{23}$ and are in agreement at 1 $\sigma$. The CPTv fit prefers lower values of $\Delta m^2_{32}$ and $\Delta\bar{m}^2_{32}$ than T2K but are also consistent at the 1 $\sigma$ level. However, NOvA's measurements are more precise than T2K's. The uncertainties on $\Delta m^2_{32}(\Delta\bar{m}^2_{32})$ are about a factor of two smaller than T2K's. Thus the CPTv results from this thesis yields the best measurement of $\Delta m^2_{32}$. NOvA's uncertainties on $\sin^2\theta_{23}(\sin^2\bar{\theta}_{23})$ are only marginally smaller than T2K's. The Daya Bay experiment has measured the disappearance of $\bar{\nu}_e$ produced at nuclear reactors and yield a best fit of the antineutrino mass splitting at $\Delta\bar{m}^2_{32} = 2.471^{+0.068}_{-0.070} \times 10^{-3}$ eV$^2$ [35]. The uncertainties on that measurement are a factor of two smaller than NOvA's. Figure 7.15 also displays the 1 $\sigma$ range for the value of $\Delta\bar{m}^2_{32}$ from Daya Bay's measurement.

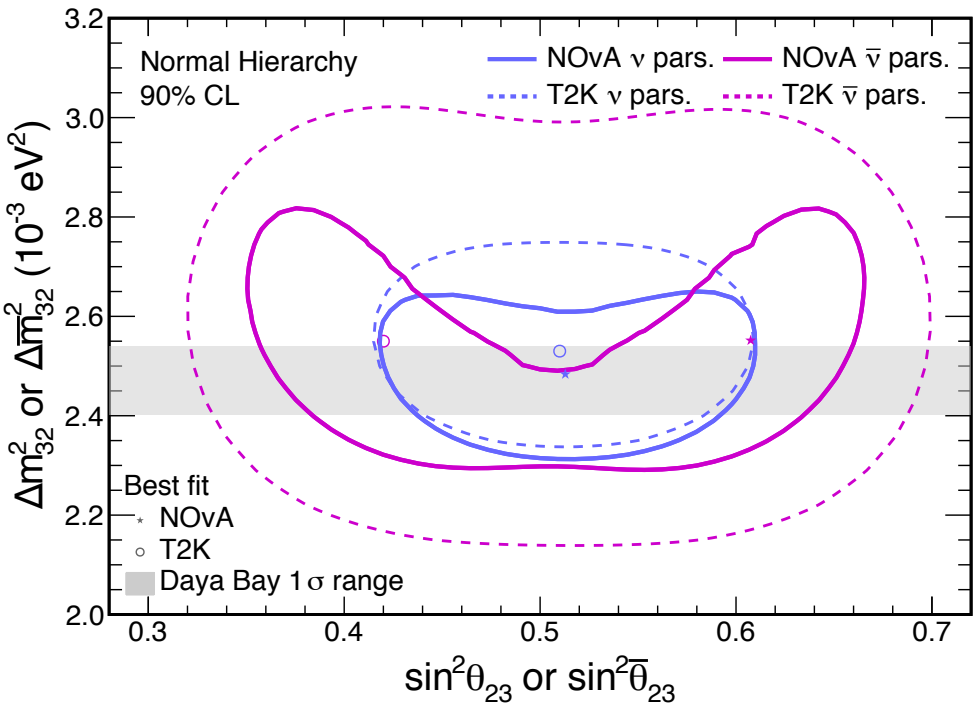


**Figure 7.15:** Constraints on the $\nu$ and $\bar{\nu}$ oscillation parameters from the NOvA CPTv analysis compared with T2K. The 90% confidence regions of the mixing angle and the mass squared difference are displayed in solid blue for the neutrino and in solid purple for the antineutrino parameters. The latest equivalent results from the T2K experiment [57] are plotted with dashed lines for reference. The best fit points of the CPTv analysis and T2K are represented by the stars and circles, respectively. The 1 $\sigma$ C.L. from Daya Bay's measurement of $\Delta\bar{m}^2_{32}$ [35] is displayed by the gray region.

# Chapter 8

# Conclusions

Neutrino and antineutrino data from the NOvA experiment has been analysed in this thesis to extract the atmospheric-scale mixing angle and mass splitting parameters. The data was collected between 2014 and 2019, during which time the NOvA detectors were exposed to $8.85 \times 10^{20}$ and $12.33 \times 10^{20}$ POT for the production of the $\nu_\mu$ and $\bar{\nu}_\mu$ beams respectively.

Two analyses of $\nu_\mu$ and $\bar{\nu}_\mu$ disappearance were performed. One analysis assumed identical neutrino and antineutrino oscillation parameters in the standard three flavour model. In the normal hierarchy, this analysis yields best fits at $\Delta m^2_{32} = 2.48^{+0.08}_{-0.06} \times 10^{-3}$ eV$^2$ and $\sin^2\theta_{23} = 0.57$ in the range $[0.53, 0.59]$ and $[0.44, 0.48]$ allowed at 1 $\sigma$. A disappearance analysis where neutrinos and antineutrinos are allowed to oscillate independently was also performed to constrain both the neutrino oscillation parameters $\sin^2\theta_{23}$ and $\Delta m^2_{32}$, and the antineutrino parameters $\sin^2\bar{\theta}_{23}$ and $\Delta\bar{m}^2_{32}$. The presence of the intrinsic wrong sign beam contamination, which is the $\bar{\nu}_\mu$ in the $\nu_\mu$ beam and vice versa, showed only a small impact on the measurement of $\Delta\bar{m}^2_{32}$ and $\sin^2\bar{\theta}_{23}$ and almost none on the neutrino parameters. Furthermore, the uncertainty on the size of the wrong sign component was shown to have a negligible impact on the results. The best fits to data for the mass splittings are

$$\begin{aligned} \Delta m^2_{32} &= 2.48^{+0.07}_{-0.09} \times 10^{-3} \text{ eV}^2 \text{ and} \\ \Delta\bar{m}^2_{32} &= 2.55^{+0.12}_{-0.13} \times 10^{-3} \text{ eV}^2. \end{aligned}$$

The results for the mixing angles are

$$\begin{aligned} \sin^2\theta_{23} &= 0.51 \in [0.45, 0.57] \text{ and} \\ \sin^2\bar{\theta}_{23} &= 0.41 \in [0.38, 0.45] \cup 0.61 \in [0.57, 0.64], \end{aligned}$$

where the quoted intervals are the $1\sigma$ ranges for the $\sin^2\theta_{23}$ best fit and the two statistically degenerate best fits for $\sin^2\bar{\theta}_{23}$. No evidence of a significant difference between the neutrino and antineutrino atmospheric scale oscillation parameters was found.

These results are consistent with the equivalent analysis from the accelerator based T2K experiment [57], which also measures $\nu_\mu$ and $\bar{\nu}_\mu$ disappearance. NOvA's uncertainties on $\Delta m^2_{32}$ and $\Delta \bar{m}^2_{32}$ are about a factor of two smaller than T2K's. The uncertainties on $\sin^2\theta_{23}$ and $\sin^2\bar{\theta}_{23}$ are only marginaly smaller than T2K's. The Daya Bay experiment has measured the disappearance of $\bar{\nu}_e$ from nuclear reactors and currently has the best measurement of $\Delta\bar{m}^2_{32}$=$2.471^{+0.068}_{-0.070}$ [35] but is not sensitive to $\bar{\theta}_{23}$. The uncertainty on that measurement is about a factor of two smaller than that reported in this thesis. The consistency between measurements done using $\bar{\nu}_e$ and $\bar{\nu}_\mu$ disappearance further supports the standard three flavour oscillation model. Since there is no measurement of $\Delta m^2_{32}$ other than with $\nu_\mu$ disappearance, this thesis contains the best current measurement of $\Delta m^2_{32}$ using just neutrinos.

Over the next five years, NOvA is expected to quadruple and triple the $\nu_\mu$ and $\bar{\nu}_\mu$ beam exposure, respectively, for a total of about $72 \times 10^{20}$ POT. In the near future, NOvA's increased exposure is likely to significantly improve the results of this thesis. Next generation experiments such as the reactor experiment JUNO [111] that is expected to start collecting data in 2021 will improve these measurements. In the longer term, accelerator based experiments such as DUNE [52] and Hyper Kamiokande [112], which are expected to start operations around 2026, will significantly improve these measurements.

# Appendix A

# Computation of FD predictions

This appendix describes the ND decomposition and extrapolation procedures for the computation of predictions at the NOvA FD.

## A.1 Decomposition and Extrapolation

The decomposition procedure assigns fractions of the selected ND data events to the neutrino flavour components in the simulation. The disappearance analysis uses the `ana::NumuDecomp` class from CAFAna for this purpose. In this procedure, the reconstructed energy spectrum of selected ND $\nu_\mu$ CC events is decomposed into $\nu_\mu$ (and $\bar{\nu}_\mu$), $\nu_e$ (and $\bar{\nu}_e$) and NC components. The background fraction from the $\nu_e$, $\bar{\nu}_e$ and NC components do not significantly contribute to the flux. Thus, it is assumed that any discrepancy between data and simulation is due to a mis-estimation of the $\nu_\mu$ and $\bar{\nu}_\mu$ components and the ND data measurements are used to correct the expectation. Explicitly,

$$\overset{(-)}{\nu}_\mu \text{ CC corrected data} = (\text{data} - \text{not } \nu_\mu \text{ CC}) \frac{\overset{(-)}{\nu}_\mu}{\nu_\mu + \bar{\nu}_\mu} \tag{A.1}$$

where *data* refers to the corrected ND prediction. The decomposition returns terms of the form $N(E_i^{reco})_{ND\ data,\alpha}$, which are input to the extrapolation. The decomposed ND data is indicated by *data*, where $\alpha \in \{\nu_\mu, \bar{\nu}_\mu\}$ and $i = 1, ..., 19$ runs over the $\nu_\mu$ CC energy bins. Figure A.1 shows a diagram summarizing the beam decomposition procedure.

Following the ND decomposition, the disappearance analysis uses the `Numu` extrapolation object from the `ModularExtrap` CAFAna class [113]. The first step computes corrected ND simulations in true energy, $N(E_i^{true})_{ND\ sim,\alpha}$, by translating the decomposed data into bins of true energy via a *reconstructed-to-true energy* matrix $M_{ij}^{ND}$. This matrix is a histogram of reconstructed vs. truth energy created from simulation. The predicted count at the $i-$th truth energy bin is calculated from the sum of all the $i-th$ row entries following a re-weight by data/MC ratios in reconstructed energy:

$$N(E_i^{true})_{ND\ sim,\alpha} = \Sigma_j M_{ij}^{ND} \frac{N(E_j^{reco})_{ND\ data,\alpha}}{N(E_j^{reco})_{ND\ MC,\alpha}} \tag{A.2}$$

A similar procedure is followed to convert true to reconstructed energy spectra at the FD. This is achieved via a *true-to-reconstructed energy* matrix $M_{ij}^{FD}$, which is also constructed from MC files and is corrected by data/MC ratios in true energy[1]:

$$M_{ij}^{FD*} = \Sigma_j M_{ij}^{FD} \frac{N(E_j^{true})_{ND\ sim,\alpha}}{N(E_j^{true})_{ND\ MC,\alpha}} \tag{A.3}$$

Figure A.2 shows a the diagram summarizing the modular extrapolation procedure.

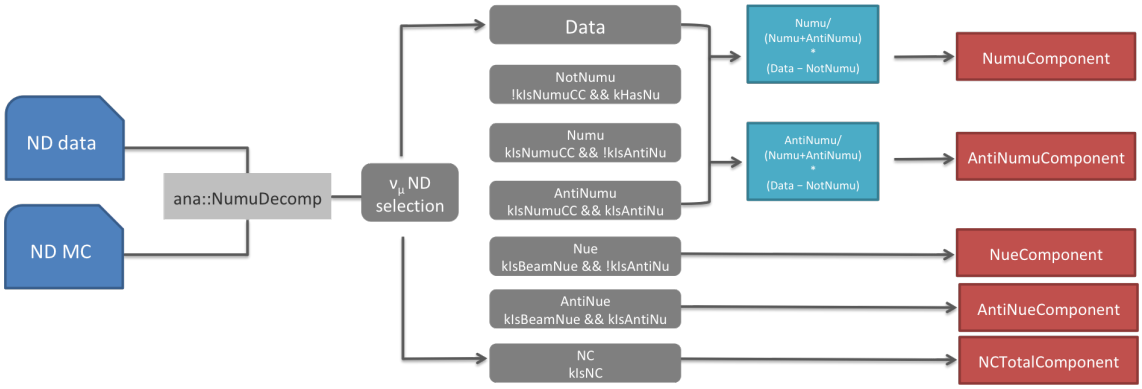


**Figure A.1:** Flow chart of the ND decomposition technique for NOvA's disappearance analysis for which the `ana::NumuDecomp` class in the CAFAna framework is used. Input files, selection cuts, computations and outputs are represented in dark blue, gray, light blue and red, respectively. The decomposition takes real and simulated data and applies the $\nu_\mu$ CC ND selection to each sample. The MC is additionally applied a truth selection cut to separate the events by interaction type. The selected data is used to correct the $\nu_\mu$ (`NumuComponent`) and $\bar{\nu}_\mu$ (`AntiNumuComponent`) components.

## A.2 Extrapolated prediction

Each row of reconstructed energy in the corrected $M_{ij}^{FD*}$ matrix, is projected by a FD MC spectra in true energy with event counts of the form $F(E_i^{true})_{MC,\alpha\to\alpha}$, $\alpha \in \{\nu_\mu, \bar{\nu}_\mu\}$. The sum of the projections is assigned to the reconstructed energy bins and FD spectra are constructed as a result. These spectra are weighted with oscillation probabilities $P(E, L, \psi_k)_{\alpha\to\alpha}$, which are a function of the neutrino energy $E$, the distance $L$ traveled by the neutrinos and the oscillation parameters $\vartheta_k$

$$F(E_i^{reco})_{MC,\alpha\to\alpha} = \Sigma_j M_{ij}^{FD*} F(E_j^{true})_{MC,\alpha} \times P(E, L, \vartheta_k)_{\alpha\to\alpha} \tag{A.4}$$

Oscillation probability weights are directly applied to the flux and tau-swap files to compute the expectation of $\nu_e, \bar{\nu}_e, \nu_\tau, \bar{\nu}_\tau$ and NC events at the FD. The standard NOvA oscillation analysis use the same values of $\vartheta_k$ for neutrinos and antineutrinos to compute the probability weights. In

[1]Note that in this case, *data* refers to a the corrected ND prediction $N(E_i^{true})_{sim,\alpha}$.

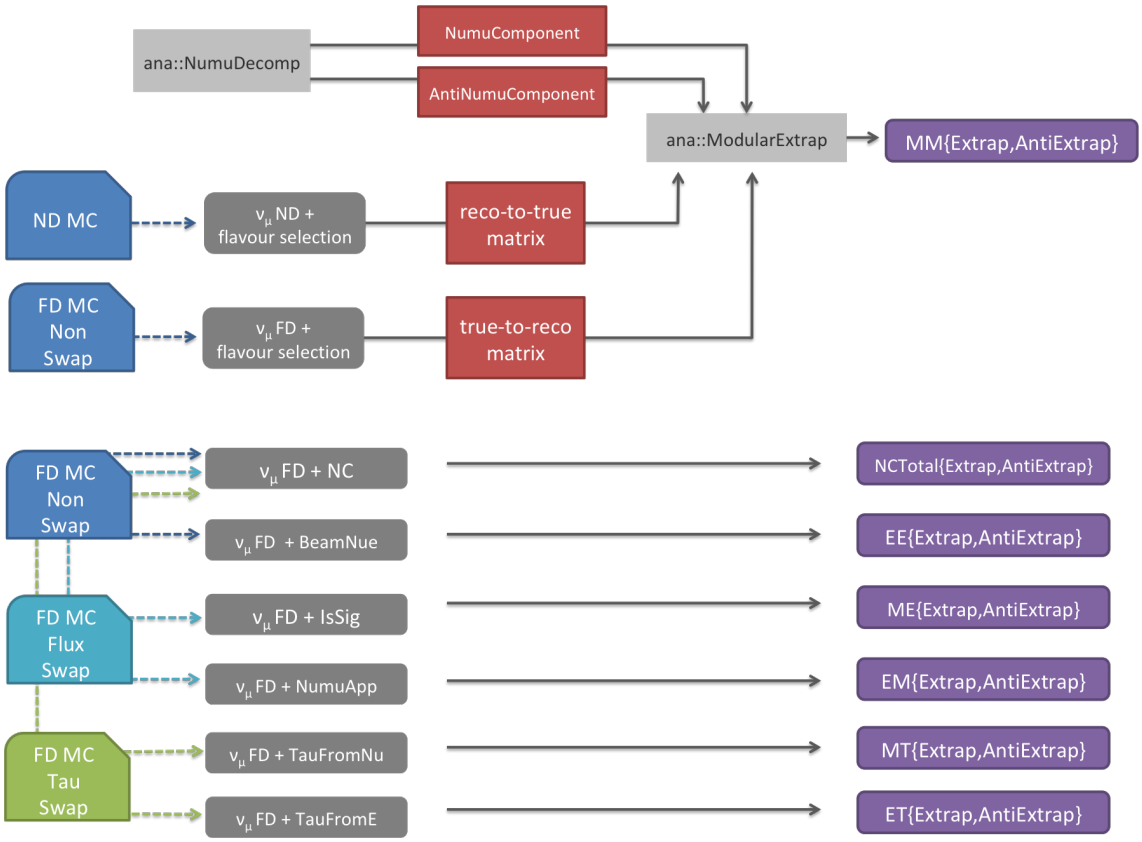


**Figure A.2:** Diagram summarizing the extrapolation for the $\nu_\mu$ and $\bar{\nu}_\mu$ disappearance analysis. The `ModularExtrapolation` class in the CAFAna framework is used for this extrapolation. The procedure takes the decomposition results and calculates the matrices (red squared boxes) to convert reconstructed to true energy, and vice versa, for the estimation of the $\nu_\mu$ (`MMExtrap`) and $\bar{\nu}_\mu$ (`MMAntiExtrap`) components at the FD. The gray boxes represent a selection cut being applied to the input ND and FD files. The purple boxes represent output FD spectra with a label format XY{Extrap,Antiextrap}, where $X, Y \in \{M = \mu, E = e, T = \tau\}$. This means that a XY pair represents the $X \to Y$ oscillation. *Extrap* refers to particles and *Antiextrap* refers to antiparticles.

other words, $\vartheta_k = \bar{\vartheta}_k$. For the main analysis presented in this thesis the values of the oscillation parameters are instead allowed to differ between neutrinos and antineutrinos.

# Appendix B

# FD predicted energy spectra with no extrapolation

This appendix follows from Section § 6.3. FD predicted energy spectra of selected $\nu_\mu$ and $\bar{\nu}_\mu$ CC events are presented without ND constrains, or *without extrapolation*. Three sets of parameter values are chosen to oscillate the $\nu$ and $\bar{\nu}$ either with the same or with different values. The values used are from the CPTc normal hierarchy best fits summarised in 5.5 and the three oscillation combinations are as follow

- $\nu$ and $\bar{\nu}$ oscillate with the FHC+RHC best fit,
- $\nu$ oscillate with the FHC only best fit, $\bar{\nu}$ oscillate with the RHC only best fit,
- $\nu$ oscillate with the RHC only best fit, $\bar{\nu}$ oscillate with the FHC only best fit.

Figures B.1 and B.2 show the simulated reconstructed energy spectra at the FD, of selected $\nu_\mu$ and $\bar{\nu}_\mu$ CC events from the FHC and RHC beam modes without extrapolation and assuming the above oscillation scenarios. The $1\sigma$ systematic range around the total simulation corresponds to the $1\sigma$ uncertainty from the calibration systematic. Figures B.3 and B.4 contain the analogous plots with the $1\sigma$ uncertainty band from the wrong sign systematic.

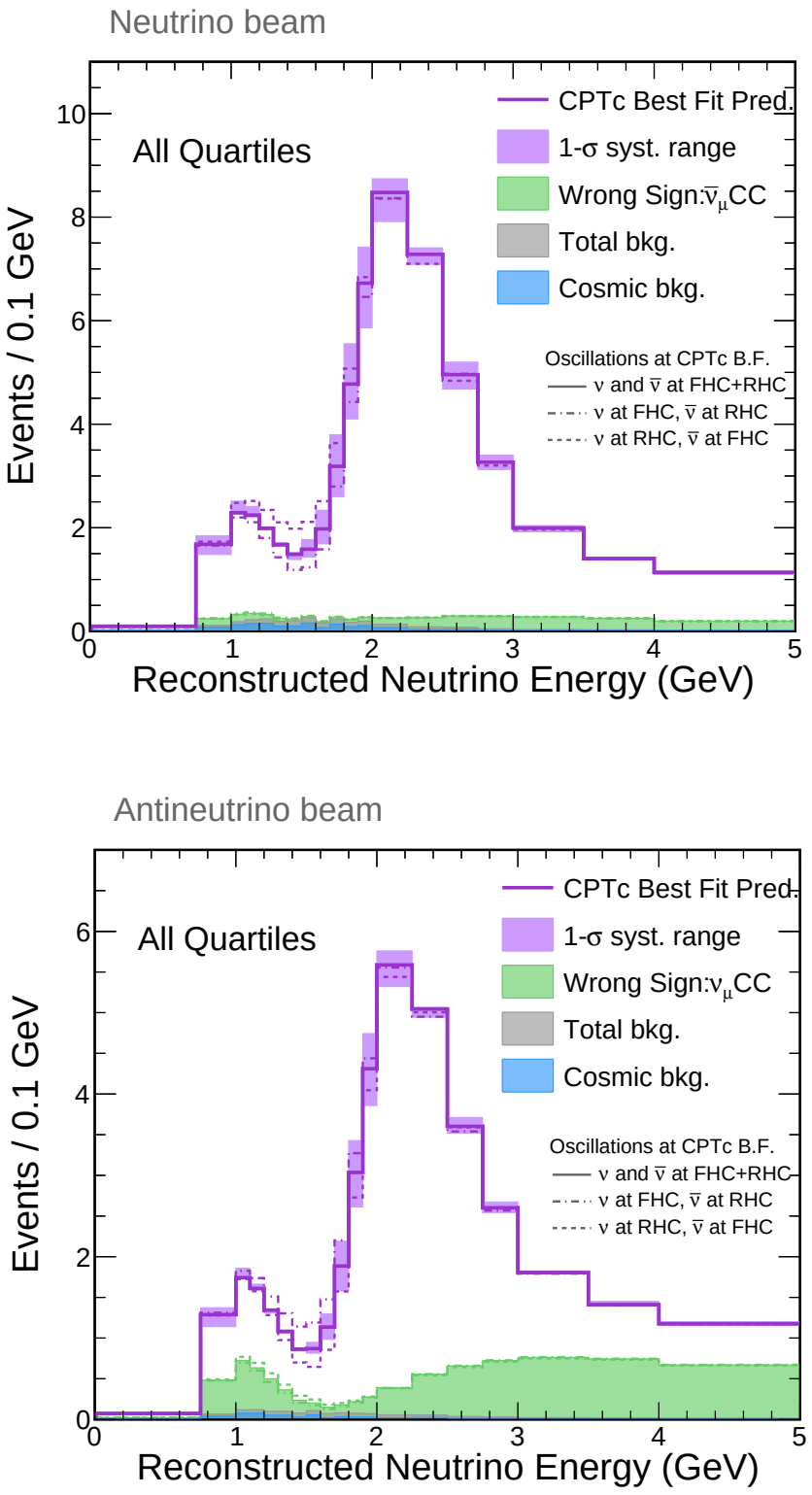


**Figure B.1:** Simulated FD reconstructed energy spectra, without ND data constraints, from selected $\nu_\mu$ and $\bar{\nu}_\mu$ CC events in the FHC (top) and RHC (bottom) beam modes, for the combination of all energy resolution bins. The total number of predicted events passing this selection are represented in the purple histogram, where the shadowed regions is the $1\sigma$ **calibration only error band**. The solid distributions assume that both $\nu$ and $\bar{\nu}$ oscillate with the FHC+RHC CPTc best fit values. The dashed lines corresponds to $\nu$ oscillations with the FHC best fit and $\bar{\nu}$ oscillations with the RHC best fit, and the inverse case for the dotted lines.

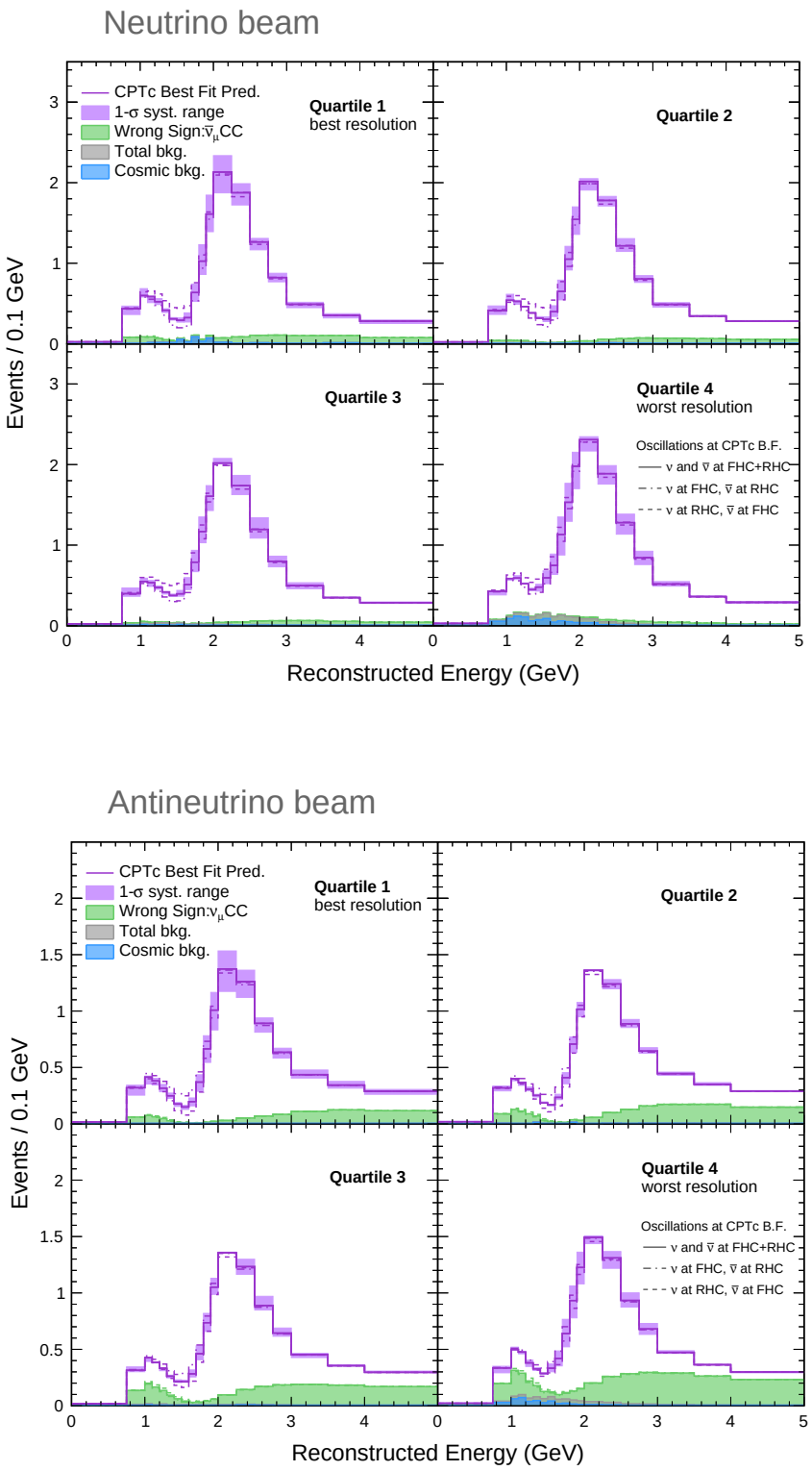


**Figure B.2:** Simulated FD reconstructed energy spectra, without ND data constraints, from selected $\nu_\mu$ and $\bar{\nu}_\mu$ CC events in the FHC (top) and RHC (bottom) beam modes per energy resolution bins. The total number of predicted events passing this selection are represented in the purple histogram, where the shadowed regions is the $1\sigma$ **calibration only error band**. The solid distributions assume that both $\nu$ and $\bar{\nu}$ oscillate with the FHC+RHC CPTc best fit values. The dashed lines corresponds to $\nu$ oscillations with the FHC best fit and $\bar{\nu}$ oscillations with the RHC best fit, and the inverse case for the dotted lines.

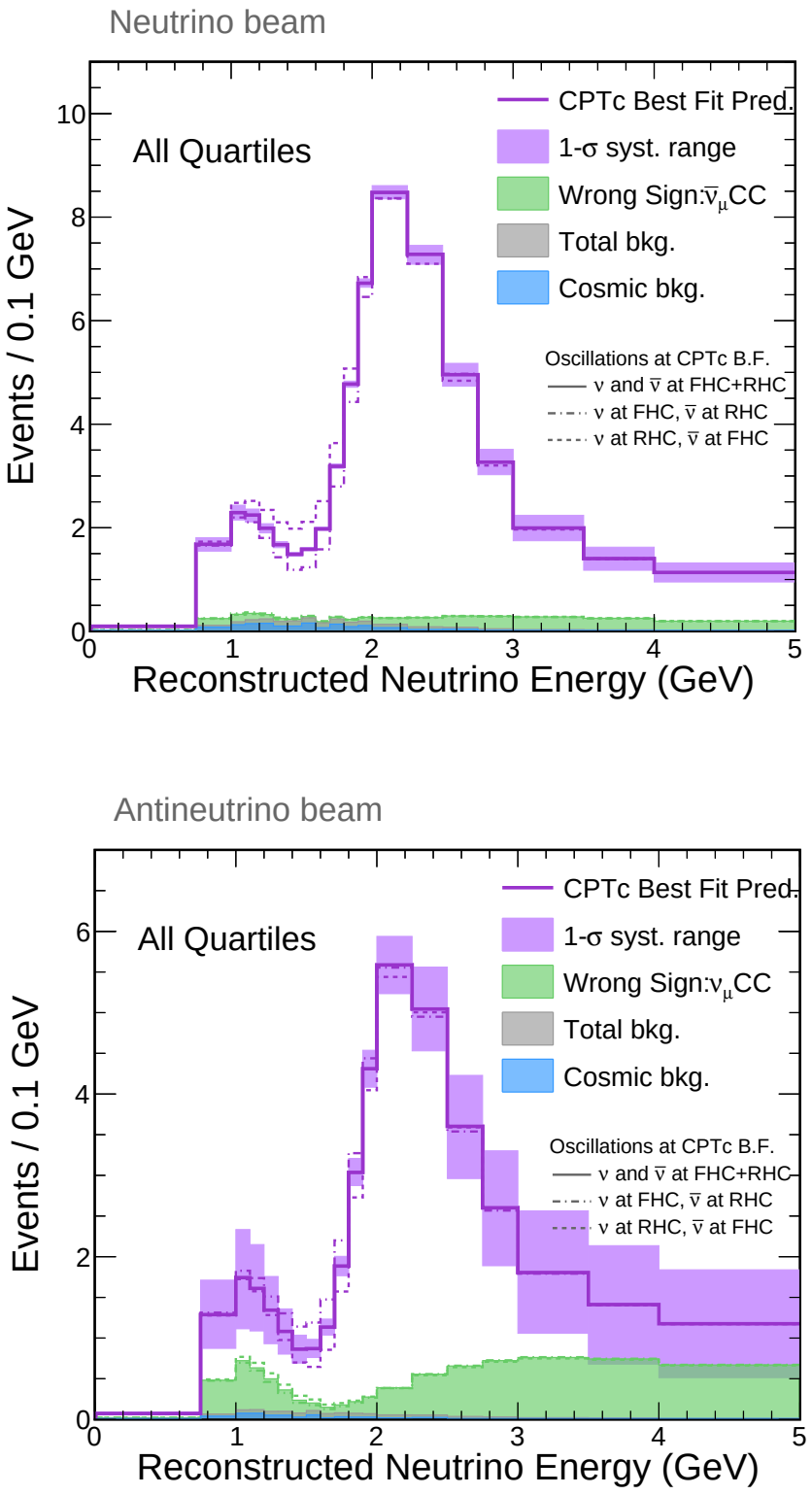


**Figure B.3:** Simulated FD reconstructed energy spectra, without ND data constraints, from selected $\nu_\mu$ and $\bar{\nu}_\mu$ CC events in the FHC (top) and RHC (bottom) beam modes, for the combination of all energy resolution bins. The total number of predicted events passing this selection are represented in the purple histogram, where the shadowed regions is the $1\sigma$ **100% wrong sign scale only error band**. The solid distributions assume that both $\nu$ and $\bar{\nu}$ oscillate with the FHC+RHC CPTc best fit values. The dashed lines corresponds to $\nu$ oscillations with the FHC best fit and $\bar{\nu}$ oscillations with the RHC best fit, and the inverse case for the dotted lines.

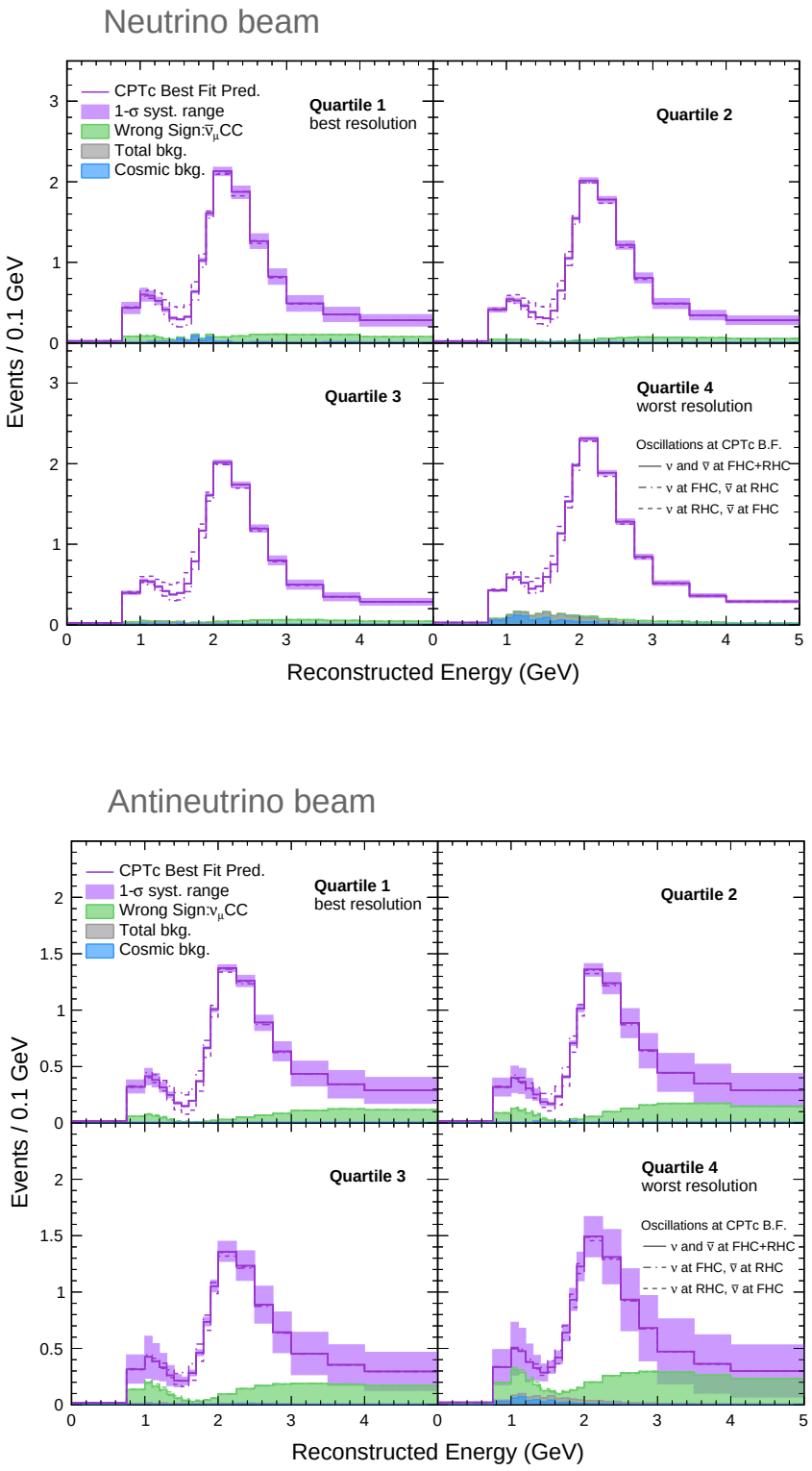


**Figure B.4:** Simulated FD reconstructed energy spectra, without ND data constraints, from selected $\nu_\mu$ and $\bar{\nu}_\mu$ CC events in the FHC (top) and RHC (bottom) beam modes per energy resolution bins. The total number of predicted events passing this selection are represented in the purple histogram, where the shadowed regions is the $1\sigma$ **100% wrong sign scale only error band**. The solid distributions assume that both $\nu$ and $\bar{\nu}$ oscillate with the FHC+RHC CPTc best fit values. The dashed lines corresponds to $\nu$ oscillations with the FHC best fit and $\bar{\nu}$ oscillations with the RHC best fit, and the inverse case for the dotted lines.

# Appendix C

# Tables with systematically shifted simulations

The tables in this appendix show the integral of nominal and systematically shifted simulations, denoted as $\eta_{nom}$ and $\eta_{shift}$, respectively. The listed numbers correspond to the systematic uncertainties accounted for in the analysis of this thesis, plus the number for the 100% wrong sign scale tested in Section § 6.3. The simulations are split into the $\nu_\mu$, $\bar{\nu}_\mu$ and background components.

The tables in Sections appendix C.1 and appendix C.2 show the information for the ND simulation and predictions at the FD, respectively. A single table presents the simulated number for the FHC and RHC beams, but they are separated by individual quartiles. A table without the split per quartiles is also shown. However, this table is only representative of the combination of all the quartiles but does not exactly correspond to sum of them. This is due to the extrapolation technique which yields different results when it is performed with or without the separation per hadronic energy fractions.

In the tables, the numbers in parenthesis correspond to the Figure of Merit (FOM) defined as

$$\frac{\eta_{dif}}{\eta_{mean}} = 2\,\frac{\eta_{shift} - \eta_{nom}}{\eta_{shift} + \eta_{nom}} \tag{C.1a}$$

The FOM helps identify the systematic uncertainties that have a large impact in the simulation. Some cells in the tables are highlighted according to the following convention:

- Green: $|FOM| = [0.05, 0.10)$
- Yellow: $|FOM| = [0.10, 0.15)$
- Red: $|FOM| > 0.15$

# C.1 Near Detector

**All quartiles**

| | | Neutrino Beam | | | Antineutrino Beam | | |
|---|---|---|---|---|---|---|---|
| Prediction | Shift | Right Sign ($\nu_\mu$) | Wrong Sign ($\bar{\nu}_\mu$) | Background | Right Sign ($\bar{\nu}_\mu$) | Wrong Sign ($\nu_\mu$) | Background |
| Nominal | - | 1838093.862 | 53201.658 | 6285.528 | 346585.279 | 41200.610 | 1049.198 |
| MECEnuShapeNu | +1 $\sigma$ | 1916594.843 (0.042) | 53201.658 (0.000) | 6285.809 (0.000) | 346585.279 (0.000) | 43201.913 (0.047) | 1049.231(0.000) |
| | -1 $\sigma$ | 1759592.880 (0.000) | 53201.658 (0.000) | 6285.247 (-0.000) | 346585.279 (0.000) | 39199.307 (-0.050) | 1049.165 (-0.000) |
| MECEnuShapeAntiNu | +1 $\sigma$ | 1838093.862 (0.000) | 55692.048 (0.046) | 6285.596 (0.000) | 361758.593 (0.043) | 41200.610 (0.000) | 1049.249(0.000) |
| | -1 $\sigma$ | 1838093.862 (-0.045) | 50711.268 (-0.048) | 6285.460 (-0.000) | 331411.965 (-0.045) | 41200.610 (0.000) | 1049.147 (-0.000) |
| MECShape2018Nu | +1 $\sigma$ | 1844088.066 (0.003) | 53201.658 (0.000) | 6286.148 (0.000) | 346585.279 (0.000) | 41333.747 (0.003) | 1049.244(0.000) |
| | -1 $\sigma$ | 1758349.083 (0.000) | 53201.658 (0.000) | 6280.725 (-0.001) | 346585.279 (0.000) | 39204.406 (-0.050) | 1048.536 (-0.001) |
| MECShape2018AntiNu | +1 $\sigma$ | 1838093.862 (0.000) | 51342.668 (-0.036) | 6285.995 (0.000) | 333242.167 (-0.039) | 41200.610 (0.000) | 1050.075(0.001) |
| | -1 $\sigma$ | 1838093.862 (0.001) | 53215.561 (0.000) | 6285.332 (-0.000) | 346980.222 (0.001) | 41200.610 (0.000) | 1048.549 (-0.001) |
| MECInitStateNPFracNu | +1 $\sigma$ | 1861326.668 (0.013) | 53201.658 (0.000) | 6286.064 (0.000) | 346585.279 (0.000) | 41734.883 (0.013) | 1049.332(0.000) |
| | -1 $\sigma$ | 1814861.055 (0.000) | 53201.658 (0.000) | 6284.991 (-0.000) | 346585.279 (0.000) | 40666.337 (-0.013) | 1049.064 (-0.000) |
| MECInitStateNPFracAntiNu | +1 $\sigma$ | 1838093.862 (0.000) | 53825.526 (0.012) | 6285.575 (0.000) | 351048.837 (0.013) | 41200.610 (0.000) | 1049.168(-0.000) |
| | -1 $\sigma$ | 1838093.862 (-0.013) | 52577.790 (-0.012) | 6285.481 (-0.000) | 342121.722 (-0.013) | 41200.610 (0.000) | 1049.228 (0.000) |
| MaCCQE_reduced_2018 | +1 $\sigma$ | 1854196.373 (0.009) | 53662.621 (0.009) | 6285.692 (0.000) | 349617.514 (0.009) | 41576.500 (0.009) | 1049.223(0.000) |
| | -1 $\sigma$ | 1822218.421 (-0.009) | 52748.198 (-0.009) | 6285.369 (-0.000) | 343602.337 (-0.009) | 40829.752 (-0.009) | 1049.173 (-0.000) |
| RPAShapeRES2018 | +1 $\sigma$ | 1973549.172 (0.071) | 57300.661 (0.074) | 6285.707 (0.000) | 376117.862 (0.082) | 43960.930 (0.065) | 1049.309(0.000) |
| | -1 $\sigma$ | 1838093.862 (0.000) | 53201.658 (0.000) | 6285.528 (0.000) | 346585.279 (0.000) | 41200.610 (0.000) | 1049.198 (0.000) |
| RPAShapeenh2018 | +1 $\sigma$ | 1864021.179 (0.014) | 54081.414 (0.016) | 6285.671 (0.000) | 352108.427 (0.016) | 41811.596 (0.015) | 1049.265(0.000) |
| | -1 $\sigma$ | 1816351.782 (-0.015) | 52396.199 (-0.015) | 6285.394 (-0.000) | 341555.653 (-0.015) | 40680.701 (-0.013) | 1049.145 (-0.000) |
| COHCCScale2018 | +1 $\sigma$ | 1844815.862 (0.004) | 53534.489 (0.006) | 6285.904 (0.000) | 348769.833 (0.006) | 41347.469 (0.004) | 1049.245(0.000) |
| | -1 $\sigma$ | 1831371.862 (-0.006) | 52868.827 (-0.006) | 6285.151 (-0.000) | 344400.726 (-0.006) | 41053.751 (-0.004) | 1049.151 (-0.000) |
| COHNCScale2018 | +1 $\sigma$ | 1838093.862 (0.000) | 53201.658 (0.000) | 6285.916 (0.000) | 346585.279 (0.000) | 41200.610 (0.000) | 1049.288(0.000) |
| | -1 $\sigma$ | 1838093.862 (0.000) | 53201.658 (0.000) | 6285.140 (-0.000) | 346585.279 (0.000) | 41200.610 (0.000) | 1049.108 (-0.000) |
| MaCCRES | +1 $\sigma$ | 1962327.763 (0.065) | 55714.609 (0.046) | 6292.641 (0.001) | 364251.506 (0.050) | 43492.189 (0.054) | 1050.049(0.001) |
| | -1 $\sigma$ | 1699716.478 (-0.052) | 50689.365 (-0.048) | 6280.092 (-0.001) | 328961.315 (-0.052) | 38611.035 (-0.065) | 1048.690 (-0.000) |
| MaNCRES | +1 $\sigma$ | 1838093.862 (0.000) | 53201.658 (0.000) | 6982.245 (0.105) | 346585.279 (0.000) | 41200.610 (0.000) | 1208.962(0.141) |
| | -1 $\sigma$ | 1838093.862 (0.000) | 53201.658 (0.000) | 5729.914 (-0.092) | 346585.279 (0.000) | 41200.610 (0.000) | 938.192 (-0.112) |
| MvCCRES | +1 $\sigma$ | 1908530.009 (0.038) | 54038.243 (0.016) | 6289.306 (0.001) | 352420.121 (0.017) | 42485.235 (0.031) | 1049.588(0.000) |
| | -1 $\sigma$ | 1771199.889 (-0.012) | 52583.965 (-0.012) | 6282.505 (-0.000) | 342307.920 (-0.012) | 39970.996 (-0.030) | 1048.942 (-0.000) |
| CCQEPauliSupViaKF | +1 $\sigma$ | 1806348.294 (-0.017) | 51751.182 (-0.028) | 6290.308 (0.001) | 337854.856 (-0.026) | 40436.283 (-0.019) | 1049.389(0.000) |
| | -1 $\sigma$ | 1868016.952 (0.025) | 54733.356 (0.028) | 6290.478 (0.001) | 355530.126 (0.025) | 41931.510 (0.018) | 1049.422 (0.000) |
| FrElas_N | +1 $\sigma$ | 1840136.526 (0.001) | 53079.806 (-0.002) | 6274.274 (-0.002) | 346431.850 (-0.000) | 41245.718 (0.001) | 1044.038(-0.005) |
| | -1 $\sigma$ | 1836030.355 (0.000) | 53293.315 (0.002) | 6306.461 (0.003) | 346692.458 (0.000) | 41153.032 (-0.001) | 1054.782 (0.005) |
| FrCEx_N | +1 $\sigma$ | 1837081.439 (-0.001) | 53246.698 (0.001) | 6289.106 (0.001) | 346735.484 (0.000) | 41179.728 (-0.001) | 1050.204(0.001) |
| | -1 $\sigma$ | 1839095.749 (-0.001) | 53143.938 (-0.001) | 6291.801 (0.001) | 346409.782 (-0.001) | 41220.145 (0.000) | 1048.618 (-0.001) |
| FrAbs_N | +1 $\sigma$ | 1837715.606 (-0.000) | 53217.465 (0.000) | 6304.204 (0.003) | 346516.790 (-0.000) | 41197.785 (-0.000) | 1052.024(0.003) |
| | -1 $\sigma$ | 1838503.570 (0.000) | 53166.199 (-0.001) | 6276.567 (-0.001) | 346626.675 (0.000) | 41204.032 (0.000) | 1046.779 (-0.002) |
| FrInel_pi | +1 $\sigma$ | 1835360.861 (-0.001) | 53157.437 (-0.001) | 6389.810 (0.016) | 346107.196 (-0.001) | 41142.397 (-0.001) | 1065.003(0.015) |
| | -1 $\sigma$ | 1840811.299 (0.001) | 53236.726 (0.001) | 6188.110 (-0.016) | 347050.706 (0.001) | 41258.476 (0.001) | 1034.657 (-0.014) |
| FormZone | +1 $\sigma$ | 1851710.940 (0.007) | 53510.651 (0.006) | 6678.629 (0.061) | 348242.369 (0.005) | 41580.999 (0.009) | 1118.942(0.064) |
| | -1 $\sigma$ | 1818495.826 (-0.006) | 52759.342 (-0.008) | 5657.804 (-0.105) | 344560.350 (-0.006) | 40552.525 (-0.016) | 936.248 (-0.114) |

**All quartiles**

| | | Neutrino Beam | | | Antineutrino Beam | | |
|---|---|---|---|---|---|---|---|
| Prediction | Shift | Right Sign ($\nu_\mu$) | Wrong Sign ($\bar{\nu}_\mu$) | Background | Right Sign ($\bar{\nu}_\mu$) | Wrong Sign ($\nu_\mu$) | Background |
| Nominal | - | 1838093.862 | 53201.658 | 6285.528 | 346585.279 | 41200.610 | 1049.198 |
| genie_small_pc00 | +1 $\sigma$ | 1857380.565 (0.010) | 53741.384 (0.010) | 7495.108 (0.176) | 349765.387 (0.009) | 41580.961 (0.009) | 1156.455(0.097) |
| | -1 $\sigma$ | 1818835.306 (-0.009) | 52642.470 (-0.011) | 5085.677 (-0.211) | 343381.077 (-0.009) | 40820.475 (-0.009) | 942.352 (-0.107) |
| genie_small_pc01 | +1 $\sigma$ | 1825827.691 (-0.007) | 52881.328 (-0.006) | 6493.040 (0.032) | 344201.695 (-0.007) | 40924.862 (-0.007) | 958.806(-0.090) |
| | -1 $\sigma$ | 1850388.180 (0.007) | 53502.526 (0.006) | 6087.746 (-0.032) | 348944.770 (0.007) | 41476.574 (0.007) | 1140.001 (0.083) |
| genie_small_pc02 | +1 $\sigma$ | 1863064.361 (0.013) | 54067.577 (0.016) | 6300.281 (0.002) | 347937.933 (0.004) | 41484.066 (0.007) | 1050.397(0.001) |
| | -1 $\sigma$ | 1813151.510 (-0.004) | 52316.277 (-0.017) | 6280.504 (-0.001) | 345208.531 (-0.004) | 40917.370 (-0.007) | 1048.410 (-0.001) |
| genie_small_pc03 | +1 $\sigma$ | 1838078.507 (-0.000) | 53009.312 (-0.004) | 6220.036 (-0.010) | 343434.933 (-0.009) | 40946.511 (-0.006) | 1043.394(-0.006) |
| | -1 $\sigma$ | 1838137.363 (0.009) | 53374.541 (0.003) | 6360.749 (0.012) | 349711.531 (0.009) | 41454.926 (0.006) | 1055.413 (0.006) |
| genie_small_pc04 | +1 $\sigma$ | 1838824.588 (0.000) | 53348.039 (0.003) | 6215.523 (-0.011) | 347883.313 (0.004) | 41298.437 (0.002) | 1040.849(-0.008) |
| | -1 $\sigma$ | 1837391.282 (-0.004) | 53035.815 (-0.003) | 6365.262 (0.013) | 345263.151 (-0.004) | 41102.999 (-0.002) | 1057.958 (0.008) |
| NuTauScale | +1 $\sigma$ | 1838107.935 (0.000) | 53191.927 (-0.000) | 6290.393 (0.001) | 346573.232 (-0.000) | 41200.718(0.000) | 1049.403 (0.000) |
| ppfx_hadp_beam_pc00 | +1 $\sigma$ | 1861147.378 (0.012) | 54574.804 (0.025) | 6388.194 (0.016) | 356397.611 (0.028) | 41816.173 (0.015) | 1080.634(0.030) |
| | -1 $\sigma$ | 1815040.346 (-0.029) | 51828.512 (-0.026) | 6182.862 (-0.016) | 336772.948 (-0.029) | 40585.047 (-0.015) | 1017.762 (-0.030) |
| ppfx_hadp_beam_pc01 | +1 $\sigma$ | 1970708.682 (0.070) | 60654.900 (0.131) | 6763.653 (0.073) | 369835.437 (0.065) | 47537.337 (0.143) | 1144.803(0.087) |
| | -1 $\sigma$ | 1705479.042 (-0.069) | 45748.416 (-0.151) | 5807.402 (-0.079) | 323335.121 (-0.069) | 34863.883 (-0.167) | 953.593 (-0.095) |
| ppfx_hadp_beam_pc02 | +1 $\sigma$ | 1814381.359 (-0.013) | 53719.266 (0.010) | 6118.151 (-0.027) | 348505.399 (0.006) | 40642.289 (-0.014) | 1034.958(-0.014) |
| | -1 $\sigma$ | 1861806.365 (-0.006) | 52684.050 (-0.010) | 6452.905 (0.026) | 344665.160 (-0.006) | 41758.930 (0.013) | 1063.438 (0.013) |
| ppfx_hadp_beam_pc03 | +1 $\sigma$ | 1838025.598 (-0.000) | 53448.012 (0.005) | 6306.859 (0.003) | 351989.300 (0.015) | 41003.273 (-0.005) | 1069.240(0.019) |
| | -1 $\sigma$ | 1838162.126 (-0.016) | 52955.304 (-0.005) | 6264.197 (-0.003) | 341181.258 (-0.016) | 41397.947 (0.005) | 1029.156 (-0.019) |
| ppfx_hadp_beam_pc04 | +1 $\sigma$ | 1844840.797 (0.004) | 54276.757 (0.020) | 6322.838 (0.006) | 348813.351 (0.006) | 41757.556 (0.013) | 1060.033(0.010) |
| | -1 $\sigma$ | 1831346.927 (-0.006) | 52126.559 (-0.020) | 6248.218 (-0.006) | 344357.207 (-0.006) | 40643.664 (-0.014) | 1038.362 (-0.010) |
| Calibration | +1 $\sigma$ | 1813731.126 (-0.013) | 52432.573 (-0.015) | 5309.307 (-0.168) | 343048.778 (-0.010) | 40116.465 (-0.027) | 886.583(-0.168) |
| | -1 $\sigma$ | 1865511.310 (0.002) | 53477.972 (0.005) | 7179.866 (0.133) | 347279.414 (0.002) | 41839.377 (0.015) | 1250.524 (0.175) |
| CalibShape | +1 $\sigma$ | 1865460.953 (0.015) | 54670.638 (0.027) | 6745.689 (0.071) | 349055.517 (0.007) | 41552.710(0.009) | 1101.587 (0.049) |
| Lightlevel | +1 $\sigma$ | 1846274.847 (0.004) | 53037.099 (-0.003) | 6473.134 (0.029) | 345065.344 (-0.004) | 41243.835 (0.001) | 1076.311(0.026) |
| | -1 $\sigma$ | 1855649.898 (0.002) | 53548.646 (0.007) | 6504.636 (0.034) | 347402.669 (0.002) | 41460.743 (0.006) | 1090.447 (0.039) |
| Cherenkov | +1 $\sigma$ | 1854271.600 (0.009) | 53618.224 (0.008) | 6607.477 (0.050) | 346419.268 (-0.000) | 41470.835(0.007) | 1119.422 (0.065) |
| NeutronEvisPrimariesSyst2018 | +1 $\sigma$ | 1840251.332 (0.001) | 53216.027 (0.000) | 6318.194 (0.005) | 347104.569 (0.001) | 41052.385 (-0.004) | 1022.897(-0.025) |
| | -1 $\sigma$ | 1840322.298 (0.002) | 53222.212 (0.000) | 6321.343 (0.006) | 347113.355 (0.002) | 41067.446 (-0.003) | 1022.897 (-0.025) |
| AbsMuEScale2017 | +1 $\sigma$ | 1838156.443 (0.000) | 53212.122 (0.000) | 6286.010 (0.000) | 346593.897 (0.000) | 41211.579 (0.000) | 1049.445(0.000) |
| | -1 $\sigma$ | 1838030.694 (-0.000) | 53193.408 (-0.000) | 6284.077 (-0.000) | 346576.727 (-0.000) | 41190.402 (-0.000) | 1048.869 (-0.000) |
| RelMuEScale2017 | +1 $\sigma$ | 1838108.366 (0.000) | 53204.269 (0.000) | 6285.528 (0.000) | 346587.747 (0.000) | 41203.713 (0.000) | 1049.263(0.000) |
| | -1 $\sigma$ | 1838079.934 (-0.000) | 53199.106 (-0.000) | 6285.528 (0.000) | 346583.008 (-0.000) | 41197.513 (-0.000) | 1049.198 (0.000) |

**Table C.1:** Expected number of events at the ND from the +1 or -1 $\sigma$ systematic shifts in the MC, all quartiles, with an exposure to 8.025 $\times 10^{20}$ and 3.097 $\times 10^{20}$ POT for the production of the neutrino and antineutrino beam respectively. The numbers in parentheses correspond to relative difference with the mean between the nominal and the shifted predictions.

**Quartile 1**

| | | Neutrino Beam | | | Antineutrino Beam | | |
|---|---|---|---|---|---|---|---|
| Prediction | Shift | Right Sign ($\nu_\mu$) | Wrong Sign ($\bar{\nu}_\mu$) | Background | Right Sign ($\bar{\nu}_\mu$) | Wrong Sign ($\nu_\mu$) | Background |
| Nominal | - | 566755.259 | 27472.335 | 406.422 | 121094.429 | 6218.343 | 46.271 |
| MECEnuShapeNu | +1 $\sigma$ | 599977.410 (0.057) | 27472.335 (0.000) | 406.433 (0.000) | 121094.429 (0.000) | 6504.936 (0.045) | 46.278(0.000) |
| | -1 $\sigma$ | 533533.108 (0.000) | 27472.335 (0.000) | 406.410 (-0.000) | 121094.429 (0.000) | 5931.750 (-0.047) | 46.263 (-0.000) |
| MECEnuShapeAntiNu | +1 $\sigma$ | 566755.259 (0.000) | 29103.948 (0.058) | 406.422 (0.000) | 127827.225 (0.054) | 6218.343 (0.000) | 46.271(0.000) |
| | -1 $\sigma$ | 566755.259 (-0.057) | 25840.722 (-0.061) | 406.422 (0.000) | 114361.633 (-0.057) | 6218.343 (0.000) | 46.271 (0.000) |
| MECShape2018Nu | +1 $\sigma$ | 504053.192 (-0.117) | 27472.335 (0.000) | 406.441 (0.000) | 121094.429 (0.000) | 5388.526 (-0.143) | 46.278(0.000) |
| | -1 $\sigma$ | 601736.620 (0.000) | 27472.335 (0.000) | 406.140 (-0.001) | 121094.429 (0.000) | 6858.349 (0.098) | 46.160 (-0.002) |
| MECShape2018AntiNu | +1 $\sigma$ | 566755.259 (0.000) | 24945.671 (-0.096) | 406.422 (0.000) | 104425.362 (-0.148) | 6218.343 (0.000) | 46.271(0.000) |
| | -1 $\sigma$ | 566755.259 (0.073) | 28758.753 (0.046) | 406.422 (0.000) | 130322.537 (0.073) | 6218.343 (0.000) | 46.271 (0.000) |
| MECInitStateNPFracNu | +1 $\sigma$ | 574542.863 (0.014) | 27472.335 (0.000) | 406.479 (0.000) | 121094.429 (0.000) | 6272.518 (0.009) | 46.293(0.000) |
| | -1 $\sigma$ | 558967.655 (0.000) | 27472.335 (0.000) | 406.364 (-0.000) | 121094.429 (0.000) | 6164.168 (-0.009) | 46.248 (-0.000) |
| MECInitStateNPFracAntiNu | +1 $\sigma$ | 566755.259 (0.000) | 28043.426 (0.021) | 406.422 (0.000) | 123888.826 (0.023) | 6218.343 (0.000) | 46.271(0.000) |
| | -1 $\sigma$ | 566755.259 (-0.023) | 26901.244 (-0.021) | 406.422 (0.000) | 118300.032 (-0.023) | 6218.343 (0.000) | 46.271 (0.000) |
| MaCCQE_reduced_2018 | +1 $\sigma$ | 574583.557 (0.014) | 27846.778 (0.014) | 406.422 (0.000) | 122995.995 (0.016) | 6301.050 (0.013) | 46.271(0.000) |
| | -1 $\sigma$ | 558998.510 (-0.016) | 27102.719 (-0.014) | 406.422 (0.000) | 119215.894 (-0.016) | 6136.205 (-0.013) | 46.271 (0.000) |
| RPAShapeRES2018 | +1 $\sigma$ | 590709.771 (0.041) | 28392.374 (0.033) | 406.422 (0.000) | 122454.519 (0.011) | 6354.528 (0.022) | 46.271(0.000) |
| | -1 $\sigma$ | 566755.259 (0.000) | 27472.335 (0.000) | 406.422 (0.000) | 121094.429 (0.000) | 6218.343 (0.000) | 46.271 (0.000) |
| RPAShapeenh2018 | +1 $\sigma$ | 580102.438 (0.023) | 28206.691 (0.026) | 406.422 (0.000) | 124803.186 (0.030) | 6397.335 (0.028) | 46.271(0.000) |
| | -1 $\sigma$ | 554448.875 (-0.029) | 26785.499 (-0.025) | 406.422 (0.000) | 117590.140 (-0.029) | 6047.267 (-0.028) | 46.271 (0.000) |
| COHCCScale2018 | +1 $\sigma$ | 568383.118 (0.003) | 27528.757 (0.002) | 406.422 (0.000) | 121155.491 (0.001) | 6227.764 (0.002) | 46.271(0.000) |
| | -1 $\sigma$ | 565127.400 (-0.001) | 27415.913 (-0.002) | 406.422 (0.000) | 121033.367 (-0.001) | 6208.922 (-0.002) | 46.271 (0.000) |
| COHNCScale2018 | +1 $\sigma$ | 566755.259 (0.000) | 27472.335 (0.000) | 406.422 (0.000) | 121094.429 (0.000) | 6218.343 (0.000) | 46.271(0.000) |
| | -1 $\sigma$ | 566755.259 (0.000) | 27472.335 (0.000) | 406.422 (0.000) | 121094.429 (0.000) | 6218.343 (0.000) | 46.271 (0.000) |
| MaCCRES | +1 $\sigma$ | 573165.433 (0.011) | 27813.159 (0.012) | 406.422 (0.000) | 121569.663 (0.004) | 6259.295 (0.007) | 46.271(0.000) |
| | -1 $\sigma$ | 558165.241 (-0.005) | 27063.124 (-0.015) | 406.422 (0.000) | 120517.677 (-0.005) | 6165.628 (-0.009) | 46.271 (0.000) |
| MaNCRES | +1 $\sigma$ | 566755.259 (0.000) | 27472.335 (0.000) | 467.955 (0.141) | 121094.429 (0.000) | 6218.343 (0.000) | 53.123(0.138) |
| | -1 $\sigma$ | 566755.259 (0.000) | 27472.335 (0.000) | 348.109 (-0.155) | 121094.429 (0.000) | 6218.343 (0.000) | 40.123 (-0.142) |
| MvCCRES | +1 $\sigma$ | 569698.893 (0.005) | 27586.826 (0.004) | 406.422 (0.000) | 121248.292 (0.001) | 6237.201 (0.003) | 46.271(0.000) |
| | -1 $\sigma$ | 563681.780 (-0.001) | 27370.397 (-0.004) | 406.422 (0.000) | 120957.449 (-0.001) | 6199.235 (-0.003) | 46.271 (0.000) |
| CCQEPauliSupViaKF | +1 $\sigma$ | 538717.331 (-0.051) | 26135.999 (-0.050) | 407.782 (0.003) | 114168.440 (-0.059) | 5766.921 (-0.075) | 46.331(0.001) |
| | -1 $\sigma$ | 594443.243 (0.059) | 28909.772 (0.051) | 407.782 (0.003) | 128515.112 (0.059) | 6722.734 (0.078) | 46.331 (0.001) |
| FrElas_N | +1 $\sigma$ | 557941.538 (-0.016) | 27529.002 (0.002) | 406.879 (0.001) | 122261.933 (0.010) | 6022.071 (-0.032) | 46.229(-0.001) |
| | -1 $\sigma$ | 575627.088 (-0.010) | 27389.534 (-0.003) | 408.690 (0.006) | 119947.116 (-0.010) | 6418.245 (0.032) | 46.432 (0.003) |
| FrCEx_N | +1 $\sigma$ | 569143.407 (0.004) | 27411.399 (-0.002) | 408.181 (0.004) | 120661.102 (-0.004) | 6283.187 (0.010) | 46.406(0.003) |
| | -1 $\sigma$ | 564437.127 (0.004) | 27521.171 (0.002) | 407.374 (0.002) | 121542.093 (0.004) | 6153.313 (-0.011) | 46.255 (-0.000) |
| FrAbs_N | +1 $\sigma$ | 569500.105 (0.005) | 27458.865 (-0.000) | 409.598 (0.008) | 120693.527 (-0.003) | 6254.602 (0.006) | 46.568(0.006) |
| | -1 $\sigma$ | 564090.666 (0.003) | 27472.749 (0.000) | 405.968 (-0.001) | 121503.217 (0.003) | 6183.228 (-0.006) | 46.093 (-0.004) |
| FrInel_pi | +1 $\sigma$ | 568830.703 (0.004) | 27399.082 (-0.003) | 410.172 (0.009) | 120783.917 (-0.003) | 6232.605 (0.002) | 46.464(0.004) |
| | -1 $\sigma$ | 564722.040 (0.003) | 27537.905 (0.002) | 404.069 (-0.006) | 121410.547 (0.003) | 6204.038 (-0.002) | 46.137 (-0.003) |
| FormZone | +1 $\sigma$ | 567077.172 (0.001) | 27485.857 (0.000) | 424.219 (0.043) | 121111.311 (0.000) | 6221.574 (0.001) | 48.787(0.053) |
| | -1 $\sigma$ | 566403.041 (-0.000) | 27457.341 (-0.001) | 374.089 (-0.083) | 121077.282 (-0.000) | 6214.116 (-0.001) | 42.634 (-0.082) |

**Quartile 1**

| | | Neutrino Beam | | | Antineutrino Beam | | |
|---|---|---|---|---|---|---|---|
| Prediction | Shift | Right Sign ($\nu_\mu$) | Wrong Sign ($\bar{\nu}_\mu$) | Background | Right Sign ($\bar{\nu}_\mu$) | Wrong Sign ($\nu_\mu$) | Background |
| Nominal | - | 566755.259 | 27472.335 | 406.422 | 121094.429 | 6218.343 | 46.271 |
| genie_small_pc00 | +1 $\sigma$ | 572173.676 (0.010) | 27726.106 (0.009) | 484.920 (0.176) | 122199.337 (0.009) | 6275.018 (0.009) | 50.572(0.089) |
| | -1 $\sigma$ | 561427.844 (-0.009) | 27205.323 (-0.010) | 330.645 (-0.206) | 120000.819 (-0.009) | 6161.811 (-0.009) | 42.089 (-0.095) |
| genie_small_pc01 | +1 $\sigma$ | 564033.639 (-0.005) | 27340.170 (-0.005) | 420.871 (0.035) | 120533.661 (-0.005) | 6190.679 (-0.004) | 41.663(-0.105) |
| | -1 $\sigma$ | 569567.881 (0.005) | 27591.260 (0.004) | 394.694 (-0.029) | 121666.495 (0.005) | 6246.149 (0.004) | 50.998 (0.097) |
| genie_small_pc02 | +1 $\sigma$ | 573457.126 (0.012) | 27814.614 (0.012) | 407.998 (0.004) | 122001.974 (0.007) | 6281.630 (0.010) | 46.353(0.002) |
| | -1 $\sigma$ | 560144.393 (-0.007) | 27116.816 (-0.013) | 407.566 (0.003) | 120198.182 (-0.007) | 6155.199 (-0.010) | 46.308 (0.001) |
| genie_small_pc03 | +1 $\sigma$ | 559325.268 (-0.013) | 27111.424 (-0.013) | 403.159 (-0.008) | 117586.978 (-0.029) | 6040.019 (-0.029) | 46.075(-0.004) |
| | -1 $\sigma$ | 574276.252 (0.029) | 27820.006 (0.013) | 412.405 (0.015) | 124613.178 (0.029) | 6396.809 (0.028) | 46.586 (0.007) |
| genie_small_pc04 | +1 $\sigma$ | 571550.350 (0.008) | 27709.681 (0.009) | 403.548 (-0.007) | 122787.078 (0.014) | 6306.393 (0.014) | 45.969(-0.007) |
| | -1 $\sigma$ | 562051.169 (-0.014) | 27221.749 (-0.009) | 412.017 (0.014) | 119413.078 (-0.014) | 6130.435 (-0.014) | 46.692 (0.009) |
| NuTauScale | +1 $\sigma$ | 566800.760 (0.000) | 27465.715 (-0.000) | 407.782 (0.003) | 121100.078 (0.000) | 6218.414(0.000) | 46.331 (0.001) |
| ppfx_hadp_beam_pc00 | +1 $\sigma$ | 573754.662 (0.012) | 28146.861 (0.024) | 412.378 (0.015) | 124506.704 (0.028) | 6326.965 (0.017) | 47.858(0.034) |
| | -1 $\sigma$ | 559755.856 (-0.029) | 26797.809 (-0.025) | 400.465 (-0.015) | 117682.153 (-0.029) | 6109.722 (-0.018) | 44.683 (-0.035) |
| ppfx_hadp_beam_pc01 | +1 $\sigma$ | 607359.484 (0.069) | 31335.552 (0.131) | 437.117 (0.073) | 129218.443 (0.065) | 7163.085 (0.141) | 50.231(0.082) |
| | -1 $\sigma$ | 526151.035 (-0.069) | 23609.119 (-0.151) | 375.727 (-0.078) | 112970.415 (-0.069) | 5273.601 (-0.164) | 42.311 (-0.089) |
| ppfx_hadp_beam_pc02 | +1 $\sigma$ | 559604.146 (-0.013) | 27732.196 (0.009) | 397.114 (-0.023) | 121761.715 (0.005) | 6129.860 (-0.014) | 45.823(-0.010) |
| | -1 $\sigma$ | 573906.372 (-0.006) | 27212.474 (-0.010) | 415.730 (0.023) | 120427.142 (-0.006) | 6306.826 (0.014) | 46.719 (0.010) |
| ppfx_hadp_beam_pc03 | +1 $\sigma$ | 566723.271 (-0.000) | 27544.892 (0.003) | 407.498 (0.003) | 122962.542 (0.015) | 6188.999 (-0.005) | 47.076(0.017) |
| | -1 $\sigma$ | 566787.247 (-0.016) | 27399.779 (-0.003) | 405.345 (-0.003) | 119226.315 (-0.016) | 6247.688 (0.005) | 45.466 (-0.018) |
| ppfx_hadp_beam_pc04 | +1 $\sigma$ | 568825.413 (0.004) | 28025.536 (0.020) | 408.540 (0.005) | 121866.596 (0.006) | 6300.520 (0.013) | 46.681(0.009) |
| | -1 $\sigma$ | 564685.105 (-0.006) | 26919.135 (-0.020) | 404.304 (-0.005) | 120322.261 (-0.006) | 6136.166 (-0.013) | 45.861 (-0.009) |
| Calibration | +1 $\sigma$ | 524132.936 (-0.078) | 26156.912 (-0.049) | 327.280 (-0.216) | 109590.620 (-0.100) | 5510.500 (-0.121) | 42.873(-0.076) |
| | -1 $\sigma$ | 614075.713 (0.068) | 28567.703 (0.039) | 409.649 (0.008) | 129644.740 (0.068) | 6844.699 (0.096) | 60.942 (0.274) |
| CalibShape | +1 $\sigma$ | 586570.734 (0.034) | 28733.539 (0.045) | 333.890 (-0.196) | 124030.025 (0.024) | 6431.353(0.034) | 53.672 (0.148) |
| Lightlevel | +1 $\sigma$ | 578069.646 (0.020) | 27735.313 (0.010) | 372.933 (-0.086) | 121843.757 (0.006) | 6324.689 (0.017) | 52.276(0.122) |
| | -1 $\sigma$ | 572011.547 (0.010) | 27797.716 (0.012) | 379.551 (-0.068) | 122324.286 (0.010) | 6291.968 (0.012) | 55.350 (0.179) |
| Cherenkov | +1 $\sigma$ | 583433.316 (0.029) | 27990.146 (0.019) | 387.835 (-0.047) | 123043.538 (0.016) | 6416.200(0.031) | 56.748 (0.203) |
| NeutronEvisPrimariesSyst2018 | +1 $\sigma$ | 548359.969 (-0.033) | 25534.149 (-0.073) | 378.398 (-0.071) | 106415.488 (-0.129) | 5894.942 (-0.053) | 36.954(-0.224) |
| | -1 $\sigma$ | 593409.579 (0.120) | 29064.133 (0.056) | 478.562 (0.163) | 136620.089 (0.120) | 6760.814 (0.084) | 60.964 (0.274) |
| AbsMuEScale2017 | +1 $\sigma$ | 562474.805 (-0.008) | 27327.112 (-0.005) | 400.937 (-0.014) | 120318.620 (-0.006) | 6146.373 (-0.012) | 45.642(-0.014) |
| | -1 $\sigma$ | 571145.705 (0.006) | 27610.094 (0.005) | 412.668 (0.015) | 121882.453 (0.006) | 6286.384 (0.011) | 46.535 (0.006) |
| RelMuEScale2017 | +1 $\sigma$ | 565707.796 (-0.002) | 27445.178 (-0.001) | 405.871 (-0.001) | 120897.404 (-0.002) | 6199.871 (-0.003) | 45.954(-0.007) |
| | -1 $\sigma$ | 567864.932 (0.002) | 27503.236 (0.001) | 407.202 (0.002) | 121303.526 (0.002) | 6236.185 (0.003) | 46.196 (-0.002) |

**Table C.2:** Expected number of events at the ND from the +1 or -1 $\sigma$ systematic shifts in the MC, quartile 1, with an exposure to 8.025 $\times 10^{20}$ and 3.097 $\times 10^{20}$ POT for the production of the neutrino and antineutrino beam respectively. The numbers in parentheses correspond to relative difference with the mean between the nominal and the shifted predictions.

**Quartile 2**

| | | Neutrino Beam | | | Antineutrino Beam | | |
|---|---|---|---|---|---|---|---|
| Prediction | Shift | Right Sign ($\nu_\mu$) | Wrong Sign ($\bar{\nu}_\mu$) | Background | Right Sign ($\bar{\nu}_\mu$) | Wrong Sign ($\nu_\mu$) | Background |
| Nominal | - | 451992.522 | 11080.124 | 503.260 | 81883.197 | 8804.814 | 62.457 |
| MECEnuShapeNu | +1 $\sigma$ | 479081.943 (0.058) | 11080.124 (0.000) | 503.285 (0.000) | 81883.197 (0.000) | 9344.463 (0.059) | 62.460(0.000) |
| | -1 $\sigma$ | 424903.101 (0.000) | 11080.124 (0.000) | 503.235 (-0.000) | 81883.197 (0.000) | 8265.165 (-0.063) | 62.454 (-0.000) |
| MECEnuShapeAntiNu | +1 $\sigma$ | 451992.522 (0.000) | 11626.108 (0.048) | 503.260 (0.000) | 87333.156 (0.064) | 8804.814 (0.000) | 62.457(0.000) |
| | -1 $\sigma$ | 451992.522 (-0.069) | 10534.140 (-0.051) | 503.260 (0.000) | 76433.239 (-0.069) | 8804.814 (0.000) | 62.457 (0.000) |
| MECShape2018Nu | +1 $\sigma$ | 478917.725 (0.058) | 11080.124 (0.000) | 503.297 (0.000) | 81883.197 (0.000) | 8598.342 (-0.024) | 62.464(0.000) |
| | -1 $\sigma$ | 388021.716 (0.000) | 11080.124 (0.000) | 502.722 (-0.001) | 81883.197 (0.000) | 8491.925 (-0.036) | 62.353 (-0.002) |
| MECShape2018AntiNu | +1 $\sigma$ | 451992.522 (0.000) | 11484.090 (0.036) | 503.260 (0.000) | 80600.878 (-0.016) | 8804.814 (0.000) | 62.457(0.000) |
| | -1 $\sigma$ | 451992.522 (-0.027) | 10285.851 (-0.074) | 503.260 (0.000) | 79718.143 (-0.027) | 8804.814 (0.000) | 62.457 (0.000) |
| MECInitStateNPFracNu | +1 $\sigma$ | 461475.203 (0.021) | 11080.124 (0.000) | 503.219 (-0.000) | 81883.197 (0.000) | 8953.075 (0.017) | 62.478(0.000) |
| | -1 $\sigma$ | 442509.841 (0.000) | 11080.124 (0.000) | 503.301 (0.000) | 81883.197 (0.000) | 8656.553 (-0.017) | 62.436 (-0.000) |
| MECInitStateNPFracAntiNu | +1 $\sigma$ | 451992.522 (0.000) | 11139.504 (0.005) | 503.260 (0.000) | 83316.329 (0.017) | 8804.814 (0.000) | 62.457(0.000) |
| | -1 $\sigma$ | 451992.522 (-0.018) | 11020.744 (-0.005) | 503.260 (0.000) | 80450.066 (-0.018) | 8804.814 (0.000) | 62.457 (0.000) |
| MaCCQE_reduced_2018 | +1 $\sigma$ | 456234.711 (0.009) | 11139.063 (0.005) | 503.300 (0.000) | 82682.954 (0.010) | 8911.062 (0.012) | 62.457(0.000) |
| | -1 $\sigma$ | 447818.168 (-0.010) | 11022.551 (-0.005) | 503.221 (-0.000) | 81097.756 (-0.010) | 8699.834 (-0.012) | 62.457 (0.000) |
| RPAShapeRES2018 | +1 $\sigma$ | 506261.543 (0.113) | 12622.802 (0.130) | 503.325 (0.000) | 89267.066 (0.086) | 9503.755 (0.076) | 62.457(0.000) |
| | -1 $\sigma$ | 451992.522 (0.000) | 11080.124 (0.000) | 503.260 (0.000) | 81883.197 (0.000) | 8804.814 (0.000) | 62.457 (0.000) |
| RPAShapeenh2018 | +1 $\sigma$ | 458294.549 (0.014) | 11177.019 (0.009) | 503.279 (0.000) | 83107.049 (0.015) | 8955.005 (0.017) | 62.457(0.000) |
| | -1 $\sigma$ | 447080.401 (-0.013) | 11000.006 (-0.007) | 503.241 (-0.000) | 80823.834 (-0.013) | 8674.763 (-0.015) | 62.457 (0.000) |
| COHCCScale2018 | +1 $\sigma$ | 454236.315 (0.005) | 11195.008 (0.010) | 503.260 (0.000) | 82403.365 (0.006) | 8844.494 (0.004) | 62.457(0.000) |
| | -1 $\sigma$ | 449748.730 (-0.006) | 10965.240 (-0.010) | 503.260 (0.000) | 81363.030 (-0.006) | 8765.134 (-0.005) | 62.457 (0.000) |
| COHNCScale2018 | +1 $\sigma$ | 451992.522 (0.000) | 11080.124 (0.000) | 503.260 (0.000) | 81883.197 (0.000) | 8804.814 (0.000) | 62.457(0.000) |
| | -1 $\sigma$ | 451992.522 (0.000) | 11080.124 (0.000) | 503.260 (0.000) | 81883.197 (0.000) | 8804.814 (0.000) | 62.457 (0.000) |
| MaCCRES | +1 $\sigma$ | 475451.934 (0.051) | 11775.197 (0.061) | 503.307 (0.000) | 84462.156 (0.031) | 9084.689 (0.031) | 62.457(0.000) |
| | -1 $\sigma$ | 422242.208 (-0.039) | 10286.403 (-0.074) | 503.197 (-0.000) | 78753.036 (-0.039) | 8453.613 (-0.041) | 62.457 (0.000) |
| MaNCRES | +1 $\sigma$ | 451992.522 (0.000) | 11080.124 (0.000) | 574.572 (0.132) | 81883.197 (0.000) | 8804.814 (0.000) | 75.471(0.189) |
| | -1 $\sigma$ | 451992.522 (0.000) | 11080.124 (0.000) | 439.556 (-0.135) | 81883.197 (0.000) | 8804.814 (0.000) | 51.875 (-0.185) |
| MvCCRES | +1 $\sigma$ | 463913.454 (0.026) | 11319.440 (0.021) | 503.302 (0.000) | 82703.379 (0.010) | 8941.809 (0.015) | 62.457(0.000) |
| | -1 $\sigma$ | 439878.092 (-0.009) | 10876.482 (-0.019) | 503.216 (-0.000) | 81156.262 (-0.009) | 8667.375 (-0.016) | 62.457 (0.000) |
| CCQEPauliSupViaKF | +1 $\sigma$ | 449133.759 (-0.006) | 10990.828 (-0.008) | 503.381 (0.000) | 80353.815 (-0.019) | 8596.325 (-0.024) | 62.771(0.005) |
| | -1 $\sigma$ | 453730.178 (0.016) | 11159.558 (0.007) | 503.381 (0.000) | 83196.605 (0.016) | 8970.277 (0.019) | 62.771 (0.005) |
| FrElas_N | +1 $\sigma$ | 456097.569 (0.009) | 10983.461 (-0.009) | 499.184 (-0.008) | 81249.938 (-0.008) | 8807.614 (0.000) | 61.533(-0.015) |
| | -1 $\sigma$ | 447754.258 (0.007) | 11177.050 (0.009) | 507.578 (0.009) | 82466.692 (0.007) | 8799.386 (-0.001) | 64.013 (0.025) |
| FrCEx_N | +1 $\sigma$ | 450565.671 (-0.003) | 11138.040 (0.005) | 504.699 (0.003) | 82062.961 (0.002) | 8796.217 (-0.001) | 63.597(0.018) |
| | -1 $\sigma$ | 453340.275 (-0.003) | 11024.698 (-0.005) | 502.063 (-0.002) | 81678.735 (-0.003) | 8815.044 (0.001) | 61.983 (-0.008) |
| FrAbs_N | +1 $\sigma$ | 451422.721 (-0.001) | 11104.037 (0.002) | 505.445 (0.004) | 82176.005 (0.004) | 8835.007 (0.003) | 63.301(0.013) |
| | -1 $\sigma$ | 452508.555 (-0.004) | 11054.809 (-0.002) | 501.316 (-0.004) | 81570.612 (-0.004) | 8775.988 (-0.003) | 62.241 (-0.003) |
| FrInel_pi | +1 $\sigma$ | 452125.893 (0.000) | 11093.259 (0.001) | 507.099 (0.008) | 81642.832 (-0.003) | 8829.239 (0.003) | 63.557(0.017) |
| | -1 $\sigma$ | 451826.067 (0.003) | 11067.084 (-0.001) | 500.408 (-0.006) | 82112.962 (0.003) | 8782.272 (-0.003) | 61.685 (-0.012) |
| FormZone | +1 $\sigma$ | 452662.138 (0.001) | 11125.878 (0.004) | 528.063 (0.048) | 81969.210 (0.001) | 8817.537 (0.001) | 65.882(0.053) |
| | -1 $\sigma$ | 451235.807 (-0.001) | 11029.142 (-0.005) | 456.865 (-0.097) | 81805.394 (-0.001) | 8789.333 (-0.002) | 57.188 (-0.088) |

**Quartile 2**

| | | Neutrino Beam | | | Antineutrino Beam | | |
|---|---|---|---|---|---|---|---|
| Prediction | Shift | Right Sign ($\nu_\mu$) | Wrong Sign ($\bar{\nu}_\mu$) | Background | Right Sign ($\bar{\nu}_\mu$) | Wrong Sign ($\nu_\mu$) | Background |
| Nominal | - | 451992.522 | 11080.124 | 503.260 | 81883.197 | 8804.814 | 62.457 |
| genie_small_pc00 | +1 $\sigma$ | 456784.309 (0.011) | 11202.450 (0.011) | 598.802 (0.173) | 82628.705 (0.009) | 8887.134 (0.009) | 68.481(0.092) |
| | -1 $\sigma$ | 447145.806 (-0.009) | 10956.640 (-0.011) | 407.960 (-0.209) | 81117.303 (-0.009) | 8724.637 (-0.009) | 57.061 (-0.090) |
| genie_small_pc01 | +1 $\sigma$ | 448792.956 (-0.007) | 11002.658 (-0.007) | 519.559 (0.032) | 81297.637 (-0.007) | 8750.579 (-0.006) | 56.478(-0.101) |
| | -1 $\sigma$ | 455137.159 (0.007) | 11156.433 (0.007) | 487.203 (-0.032) | 82448.371 (0.007) | 8861.191 (0.006) | 69.064 (0.100) |
| genie_small_pc02 | +1 $\sigma$ | 458180.788 (0.014) | 11296.890 (0.019) | 503.698 (0.001) | 82194.855 (0.004) | 8874.437 (0.008) | 62.795(0.005) |
| | -1 $\sigma$ | 445749.327 (-0.004) | 10862.201 (-0.020) | 503.064 (-0.000) | 81551.152 (-0.004) | 8737.333 (-0.008) | 62.747 (0.005) |
| genie_small_pc03 | +1 $\sigma$ | 452856.089 (0.002) | 11127.750 (0.004) | 497.763 (-0.011) | 81243.550 (-0.008) | 8697.400 (-0.012) | 62.420(-0.001) |
| | -1 $\sigma$ | 451074.025 (0.008) | 11031.340 (-0.004) | 508.999 (0.011) | 82502.458 (0.008) | 8914.370 (0.012) | 63.122 (0.011) |
| genie_small_pc04 | +1 $\sigma$ | 451583.373 (-0.001) | 11059.203 (-0.002) | 498.068 (-0.010) | 82127.099 (0.003) | 8854.823 (0.006) | 62.279(-0.003) |
| | -1 $\sigma$ | 452346.741 (-0.003) | 11099.887 (0.002) | 508.694 (0.011) | 81618.909 (-0.003) | 8756.947 (-0.005) | 63.263 (0.013) |
| NuTauScale | +1 $\sigma$ | 451965.057 (-0.000) | 11079.545 (-0.000) | 503.381 (0.000) | 81873.004 (-0.000) | 8805.885(0.000) | 62.771 (0.005) |
| ppfx_hadp_beam_pc00 | +1 $\sigma$ | 457696.247 (0.013) | 11374.653 (0.026) | 510.920 (0.015) | 84207.334 (0.028) | 8950.201 (0.016) | 64.225(0.028) |
| | -1 $\sigma$ | 446288.798 (-0.029) | 10785.595 (-0.027) | 495.599 (-0.015) | 79559.060 (-0.029) | 8659.427 (-0.017) | 60.689 (-0.029) |
| ppfx_hadp_beam_pc01 | +1 $\sigma$ | 484518.784 (0.069) | 12628.945 (0.131) | 541.317 (0.073) | 87373.698 (0.065) | 10145.149 (0.141) | 67.617(0.079) |
| | -1 $\sigma$ | 419466.261 (-0.069) | 9531.303 (-0.150) | 465.203 (-0.079) | 76392.697 (-0.069) | 7464.479 (-0.165) | 57.297 (-0.086) |
| ppfx_hadp_beam_pc02 | +1 $\sigma$ | 446424.768 (-0.012) | 11190.212 (0.010) | 492.088 (-0.022) | 82349.512 (0.006) | 8677.523 (-0.015) | 62.200(-0.004) |
| | -1 $\sigma$ | 457560.276 (-0.006) | 10970.036 (-0.010) | 514.432 (0.022) | 81416.883 (-0.006) | 8932.105 (0.014) | 62.714 (0.004) |
| ppfx_hadp_beam_pc03 | +1 $\sigma$ | 451941.622 (-0.000) | 11147.839 (0.006) | 504.750 (0.003) | 83236.810 (0.016) | 8763.047 (-0.005) | 63.678(0.019) |
| | -1 $\sigma$ | 452043.422 (-0.017) | 11012.408 (-0.006) | 501.770 (-0.003) | 80529.584 (-0.017) | 8846.581 (0.005) | 61.236 (-0.020) |
| ppfx_hadp_beam_pc04 | +1 $\sigma$ | 453646.852 (0.004) | 11305.562 (0.020) | 505.960 (0.005) | 82415.840 (0.006) | 8920.708 (0.013) | 63.060(0.010) |
| | -1 $\sigma$ | 450338.193 (-0.007) | 10854.686 (-0.021) | 500.560 (-0.005) | 81350.554 (-0.007) | 8688.920 (-0.013) | 61.854 (-0.010) |
| Calibration | +1 $\sigma$ | 458913.092 (0.015) | 11394.454 (0.028) | 449.857 (-0.112) | 84989.187 (0.037) | 8618.730 (-0.021) | 53.762(-0.150) |
| | -1 $\sigma$ | 449235.083 (-0.030) | 10844.788 (-0.021) | 582.199 (0.145) | 79468.343 (-0.030) | 9114.125 (0.035) | 64.168 (0.027) |
| CalibShape | +1 $\sigma$ | 454993.061 (0.007) | 11069.195 (-0.001) | 561.002 (0.109) | 80999.917 (-0.011) | 8932.106(0.014) | 59.570 (-0.047) |
| Lightlevel | +1 $\sigma$ | 451324.263 (-0.001) | 10803.896 (-0.025) | 524.721 (0.042) | 80935.832 (-0.012) | 8921.578 (0.013) | 58.154(-0.071) |
| | -1 $\sigma$ | 454322.689 (-0.012) | 11056.783 (-0.002) | 522.318 (0.037) | 80885.053 (-0.012) | 8875.743 (0.008) | 58.947 (-0.058) |
| Cherenkov | +1 $\sigma$ | 453982.623 (0.004) | 11053.578 (-0.002) | 566.779 (0.119) | 81211.266 (-0.008) | 8967.442(0.018) | 58.467 (-0.066) |
| NeutronEvisPrimariesSyst2018 | +1 $\sigma$ | 455375.636 (0.007) | 12087.786 (0.087) | 490.080 (-0.027) | 86384.762 (0.054) | 8700.697 (-0.012) | 56.457(-0.101) |
| | -1 $\sigma$ | 443517.166 (-0.095) | 10240.614 (-0.079) | 513.627 (0.020) | 74452.689 (-0.095) | 8759.029 (-0.005) | 60.638 (-0.030) |
| AbsMuEScale2017 | +1 $\sigma$ | 451017.437 (-0.002) | 11092.100 (0.001) | 495.652 (-0.015) | 81668.300 (-0.003) | 8743.052 (-0.007) | 61.974(-0.008) |
| | -1 $\sigma$ | 452802.613 (0.002) | 11074.106 (-0.001) | 508.909 (0.011) | 82064.002 (0.002) | 8871.896 (0.008) | 63.447 (0.016) |
| RelMuEScale2017 | +1 $\sigma$ | 451913.743 (-0.000) | 11080.816 (0.000) | 501.847 (-0.003) | 81827.833 (-0.001) | 8790.832 (-0.002) | 62.540(0.001) |
| | -1 $\sigma$ | 451993.324 (0.000) | 11076.276 (-0.000) | 503.017 (-0.000) | 81910.084 (0.000) | 8817.310 (0.001) | 62.644 (0.003) |

**Table C.3:** Expected number of events at the ND from the +1 or -1 $\sigma$ systematic shifts in the MC, quartile 2, with an exposure to 8.025 $\times 10^{20}$ and 3.097 $\times 10^{20}$ POT for the production of the neutrino and antineutrino beam respectively. The numbers in parentheses correspond to relative difference with the mean between the nominal and the shifted predictions.

**Quartile 3**

| | | Neutrino Beam | | | Antineutrino Beam | | |
|---|---|---|---|---|---|---|---|
| Prediction | Shift | Right Sign ($\nu_\mu$) | Wrong Sign ($\bar{\nu}_\mu$) | Background | Right Sign ($\bar{\nu}_\mu$) | Wrong Sign ($\nu_\mu$) | Background |
| Nominal | - | 352297.178 | 8252.967 | 991.446 | 75039.813 | 10858.119 | 132.353 |
| MECEnuShapeNu | +1 $\sigma$ | 365058.347 (0.036) | 8252.967 (0.000) | 991.466 (0.000) | 75039.813 (0.000) | 11504.827 (0.058) | 132.353(0.000) |
| | -1 $\sigma$ | 339536.009 (0.000) | 8252.967 (0.000) | 991.427 (-0.000) | 75039.813 (0.000) | 10211.411 (-0.061) | 132.353 (0.000) |
| MECEnuShapeAntiNu | +1 $\sigma$ | 352297.178 (0.000) | 8463.175 (0.025) | 991.449 (0.000) | 77447.355 (0.032) | 10858.119 (0.000) | 132.359(0.000) |
| | -1 $\sigma$ | 352297.178 (-0.033) | 8042.758 (-0.026) | 991.444 (-0.000) | 72632.272 (-0.033) | 10858.119 (0.000) | 132.347 (-0.000) |
| MECShape2018Nu | +1 $\sigma$ | 385907.508 (0.091) | 8252.967 (0.000) | 991.333 (-0.000) | 75039.813 (0.000) | 11458.298 (0.054) | 132.353(0.000) |
| | -1 $\sigma$ | 312667.891 (0.000) | 8252.967 (0.000) | 991.549 (0.000) | 75039.813 (0.000) | 9536.555 (-0.130) | 132.353 (0.000) |
| MECShape2018AntiNu | +1 $\sigma$ | 352297.178 (0.000) | 8457.192 (0.024) | 991.560 (0.000) | 78835.281 (0.049) | 10858.119 (0.000) | 132.564(0.002) |
| | -1 $\sigma$ | 352297.178 (-0.078) | 7911.305 (-0.042) | 991.355 (-0.000) | 69391.508 (-0.078) | 10858.119 (0.000) | 132.184 (-0.001) |
| MECInitStateNPFracNu | +1 $\sigma$ | 356751.589 (0.013) | 8252.967 (0.000) | 991.533 (0.000) | 75039.813 (0.000) | 11052.727 (0.018) | 132.353(0.000) |
| | -1 $\sigma$ | 347842.768 (0.000) | 8252.967 (0.000) | 991.360 (-0.000) | 75039.813 (0.000) | 10663.511 (-0.018) | 132.353 (0.000) |
| MECInitStateNPFracAntiNu | +1 $\sigma$ | 352297.178 (0.000) | 8255.712 (0.000) | 991.459 (0.000) | 75246.475 (0.003) | 10858.119 (0.000) | 132.339(-0.000) |
| | -1 $\sigma$ | 352297.178 (-0.003) | 8250.221 (-0.000) | 991.434 (-0.000) | 74833.151 (-0.003) | 10858.119 (0.000) | 132.367 (0.000) |
| MaCCQE_reduced_2018 | +1 $\sigma$ | 354261.242 (0.006) | 8271.854 (0.002) | 991.446 (0.000) | 75297.393 (0.003) | 10946.895 (0.008) | 132.353(0.000) |
| | -1 $\sigma$ | 350371.201 (-0.003) | 8234.726 (-0.002) | 991.446 (0.000) | 74789.696 (-0.003) | 10770.704 (-0.008) | 132.353 (0.000) |
| RPAShapeRES2018 | +1 $\sigma$ | 392294.224 (0.107) | 9360.388 (0.126) | 991.485 (0.000) | 87659.292 (0.155) | 11974.723 (0.098) | 132.373(0.000) |
| | -1 $\sigma$ | 352297.178 (0.000) | 8252.967 (0.000) | 991.446 (0.000) | 75039.813 (0.000) | 10858.119 (0.000) | 132.353 (0.000) |
| RPAShapeenh2018 | +1 $\sigma$ | 355756.058 (0.010) | 8285.112 (0.004) | 991.457 (0.000) | 75496.499 (0.006) | 10989.134 (0.012) | 132.353(0.000) |
| | -1 $\sigma$ | 349639.531 (-0.005) | 8227.193 (-0.003) | 991.436 (-0.000) | 74677.720 (-0.005) | 10754.739 (-0.010) | 132.353 (0.000) |
| COHCCScale2018 | +1 $\sigma$ | 353876.531 (0.004) | 8350.117 (0.012) | 991.622 (0.000) | 75916.648 (0.012) | 10909.778 (0.005) | 132.370(0.000) |
| | -1 $\sigma$ | 350717.826 (-0.012) | 8155.816 (-0.012) | 991.271 (-0.000) | 74162.978 (-0.012) | 10806.461 (-0.005) | 132.337 (-0.000) |
| COHNCScale2018 | +1 $\sigma$ | 352297.178 (0.000) | 8252.967 (0.000) | 991.554 (0.000) | 75039.813 (0.000) | 10858.119 (0.000) | 132.382(0.000) |
| | -1 $\sigma$ | 352297.178 (0.000) | 8252.967 (0.000) | 991.339 (-0.000) | 75039.813 (0.000) | 10858.119 (0.000) | 132.325 (-0.000) |
| MaCCRES | +1 $\sigma$ | 386356.556 (0.092) | 8975.056 (0.084) | 992.049 (0.001) | 80962.996 (0.076) | 11506.723 (0.058) | 132.391(0.000) |
| | -1 $\sigma$ | 312633.876 (-0.093) | 7506.358 (-0.095) | 990.955 (-0.000) | 68338.105 (-0.093) | 10078.094 (-0.075) | 132.325 (-0.000) |
| MaNCRES | +1 $\sigma$ | 352297.178 (0.000) | 8252.967 (0.000) | 1107.539 (0.111) | 75039.813 (0.000) | 10858.119 (0.000) | 155.341(0.160) |
| | -1 $\sigma$ | 352297.178 (0.000) | 8252.967 (0.000) | 895.682 (-0.101) | 75039.813 (0.000) | 10858.119 (0.000) | 114.457 (-0.145) |
| MvCCRES | +1 $\sigma$ | 371595.051 (0.053) | 8508.416 (0.030) | 991.776 (0.000) | 77003.390 (0.026) | 11203.611 (0.031) | 132.373(0.000) |
| | -1 $\sigma$ | 333497.800 (-0.022) | 8052.942 (-0.025) | 991.177 (-0.000) | 73405.597 (-0.022) | 10516.850 (-0.032) | 132.338 (-0.000) |
| CCQEPauliSupViaKF | +1 $\sigma$ | 351666.957 (-0.002) | 8231.977 (-0.003) | 993.287 (0.002) | 74812.099 (-0.003) | 10786.191 (-0.007) | 132.252(-0.001) |
| | -1 $\sigma$ | 352676.179 (0.002) | 8264.641 (0.001) | 993.371 (0.002) | 75222.839 (0.002) | 10901.746 (0.004) | 132.252 (-0.001) |
| FrElas_N | +1 $\sigma$ | 356036.759 (0.011) | 8201.216 (-0.006) | 987.919 (-0.004) | 74485.085 (-0.007) | 10953.555 (0.009) | 131.127(-0.009) |
| | -1 $\sigma$ | 348581.013 (0.007) | 8299.673 (0.006) | 998.697 (0.007) | 75589.402 (0.007) | 10758.591 (-0.009) | 133.376 (0.008) |
| FrCEx_N | +1 $\sigma$ | 351127.298 (-0.003) | 8279.859 (0.003) | 993.968 (0.003) | 75319.034 (0.004) | 10829.228 (-0.003) | 132.261(-0.001) |
| | -1 $\sigma$ | 353446.513 (-0.004) | 8221.500 (-0.004) | 992.686 (0.001) | 74754.670 (-0.004) | 10883.517 (0.002) | 132.243 (-0.001) |
| FrAbs_N | +1 $\sigma$ | 351088.106 (-0.003) | 8256.476 (0.000) | 997.813 (0.006) | 75124.958 (0.001) | 10840.467 (-0.002) | 132.916(0.004) |
| | -1 $\sigma$ | 353492.056 (-0.001) | 8244.116 (-0.001) | 988.827 (-0.003) | 74949.423 (-0.001) | 10873.214 (0.001) | 131.587 (-0.006) |
| FrInel_pi | +1 $\sigma$ | 350260.583 (-0.006) | 8260.345 (0.001) | 1010.699 (0.019) | 75153.861 (0.002) | 10845.570 (-0.001) | 133.471(0.008) |
| | -1 $\sigma$ | 354341.541 (-0.002) | 8244.614 (-0.001) | 974.656 (-0.017) | 74923.937 (-0.002) | 10868.292 (0.001) | 131.089 (-0.010) |
| FormZone | +1 $\sigma$ | 354311.946 (0.006) | 8348.218 (0.011) | 1054.589 (0.062) | 75392.501 (0.005) | 10911.769 (0.005) | 139.676(0.054) |
| | -1 $\sigma$ | 349683.147 (-0.005) | 8119.079 (-0.016) | 888.354 (-0.110) | 74668.353 (-0.005) | 10775.545 (-0.008) | 118.373 (-0.112) |

**Quartile 3**

| | | Neutrino Beam | | | Antineutrino Beam | | |
|---|---|---|---|---|---|---|---|
| Prediction | Shift | Right Sign ($\nu_\mu$) | Wrong Sign ($\bar{\nu}_\mu$) | Background | Right Sign ($\bar{\nu}_\mu$) | Wrong Sign ($\nu_\mu$) | Background |
| Nominal | - | 352297.178 | 8252.967 | 991.446 | 75039.813 | 10858.119 | 132.353 |
| genie_small_pc00 | +1 $\sigma$ | 356162.850 (0.011) | 8344.245 (0.011) | 1183.019 (0.176) | 75736.140 (0.009) | 10957.880 (0.009) | 144.917(0.091) |
| | -1 $\sigma$ | 348409.538 (-0.009) | 8156.137 (-0.012) | 803.633 (-0.209) | 74338.262 (-0.009) | 10755.682 (-0.009) | 119.586 (-0.101) |
| genie_small_pc01 | +1 $\sigma$ | 349602.679 (-0.008) | 8190.170 (-0.008) | 1025.533 (0.034) | 74406.043 (-0.008) | 10777.526 (-0.007) | 119.587(-0.101) |
| | -1 $\sigma$ | 354969.709 (0.008) | 8310.212 (0.007) | 961.118 (-0.031) | 75668.359 (0.008) | 10936.036 (0.007) | 144.917 (0.091) |
| genie_small_pc02 | +1 $\sigma$ | 357319.483 (0.014) | 8438.512 (0.022) | 994.546 (0.003) | 75145.334 (0.001) | 10917.414 (0.005) | 132.338(-0.000) |
| | -1 $\sigma$ | 347252.905 (-0.001) | 8061.869 (-0.023) | 992.106 (0.001) | 74929.068 (-0.001) | 10796.148 (-0.006) | 132.165 (-0.001) |
| genie_small_pc03 | +1 $\sigma$ | 354780.625 (0.007) | 8312.856 (0.007) | 982.256 (-0.009) | 75433.735 (0.005) | 10842.486 (-0.001) | 131.500(-0.006) |
| | -1 $\sigma$ | 349791.763 (-0.005) | 8187.526 (-0.008) | 1004.396 (0.013) | 74640.667 (-0.005) | 10871.076 (0.001) | 133.003 (0.005) |
| genie_small_pc04 | +1 $\sigma$ | 350909.638 (-0.004) | 8216.896 (-0.004) | 982.035 (-0.010) | 74773.952 (-0.004) | 10855.084 (-0.000) | 131.180(-0.009) |
| | -1 $\sigma$ | 353662.750 (0.003) | 8283.486 (0.004) | 1004.617 (0.013) | 75300.450 (0.003) | 10858.478 (0.000) | 133.323 (0.007) |
| NuTauScale | +1 $\sigma$ | 352286.194 (-0.000) | 8250.191 (-0.000) | 993.326 (0.002) | 75037.201 (-0.000) | 10856.781(-0.000) | 132.252 (-0.001) |
| ppfx_hadp_beam_pc00 | +1 $\sigma$ | 356806.385 (0.013) | 8482.587 (0.027) | 1007.256 (0.016) | 77169.862 (0.028) | 10995.783 (0.013) | 136.164(0.028) |
| | -1 $\sigma$ | 347787.971 (-0.029) | 8023.346 (-0.028) | 975.637 (-0.016) | 72909.765 (-0.029) | 10720.456 (-0.013) | 128.543 (-0.029) |
| ppfx_hadp_beam_pc01 | +1 $\sigma$ | 377903.616 (0.070) | 9401.961 (0.130) | 1066.361 (0.073) | 80075.422 (0.065) | 12536.658 (0.143) | 143.841(0.083) |
| | -1 $\sigma$ | 326690.740 (-0.069) | 7103.973 (-0.150) | 916.532 (-0.079) | 70004.204 (-0.069) | 9179.580 (-0.168) | 120.866 (-0.091) |
| ppfx_hadp_beam_pc02 | +1 $\sigma$ | 347584.783 (-0.013) | 8337.842 (0.010) | 967.044 (-0.025) | 75460.400 (0.006) | 10728.857 (-0.012) | 131.202(-0.009) |
| | -1 $\sigma$ | 357009.574 (-0.006) | 8168.092 (-0.010) | 1015.849 (0.024) | 74619.227 (-0.006) | 10987.381 (0.012) | 133.505 (0.009) |
| ppfx_hadp_beam_pc03 | +1 $\sigma$ | 352300.109 (0.000) | 8325.946 (0.009) | 994.585 (0.003) | 76238.787 (0.016) | 10803.963 (-0.005) | 135.063(0.020) |
| | -1 $\sigma$ | 352294.247 (-0.016) | 8179.988 (-0.009) | 988.308 (-0.003) | 73840.839 (-0.016) | 10912.275 (0.005) | 129.644 (-0.021) |
| ppfx_hadp_beam_pc04 | +1 $\sigma$ | 353586.986 (0.004) | 8420.684 (0.020) | 997.124 (0.006) | 75525.636 (0.006) | 11004.876 (0.013) | 133.658(0.010) |
| | -1 $\sigma$ | 351007.371 (-0.006) | 8085.249 (-0.021) | 985.769 (-0.006) | 74553.990 (-0.006) | 10711.362 (-0.014) | 131.049 (-0.010) |
| Calibration | +1 $\sigma$ | 367934.337 (0.043) | 8587.365 (0.040) | 847.636 (-0.156) | 78433.620 (0.044) | 10929.681 (0.007) | 124.221(-0.063) |
| | -1 $\sigma$ | 340814.906 (-0.041) | 7956.989 (-0.037) | 1113.644 (0.116) | 72055.473 (-0.041) | 10599.944 (-0.024) | 159.240 (0.184) |
| CalibShape | +1 $\sigma$ | 354566.198 (0.006) | 8274.450 (0.003) | 1071.678 (0.078) | 75113.221 (0.001) | 10784.859(-0.007) | 141.872 (0.069) |
| Lightlevel | +1 $\sigma$ | 350519.154 (-0.005) | 8185.594 (-0.008) | 1005.937 (0.015) | 74358.368 (-0.009) | 10684.219 (-0.016) | 140.334(0.059) |
| | -1 $\sigma$ | 355339.639 (0.001) | 8326.271 (0.009) | 999.718 (0.008) | 75143.937 (0.001) | 10794.177 (-0.006) | 143.430 (0.080) |
| Cherenkov | +1 $\sigma$ | 349713.218 (-0.007) | 8266.993 (0.002) | 1001.165 (0.010) | 74162.703 (-0.012) | 10752.882(-0.010) | 154.867 (0.157) |
| NeutronEvisPrimariesSyst2018 | +1 $\sigma$ | 360841.484 (0.024) | 8863.997 (0.071) | 987.759 (-0.004) | 82240.136 (0.092) | 10959.005 (0.009) | 134.808(0.018) |
| | -1 $\sigma$ | 345186.931 (-0.069) | 7774.490 (-0.060) | 997.944 (0.007) | 70036.531 (-0.069) | 10620.632 (-0.022) | 132.436 (0.001) |
| AbsMuEScale2017 | +1 $\sigma$ | 352672.001 (0.001) | 8286.117 (0.004) | 979.644 (-0.012) | 75248.018 (0.003) | 10848.750 (-0.001) | 129.803(-0.019) |
| | -1 $\sigma$ | 351907.080 (-0.003) | 8218.492 (-0.004) | 1005.026 (0.014) | 74831.399 (-0.003) | 10873.495 (0.001) | 136.100 (0.028) |
| RelMuEScale2017 | +1 $\sigma$ | 352583.118 (0.001) | 8259.542 (0.001) | 988.163 (-0.003) | 75135.370 (0.001) | 10863.228 (0.000) | 131.884(-0.004) |
| | -1 $\sigma$ | 352010.369 (-0.001) | 8242.118 (-0.001) | 994.779 (0.003) | 74953.561 (-0.001) | 10855.598 (-0.000) | 133.081 (0.005) |

**Table C.4:** Expected number of events at the ND from the +1 or -1 $\sigma$ systematic shifts in the MC, quartile 3, with an exposure to 8.025 $\times 10^{20}$ and 3.097 $\times 10^{20}$ POT for the production of the neutrino and antineutrino beam respectively. The numbers in parentheses correspond to relative difference with the mean between the nominal and the shifted predictions.

**Quartile 4**

| | | Neutrino Beam | | | Antineutrino Beam | | |
|---|---|---|---|---|---|---|---|
| Prediction | Shift | Right Sign ($\nu_\mu$) | Wrong Sign ($\bar{\nu}_\mu$) | Background | Right Sign ($\bar{\nu}_\mu$) | Wrong Sign ($\nu_\mu$) | Background |
| Nominal | - | 467048.902 | 6396.233 | 4384.400 | 68567.840 | 15319.334 | 808.117 |
| MECEnuShapeNu | +1 $\sigma$ | 472477.142 (0.012) | 6396.233 (0.000) | 4384.625 (0.000) | 68567.840 (0.000) | 15847.687 (0.034) | 808.139(0.000) |
| | -1 $\sigma$ | 461620.662 (0.000) | 6396.233 (0.000) | 4384.175 (-0.000) | 68567.840 (0.000) | 14790.981 (-0.035) | 808.095 (-0.000) |
| MECEnuShapeAntiNu | +1 $\sigma$ | 467048.902 (0.000) | 6498.817 (0.016) | 4384.465 (0.000) | 69150.858 (0.008) | 15319.334 (0.000) | 808.162(0.000) |
| | -1 $\sigma$ | 467048.902 (-0.009) | 6293.648 (-0.016) | 4384.335 (-0.000) | 67984.823 (-0.009) | 15319.334 (0.000) | 808.072 (-0.000) |
| MECShape2018Nu | +1 $\sigma$ | 475209.641 (0.017) | 6396.233 (0.000) | 4385.076 (0.000) | 68567.840 (0.000) | 15888.581 (0.036) | 808.148(0.000) |
| | -1 $\sigma$ | 455922.856 (0.000) | 6396.233 (0.000) | 4380.314 (-0.001) | 68567.840 (0.000) | 14317.577 (-0.068) | 807.671 (-0.001) |
| MECShape2018AntiNu | +1 $\sigma$ | 467048.902 (0.000) | 6455.715 (0.009) | 4384.753 (0.000) | 69380.647 (0.012) | 15319.334 (0.000) | 808.783(0.001) |
| | -1 $\sigma$ | 467048.902 (-0.015) | 6259.652 (-0.022) | 4384.295 (-0.000) | 67548.034 (-0.015) | 15319.334 (0.000) | 807.637 (-0.001) |
| MECInitStateNPFracNu | +1 $\sigma$ | 468557.013 (0.003) | 6396.233 (0.000) | 4384.834 (0.000) | 68567.840 (0.000) | 15456.563 (0.009) | 808.207(0.000) |
| | -1 $\sigma$ | 465540.791 (0.000) | 6396.233 (0.000) | 4383.966 (-0.000) | 68567.840 (0.000) | 15182.105 (-0.009) | 808.026 (-0.000) |
| MECInitStateNPFracAntiNu | +1 $\sigma$ | 467048.902 (0.000) | 6386.884 (-0.001) | 4384.434 (0.000) | 68597.207 (0.000) | 15319.334 (0.000) | 808.101(-0.000) |
| | -1 $\sigma$ | 467048.902 (-0.000) | 6405.581 (0.001) | 4384.366 (-0.000) | 68538.473 (-0.000) | 15319.334 (0.000) | 808.133 (0.000) |
| MaCCQE_reduced_2018 | +1 $\sigma$ | 469116.864 (0.004) | 6404.926 (0.001) | 4384.523 (0.000) | 68641.173 (0.001) | 15417.493 (0.006) | 808.142(0.000) |
| | -1 $\sigma$ | 465030.542 (-0.001) | 6388.201 (-0.001) | 4384.280 (-0.000) | 68498.992 (-0.001) | 15223.010 (-0.006) | 808.092 (-0.000) |
| RPAShapeRES2018 | +1 $\sigma$ | 484283.634 (0.036) | 6925.097 (0.079) | 4384.475 (0.000) | 76736.986 (0.112) | 16127.924 (0.051) | 808.208(0.000) |
| | -1 $\sigma$ | 467048.902 (0.000) | 6396.233 (0.000) | 4384.400 (0.000) | 68567.840 (0.000) | 15319.334 (0.000) | 808.117 (0.000) |
| RPAShapeenh2018 | +1 $\sigma$ | 469868.135 (0.006) | 6412.593 (0.003) | 4384.513 (0.000) | 68701.693 (0.002) | 15470.121 (0.010) | 808.184(0.000) |
| | -1 $\sigma$ | 465182.975 (-0.002) | 6383.502 (-0.002) | 4384.296 (-0.000) | 68463.958 (-0.002) | 15203.932 (-0.008) | 808.064 (-0.000) |
| COHCCScale2018 | +1 $\sigma$ | 468319.898 (0.003) | 6460.607 (0.010) | 4384.601 (0.000) | 69294.330 (0.011) | 15365.434 (0.003) | 808.148(0.000) |
| | -1 $\sigma$ | 465777.906 (-0.011) | 6331.858 (-0.010) | 4384.199 (-0.000) | 67841.351 (-0.011) | 15273.234 (-0.003) | 808.086 (-0.000) |
| COHNCScale2018 | +1 $\sigma$ | 467048.902 (0.000) | 6396.233 (0.000) | 4384.680 (0.000) | 68567.840 (0.000) | 15319.334 (0.000) | 808.178(0.000) |
| | -1 $\sigma$ | 467048.902 (0.000) | 6396.233 (0.000) | 4384.119 (-0.000) | 68567.840 (0.000) | 15319.334 (0.000) | 808.055 (-0.000) |
| MaCCRES | +1 $\sigma$ | 527353.841 (0.121) | 7151.197 (0.111) | 4390.864 (0.001) | 77256.691 (0.119) | 16641.481 (0.083) | 808.930(0.001) |
| | -1 $\sigma$ | 406675.154 (-0.111) | 5833.479 (-0.092) | 4379.518 (-0.001) | 61352.497 (-0.111) | 13913.700 (-0.096) | 807.638 (-0.001) |
| MaNCRES | +1 $\sigma$ | 467048.902 (0.000) | 6396.233 (0.000) | 4832.179 (0.097) | 68567.840 (0.000) | 15319.334 (0.000) | 925.026(0.135) |
| | -1 $\sigma$ | 467048.902 (0.000) | 6396.233 (0.000) | 4046.567 (-0.080) | 68567.840 (0.000) | 15319.334 (0.000) | 731.737 (-0.099) |
| MvCCRES | +1 $\sigma$ | 503322.611 (0.075) | 6623.561 (0.035) | 4387.806 (0.001) | 71465.060 (0.041) | 16102.614 (0.050) | 808.487(0.000) |
| | -1 $\sigma$ | 434142.217 (-0.026) | 6284.144 (-0.018) | 4381.691 (-0.001) | 66788.613 (-0.026) | 14587.535 (-0.049) | 807.877 (-0.000) |
| CCQEPauliSupViaKF | +1 $\sigma$ | 466830.247 (-0.000) | 6392.377 (-0.001) | 4385.858 (0.000) | 68520.503 (-0.001) | 15286.846 (-0.002) | 808.035(-0.000) |
| | -1 $\sigma$ | 467167.352 (0.000) | 6399.386 (0.000) | 4385.943 (0.000) | 68595.570 (0.000) | 15336.753 (0.001) | 808.069 (-0.000) |
| FrElas_N | +1 $\sigma$ | 470060.661 (0.006) | 6366.127 (-0.005) | 4380.292 (-0.001) | 68434.894 (-0.002) | 15462.478 (0.009) | 805.148(-0.004) |
| | -1 $\sigma$ | 464067.996 (0.002) | 6427.058 (0.005) | 4391.497 (0.002) | 68689.248 (0.002) | 15176.810 (-0.009) | 810.960 (0.004) |
| FrCEx_N | +1 $\sigma$ | 466245.063 (-0.002) | 6417.399 (0.003) | 4382.257 (-0.000) | 68692.387 (0.002) | 15271.096 (-0.003) | 807.940(-0.000) |
| | -1 $\sigma$ | 467871.834 (-0.002) | 6376.568 (-0.003) | 4389.678 (0.001) | 68434.284 (-0.002) | 15368.271 (0.003) | 808.137 (0.000) |
| FrAbs_N | +1 $\sigma$ | 465704.674 (-0.003) | 6398.087 (0.000) | 4391.348 (0.002) | 68522.300 (-0.001) | 15267.710 (-0.003) | 809.238(0.001) |
| | -1 $\sigma$ | 468412.294 (0.001) | 6394.525 (-0.000) | 4380.455 (-0.001) | 68603.422 (0.001) | 15371.602 (0.003) | 806.857 (-0.002) |
| FrInel_pi | +1 $\sigma$ | 464143.682 (-0.006) | 6404.752 (0.001) | 4461.840 (0.018) | 68526.586 (-0.001) | 15234.983 (-0.006) | 821.511(0.016) |
| | -1 $\sigma$ | 469921.651 (0.001) | 6387.124 (-0.001) | 4308.977 (-0.017) | 68603.260 (0.001) | 15403.875 (0.006) | 795.746 (-0.015) |
| FormZone | +1 $\sigma$ | 477659.684 (0.022) | 6550.699 (0.024) | 4671.759 (0.063) | 69769.347 (0.017) | 15630.120 (0.020) | 864.597(0.068) |
| | -1 $\sigma$ | 451173.830 (-0.023) | 6153.780 (-0.039) | 3938.496 (-0.107) | 67009.321 (-0.023) | 14773.530 (-0.036) | 718.053 (-0.118) |

**Quartile 4**

| | | Neutrino Beam | | | Antineutrino Beam | | |
|---|---|---|---|---|---|---|---|
| Prediction | Shift | Right Sign ($\nu_\mu$) | Wrong Sign ($\bar{\nu}_\mu$) | Background | Right Sign ($\bar{\nu}_\mu$) | Wrong Sign ($\nu_\mu$) | Background |
| Nominal | - | 467048.902 | 6396.233 | 4384.400 | 68567.840 | 15319.334 | 808.117 |
| genie_small_pc00 | +1 $\sigma$ | 472259.730 (0.011) | 6468.583 (0.011) | 5228.368 (0.176) | 69201.205 (0.009) | 15460.930 (0.009) | 892.485(0.099) |
| | -1 $\sigma$ | 461852.119 (-0.009) | 6324.369 (-0.011) | 3543.439 (-0.212) | 67924.693 (-0.009) | 15178.345 (-0.009) | 723.616 (-0.110) |
| genie_small_pc01 | +1 $\sigma$ | 463398.418 (-0.008) | 6348.331 (-0.008) | 4527.077 (0.032) | 67964.353 (-0.009) | 15206.077 (-0.007) | 741.079(-0.087) |
| | -1 $\sigma$ | 470713.430 (0.009) | 6444.621 (0.008) | 4244.730 (-0.032) | 69161.545 (0.009) | 15433.198 (0.007) | 875.022 (0.080) |
| genie_small_pc02 | +1 $\sigma$ | 474106.963 (0.015) | 6517.561 (0.019) | 4394.039 (0.002) | 68595.769 (0.000) | 15410.584 (0.006) | 808.911(0.001) |
| | -1 $\sigma$ | 460004.885 (-0.001) | 6275.391 (-0.019) | 4377.768 (-0.002) | 68530.129 (-0.001) | 15228.691 (-0.006) | 807.189 (-0.001) |
| genie_small_pc03 | +1 $\sigma$ | 471116.526 (0.009) | 6457.282 (0.009) | 4336.858 (-0.011) | 69170.670 (0.009) | 15366.605 (0.003) | 803.399(-0.006) |
| | -1 $\sigma$ | 462995.323 (-0.009) | 6335.670 (-0.010) | 4434.949 (0.011) | 67955.229 (-0.009) | 15272.671 (-0.003) | 812.701 (0.006) |
| genie_small_pc04 | +1 $\sigma$ | 464781.227 (-0.005) | 6362.259 (-0.005) | 4331.873 (-0.012) | 68195.184 (-0.005) | 15282.136 (-0.002) | 801.420(-0.008) |
| | -1 $\sigma$ | 469330.622 (0.005) | 6430.692 (0.005) | 4439.934 (0.013) | 68930.714 (0.005) | 15357.139 (0.002) | 814.680 (0.008) |
| NuTauScale | +1 $\sigma$ | 467055.924 (0.000) | 6396.476 (0.000) | 4385.904 (0.000) | 68562.949 (-0.000) | 15319.638(0.000) | 808.050 (-0.000) |
| ppfx_hadp_beam_pc00 | +1 $\sigma$ | 472890.083 (0.012) | 6570.703 (0.027) | 4457.639 (0.017) | 70513.710 (0.028) | 15543.225 (0.015) | 832.386(0.030) |
| | -1 $\sigma$ | 461207.721 (-0.029) | 6221.762 (-0.028) | 4311.161 (-0.017) | 66621.970 (-0.029) | 15095.443 (-0.015) | 783.848 (-0.030) |
| ppfx_hadp_beam_pc01 | +1 $\sigma$ | 500926.798 (0.070) | 7288.443 (0.130) | 4718.859 (0.073) | 73167.875 (0.065) | 17692.445 (0.144) | 883.115(0.089) |
| | -1 $\sigma$ | 433171.006 (-0.069) | 5504.022 (-0.150) | 4049.941 (-0.079) | 63967.806 (-0.069) | 12946.223 (-0.168) | 733.119 (-0.097) |
| ppfx_hadp_beam_pc02 | +1 $\sigma$ | 460767.662 (-0.014) | 6459.016 (0.010) | 4261.906 (-0.028) | 68933.772 (0.005) | 15106.049 (-0.014) | 795.734(-0.015) |
| | -1 $\sigma$ | 473330.143 (-0.005) | 6333.449 (-0.010) | 4506.894 (0.028) | 68201.908 (-0.005) | 15532.618 (0.014) | 820.500 (0.015) |
| ppfx_hadp_beam_pc03 | +1 $\sigma$ | 467060.594 (0.000) | 6429.336 (0.005) | 4400.026 (0.004) | 69551.160 (0.014) | 15247.264 (-0.005) | 823.423(0.019) |
| | -1 $\sigma$ | 467037.210 (-0.014) | 6363.129 (-0.005) | 4368.773 (-0.004) | 67584.520 (-0.014) | 15391.403 (0.005) | 792.811 (-0.019) |
| ppfx_hadp_beam_pc04 | +1 $\sigma$ | 468781.546 (0.004) | 6524.976 (0.020) | 4411.215 (0.006) | 69005.278 (0.006) | 15531.453 (0.014) | 816.634(0.010) |
| | -1 $\sigma$ | 465316.258 (-0.006) | 6267.489 (-0.020) | 4357.585 (-0.006) | 68130.402 (-0.006) | 15107.215 (-0.014) | 799.599 (-0.011) |
| Calibration | +1 $\sigma$ | 462750.761 (-0.009) | 6293.842 (-0.016) | 3684.533 (-0.173) | 70035.352 (0.021) | 15057.554 (-0.017) | 665.727(-0.193) |
| | -1 $\sigma$ | 461385.608 (-0.036) | 6108.492 (-0.046) | 5074.374 (0.146) | 66110.858 (-0.036) | 15280.609 (-0.003) | 966.174 (0.178) |
| CalibShape | +1 $\sigma$ | 469330.960 (0.005) | 6593.455 (0.030) | 4779.119 (0.086) | 68912.353 (0.005) | 15404.392(0.006) | 846.473 (0.046) |
| Lightlevel | +1 $\sigma$ | 466361.784 (-0.001) | 6312.297 (-0.013) | 4569.543 (0.041) | 67927.388 (-0.009) | 15313.348 (-0.000) | 825.546(0.021) |
| | -1 $\sigma$ | 473976.024 (0.007) | 6367.877 (-0.004) | 4603.048 (0.049) | 69049.394 (0.007) | 15498.856 (0.012) | 832.721 (0.030) |
| Cherenkov | +1 $\sigma$ | 467142.443 (0.000) | 6307.507 (-0.014) | 4651.698 (0.059) | 68001.761 (-0.008) | 15334.312(0.001) | 849.339 (0.050) |
| NeutronEvisPrimariesSyst2018 | +1 $\sigma$ | 475674.242 (0.018) | 6730.094 (0.051) | 4461.957 (0.018) | 72064.183 (0.050) | 15497.742 (0.012) | 794.679(-0.017) |
| | -1 $\sigma$ | 458208.622 (-0.038) | 6142.975 (-0.040) | 4331.210 (-0.012) | 66004.046 (-0.038) | 14926.971 (-0.026) | 768.859 (-0.050) |
| AbsMuEScale2017 | +1 $\sigma$ | 471992.200 (0.011) | 6506.793 (0.017) | 4409.778 (0.006) | 69358.959 (0.011) | 15473.403 (0.010) | 812.026(0.005) |
| | -1 $\sigma$ | 462175.295 (-0.011) | 6290.716 (-0.017) | 4357.474 (-0.006) | 67798.872 (-0.011) | 15158.627 (-0.011) | 802.787 (-0.007) |
| RelMuEScale2017 | +1 $\sigma$ | 467903.710 (0.002) | 6418.733 (0.004) | 4389.648 (0.001) | 68727.139 (0.002) | 15349.783 (0.002) | 808.885(0.001) |
| | -1 $\sigma$ | 466211.310 (-0.002) | 6377.475 (-0.003) | 4380.530 (-0.001) | 68415.836 (-0.002) | 15288.420 (-0.002) | 807.277 (-0.001) |

**Table C.5:** Expected number of events at the ND from the +1 or -1 $\sigma$ systematic shifts in the MC, quartile 4, with an exposure to 8.025 $\times 10^{20}$ and 3.097 $\times 10^{20}$ POT for the production of the neutrino and antineutrino beam respectively. The numbers in parentheses correspond to relative difference with the mean between the nominal and the shifted predictions.

## C.2 Far Detector

**All quartiles**

| | | Neutrino Beam | | | Antineutrino Beam | | |
|---|---|---|---|---|---|---|---|
| Prediction | Shift | Right Sign ($\nu_\mu$) | Wrong Sign ($\bar{\nu}_\mu$) | Background | Right Sign ($\bar{\nu}_\mu$) | Wrong Sign ($\nu_\mu$) | Background |
| Nominal | - | 107.786 | 7.256 | 1.946 | 68.186 | 22.992 | 1.262 |
| MECEnuShapeNu | +1 $\sigma$ | 107.206 (-0.005) | 7.067 (-0.026) | 1.958 (0.006) | 67.890 (-0.004) | 23.391 (0.017) | 1.267(0.004) |
| | -1 $\sigma$ | 108.390 (0.004) | 7.461 (0.028) | 1.935 (-0.006) | 68.488 (0.004) | 22.582 (-0.018) | 1.258 (-0.004) |
| MECEnuShapeAntiNu | +1 $\sigma$ | 107.662 (-0.001) | 7.431 (0.024) | 1.947 (0.000) | 68.200 (0.000) | 22.510 (-0.021) | 1.267(0.004) |
| | -1 $\sigma$ | 107.911 (-0.000) | 7.080 (-0.025) | 1.945 (-0.000) | 68.165 (-0.000) | 23.510 (0.022) | 1.257 (-0.004) |
| MECShape2018Nu | +1 $\sigma$ | 107.759 (-0.000) | 7.150 (-0.015) | 1.950 (0.002) | 68.081 (-0.002) | 23.006 (0.001) | 1.263(0.000) |
| | -1 $\sigma$ | 108.863 (0.006) | 7.550 (0.040) | 1.926 (-0.011) | 68.571 (0.006) | 22.651 (-0.015) | 1.253 (-0.007) |
| MECShape2018AntiNu | +1 $\sigma$ | 107.874 (0.001) | 7.128 (-0.018) | 1.947 (0.001) | 68.983 (0.012) | 23.480 (0.021) | 1.264(0.001) |
| | -1 $\sigma$ | 107.794 (-0.003) | 7.272 (0.002) | 1.945 (-0.001) | 67.988 (-0.003) | 22.990 (-0.000) | 1.258 (-0.003) |
| MECInitStateNPFracNu | +1 $\sigma$ | 107.503 (-0.003) | 7.183 (-0.010) | 1.952 (0.003) | 68.089 (-0.001) | 23.120 (0.006) | 1.265(0.002) |
| | -1 $\sigma$ | 108.076 (0.001) | 7.330 (0.010) | 1.940 (-0.003) | 68.283 (0.001) | 22.862 (-0.006) | 1.259 (-0.002) |
| MECInitStateNPFracAntiNu | +1 $\sigma$ | 107.746 (-0.000) | 7.315 (0.008) | 1.947 (0.000) | 68.230 (0.001) | 22.832 (-0.007) | 1.265(0.002) |
| | -1 $\sigma$ | 107.826 (-0.001) | 7.197 (-0.008) | 1.945 (-0.000) | 68.140 (-0.001) | 23.154 (0.007) | 1.260 (-0.002) |
| MaCCQE_reduced_2018 | +1 $\sigma$ | 108.360 (0.005) | 7.290 (0.005) | 1.959 (0.007) | 68.502 (0.005) | 23.075 (0.004) | 1.274(0.009) |
| | -1 $\sigma$ | 107.221 (-0.005) | 7.223 (-0.005) | 1.934 (-0.006) | 67.878 (-0.005) | 22.910 (-0.004) | 1.251 (-0.009) |
| RPAShapeRES2018 | +1 $\sigma$ | 103.646 (-0.039) | 7.094 (-0.023) | 1.947 (0.000) | 66.323 (-0.028) | 21.903 (-0.048) | 1.262(0.000) |
| | -1 $\sigma$ | 107.786 (0.000) | 7.256 (0.000) | 1.946 (0.000) | 68.186 (0.000) | 22.992 (0.000) | 1.262 (0.000) |
| RPAShapeenh2018 | +1 $\sigma$ | 108.346 (0.005) | 7.299 (0.006) | 1.962 (0.008) | 68.507 (0.005) | 23.041 (0.002) | 1.276(0.011) |
| | -1 $\sigma$ | 107.414 (-0.004) | 7.217 (-0.005) | 1.934 (-0.006) | 67.942 (-0.004) | 22.982 (-0.000) | 1.251 (-0.009) |
| COHCCScale2018 | +1 $\sigma$ | 107.548 (-0.002) | 7.250 (-0.001) | 1.947 (0.000) | 68.014 (-0.003) | 22.874 (-0.005) | 1.263(0.001) |
| | -1 $\sigma$ | 108.026 (0.003) | 7.262 (0.001) | 1.945 (-0.000) | 68.360 (0.003) | 23.111 (0.005) | 1.261 (-0.001) |
| COHNCScale2018 | +1 $\sigma$ | 107.786 (-0.000) | 7.256 (-0.000) | 1.946 (0.000) | 68.186 (-0.000) | 22.992 (-0.000) | 1.262(0.000) |
| | -1 $\sigma$ | 107.786 (0.000) | 7.256 (0.000) | 1.946 (0.000) | 68.186 (0.000) | 22.992 (0.000) | 1.262 (-0.000) |
| MaCCRES | +1 $\sigma$ | 111.183 (0.031) | 7.456 (0.027) | 2.047 (0.050) | 70.133 (0.028) | 23.860 (0.037) | 1.345(0.064) |
| | -1 $\sigma$ | 105.223 (-0.012) | 7.241 (-0.002) | 1.867 (-0.042) | 67.378 (-0.012) | 22.343 (-0.029) | 1.204 (-0.047) |
| MaNCRES | +1 $\sigma$ | 107.758 (-0.000) | 7.254 (-0.000) | 2.062 (0.058) | 68.165 (-0.000) | 22.984 (-0.000) | 1.351(0.068) |
| | -1 $\sigma$ | 107.808 (0.000) | 7.258 (0.000) | 1.856 (-0.048) | 68.200 (0.000) | 22.998 (0.000) | 1.201 (-0.049) |
| MvCCRES | +1 $\sigma$ | 109.844 (0.019) | 7.280 (0.003) | 1.999 (0.027) | 68.909 (0.011) | 23.611 (0.027) | 1.301(0.031) |
| | -1 $\sigma$ | 106.113 (-0.004) | 7.298 (0.006) | 1.904 (-0.022) | 67.904 (-0.004) | 22.455 (-0.024) | 1.234 (-0.023) |
| CCQEPauliSupViaKF | +1 $\sigma$ | 108.410 (0.006) | 7.244 (-0.002) | 1.943 (-0.002) | 68.528 (0.005) | 23.169 (0.008) | 1.259(-0.003) |
| | -1 $\sigma$ | 107.132 (-0.006) | 7.268 (0.002) | 1.949 (0.002) | 67.774 (-0.006) | 22.794 (-0.009) | 1.265 (0.002) |
| FrElas_N | +1 $\sigma$ | 107.540 (-0.002) | 7.254 (-0.000) | 1.943 (-0.002) | 68.243 (0.001) | 23.018 (0.001) | 1.259(-0.003) |
| | -1 $\sigma$ | 108.044 (-0.001) | 7.253 (-0.000) | 1.950 (0.002) | 68.117 (-0.001) | 22.961 (-0.001) | 1.265 (0.003) |
| FrCEx_N | +1 $\sigma$ | 107.891 (0.001) | 7.256 (-0.000) | 1.946 (0.000) | 68.138 (-0.001) | 22.984 (-0.000) | 1.262(0.000) |
| | -1 $\sigma$ | 107.684 (0.001) | 7.255 (-0.000) | 1.947 (0.000) | 68.237 (0.001) | 23.001 (0.000) | 1.262 (0.000) |
| FrAbs_N | +1 $\sigma$ | 107.877 (0.001) | 7.263 (0.001) | 1.950 (0.002) | 68.200 (0.000) | 22.995 (0.000) | 1.265(0.002) |
| | -1 $\sigma$ | 107.704 (-0.000) | 7.249 (-0.001) | 1.943 (-0.002) | 68.172 (-0.000) | 22.991 (-0.000) | 1.260 (-0.002) |
| FrInel_pi | +1 $\sigma$ | 108.046 (0.002) | 7.278 (0.003) | 1.969 (0.012) | 68.218 (0.000) | 23.007 (0.001) | 1.274(0.009) |
| | -1 $\sigma$ | 107.537 (-0.000) | 7.233 (-0.003) | 1.923 (-0.012) | 68.157 (-0.000) | 22.986 (-0.000) | 1.250 (-0.009) |
| FormZone | +1 $\sigma$ | 107.847 (0.001) | 7.193 (-0.009) | 2.059 (0.056) | 68.120 (-0.001) | 23.064 (0.003) | 1.313(0.040) |
| | -1 $\sigma$ | 107.528 (0.002) | 7.376 (0.016) | 1.771 (-0.094) | 68.311 (0.002) | 22.714 (-0.012) | 1.171 (-0.075) |

**All quartiles**

| | | Neutrino Beam | | | Antineutrino Beam | | |
|---|---|---|---|---|---|---|---|
| Prediction | Shift | Right Sign ($\nu_\mu$) | Wrong Sign ($\bar{\nu}_\mu$) | Background | Right Sign ($\bar{\nu}_\mu$) | Wrong Sign ($\nu_\mu$) | Background |
| Nominal | - | 107.786 | 7.256 | 1.946 | 68.186 | 22.992 | 1.262 |
| genie_small_pc00 | +1 $\sigma$ | 107.725 (-0.001) | 7.250 (-0.001) | 2.199 (0.122) | 68.160 (-0.000) | 22.999 (0.000) | 1.357(0.072) |
| | -1 $\sigma$ | 107.854 (0.000) | 7.262 (0.001) | 1.694 (-0.139) | 68.212 (0.000) | 22.987 (-0.000) | 1.168 (-0.078) |
| genie_small_pc01 | +1 $\sigma$ | 107.839 (0.000) | 7.259 (0.000) | 1.983 (0.019) | 68.239 (0.001) | 23.010 (0.001) | 1.211(-0.042) |
| | -1 $\sigma$ | 107.741 (-0.001) | 7.252 (-0.000) | 1.910 (-0.019) | 68.133 (-0.001) | 22.976 (-0.001) | 1.314 (0.040) |
| genie_small_pc02 | +1 $\sigma$ | 107.649 (-0.001) | 7.230 (-0.004) | 1.953 (0.003) | 68.194 (0.000) | 23.097 (0.005) | 1.266(0.003) |
| | -1 $\sigma$ | 107.948 (-0.000) | 7.285 (0.004) | 1.940 (-0.003) | 68.178 (-0.000) | 22.887 (-0.005) | 1.259 (-0.002) |
| genie_small_pc03 | +1 $\sigma$ | 108.552 (0.007) | 7.295 (0.005) | 1.951 (0.002) | 68.594 (0.006) | 23.162 (0.007) | 1.262(-0.000) |
| | -1 $\sigma$ | 107.030 (-0.006) | 7.217 (-0.005) | 1.943 (-0.002) | 67.784 (-0.006) | 22.826 (-0.007) | 1.263 (0.001) |
| genie_small_pc04 | +1 $\sigma$ | 107.393 (-0.004) | 7.237 (-0.003) | 1.935 (-0.006) | 68.026 (-0.002) | 22.921 (-0.003) | 1.256(-0.005) |
| | -1 $\sigma$ | 108.187 (0.002) | 7.274 (0.002) | 1.958 (0.006) | 68.347 (0.002) | 23.066 (0.003) | 1.269 (0.005) |
| NuTauScale | +1 $\sigma$ | 107.790 (0.000) | 7.256 (-0.000) | 2.185 (0.115) | 68.186 (0.000) | 22.993(0.000) | 1.491 (0.166) |
| ppfx_hadp_beam_pc00 | +1 $\sigma$ | 107.395 (-0.004) | 7.388 (0.018) | 1.983 (0.019) | 68.054 (-0.002) | 23.064 (0.003) | 1.293(0.024) |
| | -1 $\sigma$ | 108.163 (0.002) | 7.112 (-0.020) | 1.908 (-0.020) | 68.323 (0.002) | 22.885 (-0.005) | 1.231 (-0.025) |
| ppfx_hadp_beam_pc01 | +1 $\sigma$ | 107.648 (-0.001) | 7.461 (0.028) | 2.093 (0.073) | 67.562 (-0.009) | 23.630 (0.027) | 1.372(0.083) |
| | -1 $\sigma$ | 107.938 (0.011) | 6.981 (-0.039) | 1.798 (-0.079) | 68.920 (0.011) | 22.130 (-0.038) | 1.150 (-0.093) |
| ppfx_hadp_beam_pc02 | +1 $\sigma$ | 107.306 (-0.004) | 7.767 (0.068) | 1.919 (-0.014) | 68.717 (0.008) | 21.902 (-0.049) | 1.244(-0.015) |
| | -1 $\sigma$ | 108.174 (-0.008) | 6.812 (-0.063) | 1.972 (0.013) | 67.666 (-0.008) | 24.065 (0.046) | 1.280 (0.014) |
| ppfx_hadp_beam_pc03 | +1 $\sigma$ | 107.741 (-0.000) | 7.460 (0.028) | 1.949 (0.002) | 68.763 (0.008) | 22.081 (-0.040) | 1.273(0.009) |
| | -1 $\sigma$ | 107.834 (-0.010) | 7.048 (-0.029) | 1.943 (-0.002) | 67.517 (-0.010) | 24.011 (0.043) | 1.251 (-0.009) |
| ppfx_hadp_beam_pc04 | +1 $\sigma$ | 107.711 (-0.001) | 7.357 (0.014) | 1.962 (0.008) | 68.234 (0.001) | 22.987 (-0.000) | 1.276(0.010) |
| | -1 $\sigma$ | 107.862 (-0.001) | 7.153 (-0.014) | 1.931 (-0.008) | 68.137 (-0.001) | 22.997 (0.000) | 1.249 (-0.011) |
| Calibration | +1 $\sigma$ | 101.415 (-0.061) | 6.680 (-0.083) | 1.641 (-0.170) | 66.006 (-0.032) | 20.987 (-0.091) | 1.149(-0.094) |
| | -1 $\sigma$ | 112.241 (0.029) | 7.689 (0.058) | 2.145 (0.097) | 70.208 (0.029) | 25.016 (0.084) | 1.422 (0.119) |
| CalibShape | +1 $\sigma$ | 106.615 (-0.011) | 7.100 (-0.022) | 1.906 (-0.021) | 68.118 (-0.001) | 22.874(-0.005) | 1.291 (0.023) |
| Lightlevel | +1 $\sigma$ | 107.627 (-0.001) | 7.466 (0.029) | 1.949 (0.002) | 68.575 (0.006) | 23.212 (0.010) | 1.304(0.032) |
| | -1 $\sigma$ | 105.924 (-0.008) | 7.328 (0.010) | 1.896 (-0.026) | 67.630 (-0.008) | 22.654 (-0.015) | 1.270 (0.006) |
| Cherenkov | +1 $\sigma$ | 104.618 (-0.030) | 7.235 (-0.003) | 1.909 (-0.019) | 68.415 (0.003) | 23.209(0.009) | 1.310 (0.037) |
| NeutronEvisPrimariesSyst2018 | +1 $\sigma$ | 106.806 (-0.009) | 7.169 (-0.012) | 1.945 (-0.001) | 66.716 (-0.022) | 22.245 (-0.033) | 1.261(-0.001) |
| | -1 $\sigma$ | 109.327 (0.016) | 7.396 (0.019) | 1.948 (0.001) | 69.257 (0.016) | 23.369 (0.016) | 1.264 (0.001) |
| AbsMuEScale2017 | +1 $\sigma$ | 109.797 (0.018) | 7.502 (0.033) | 1.949 (0.001) | 69.350 (0.017) | 23.837 (0.036) | 1.265(0.002) |
| | -1 $\sigma$ | 105.850 (-0.016) | 7.017 (-0.034) | 1.944 (-0.001) | 67.071 (-0.016) | 22.192 (-0.035) | 1.260 (-0.002) |
| RelMuEScale2017 | +1 $\sigma$ | 108.224 (0.004) | 7.306 (0.007) | 1.946 (-0.000) | 68.426 (0.004) | 23.156 (0.007) | 1.262(-0.000) |
| | -1 $\sigma$ | 107.359 (-0.004) | 7.210 (-0.006) | 1.947 (0.000) | 67.945 (-0.004) | 22.826 (-0.007) | 1.263 (0.000) |

**Table C.6:** Expected number of selected events at the FD from the systematically shifted predictions, with extrapolation, without quartile separation. The proton exposure used is 9.480 $\times 10^{20}$ and 12.332 $\times 10^{20}$ POT for the production of the neutrino and antineutrino beam respectively. These numbers assume oscillations with $\sin^2\theta_{23} = 0.513$ and $\sin^2\bar{\theta}_{23} = 0.597$, and $\Delta m^2_{32} = 2.453$ and $\Delta\bar{m}^2_{32} = 2.532$, where the barred parameters determine antineutrino oscillations.. The numbers in parentheses correspond to relative difference with the mean between the nominal and the shifted predictions.

**Quartile 1**

| | | Neutrino Beam | | | Antineutrino Beam | | |
|---|---|---|---|---|---|---|---|
| Prediction | Shift | Right Sign ($\nu_\mu$) | Wrong Sign ($\bar{\nu}_\mu$) | Background | Right Sign ($\bar{\nu}_\mu$) | Wrong Sign ($\nu_\mu$) | Background |
| Nominal | - | 26.495 | 3.197 | 0.198 | 20.907 | 3.664 | 0.113 |
| MECEnuShapeNu | +1 $\sigma$ | 26.471 (-0.001) | 3.076 (-0.039) | 0.202 (0.021) | 20.840 (-0.003) | 3.757 (0.025) | 0.114(0.006) |
| | -1 $\sigma$ | 26.524 (0.003) | 3.329 (0.041) | 0.194 (-0.021) | 20.974 (0.003) | 3.570 (-0.026) | 0.112 (-0.006) |
| MECEnuShapeAntiNu | +1 $\sigma$ | 26.422 (-0.003) | 3.306 (0.034) | 0.198 (0.002) | 20.893 (-0.001) | 3.550 (-0.032) | 0.115(0.016) |
| | -1 $\sigma$ | 26.569 (0.001) | 3.087 (-0.035) | 0.197 (-0.002) | 20.924 (0.001) | 3.787 (0.033) | 0.111 (-0.017) |
| MECShape2018Nu | +1 $\sigma$ | 26.605 (0.004) | 3.427 (0.069) | 0.187 (-0.058) | 21.085 (0.008) | 3.390 (-0.077) | 0.110(-0.031) |
| | -1 $\sigma$ | 26.607 (-0.005) | 3.134 (-0.020) | 0.206 (0.041) | 20.798 (-0.005) | 3.852 (0.050) | 0.116 (0.026) |
| MECShape2018AntiNu | +1 $\sigma$ | 26.608 (0.004) | 2.970 (-0.073) | 0.196 (-0.008) | 20.684 (-0.011) | 4.003 (0.088) | 0.105(-0.074) |
| | -1 $\sigma$ | 26.451 (0.018) | 3.332 (0.041) | 0.199 (0.006) | 21.279 (0.018) | 3.533 (-0.036) | 0.118 (0.043) |
| MECInitStateNPFracNu | +1 $\sigma$ | 26.495 (-0.000) | 3.155 (-0.013) | 0.199 (0.007) | 20.887 (-0.001) | 3.708 (0.012) | 0.113(0.003) |
| | -1 $\sigma$ | 26.497 (0.001) | 3.240 (0.014) | 0.196 (-0.007) | 20.926 (0.001) | 3.619 (-0.012) | 0.113 (-0.003) |
| MECInitStateNPFracAntiNu | +1 $\sigma$ | 26.464 (-0.001) | 3.242 (0.014) | 0.198 (0.002) | 20.899 (-0.000) | 3.609 (-0.015) | 0.115(0.013) |
| | -1 $\sigma$ | 26.527 (0.000) | 3.151 (-0.014) | 0.197 (-0.002) | 20.915 (0.000) | 3.721 (0.015) | 0.112 (-0.013) |
| MaCCQE_reduced_2018 | +1 $\sigma$ | 26.637 (0.005) | 3.216 (0.006) | 0.201 (0.018) | 20.996 (0.004) | 3.679 (0.004) | 0.116(0.022) |
| | -1 $\sigma$ | 26.354 (-0.004) | 3.178 (-0.006) | 0.194 (-0.018) | 20.817 (-0.004) | 3.648 (-0.004) | 0.111 (-0.022) |
| RPAShapeRES2018 | +1 $\sigma$ | 26.202 (-0.011) | 3.127 (-0.022) | 0.201 (0.016) | 20.782 (-0.006) | 3.656 (-0.002) | 0.114(0.009) |
| | -1 $\sigma$ | 26.495 (0.000) | 3.197 (0.000) | 0.198 (0.000) | 20.907 (0.000) | 3.664 (0.000) | 0.113 (0.000) |
| RPAShapeenh2018 | +1 $\sigma$ | 26.600 (0.004) | 3.218 (0.006) | 0.202 (0.023) | 20.953 (0.002) | 3.671 (0.002) | 0.116(0.029) |
| | -1 $\sigma$ | 26.417 (-0.002) | 3.178 (-0.006) | 0.194 (-0.020) | 20.872 (-0.002) | 3.659 (-0.001) | 0.110 (-0.026) |
| COHCCScale2018 | +1 $\sigma$ | 26.468 (-0.001) | 3.193 (-0.001) | 0.198 (0.001) | 20.899 (-0.000) | 3.663 (-0.000) | 0.113(0.000) |
| | -1 $\sigma$ | 26.524 (0.000) | 3.201 (0.001) | 0.197 (-0.001) | 20.914 (0.000) | 3.665 (0.000) | 0.113 (-0.000) |
| COHNCScale2018 | +1 $\sigma$ | 26.495 (0.000) | 3.197 (0.000) | 0.198 (0.000) | 20.907 (0.000) | 3.664 (0.000) | 0.113(0.000) |
| | -1 $\sigma$ | 26.495 (0.000) | 3.197 (0.000) | 0.198 (0.000) | 20.907 (0.000) | 3.664 (0.000) | 0.113 (0.000) |
| MaCCRES | +1 $\sigma$ | 26.503 (0.000) | 3.195 (-0.001) | 0.201 (0.015) | 20.875 (-0.001) | 3.672 (0.002) | 0.114(0.011) |
| | -1 $\sigma$ | 26.507 (0.002) | 3.210 (0.004) | 0.194 (-0.016) | 20.952 (0.002) | 3.655 (-0.003) | 0.112 (-0.012) |
| MaNCRES | +1 $\sigma$ | 26.493 (-0.000) | 3.196 (-0.000) | 0.207 (0.044) | 20.905 (-0.000) | 3.664 (-0.000) | 0.116(0.023) |
| | -1 $\sigma$ | 26.498 (0.000) | 3.197 (0.000) | 0.190 (-0.042) | 20.908 (0.000) | 3.664 (0.000) | 0.111 (-0.022) |
| MvCCRES | +1 $\sigma$ | 26.512 (0.001) | 3.192 (-0.001) | 0.199 (0.007) | 20.894 (-0.001) | 3.672 (0.002) | 0.114(0.005) |
| | -1 $\sigma$ | 26.482 (0.001) | 3.205 (0.002) | 0.196 (-0.007) | 20.920 (0.001) | 3.655 (-0.003) | 0.113 (-0.005) |
| CCQEPauliSupViaKF | +1 $\sigma$ | 26.680 (0.007) | 3.217 (0.006) | 0.194 (-0.018) | 21.033 (0.006) | 3.663 (-0.000) | 0.110(-0.026) |
| | -1 $\sigma$ | 26.256 (-0.009) | 3.176 (-0.007) | 0.200 (0.013) | 20.716 (-0.009) | 3.655 (-0.002) | 0.115 (0.021) |
| FrElas_N | +1 $\sigma$ | 26.308 (-0.007) | 3.242 (0.014) | 0.194 (-0.021) | 20.846 (-0.003) | 3.595 (-0.019) | 0.112(-0.013) |
| | -1 $\sigma$ | 26.692 (0.002) | 3.147 (-0.016) | 0.201 (0.019) | 20.951 (0.002) | 3.732 (0.018) | 0.115 (0.012) |
| FrCEx_N | +1 $\sigma$ | 26.579 (0.003) | 3.179 (-0.006) | 0.198 (0.003) | 20.892 (-0.001) | 3.686 (0.006) | 0.113(-0.000) |
| | -1 $\sigma$ | 26.409 (0.000) | 3.215 (0.006) | 0.197 (-0.003) | 20.915 (0.000) | 3.643 (-0.006) | 0.113 (0.001) |
| FrAbs_N | +1 $\sigma$ | 26.554 (0.002) | 3.191 (-0.002) | 0.199 (0.006) | 20.939 (0.002) | 3.682 (0.005) | 0.114(0.006) |
| | -1 $\sigma$ | 26.438 (-0.002) | 3.202 (0.002) | 0.197 (-0.006) | 20.870 (-0.002) | 3.648 (-0.004) | 0.113 (-0.005) |
| FrInel_pi | +1 $\sigma$ | 26.504 (0.000) | 3.184 (-0.004) | 0.199 (0.006) | 20.909 (0.000) | 3.678 (0.004) | 0.113(0.002) |
| | -1 $\sigma$ | 26.486 (-0.000) | 3.210 (0.004) | 0.197 (-0.006) | 20.903 (-0.000) | 3.650 (-0.004) | 0.113 (-0.002) |
| FormZone | +1 $\sigma$ | 26.484 (-0.000) | 3.195 (-0.001) | 0.199 (0.006) | 20.903 (-0.000) | 3.663 (-0.000) | 0.113(0.002) |
| | -1 $\sigma$ | 26.511 (0.000) | 3.200 (0.001) | 0.194 (-0.018) | 20.913 (0.000) | 3.666 (0.001) | 0.112 (-0.009) |

**Quartile 1**

| | | Neutrino Beam | | | Antineutrino Beam | | |
|---|---|---|---|---|---|---|---|
| Prediction | Shift | Right Sign ($\nu_\mu$) | Wrong Sign ($\bar{\nu}_\mu$) | Background | Right Sign ($\bar{\nu}_\mu$) | Wrong Sign ($\nu_\mu$) | Background |
| Nominal | - | 26.495 | 3.197 | 0.198 | 20.907 | 3.664 | 0.113 |
| genie_small_pc00 | +1 $\sigma$ | 26.471 (-0.001) | 3.194 (-0.001) | 0.209 (0.055) | 20.886 (-0.001) | 3.663 (-0.000) | 0.115(0.018) |
| | -1 $\sigma$ | 26.521 (0.001) | 3.199 (0.001) | 0.186 (-0.059) | 20.924 (0.001) | 3.666 (0.001) | 0.111 (-0.017) |
| genie_small_pc01 | +1 $\sigma$ | 26.512 (0.001) | 3.198 (0.000) | 0.199 (0.008) | 20.920 (0.001) | 3.668 (0.001) | 0.111(-0.017) |
| | -1 $\sigma$ | 26.480 (-0.001) | 3.195 (-0.001) | 0.196 (-0.008) | 20.889 (-0.001) | 3.662 (-0.000) | 0.115 (0.018) |
| genie_small_pc02 | +1 $\sigma$ | 26.390 (-0.004) | 3.184 (-0.004) | 0.199 (0.005) | 20.873 (-0.002) | 3.667 (0.001) | 0.114(0.004) |
| | -1 $\sigma$ | 26.608 (0.001) | 3.210 (0.004) | 0.197 (-0.004) | 20.937 (0.001) | 3.663 (-0.000) | 0.113 (-0.003) |
| genie_small_pc03 | +1 $\sigma$ | 26.811 (0.012) | 3.224 (0.009) | 0.198 (-0.000) | 21.145 (0.011) | 3.699 (0.010) | 0.113(-0.004) |
| | -1 $\sigma$ | 26.189 (-0.011) | 3.169 (-0.009) | 0.198 (0.000) | 20.677 (-0.011) | 3.632 (-0.009) | 0.114 (0.005) |
| genie_small_pc04 | +1 $\sigma$ | 26.281 (-0.008) | 3.177 (-0.006) | 0.197 (-0.001) | 20.789 (-0.006) | 3.644 (-0.005) | 0.113(0.002) |
| | -1 $\sigma$ | 26.714 (0.006) | 3.216 (0.006) | 0.198 (0.002) | 21.023 (0.006) | 3.686 (0.006) | 0.113 (-0.001) |
| NuTauScale | +1 $\sigma$ | 26.496 (0.000) | 3.197 (-0.000) | 0.246 (0.219) | 20.905 (-0.000) | 3.665(0.000) | 0.147 (0.263) |
| ppfx_hadp_beam_pc00 | +1 $\sigma$ | 26.403 (-0.004) | 3.260 (0.019) | 0.202 (0.021) | 20.844 (-0.003) | 3.672 (0.002) | 0.116(0.024) |
| | -1 $\sigma$ | 26.585 (0.003) | 3.129 (-0.021) | 0.193 (-0.023) | 20.973 (0.003) | 3.650 (-0.004) | 0.110 (-0.026) |
| ppfx_hadp_beam_pc01 | +1 $\sigma$ | 26.423 (-0.003) | 3.281 (0.026) | 0.213 (0.075) | 20.805 (-0.005) | 3.776 (0.030) | 0.122(0.079) |
| | -1 $\sigma$ | 26.580 (0.006) | 3.082 (-0.037) | 0.182 (-0.082) | 21.026 (0.006) | 3.516 (-0.041) | 0.104 (-0.087) |
| ppfx_hadp_beam_pc02 | +1 $\sigma$ | 26.391 (-0.004) | 3.424 (0.069) | 0.196 (-0.009) | 21.011 (0.005) | 3.456 (-0.058) | 0.112(-0.006) |
| | -1 $\sigma$ | 26.581 (-0.005) | 3.002 (-0.063) | 0.199 (0.008) | 20.803 (-0.005) | 3.872 (0.055) | 0.114 (0.005) |
| ppfx_hadp_beam_pc03 | +1 $\sigma$ | 26.471 (-0.001) | 3.278 (0.025) | 0.198 (0.003) | 20.998 (0.004) | 3.472 (-0.054) | 0.114(0.006) |
| | -1 $\sigma$ | 26.521 (-0.005) | 3.114 (-0.026) | 0.197 (-0.003) | 20.794 (-0.005) | 3.886 (0.059) | 0.112 (-0.006) |
| ppfx_hadp_beam_pc04 | +1 $\sigma$ | 26.467 (-0.001) | 3.241 (0.014) | 0.200 (0.010) | 20.930 (0.001) | 3.659 (-0.001) | 0.114(0.011) |
| | -1 $\sigma$ | 26.524 (-0.001) | 3.153 (-0.014) | 0.196 (-0.010) | 20.883 (-0.001) | 3.669 (0.001) | 0.112 (-0.011) |
| Calibration | +1 $\sigma$ | 24.797 (-0.066) | 3.025 (-0.055) | 0.170 (-0.151) | 20.083 (-0.040) | 3.311 (-0.101) | 0.100(-0.125) |
| | -1 $\sigma$ | 26.842 (0.030) | 3.191 (-0.002) | 0.219 (0.104) | 21.542 (0.030) | 3.935 (0.071) | 0.129 (0.128) |
| CalibShape | +1 $\sigma$ | 25.423 (-0.041) | 3.062 (-0.043) | 0.197 (-0.001) | 20.433 (-0.023) | 3.601(-0.017) | 0.115 (0.016) |
| Lightlevel | +1 $\sigma$ | 25.185 (-0.051) | 3.173 (-0.007) | 0.194 (-0.019) | 19.823 (-0.053) | 3.491 (-0.048) | 0.109(-0.039) |
| | -1 $\sigma$ | 24.433 (-0.106) | 3.126 (-0.022) | 0.182 (-0.082) | 18.806 (-0.106) | 3.343 (-0.092) | 0.104 (-0.083) |
| Cherenkov | +1 $\sigma$ | 24.421 (-0.081) | 3.040 (-0.050) | 0.187 (-0.057) | 19.446 (-0.072) | 3.427(-0.067) | 0.109 (-0.040) |
| NeutronEvisPrimariesSyst2018 | +1 $\sigma$ | 26.435 (-0.002) | 3.112 (-0.027) | 0.187 (-0.053) | 20.229 (-0.033) | 3.648 (-0.004) | 0.102(-0.102) |
| | -1 $\sigma$ | 27.033 (0.037) | 3.323 (0.039) | 0.214 (0.078) | 21.691 (0.037) | 3.667 (0.001) | 0.131 (0.146) |
| AbsMuEScale2017 | +1 $\sigma$ | 27.234 (0.027) | 3.385 (0.057) | 0.196 (-0.010) | 21.452 (0.026) | 3.942 (0.073) | 0.112(-0.007) |
| | -1 $\sigma$ | 25.788 (-0.024) | 3.026 (-0.055) | 0.199 (0.008) | 20.407 (-0.024) | 3.421 (-0.069) | 0.114 (0.012) |
| RelMuEScale2017 | +1 $\sigma$ | 26.814 (0.012) | 3.257 (0.019) | 0.198 (0.001) | 21.142 (0.011) | 3.759 (0.026) | 0.113(0.001) |
| | -1 $\sigma$ | 26.196 (-0.011) | 3.144 (-0.017) | 0.197 (-0.001) | 20.672 (-0.011) | 3.579 (-0.024) | 0.113 (-0.001) |

**Table C.7:** Expected number of selected events at the FD from the systematically shifted predictions, with extrapolation, in quartile 1. The proton exposure used is 9.480 $\times 10^{20}$ and 12.332 $\times 10^{20}$ POT for the production of the neutrino and antineutrino beam respectively. These numbers assume oscillations with $\sin^2\theta_{23} = 0.513$ and $\sin^2\bar{\theta}_{23} = 0.597$, and $\Delta m^2_{32} = 2.453$ and $\Delta\bar{m}^2_{32} = 2.532$, where the barred parameters determine antineutrino oscillations.. The numbers in parentheses correspond to relative difference with the mean between the nominal and the shifted predictions.

**Quartile 2**

| | | Neutrino Beam | | | Antineutrino Beam | | |
|---|---|---|---|---|---|---|---|
| Prediction | Shift | Right Sign ($\nu_\mu$) | Wrong Sign ($\bar{\nu}_\mu$) | Background | Right Sign ($\bar{\nu}_\mu$) | Wrong Sign ($\nu_\mu$) | Background |
| Nominal | - | 25.397 | 1.772 | 0.261 | 17.853 | 4.746 | 0.162 |
| MECEnuShapeNu | +1 $\sigma$ | 25.248 (-0.006) | 1.716 (-0.033) | 0.265 (0.015) | 17.754 (-0.006) | 4.860 (0.024) | 0.163(0.008) |
| | -1 $\sigma$ | 25.558 (0.006) | 1.835 (0.035) | 0.257 (-0.015) | 17.955 (0.006) | 4.629 (-0.025) | 0.160 (-0.008) |
| MECEnuShapeAntiNu | +1 $\sigma$ | 25.371 (-0.001) | 1.814 (0.023) | 0.261 (0.001) | 17.864 (0.001) | 4.630 (-0.025) | 0.163(0.010) |
| | -1 $\sigma$ | 25.422 (-0.001) | 1.731 (-0.024) | 0.261 (-0.001) | 17.844 (-0.001) | 4.875 (0.027) | 0.160 (-0.010) |
| MECShape2018Nu | +1 $\sigma$ | 25.050 (-0.014) | 1.623 (-0.088) | 0.268 (0.025) | 17.772 (-0.005) | 4.809 (0.013) | 0.162(-0.001) |
| | -1 $\sigma$ | 26.585 (0.011) | 2.017 (0.129) | 0.250 (-0.044) | 18.046 (0.011) | 4.596 (-0.032) | 0.161 (-0.007) |
| MECShape2018AntiNu | +1 $\sigma$ | 25.353 (-0.002) | 1.840 (0.038) | 0.262 (0.004) | 18.006 (0.009) | 4.668 (-0.016) | 0.164(0.013) |
| | -1 $\sigma$ | 25.445 (-0.002) | 1.696 (-0.044) | 0.260 (-0.004) | 17.826 (-0.002) | 4.897 (0.031) | 0.160 (-0.012) |
| MECInitStateNPFracNu | +1 $\sigma$ | 25.283 (-0.004) | 1.746 (-0.015) | 0.263 (0.009) | 17.815 (-0.002) | 4.780 (0.007) | 0.162(0.005) |
| | -1 $\sigma$ | 25.516 (0.002) | 1.800 (0.015) | 0.259 (-0.009) | 17.892 (0.002) | 4.712 (-0.007) | 0.161 (-0.005) |
| MECInitStateNPFracAntiNu | +1 $\sigma$ | 25.393 (-0.000) | 1.783 (0.006) | 0.261 (0.001) | 17.920 (0.004) | 4.719 (-0.006) | 0.162(0.004) |
| | -1 $\sigma$ | 25.401 (-0.004) | 1.762 (-0.006) | 0.261 (-0.001) | 17.785 (-0.004) | 4.773 (0.006) | 0.161 (-0.004) |
| MaCCQE_reduced_2018 | +1 $\sigma$ | 25.647 (0.010) | 1.779 (0.004) | 0.265 (0.015) | 18.004 (0.008) | 4.793 (0.010) | 0.165(0.019) |
| | -1 $\sigma$ | 25.149 (-0.008) | 1.766 (-0.004) | 0.257 (-0.015) | 17.706 (-0.008) | 4.699 (-0.010) | 0.159 (-0.019) |
| RPAShapeRES2018 | +1 $\sigma$ | 24.169 (-0.050) | 1.713 (-0.034) | 0.264 (0.012) | 17.269 (-0.033) | 4.476 (-0.059) | 0.164(0.014) |
| | -1 $\sigma$ | 25.397 (0.000) | 1.772 (0.000) | 0.261 (0.000) | 17.853 (0.000) | 4.746 (0.000) | 0.162 (0.000) |
| RPAShapeenh2018 | +1 $\sigma$ | 25.716 (0.012) | 1.780 (0.004) | 0.266 (0.019) | 18.031 (0.010) | 4.804 (0.012) | 0.166(0.025) |
| | -1 $\sigma$ | 25.128 (-0.008) | 1.766 (-0.004) | 0.257 (-0.015) | 17.709 (-0.008) | 4.700 (-0.010) | 0.158 (-0.021) |
| COHCCScale2018 | +1 $\sigma$ | 25.329 (-0.003) | 1.771 (-0.001) | 0.261 (0.001) | 17.801 (-0.003) | 4.718 (-0.006) | 0.162(0.001) |
| | -1 $\sigma$ | 25.465 (0.003) | 1.773 (0.001) | 0.261 (-0.001) | 17.907 (0.003) | 4.774 (0.006) | 0.162 (-0.001) |
| COHNCScale2018 | +1 $\sigma$ | 25.397 (0.000) | 1.772 (0.000) | 0.261 (0.000) | 17.853 (0.000) | 4.746 (0.000) | 0.162(0.000) |
| | -1 $\sigma$ | 25.397 (0.000) | 1.772 (0.000) | 0.261 (0.000) | 17.853 (0.000) | 4.746 (0.000) | 0.162 (0.000) |
| MaCCRES | +1 $\sigma$ | 25.784 (0.015) | 1.830 (0.032) | 0.278 (0.062) | 17.921 (0.004) | 4.854 (0.023) | 0.171(0.058) |
| | -1 $\sigma$ | 25.134 (0.002) | 1.744 (-0.016) | 0.245 (-0.061) | 17.880 (0.002) | 4.654 (-0.020) | 0.153 (-0.056) |
| MaNCRES | +1 $\sigma$ | 25.394 (-0.000) | 1.772 (-0.000) | 0.275 (0.050) | 17.851 (-0.000) | 4.745 (-0.000) | 0.168(0.040) |
| | -1 $\sigma$ | 25.400 (0.000) | 1.773 (0.000) | 0.249 (-0.047) | 17.855 (0.000) | 4.746 (0.000) | 0.156 (-0.036) |
| MvCCRES | +1 $\sigma$ | 25.679 (0.011) | 1.791 (0.010) | 0.270 (0.034) | 17.899 (0.003) | 4.839 (0.019) | 0.167(0.029) |
| | -1 $\sigma$ | 25.164 (-0.001) | 1.769 (-0.002) | 0.253 (-0.030) | 17.836 (-0.001) | 4.659 (-0.018) | 0.158 (-0.025) |
| CCQEPauliSupViaKF | +1 $\sigma$ | 25.450 (0.002) | 1.778 (0.003) | 0.261 (-0.001) | 17.919 (0.004) | 4.755 (0.002) | 0.161(-0.004) |
| | -1 $\sigma$ | 25.353 (-0.004) | 1.769 (-0.002) | 0.261 (0.000) | 17.786 (-0.004) | 4.733 (-0.003) | 0.162 (0.002) |
| FrElas_N | +1 $\sigma$ | 25.286 (-0.004) | 1.758 (-0.008) | 0.260 (-0.003) | 17.959 (0.006) | 4.776 (0.006) | 0.161(-0.002) |
| | -1 $\sigma$ | 25.510 (-0.006) | 1.789 (0.009) | 0.262 (0.003) | 17.754 (-0.006) | 4.714 (-0.007) | 0.162 (0.002) |
| FrCEx_N | +1 $\sigma$ | 25.432 (0.001) | 1.778 (0.003) | 0.261 (0.000) | 17.815 (-0.002) | 4.746 (0.000) | 0.161(-0.001) |
| | -1 $\sigma$ | 25.367 (0.003) | 1.767 (-0.003) | 0.261 (-0.000) | 17.899 (0.003) | 4.747 (0.000) | 0.162 (0.001) |
| FrAbs_N | +1 $\sigma$ | 25.433 (0.001) | 1.775 (0.001) | 0.262 (0.003) | 17.837 (-0.001) | 4.741 (-0.001) | 0.162(0.003) |
| | -1 $\sigma$ | 25.366 (0.001) | 1.771 (-0.000) | 0.260 (-0.003) | 17.875 (0.001) | 4.752 (0.001) | 0.161 (-0.003) |
| FrInel_pi | +1 $\sigma$ | 25.454 (0.002) | 1.779 (0.004) | 0.263 (0.006) | 17.851 (-0.000) | 4.751 (0.001) | 0.162(0.002) |
| | -1 $\sigma$ | 25.341 (0.000) | 1.766 (-0.004) | 0.260 (-0.005) | 17.860 (0.000) | 4.741 (-0.001) | 0.161 (-0.002) |
| FormZone | +1 $\sigma$ | 25.392 (-0.000) | 1.776 (0.002) | 0.266 (0.018) | 17.846 (-0.000) | 4.739 (-0.001) | 0.163(0.007) |
| | -1 $\sigma$ | 25.403 (0.000) | 1.770 (-0.001) | 0.253 (-0.033) | 17.855 (0.000) | 4.752 (0.001) | 0.159 (-0.016) |

**Quartile 2**

| | | Neutrino Beam | | | Antineutrino Beam | | |
|---|---|---|---|---|---|---|---|
| Prediction | Shift | Right Sign ($\nu_\mu$) | Wrong Sign ($\bar{\nu}_\mu$) | Background | Right Sign ($\bar{\nu}_\mu$) | Wrong Sign ($\nu_\mu$) | Background |
| Nominal | - | 25.397 | 1.772 | 0.261 | 17.853 | 4.746 | 0.162 |
| genie_small_pc00 | +1 $\sigma$ | 25.384 (-0.001) | 1.774 (0.001) | 0.282 (0.077) | 17.851 (-0.000) | 4.748 (0.001) | 0.166(0.028) |
| | -1 $\sigma$ | 25.415 (0.000) | 1.772 (-0.000) | 0.240 (-0.083) | 17.860 (0.000) | 4.745 (-0.000) | 0.157 (-0.028) |
| genie_small_pc01 | +1 $\sigma$ | 25.426 (0.001) | 1.773 (0.000) | 0.264 (0.011) | 17.876 (0.001) | 4.752 (0.001) | 0.158(-0.025) |
| | -1 $\sigma$ | 25.373 (-0.001) | 1.773 (0.000) | 0.258 (-0.011) | 17.835 (-0.001) | 4.741 (-0.001) | 0.166 (0.025) |
| genie_small_pc02 | +1 $\sigma$ | 25.304 (-0.004) | 1.769 (-0.002) | 0.262 (0.005) | 17.868 (0.001) | 4.757 (0.002) | 0.162(0.003) |
| | -1 $\sigma$ | 25.503 (-0.001) | 1.778 (0.003) | 0.260 (-0.005) | 17.842 (-0.001) | 4.737 (-0.002) | 0.161 (-0.003) |
| genie_small_pc03 | +1 $\sigma$ | 25.504 (0.004) | 1.784 (0.007) | 0.261 (0.002) | 17.904 (0.003) | 4.759 (0.003) | 0.162(-0.001) |
| | -1 $\sigma$ | 25.295 (-0.003) | 1.762 (-0.006) | 0.261 (-0.002) | 17.807 (-0.003) | 4.734 (-0.002) | 0.162 (0.001) |
| genie_small_pc04 | +1 $\sigma$ | 25.343 (-0.002) | 1.768 (-0.002) | 0.260 (-0.003) | 17.843 (-0.001) | 4.743 (-0.001) | 0.162(-0.001) |
| | -1 $\sigma$ | 25.456 (0.001) | 1.778 (0.003) | 0.262 (0.003) | 17.867 (0.001) | 4.750 (0.001) | 0.162 (0.001) |
| NuTauScale | +1 $\sigma$ | 25.399 (0.000) | 1.773 (0.000) | 0.322 (0.209) | 17.855 (0.000) | 4.747(0.000) | 0.213 (0.272) |
| ppfx_hadp_beam_pc00 | +1 $\sigma$ | 25.299 (-0.004) | 1.803 (0.017) | 0.266 (0.020) | 17.817 (-0.002) | 4.761 (0.003) | 0.165(0.023) |
| | -1 $\sigma$ | 25.492 (0.002) | 1.739 (-0.019) | 0.255 (-0.022) | 17.891 (0.002) | 4.724 (-0.005) | 0.158 (-0.025) |
| ppfx_hadp_beam_pc01 | +1 $\sigma$ | 25.359 (-0.001) | 1.820 (0.027) | 0.281 (0.075) | 17.702 (-0.009) | 4.879 (0.028) | 0.176(0.083) |
| | -1 $\sigma$ | 25.440 (0.010) | 1.708 (-0.037) | 0.241 (-0.082) | 18.032 (0.010) | 4.567 (-0.038) | 0.147 (-0.093) |
| ppfx_hadp_beam_pc02 | +1 $\sigma$ | 25.308 (-0.004) | 1.906 (0.073) | 0.258 (-0.013) | 17.976 (0.007) | 4.513 (-0.050) | 0.160(-0.013) |
| | -1 $\sigma$ | 25.469 (-0.007) | 1.658 (-0.067) | 0.264 (0.012) | 17.733 (-0.007) | 4.976 (0.047) | 0.164 (0.012) |
| ppfx_hadp_beam_pc03 | +1 $\sigma$ | 25.379 (-0.001) | 1.821 (0.027) | 0.262 (0.002) | 17.987 (0.007) | 4.534 (-0.046) | 0.163(0.008) |
| | -1 $\sigma$ | 25.415 (-0.009) | 1.722 (-0.029) | 0.260 (-0.002) | 17.698 (-0.009) | 4.985 (0.049) | 0.160 (-0.008) |
| ppfx_hadp_beam_pc04 | +1 $\sigma$ | 25.379 (-0.001) | 1.797 (0.014) | 0.263 (0.009) | 17.864 (0.001) | 4.743 (-0.001) | 0.163(0.011) |
| | -1 $\sigma$ | 25.414 (-0.001) | 1.747 (-0.014) | 0.259 (-0.009) | 17.843 (-0.001) | 4.749 (0.001) | 0.160 (-0.011) |
| Calibration | +1 $\sigma$ | 23.424 (-0.081) | 1.592 (-0.107) | 0.243 (-0.073) | 17.271 (-0.033) | 4.310 (-0.096) | 0.151(-0.067) |
| | -1 $\sigma$ | 26.734 (0.027) | 1.890 (0.064) | 0.283 (0.080) | 18.347 (0.027) | 5.215 (0.094) | 0.170 (0.050) |
| CalibShape | +1 $\sigma$ | 25.361 (-0.001) | 1.774 (0.001) | 0.263 (0.008) | 18.108 (0.014) | 4.810(0.014) | 0.160 (-0.013) |
| Lightlevel | +1 $\sigma$ | 25.555 (0.006) | 1.831 (0.033) | 0.264 (0.012) | 18.407 (0.031) | 4.837 (0.019) | 0.167(0.030) |
| | -1 $\sigma$ | 25.676 (0.055) | 1.835 (0.035) | 0.260 (-0.005) | 18.859 (0.055) | 4.819 (0.015) | 0.161 (-0.004) |
| Cherenkov | +1 $\sigma$ | 25.051 (-0.014) | 1.785 (0.007) | 0.258 (-0.010) | 18.656 (0.044) | 4.964(0.045) | 0.164 (0.014) |
| NeutronEvisPrimariesSyst2018 | +1 $\sigma$ | 24.979 (-0.017) | 1.798 (0.014) | 0.257 (-0.017) | 17.182 (-0.038) | 4.359 (-0.085) | 0.160(-0.011) |
| | -1 $\sigma$ | 25.971 (0.013) | 1.749 (-0.013) | 0.262 (0.002) | 18.080 (0.013) | 5.016 (0.055) | 0.161 (-0.008) |
| AbsMuEScale2017 | +1 $\sigma$ | 25.870 (0.018) | 1.855 (0.046) | 0.260 (-0.002) | 18.224 (0.021) | 4.972 (0.047) | 0.161(-0.007) |
| | -1 $\sigma$ | 24.943 (-0.019) | 1.696 (-0.044) | 0.263 (0.007) | 17.514 (-0.019) | 4.553 (-0.041) | 0.162 (0.001) |
| RelMuEScale2017 | +1 $\sigma$ | 25.548 (0.006) | 1.790 (0.010) | 0.261 (0.001) | 17.954 (0.006) | 4.803 (0.012) | 0.162(-0.000) |
| | -1 $\sigma$ | 25.246 (-0.005) | 1.755 (-0.010) | 0.261 (-0.001) | 17.764 (-0.005) | 4.689 (-0.012) | 0.162 (-0.000) |

**Table C.8:** Expected number of selected events at the FD from the systematically shifted predictions, with extrapolation, in quartile 2. The proton exposure used is 9.480 $\times 10^{20}$ and 12.332 $\times 10^{20}$ POT for the production of the neutrino and antineutrino beam respectively. These numbers assume oscillations with $\sin^2\theta_{23} = 0.513$ and $\sin^2\bar{\theta}_{23} = 0.597$, and $\Delta m^2_{32} = 2.453$ and $\Delta\bar{m}^2_{32} = 2.532$, where the barred parameters determine antineutrino oscillations.. The numbers in parentheses correspond to relative difference with the mean between the nominal and the shifted predictions.

**Quartile 3**

| | | Neutrino Beam | | | Antineutrino Beam | | |
|---|---|---|---|---|---|---|---|
| Prediction | Shift | Right Sign ($\nu_\mu$) | Wrong Sign ($\bar{\nu}_\mu$) | Background | Right Sign ($\bar{\nu}_\mu$) | Wrong Sign ($\nu_\mu$) | Background |
| Nominal | - | 26.042 | 1.504 | 0.412 | 15.478 | 5.524 | 0.258 |
| MECEnuShapeNu | +1 $\sigma$ | 25.895 (-0.006) | 1.477 (-0.018) | 0.414 (0.006) | 15.395 (-0.005) | 5.621 (0.017) | 0.260(0.005) |
| | -1 $\sigma$ | 26.189 (0.005) | 1.534 (0.019) | 0.409 (-0.006) | 15.562 (0.005) | 5.422 (-0.018) | 0.257 (-0.005) |
| MECEnuShapeAntiNu | +1 $\sigma$ | 26.031 (-0.000) | 1.523 (0.012) | 0.412 (0.000) | 15.542 (0.004) | 5.441 (-0.015) | 0.259(0.004) |
| | -1 $\sigma$ | 26.053 (-0.005) | 1.485 (-0.013) | 0.412 (-0.000) | 15.404 (-0.005) | 5.616 (0.017) | 0.257 (-0.004) |
| MECShape2018Nu | +1 $\sigma$ | 25.038 (-0.039) | 1.448 (-0.038) | 0.418 (0.014) | 15.351 (-0.008) | 5.594 (0.013) | 0.260(0.007) |
| | -1 $\sigma$ | 27.076 (0.014) | 1.585 (0.052) | 0.401 (-0.027) | 15.690 (0.014) | 5.379 (-0.027) | 0.254 (-0.018) |
| MECShape2018AntiNu | +1 $\sigma$ | 26.032 (-0.000) | 1.517 (0.008) | 0.413 (0.002) | 15.657 (0.012) | 5.437 (-0.016) | 0.262(0.016) |
| | -1 $\sigma$ | 26.057 (-0.005) | 1.476 (-0.019) | 0.411 (-0.002) | 15.405 (-0.005) | 5.667 (0.026) | 0.254 (-0.016) |
| MECInitStateNPFracNu | +1 $\sigma$ | 25.956 (-0.003) | 1.493 (-0.007) | 0.413 (0.004) | 15.449 (-0.002) | 5.551 (0.005) | 0.259(0.003) |
| | -1 $\sigma$ | 26.130 (0.002) | 1.515 (0.007) | 0.410 (-0.004) | 15.506 (0.002) | 5.496 (-0.005) | 0.257 (-0.003) |
| MECInitStateNPFracAntiNu | +1 $\sigma$ | 26.042 (-0.000) | 1.508 (0.003) | 0.412 (0.000) | 15.515 (0.002) | 5.509 (-0.003) | 0.259(0.001) |
| | -1 $\sigma$ | 26.043 (-0.002) | 1.500 (-0.003) | 0.412 (-0.000) | 15.441 (-0.002) | 5.538 (0.003) | 0.258 (-0.001) |
| MaCCQE_reduced_2018 | +1 $\sigma$ | 26.256 (0.008) | 1.504 (-0.000) | 0.415 (0.008) | 15.573 (0.006) | 5.562 (0.007) | 0.261(0.012) |
| | -1 $\sigma$ | 25.833 (-0.006) | 1.504 (0.000) | 0.408 (-0.008) | 15.387 (-0.006) | 5.486 (-0.007) | 0.255 (-0.012) |
| RPAShapeRES2018 | +1 $\sigma$ | 24.238 (-0.072) | 1.440 (-0.043) | 0.410 (-0.004) | 14.633 (-0.056) | 5.083 (-0.083) | 0.259(0.001) |
| | -1 $\sigma$ | 26.042 (0.000) | 1.504 (0.000) | 0.412 (0.000) | 15.478 (0.000) | 5.524 (0.000) | 0.258 (0.000) |
| RPAShapeenh2018 | +1 $\sigma$ | 26.265 (0.009) | 1.502 (-0.002) | 0.416 (0.010) | 15.612 (0.009) | 5.561 (0.007) | 0.262(0.015) |
| | -1 $\sigma$ | 25.889 (-0.007) | 1.507 (0.002) | 0.409 (-0.007) | 15.368 (-0.007) | 5.500 (-0.004) | 0.255 (-0.012) |
| COHCCScale2018 | +1 $\sigma$ | 25.949 (-0.004) | 1.501 (-0.002) | 0.412 (0.000) | 15.397 (-0.005) | 5.481 (-0.008) | 0.258(0.001) |
| | -1 $\sigma$ | 26.136 (0.005) | 1.507 (0.002) | 0.411 (-0.000) | 15.560 (0.005) | 5.567 (0.008) | 0.258 (-0.001) |
| COHNCScale2018 | +1 $\sigma$ | 26.042 (-0.000) | 1.504 (-0.000) | 0.412 (0.000) | 15.478 (-0.000) | 5.524 (-0.000) | 0.258(0.000) |
| | -1 $\sigma$ | 26.042 (0.000) | 1.504 (0.000) | 0.412 (0.000) | 15.478 (0.000) | 5.524 (0.000) | 0.258 (0.000) |
| MaCCRES | +1 $\sigma$ | 27.257 (0.046) | 1.611 (0.069) | 0.446 (0.081) | 15.993 (0.033) | 5.811 (0.051) | 0.285(0.097) |
| | -1 $\sigma$ | 25.172 (-0.014) | 1.477 (-0.018) | 0.384 (-0.068) | 15.262 (-0.014) | 5.319 (-0.038) | 0.238 (-0.080) |
| MaNCRES | +1 $\sigma$ | 26.037 (-0.000) | 1.504 (-0.000) | 0.436 (0.057) | 15.475 (-0.000) | 5.522 (-0.000) | 0.275(0.062) |
| | -1 $\sigma$ | 26.047 (0.000) | 1.504 (0.000) | 0.392 (-0.048) | 15.480 (0.000) | 5.525 (0.000) | 0.246 (-0.050) |
| MvCCRES | +1 $\sigma$ | 26.801 (0.029) | 1.532 (0.018) | 0.430 (0.044) | 15.708 (0.015) | 5.734 (0.037) | 0.271(0.049) |
| | -1 $\sigma$ | 25.430 (-0.007) | 1.506 (0.001) | 0.397 (-0.036) | 15.367 (-0.007) | 5.342 (-0.034) | 0.249 (-0.038) |
| CCQEPauliSupViaKF | +1 $\sigma$ | 26.086 (0.002) | 1.510 (0.004) | 0.412 (-0.000) | 15.502 (0.002) | 5.529 (0.001) | 0.258(-0.000) |
| | -1 $\sigma$ | 26.006 (-0.002) | 1.499 (-0.003) | 0.412 (-0.000) | 15.454 (-0.002) | 5.513 (-0.002) | 0.258 (0.000) |
| FrElas_N | +1 $\sigma$ | 25.979 (-0.002) | 1.495 (-0.006) | 0.412 (0.002) | 15.517 (0.003) | 5.551 (0.005) | 0.258(-0.002) |
| | -1 $\sigma$ | 26.110 (-0.003) | 1.514 (0.006) | 0.411 (-0.002) | 15.439 (-0.003) | 5.496 (-0.005) | 0.259 (0.001) |
| FrCEx_N | +1 $\sigma$ | 26.071 (0.001) | 1.511 (0.005) | 0.411 (-0.002) | 15.465 (-0.001) | 5.507 (-0.003) | 0.258(0.001) |
| | -1 $\sigma$ | 26.020 (0.001) | 1.498 (-0.004) | 0.412 (0.002) | 15.492 (0.001) | 5.539 (0.003) | 0.258 (-0.000) |
| FrAbs_N | +1 $\sigma$ | 26.087 (0.002) | 1.509 (0.003) | 0.412 (0.001) | 15.467 (-0.001) | 5.521 (-0.000) | 0.259(0.002) |
| | -1 $\sigma$ | 26.005 (0.001) | 1.501 (-0.002) | 0.411 (-0.001) | 15.490 (0.001) | 5.525 (0.000) | 0.258 (-0.001) |
| FrInel_pi | +1 $\sigma$ | 26.177 (0.005) | 1.517 (0.009) | 0.418 (0.015) | 15.459 (-0.001) | 5.529 (0.001) | 0.260(0.007) |
| | -1 $\sigma$ | 25.909 (0.001) | 1.490 (-0.009) | 0.405 (-0.015) | 15.496 (0.001) | 5.523 (-0.000) | 0.256 (-0.007) |
| FormZone | +1 $\sigma$ | 26.062 (0.001) | 1.497 (-0.005) | 0.434 (0.053) | 15.486 (0.001) | 5.508 (-0.003) | 0.264(0.023) |
| | -1 $\sigma$ | 25.951 (-0.002) | 1.505 (0.001) | 0.376 (-0.090) | 15.446 (-0.002) | 5.533 (0.002) | 0.246 (-0.048) |

**Quartile 3**

| | | Neutrino Beam | | | Antineutrino Beam | | |
|---|---|---|---|---|---|---|---|
| Prediction | Shift | Right Sign ($\nu_\mu$) | Wrong Sign ($\bar{\nu}_\mu$) | Background | Right Sign ($\bar{\nu}_\mu$) | Wrong Sign ($\nu_\mu$) | Background |
| Nominal | - | 26.042 | 1.504 | 0.412 | 15.478 | 5.524 | 0.258 |
| genie_small_pc00 | +1 $\sigma$ | 26.038 (-0.000) | 1.506 (0.001) | 0.459 (0.110) | 15.481 (0.000) | 5.527 (0.001) | 0.272(0.051) |
| | -1 $\sigma$ | 26.053 (-0.000) | 1.503 (-0.001) | 0.364 (-0.123) | 15.475 (-0.000) | 5.519 (-0.001) | 0.245 (-0.054) |
| genie_small_pc01 | +1 $\sigma$ | 26.066 (0.001) | 1.504 (0.000) | 0.418 (0.017) | 15.492 (0.001) | 5.529 (0.001) | 0.249(-0.036) |
| | -1 $\sigma$ | 26.025 (-0.001) | 1.505 (0.000) | 0.405 (-0.017) | 15.464 (-0.001) | 5.517 (-0.001) | 0.267 (0.035) |
| genie_small_pc02 | +1 $\sigma$ | 26.017 (-0.001) | 1.506 (0.001) | 0.413 (0.004) | 15.506 (0.002) | 5.549 (0.005) | 0.259(0.003) |
| | -1 $\sigma$ | 26.077 (-0.002) | 1.503 (-0.001) | 0.410 (-0.004) | 15.449 (-0.002) | 5.496 (-0.005) | 0.258 (-0.003) |
| genie_small_pc03 | +1 $\sigma$ | 26.123 (0.003) | 1.515 (0.007) | 0.413 (0.002) | 15.492 (0.001) | 5.532 (0.002) | 0.258(0.000) |
| | -1 $\sigma$ | 25.968 (-0.001) | 1.494 (-0.006) | 0.411 (-0.002) | 15.464 (-0.001) | 5.514 (-0.002) | 0.258 (-0.000) |
| genie_small_pc04 | +1 $\sigma$ | 26.028 (-0.001) | 1.501 (-0.002) | 0.410 (-0.005) | 15.484 (0.000) | 5.524 (0.000) | 0.257(-0.003) |
| | -1 $\sigma$ | 26.063 (-0.000) | 1.508 (0.002) | 0.414 (0.005) | 15.472 (-0.000) | 5.522 (-0.000) | 0.259 (0.004) |
| NuTauScale | +1 $\sigma$ | 26.045 (0.000) | 1.504 (0.000) | 0.480 (0.154) | 15.478 (0.000) | 5.523(-0.000) | 0.325 (0.229) |
| ppfx_hadp_beam_pc00 | +1 $\sigma$ | 25.939 (-0.004) | 1.530 (0.017) | 0.420 (0.019) | 15.458 (-0.001) | 5.540 (0.003) | 0.264(0.023) |
| | -1 $\sigma$ | 26.142 (0.001) | 1.476 (-0.019) | 0.403 (-0.021) | 15.498 (0.001) | 5.499 (-0.005) | 0.252 (-0.025) |
| ppfx_hadp_beam_pc01 | +1 $\sigma$ | 26.014 (-0.001) | 1.546 (0.028) | 0.443 (0.073) | 15.320 (-0.010) | 5.675 (0.027) | 0.281(0.084) |
| | -1 $\sigma$ | 26.073 (0.012) | 1.448 (-0.038) | 0.380 (-0.080) | 15.664 (0.012) | 5.318 (-0.038) | 0.235 (-0.094) |
| ppfx_hadp_beam_pc02 | +1 $\sigma$ | 25.934 (-0.004) | 1.612 (0.070) | 0.406 (-0.014) | 15.600 (0.008) | 5.268 (-0.047) | 0.254(-0.016) |
| | -1 $\sigma$ | 26.127 (-0.008) | 1.409 (-0.065) | 0.417 (0.013) | 15.358 (-0.008) | 5.774 (0.044) | 0.262 (0.015) |
| ppfx_hadp_beam_pc03 | +1 $\sigma$ | 26.027 (-0.001) | 1.549 (0.030) | 0.412 (0.002) | 15.608 (0.008) | 5.311 (-0.039) | 0.261(0.009) |
| | -1 $\sigma$ | 26.058 (-0.010) | 1.458 (-0.031) | 0.411 (-0.002) | 15.327 (-0.010) | 5.761 (0.042) | 0.256 (-0.009) |
| ppfx_hadp_beam_pc04 | +1 $\sigma$ | 26.028 (-0.001) | 1.525 (0.014) | 0.415 (0.008) | 15.488 (0.001) | 5.522 (-0.000) | 0.261(0.011) |
| | -1 $\sigma$ | 26.057 (-0.001) | 1.483 (-0.014) | 0.408 (-0.008) | 15.468 (-0.001) | 5.525 (0.000) | 0.256 (-0.011) |
| Calibration | +1 $\sigma$ | 24.207 (-0.073) | 1.432 (-0.049) | 0.361 (-0.130) | 14.900 (-0.038) | 5.034 (-0.093) | 0.253(-0.020) |
| | -1 $\sigma$ | 27.967 (0.049) | 1.652 (0.094) | 0.428 (0.038) | 16.259 (0.049) | 6.167 (0.110) | 0.277 (0.070) |
| CalibShape | +1 $\sigma$ | 26.220 (0.007) | 1.515 (0.007) | 0.394 (-0.044) | 15.704 (0.014) | 5.564(0.007) | 0.268 (0.036) |
| Lightlevel | +1 $\sigma$ | 26.733 (0.026) | 1.611 (0.068) | 0.415 (0.009) | 16.062 (0.037) | 5.689 (0.029) | 0.264(0.020) |
| | -1 $\sigma$ | 26.569 (0.034) | 1.599 (0.061) | 0.415 (0.008) | 16.020 (0.034) | 5.577 (0.010) | 0.264 (0.021) |
| Cherenkov | +1 $\sigma$ | 26.185 (0.005) | 1.591 (0.056) | 0.410 (-0.003) | 16.164 (0.043) | 5.698(0.031) | 0.267 (0.033) |
| NeutronEvisPrimariesSyst2018 | +1 $\sigma$ | 25.488 (-0.022) | 1.522 (0.012) | 0.414 (0.005) | 14.970 (-0.033) | 5.220 (-0.056) | 0.260(0.007) |
| | -1 $\sigma$ | 26.473 (0.015) | 1.511 (0.005) | 0.410 (-0.004) | 15.711 (0.015) | 5.689 (0.030) | 0.253 (-0.019) |
| AbsMuEScale2017 | +1 $\sigma$ | 26.413 (0.014) | 1.551 (0.031) | 0.408 (-0.009) | 15.700 (0.014) | 5.663 (0.025) | 0.257(-0.006) |
| | -1 $\sigma$ | 25.698 (-0.014) | 1.458 (-0.031) | 0.415 (0.008) | 15.262 (-0.014) | 5.390 (-0.025) | 0.261 (0.009) |
| RelMuEScale2017 | +1 $\sigma$ | 26.082 (0.002) | 1.510 (0.004) | 0.412 (0.000) | 15.492 (0.001) | 5.546 (0.004) | 0.259(0.001) |
| | -1 $\sigma$ | 26.003 (-0.001) | 1.498 (-0.004) | 0.411 (-0.000) | 15.461 (-0.001) | 5.502 (-0.004) | 0.258 (-0.002) |

**Table C.9:** Expected number of selected events at the FD from the systematically shifted predictions, with extrapolation, in quartile 3. The proton exposure used is 9.480 $\times 10^{20}$ and 12.332 $\times 10^{20}$ POT for the production of the neutrino and antineutrino beam respectively. These numbers assume oscillations with $\sin^2\theta_{23} = 0.513$ and $\sin^2\bar{\theta}_{23} = 0.597$, and $\Delta m^2_{32} = 2.453$ and $\Delta\bar{m}^2_{32} = 2.532$, where the barred parameters determine antineutrino oscillations.. The numbers in parentheses correspond to relative difference with the mean between the nominal and the shifted predictions.

**Quartile 4**

| | | Neutrino Beam | | | Antineutrino Beam | | |
|---|---|---|---|---|---|---|---|
| Prediction | Shift | Right Sign ($\nu_\mu$) | Wrong Sign ($\bar{\nu}_\mu$) | Background | Right Sign ($\bar{\nu}_\mu$) | Wrong Sign ($\nu_\mu$) | Background |
| Nominal | - | 29.468 | 0.833 | 1.076 | 13.312 | 8.387 | 0.729 |
| MECEnuShapeNu | +1 $\sigma$ | 29.515 (0.002) | 0.827 (-0.008) | 1.077 (0.001) | 13.267 (-0.003) | 8.475 (0.010) | 0.730(0.002) |
| | -1 $\sigma$ | 29.411 (0.004) | 0.841 (0.009) | 1.075 (-0.001) | 13.361 (0.004) | 8.293 (-0.011) | 0.728 (-0.002) |
| MECEnuShapeAntiNu | +1 $\sigma$ | 29.464 (-0.000) | 0.838 (0.005) | 1.076 (0.000) | 13.361 (0.004) | 8.334 (-0.006) | 0.729(0.000) |
| | -1 $\sigma$ | 29.472 (-0.004) | 0.829 (-0.005) | 1.076 (-0.000) | 13.258 (-0.004) | 8.444 (0.007) | 0.729 (-0.000) |
| MECShape2018Nu | +1 $\sigma$ | 29.448 (-0.001) | 0.827 (-0.008) | 1.078 (0.002) | 13.262 (-0.004) | 8.441 (0.006) | 0.731(0.003) |
| | -1 $\sigma$ | 29.376 (0.007) | 0.847 (0.016) | 1.069 (-0.006) | 13.402 (0.007) | 8.232 (-0.019) | 0.723 (-0.008) |
| MECShape2018AntiNu | +1 $\sigma$ | 29.467 (-0.000) | 0.841 (0.009) | 1.077 (0.001) | 13.351 (0.003) | 8.373 (-0.002) | 0.733(0.005) |
| | -1 $\sigma$ | 29.473 (-0.008) | 0.825 (-0.010) | 1.075 (-0.001) | 13.210 (-0.008) | 8.454 (0.008) | 0.726 (-0.004) |
| MECInitStateNPFracNu | +1 $\sigma$ | 29.471 (0.000) | 0.831 (-0.002) | 1.077 (0.001) | 13.300 (-0.001) | 8.412 (0.003) | 0.730(0.001) |
| | -1 $\sigma$ | 29.465 (0.001) | 0.835 (0.002) | 1.075 (-0.001) | 13.324 (0.001) | 8.362 (-0.003) | 0.728 (-0.001) |
| MECInitStateNPFracAntiNu | +1 $\sigma$ | 29.468 (0.000) | 0.833 (-0.001) | 1.076 (0.000) | 13.317 (0.000) | 8.381 (-0.001) | 0.729(0.000) |
| | -1 $\sigma$ | 29.468 (-0.000) | 0.834 (0.001) | 1.076 (-0.000) | 13.308 (-0.000) | 8.393 (0.001) | 0.729 (-0.000) |
| MaCCQE_reduced_2018 | +1 $\sigma$ | 29.515 (0.002) | 0.832 (-0.002) | 1.078 (0.002) | 13.328 (0.001) | 8.404 (0.002) | 0.732(0.004) |
| | -1 $\sigma$ | 29.422 (-0.001) | 0.835 (0.002) | 1.074 (-0.002) | 13.298 (-0.001) | 8.370 (-0.002) | 0.727 (-0.003) |
| RPAShapeRES2018 | +1 $\sigma$ | 28.517 (-0.033) | 0.825 (-0.010) | 1.072 (-0.004) | 12.780 (-0.041) | 7.983 (-0.049) | 0.726(-0.005) |
| | -1 $\sigma$ | 29.468 (0.000) | 0.833 (0.000) | 1.076 (0.000) | 13.312 (0.000) | 8.387 (0.000) | 0.729 (0.000) |
| RPAShapeenh2018 | +1 $\sigma$ | 29.511 (0.001) | 0.832 (-0.002) | 1.078 (0.002) | 13.333 (0.002) | 8.403 (0.002) | 0.732(0.004) |
| | -1 $\sigma$ | 29.466 (-0.001) | 0.835 (0.002) | 1.075 (-0.001) | 13.300 (-0.001) | 8.382 (-0.001) | 0.727 (-0.003) |
| COHCCScale2018 | +1 $\sigma$ | 29.410 (-0.002) | 0.834 (0.001) | 1.076 (0.000) | 13.263 (-0.004) | 8.325 (-0.007) | 0.730(0.001) |
| | -1 $\sigma$ | 29.527 (0.004) | 0.832 (-0.001) | 1.076 (-0.000) | 13.363 (0.004) | 8.450 (0.008) | 0.729 (-0.001) |
| COHNCScale2018 | +1 $\sigma$ | 29.468 (-0.000) | 0.833 (-0.000) | 1.076 (0.000) | 13.312 (-0.000) | 8.387 (-0.000) | 0.729(-0.000) |
| | -1 $\sigma$ | 29.468 (0.000) | 0.833 (0.000) | 1.076 (0.000) | 13.312 (0.000) | 8.387 (0.000) | 0.729 (0.000) |
| MaCCRES | +1 $\sigma$ | 30.349 (0.029) | 0.884 (0.059) | 1.122 (0.042) | 14.153 (0.061) | 8.548 (0.019) | 0.775(0.061) |
| | -1 $\sigma$ | 28.939 (-0.020) | 0.843 (0.011) | 1.042 (-0.032) | 13.053 (-0.020) | 8.301 (-0.010) | 0.700 (-0.040) |
| MaNCRES | +1 $\sigma$ | 29.450 (-0.001) | 0.833 (-0.001) | 1.146 (0.063) | 13.299 (-0.001) | 8.379 (-0.001) | 0.793(0.083) |
| | -1 $\sigma$ | 29.481 (0.001) | 0.834 (0.000) | 1.025 (-0.049) | 13.320 (0.001) | 8.392 (0.001) | 0.689 (-0.056) |
| MvCCRES | +1 $\sigma$ | 29.937 (0.016) | 0.831 (-0.003) | 1.100 (0.022) | 13.569 (0.019) | 8.553 (0.020) | 0.750(0.028) |
| | -1 $\sigma$ | 29.127 (-0.003) | 0.854 (0.025) | 1.057 (-0.017) | 13.272 (-0.003) | 8.230 (-0.019) | 0.715 (-0.019) |
| CCQEPauliSupViaKF | +1 $\sigma$ | 29.475 (0.000) | 0.834 (0.000) | 1.076 (0.000) | 13.322 (0.001) | 8.397 (0.001) | 0.729(0.000) |
| | -1 $\sigma$ | 29.456 (-0.000) | 0.832 (-0.002) | 1.076 (0.000) | 13.306 (-0.000) | 8.377 (-0.001) | 0.729 (0.000) |
| FrElas_N | +1 $\sigma$ | 29.439 (-0.001) | 0.827 (-0.008) | 1.076 (0.000) | 13.312 (-0.000) | 8.413 (0.003) | 0.728(-0.001) |
| | -1 $\sigma$ | 29.492 (0.000) | 0.838 (0.006) | 1.076 (-0.000) | 13.314 (0.000) | 8.361 (-0.003) | 0.730 (0.002) |
| FrCEx_N | +1 $\sigma$ | 29.464 (-0.000) | 0.834 (0.001) | 1.076 (0.000) | 13.315 (0.000) | 8.372 (-0.002) | 0.729(0.000) |
| | -1 $\sigma$ | 29.466 (-0.000) | 0.831 (-0.003) | 1.076 (0.000) | 13.312 (-0.000) | 8.404 (0.002) | 0.729 (-0.000) |
| FrAbs_N | +1 $\sigma$ | 29.479 (0.000) | 0.834 (0.001) | 1.077 (0.001) | 13.319 (0.000) | 8.386 (-0.000) | 0.730(0.001) |
| | -1 $\sigma$ | 29.452 (-0.000) | 0.831 (-0.003) | 1.075 (-0.001) | 13.309 (-0.000) | 8.390 (0.000) | 0.728 (-0.001) |
| FrInel_pi | +1 $\sigma$ | 29.613 (0.005) | 0.841 (0.009) | 1.090 (0.013) | 13.347 (0.003) | 8.377 (-0.001) | 0.739(0.013) |
| | -1 $\sigma$ | 29.335 (-0.002) | 0.826 (-0.009) | 1.062 (-0.013) | 13.279 (-0.002) | 8.401 (0.002) | 0.720 (-0.013) |
| FormZone | +1 $\sigma$ | 29.410 (-0.002) | 0.835 (0.002) | 1.160 (0.075) | 13.287 (-0.002) | 8.389 (0.000) | 0.773(0.058) |
| | -1 $\sigma$ | 29.431 (0.002) | 0.833 (-0.000) | 0.949 (-0.126) | 13.344 (0.002) | 8.232 (-0.019) | 0.654 (-0.109) |

**Quartile 4**

| | | Neutrino Beam | | | Antineutrino Beam | | |
|---|---|---|---|---|---|---|---|
| Prediction | Shift | Right Sign ($\nu_\mu$) | Wrong Sign ($\bar{\nu}_\mu$) | Background | Right Sign ($\bar{\nu}_\mu$) | Wrong Sign ($\nu_\mu$) | Background |
| Nominal | - | 29.468 | 0.833 | 1.076 | 13.312 | 8.387 | 0.729 |
| genie_small_pc00 | +1 $\sigma$ | 29.429 (-0.001) | 0.832 (-0.002) | 1.249 (0.149) | 13.306 (-0.000) | 8.384 (-0.000) | 0.804(0.097) |
| | -1 $\sigma$ | 29.501 (0.001) | 0.833 (-0.000) | 0.904 (-0.174) | 13.322 (0.001) | 8.391 (0.001) | 0.655 (-0.108) |
| genie_small_pc01 | +1 $\sigma$ | 29.474 (0.000) | 0.832 (-0.001) | 1.101 (0.023) | 13.328 (0.001) | 8.402 (0.002) | 0.693(-0.051) |
| | -1 $\sigma$ | 29.458 (-0.001) | 0.833 (-0.001) | 1.051 (-0.024) | 13.300 (-0.001) | 8.374 (-0.001) | 0.766 (0.049) |
| genie_small_pc02 | +1 $\sigma$ | 29.512 (0.001) | 0.835 (0.002) | 1.079 (0.003) | 13.336 (0.002) | 8.454 (0.008) | 0.731(0.002) |
| | -1 $\sigma$ | 29.419 (-0.002) | 0.830 (-0.004) | 1.074 (-0.002) | 13.291 (-0.002) | 8.321 (-0.008) | 0.727 (-0.002) |
| genie_small_pc03 | +1 $\sigma$ | 29.571 (0.003) | 0.837 (0.005) | 1.079 (0.003) | 13.344 (0.002) | 8.411 (0.003) | 0.729(0.000) |
| | -1 $\sigma$ | 29.360 (-0.002) | 0.828 (-0.007) | 1.074 (-0.002) | 13.284 (-0.002) | 8.366 (-0.003) | 0.729 (0.000) |
| genie_small_pc04 | +1 $\sigma$ | 29.453 (-0.001) | 0.831 (-0.002) | 1.068 (-0.007) | 13.311 (-0.000) | 8.385 (-0.000) | 0.723(-0.008) |
| | -1 $\sigma$ | 29.478 (0.000) | 0.834 (0.000) | 1.084 (0.008) | 13.317 (0.000) | 8.391 (0.000) | 0.735 (0.008) |
| NuTauScale | +1 $\sigma$ | 29.465 (-0.000) | 0.833 (-0.001) | 1.136 (0.055) | 13.314 (0.000) | 8.388(0.000) | 0.806 (0.100) |
| ppfx_hadp_beam_pc00 | +1 $\sigma$ | 29.367 (-0.003) | 0.850 (0.020) | 1.095 (0.018) | 13.298 (-0.001) | 8.404 (0.002) | 0.747(0.024) |
| | -1 $\sigma$ | 29.565 (0.001) | 0.815 (-0.022) | 1.056 (-0.019) | 13.328 (0.001) | 8.358 (-0.004) | 0.711 (-0.026) |
| ppfx_hadp_beam_pc01 | +1 $\sigma$ | 29.461 (-0.000) | 0.859 (0.030) | 1.156 (0.071) | 13.119 (-0.015) | 8.569 (0.021) | 0.793(0.084) |
| | -1 $\sigma$ | 29.471 (0.017) | 0.799 (-0.042) | 0.996 (-0.077) | 13.540 (0.017) | 8.129 (-0.031) | 0.664 (-0.093) |
| ppfx_hadp_beam_pc02 | +1 $\sigma$ | 29.302 (-0.006) | 0.888 (0.063) | 1.059 (-0.016) | 13.450 (0.010) | 8.049 (-0.041) | 0.717(-0.016) |
| | -1 $\sigma$ | 29.604 (-0.010) | 0.785 (-0.059) | 1.092 (0.015) | 13.179 (-0.010) | 8.713 (0.038) | 0.740 (0.015) |
| ppfx_hadp_beam_pc03 | +1 $\sigma$ | 29.479 (0.000) | 0.859 (0.030) | 1.077 (0.001) | 13.489 (0.013) | 8.160 (-0.027) | 0.736(0.009) |
| | -1 $\sigma$ | 29.458 (-0.015) | 0.808 (-0.031) | 1.074 (-0.001) | 13.118 (-0.015) | 8.632 (0.029) | 0.722 (-0.010) |
| ppfx_hadp_beam_pc04 | +1 $\sigma$ | 29.456 (-0.000) | 0.845 (0.014) | 1.084 (0.007) | 13.314 (0.000) | 8.388 (0.000) | 0.737(0.010) |
| | -1 $\sigma$ | 29.481 (-0.000) | 0.821 (-0.015) | 1.068 (-0.007) | 13.310 (-0.000) | 8.386 (-0.000) | 0.721 (-0.010) |
| Calibration | +1 $\sigma$ | 27.651 (-0.064) | 0.731 (-0.131) | 0.867 (-0.215) | 12.754 (-0.043) | 7.384 (-0.127) | 0.645(-0.122) |
| | -1 $\sigma$ | 31.596 (0.034) | 0.862 (0.034) | 1.216 (0.122) | 13.770 (0.034) | 9.396 (0.113) | 0.847 (0.149) |
| CalibShape | +1 $\sigma$ | 29.638 (0.006) | 0.789 (-0.055) | 1.052 (-0.023) | 13.406 (0.007) | 8.293(-0.011) | 0.749 (0.027) |
| Lightlevel | +1 $\sigma$ | 29.951 (0.016) | 0.848 (0.018) | 1.076 (0.000) | 13.575 (0.020) | 8.516 (0.015) | 0.765(0.048) |
| | -1 $\sigma$ | 28.787 (-0.004) | 0.822 (-0.014) | 1.039 (-0.034) | 13.260 (-0.004) | 8.205 (-0.022) | 0.741 (0.017) |
| Cherenkov | +1 $\sigma$ | 28.913 (-0.019) | 0.820 (-0.016) | 1.054 (-0.021) | 13.510 (0.015) | 8.474(0.010) | 0.770 (0.055) |
| NeutronEvisPrimariesSyst2018 | +1 $\sigma$ | 29.111 (-0.012) | 0.840 (0.007) | 1.088 (0.011) | 13.176 (-0.010) | 8.152 (-0.028) | 0.739(0.014) |
| | -1 $\sigma$ | 29.835 (0.010) | 0.830 (-0.004) | 1.062 (-0.013) | 13.444 (0.010) | 8.587 (0.024) | 0.719 (-0.014) |
| AbsMuEScale2017 | +1 $\sigma$ | 29.835 (0.012) | 0.853 (0.023) | 1.085 (0.008) | 13.455 (0.011) | 8.508 (0.014) | 0.735(0.008) |
| | -1 $\sigma$ | 29.125 (-0.010) | 0.810 (-0.028) | 1.067 (-0.008) | 13.176 (-0.010) | 8.266 (-0.015) | 0.723 (-0.008) |
| RelMuEScale2017 | +1 $\sigma$ | 29.386 (-0.003) | 0.830 (-0.004) | 1.075 (-0.001) | 13.265 (-0.004) | 8.361 (-0.003) | 0.728(-0.001) |
| | -1 $\sigma$ | 29.551 (0.004) | 0.836 (0.003) | 1.077 (0.001) | 13.360 (0.004) | 8.411 (0.003) | 0.730 (0.001) |

**Table C.10:** Expected number of selected events at the FD from the systematically shifted predictions, with extrapolation, in quartile 4. The proton exposure used is 9.480 $\times 10^{20}$ and 12.332 $\times 10^{20}$ POT for the production of the neutrino and antineutrino beam respectively. These numbers assume oscillations with $\sin^2\theta_{23} = 0.513$ and $\sin^2\bar{\theta}_{23} = 0.597$, and $\Delta m^2_{32} = 2.453$ and $\Delta\bar{m}^2_{32} = 2.532$, where the barred parameters determine antineutrino oscillations.. The numbers in parentheses correspond to relative difference with the mean between the nominal and the shifted predictions.

# Appendix D

# Error bands

Throughout this thesis, the author has presented sets of plots displaying a shadow region around different Monte Carlo spectra, which represents the $1\sigma$ uncertainty on the total nominal prediction $P$. The computational procedure to obtain these *error bands* is presented in this appendix. Other uncertainty band calculations, mostly implemented for the results in § 7.1.1, such as the one for the data over prediction ratio, $D/P$, and for a fraction of the total prediction, $P^{Comp}/P$, are also presented.

## D.1 Prediction

Let $p_i$ be the number of expected events in the $i$-th bin of a nominal prediction spectrum $P$. Let $p_i^{+1\sigma\ \psi}$ and $p_i^{-1\sigma\ \psi}$ be the expected number of events in the $i$-th bin of the $+1\sigma$ and $-1\sigma$ shifted predictions due to the $\psi$ systematic uncertainty. In the case of area normalized spectra, the computation of the error band starts by normalizing the $P^{\pm 1\sigma\ \psi}$ distributions to the area of the nominal prediction. If the spectra are only normalized to the beam exposure, then the area-normalization is skipped. At each bin, the error values

$$e_i^{\psi} = p_i - p_i^{\pm 1\sigma\ \psi}, \quad \vee\ \psi, \tag{D.1}$$

are calculated. These errors are included as elements of a set $U_i$ if $e_i^{\psi} > 0$, or as elements of a set $D_i$ if $e_i^{\psi} < 0$. This means that, regardless of $e_i^{\psi}$ being the result of a a +1 $\sigma$ or -1 $\sigma$ shift in the simulation, the differences between the nominal and the shifted simulation are separated depending if they increase or decrease the number of simulated events in an individual bin.

The elements in $U_i$ and $D_i$ are summed in quadrature and the squared root of the sum is computed to obtain the upper and lower limits, $e_i^{+1\sigma}$ and $e_i^{-1\sigma}$, of the total error band at bin $i$. Explicitly,

$$p_i^{+1\sigma} = p_i + e_i^{+1\sigma} \tag{D.2a}$$

$$p_i^{-1\sigma} = p_i + e_i^{-1\sigma} \tag{D.2b}$$

where

$$e_i^{+1\sigma} = \sqrt{\sum u^2} \quad |u \quad \in U_i \tag{D.3a}$$

$$e_i^{-1\sigma} = \sqrt{\sum d^2} \quad |d \quad \in D_i \tag{D.3b}$$

## D.2 Fraction of the prediction

Let $c_i$ be the number of events in the $i$-th bin of a simulated beam component $C$, and let $P$ be the total simulated spectra with bin contents $p_i$. The upper and lower limits, $r_i^{+1\sigma}$ and $r_i^{+1\sigma}$ respectively, of the $1\sigma$ uncertainty band on the ratio $R = C/P$ are computed similarly to the procedure outlined in appendix D. In this case,

$$r_i^{+1\sigma} = e_i^{+1\sigma} - r_i \tag{D.4a}$$

$$r_i^{-1\sigma} = r_i - e_i^{-1\sigma}. \tag{D.4b}$$

where

$$e_i^{+1\sigma} = \sqrt{\sum_{\psi} r_i^{+1\sigma\ \psi}} \tag{D.5a}$$

$$e_i^{-1\sigma} = \sqrt{\sum_{\psi} r_i^{-1\sigma\ \psi}} \tag{D.5b}$$

and

$$r_i^{+1\sigma\ \psi} = \frac{c_i^{-1\sigma\ \psi}}{p_i^{-1\sigma\ \psi}} - r_i \tag{D.6a}$$

$$r_i^{-1\sigma\ \psi} = r_i - \frac{c_i^{-1\sigma\ \psi}}{p_i^{+1\sigma\ \psi}}. \tag{D.6b}$$

In these last expressions, $c_i^{\pm 1\sigma\ \psi}$ and $p_i^{\pm 1\sigma\ \psi}$ correspond to the $\pm 1\ \sigma$ shift in $C$ and $P$, respectively, due to the systematic $\psi$.

## D.3 Data-Monte Carlo ratio

Let $d_i$ be the number of events in the $i$-th bin of a data spectrum $D$, and let $p_i^{\pm 1\sigma}$ be the number of events in the $i$-th bin of the simulation $P$ shifted by $\pm 1\sigma$. The upper and lower limit of the $1\sigma$ uncertainty band in the bin $i$ of the ratio $R = D/P$ at bin $i$ is computed as

$$r_i^{+1\sigma} = \frac{d_i}{p_i^{-1\sigma}} \tag{D.7a}$$

$$r_i^{-1\sigma} = \frac{d_i}{p_i^{+1\sigma}} \tag{D.7b}$$

where $r_i^{\pm 1\sigma}$ represents the number of events in the $i$-th bin of $R$

# Appendix E

# Wrong sign at the ND

This appendix complements Section § 7.1 with all the ND hadronic fraction distributions separated by individual bins of reconstructed $\nu$ and $\bar{\nu}$ energy as used in NOvA's disappearance analysis. Figure E.1 shows the hadronic energy distributions without separation by reconstructed energy bins and Figures E.2 to E.20 show the bin by bin distributions. For simplicity, the plots will be described in the next paragraphs and the captions under the figures will only specify the reconstructed energy bin that the spectra correspond to. The energy range is displayed at the top right of each plot. The distributions are in hadronic energy fraction of selected data and simulated $\nu_\mu$ and $\bar{\nu}_\mu$ CC event at NOvA's ND. Each figure shows to set of plots: the left and right plots correspond to the FHC and RHC samples respectively.

**Top panel** Data is shown in black dots with associated statistical errors. The simulated total and wrong sign component spectra are shown in purple and green, respectively. The total and wrong sign spectra are shown in solid lines for the nominal simulation and in dashed lines for the simulation without the corrections to the interaction model (see § 3.4). The nominal simulation is displayed with a 1 $\sigma$ error band, which is calculated from the sum in quadrature of the systematic uncertainties accounted for in the analysis.

**Middle panel** The wrong sign fraction (wrong sign / total simulation) is shown in solid green for the nominal simulation and in dashed green for the simulation without cross-section tuning. The error band around the nominal wrong sign fraction is computed as described in appendix D.

**Bottom panel** The data over the total simulation ratio is displayed in solid purple with respect to the nominal simulation and in dashed purple with respect to the simulation without cross-section tuning. The error band around the nominal ratio is computed as the ratio between the data and the $1\sigma$ bounds of nominal simulation ad explained in appendix D.

In the three panels, the distributions corresponding to the simulation without cross-section tuning are labeled as *PPFX*.

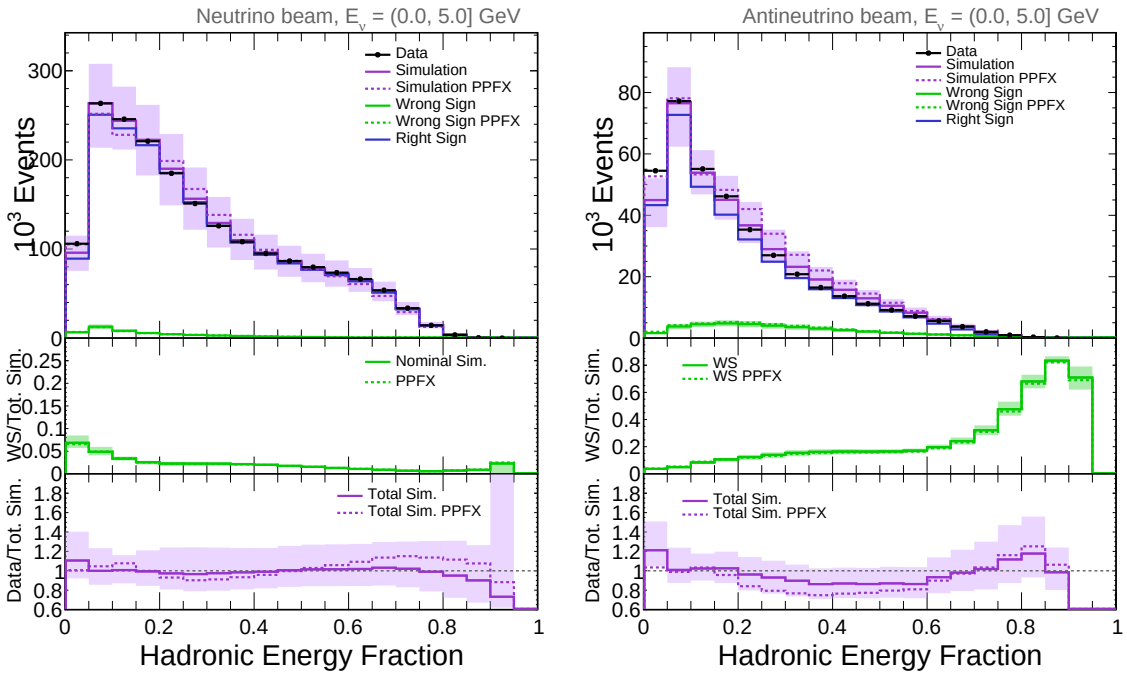


**Figure E.1:** All bins of reconstructed $\nu$ and $\bar{\nu}$ energy.

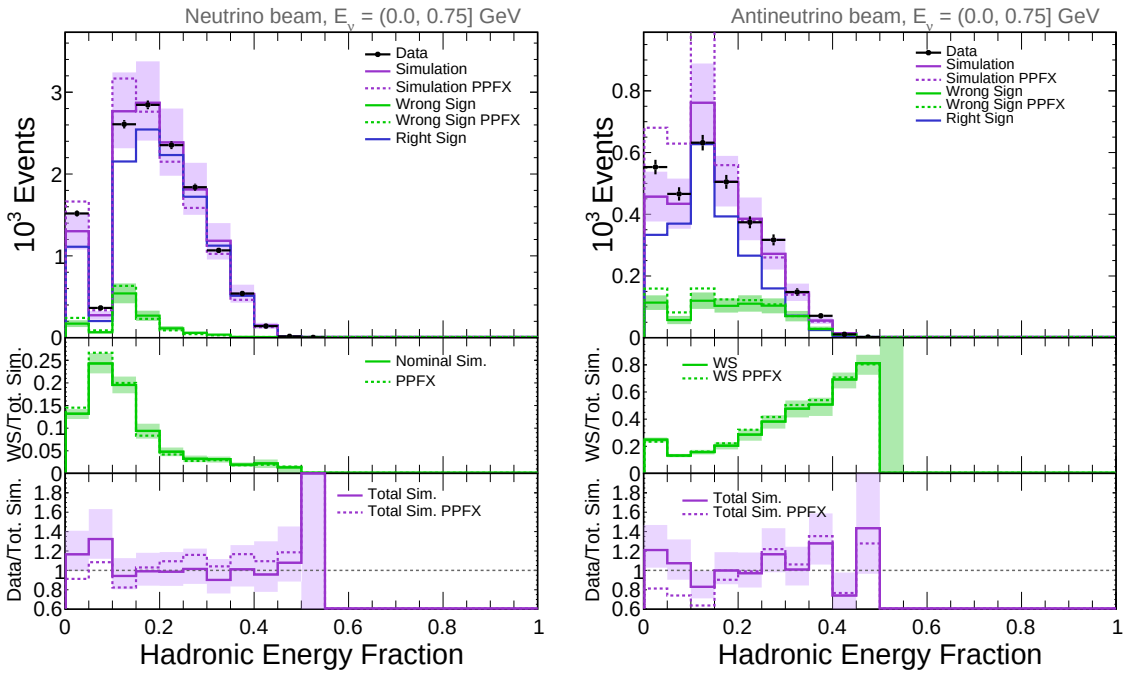


**Figure E.2:** 1st bin of reconstructed $\nu$ and $\bar{\nu}$ energy.

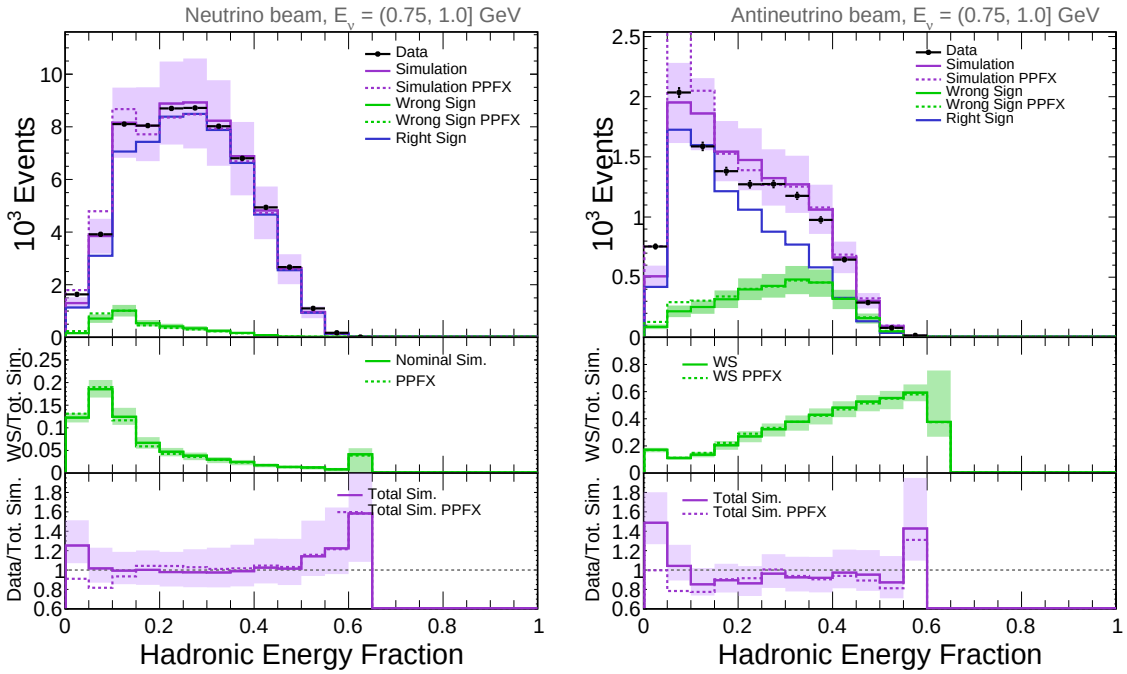


**Figure E.3:** 2nd bin of reconstructed $\nu$ and $\bar{\nu}$ energy.

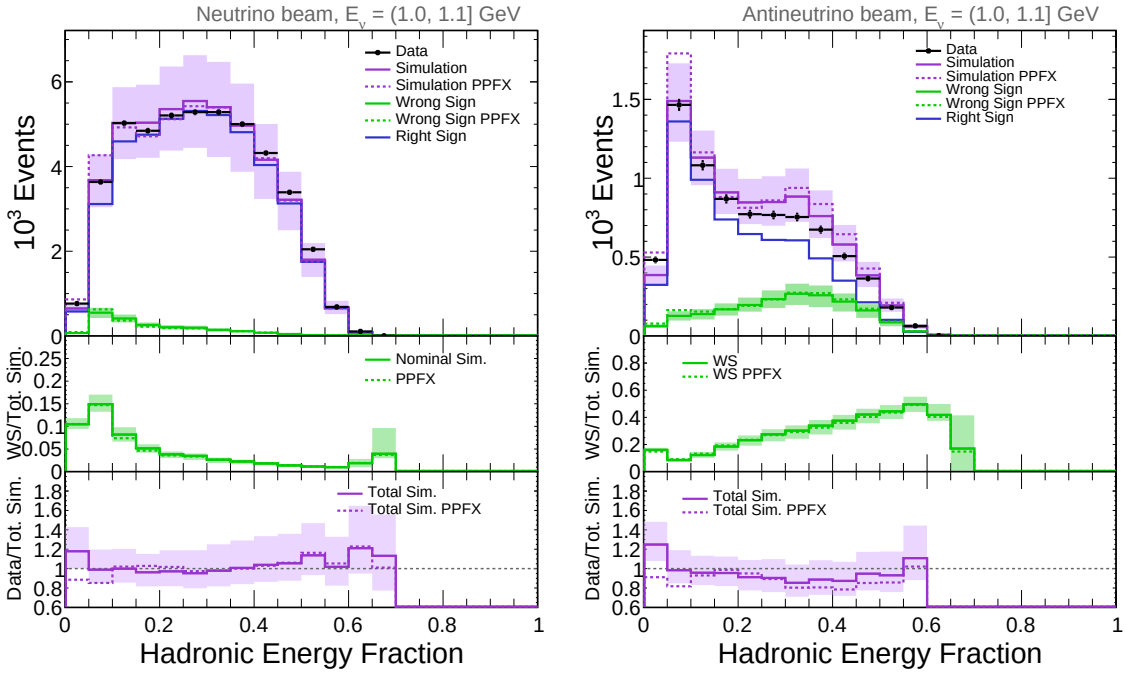


**Figure E.4:** 3rd bin of reconstructed $\nu$ and $\bar{\nu}$ energy.

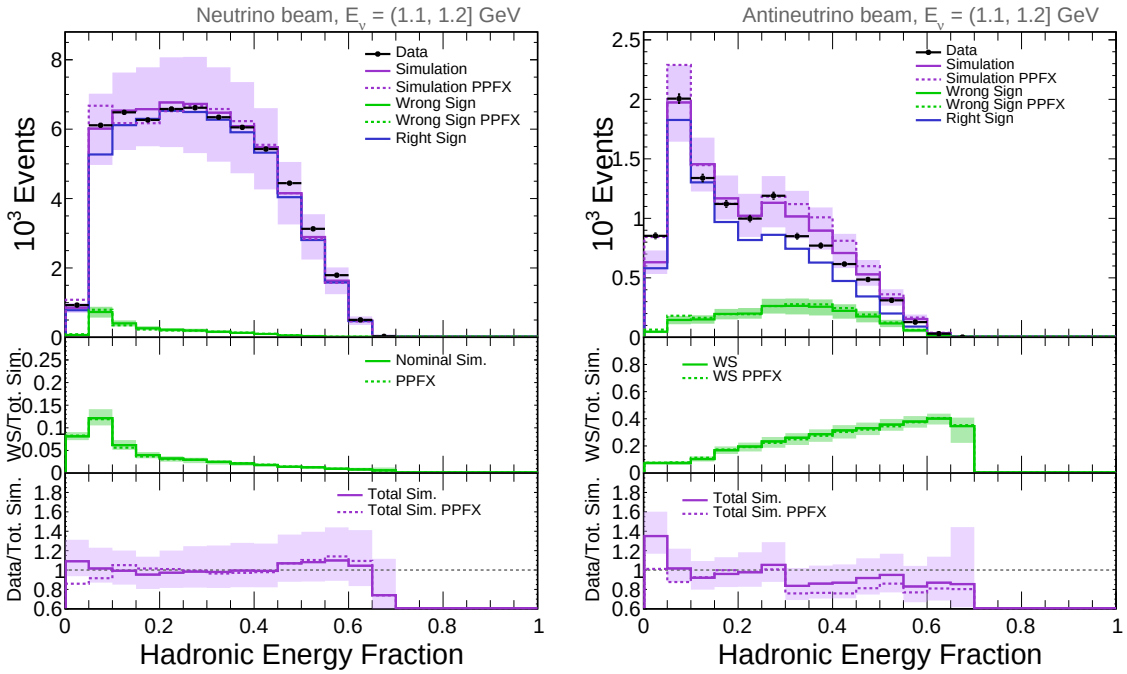


**Figure E.5:** 4th bin of reconstructed $\nu$ and $\bar{\nu}$ energy.

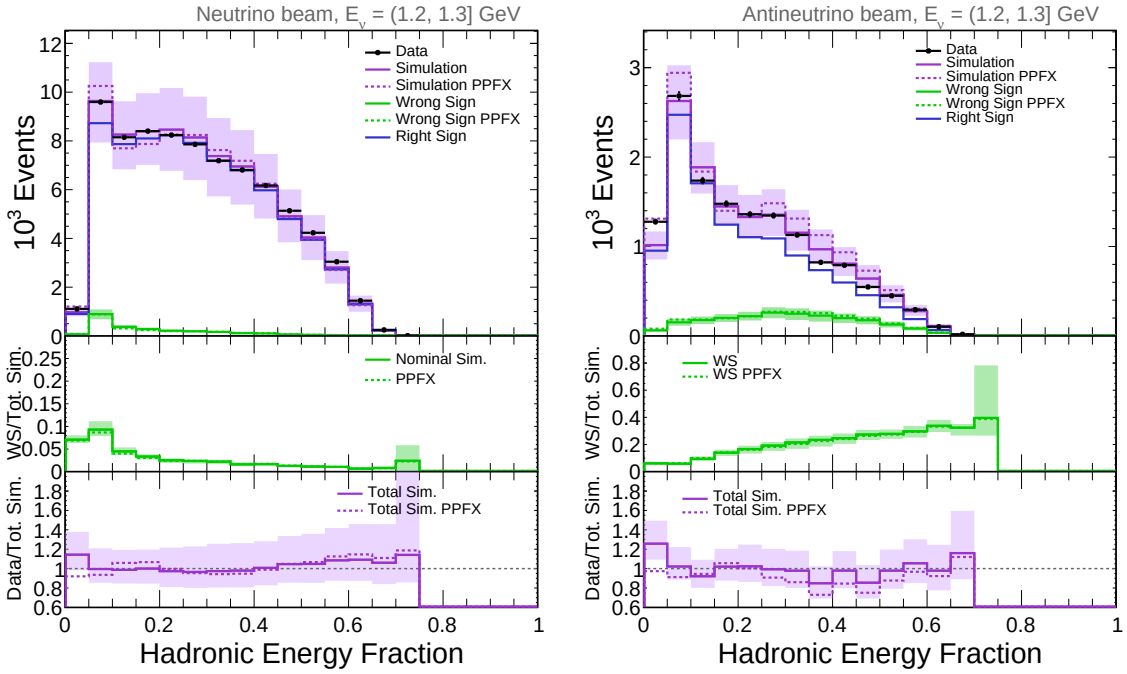


**Figure E.6:** 5th bin of reconstructed $\nu$ and $\bar{\nu}$ energy.

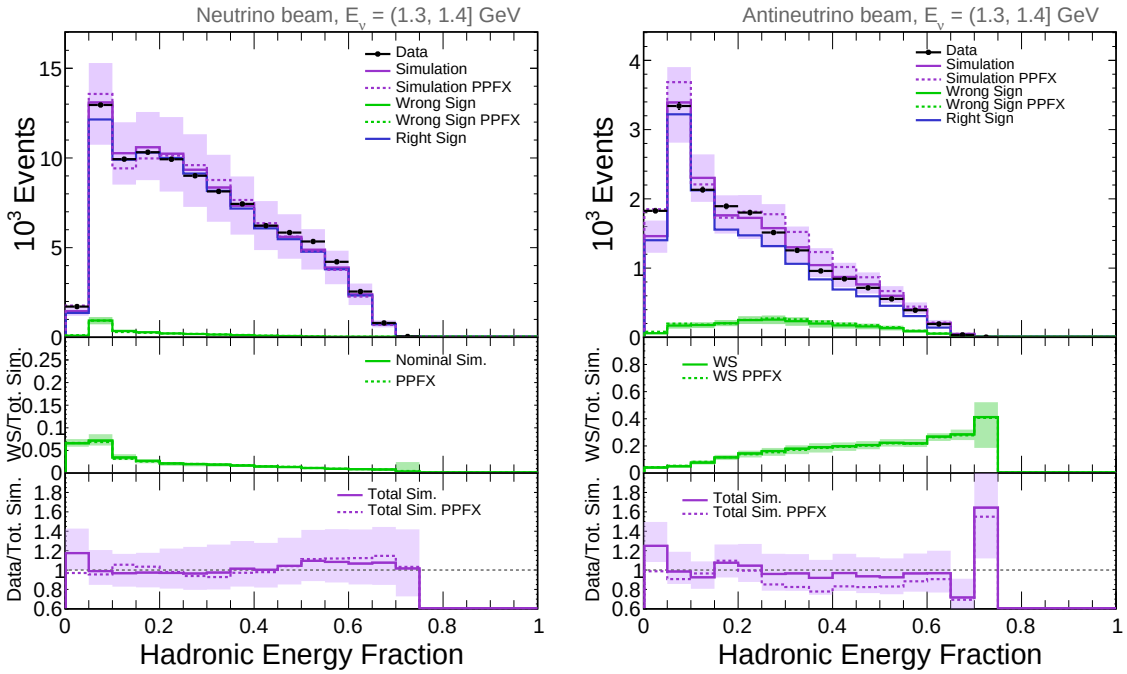


**Figure E.7:** 6th bin of reconstructed $\nu$ and $\bar{\nu}$ energy.

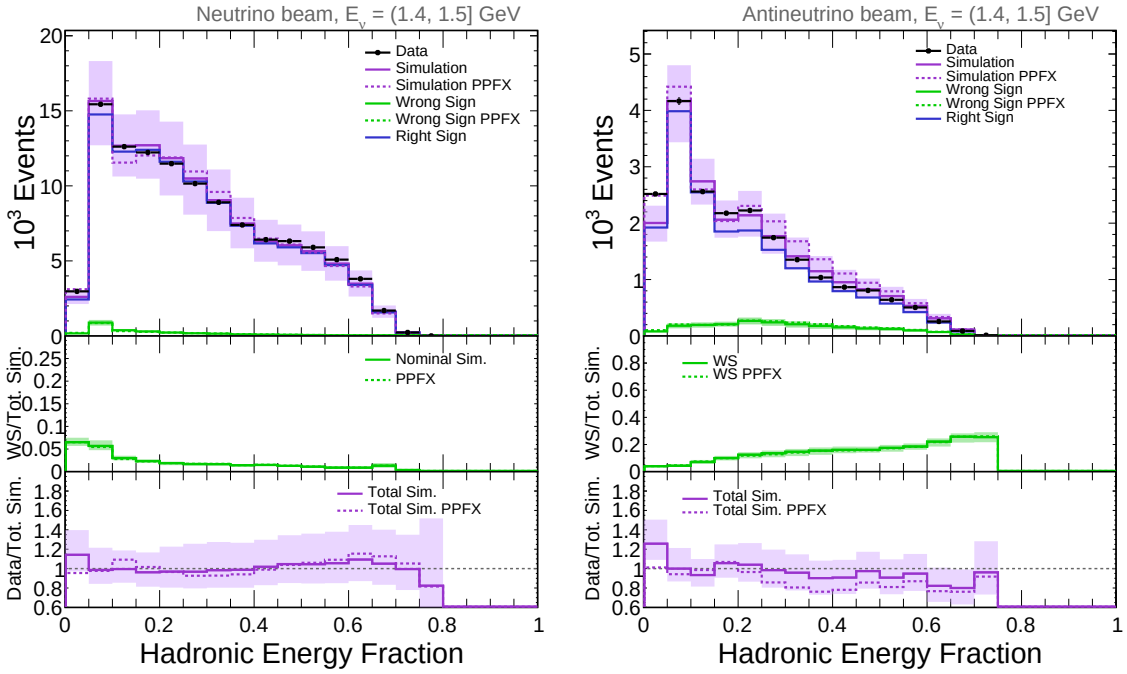


**Figure E.8:** 7th bin of reconstructed $\nu$ and $\bar{\nu}$ energy.

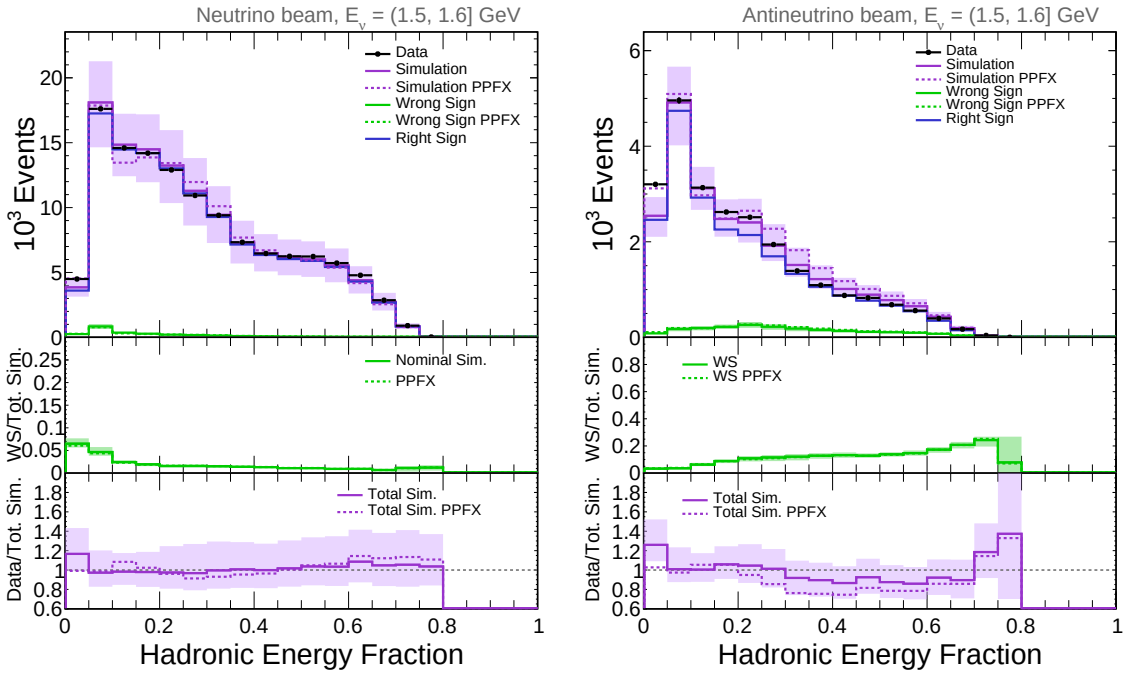


**Figure E.9:** 8th bin of reconstructed $\nu$ and $\bar{\nu}$ energy.

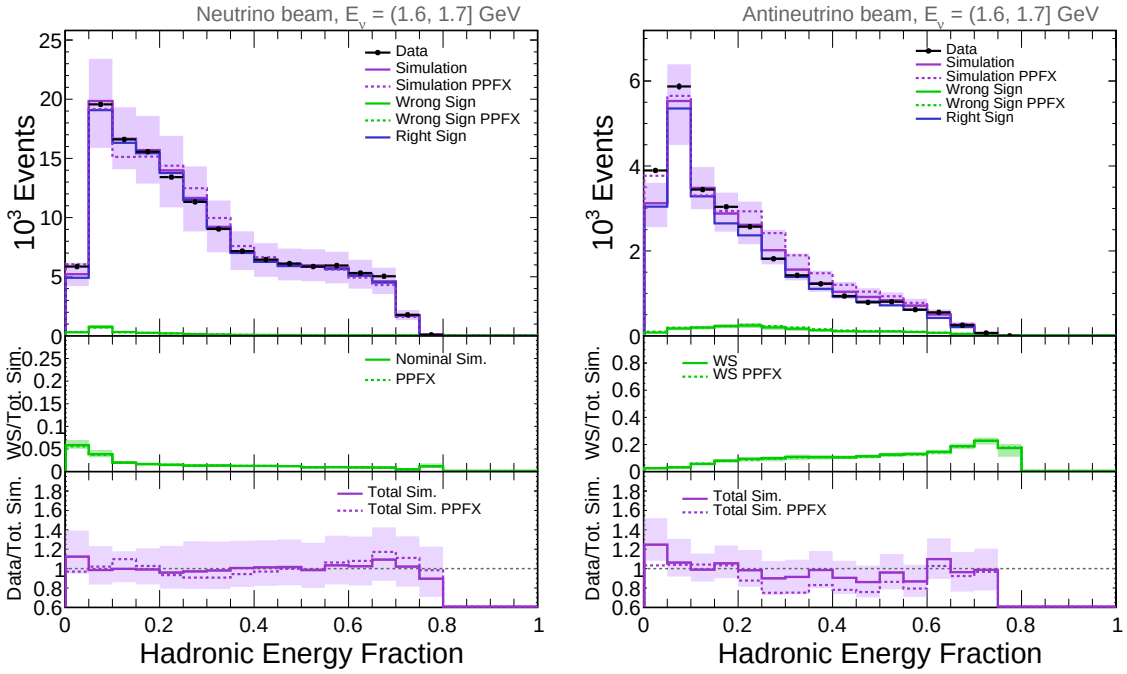


**Figure E.10:** 9th bin of reconstructed $\nu$ and $\bar{\nu}$ energy.

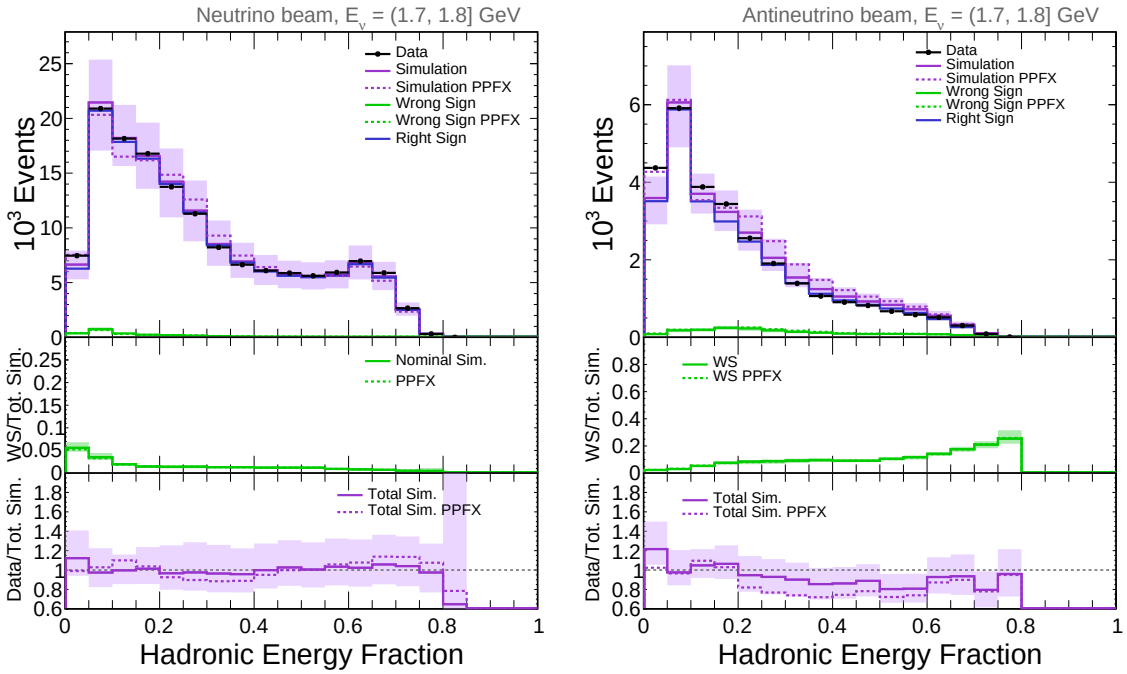


**Figure E.11:** 10th bin of reconstructed $\nu$ and $\bar{\nu}$ energy.

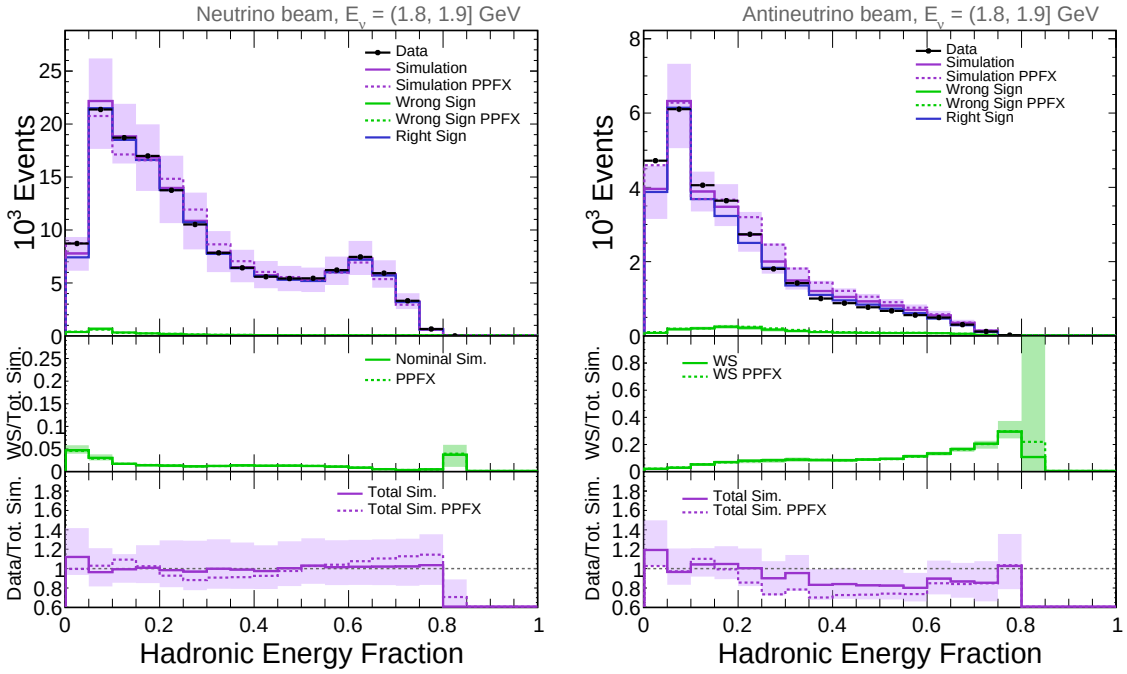


**Figure E.12:** 11th bin of reconstructed $\nu$ and $\bar{\nu}$ energy.

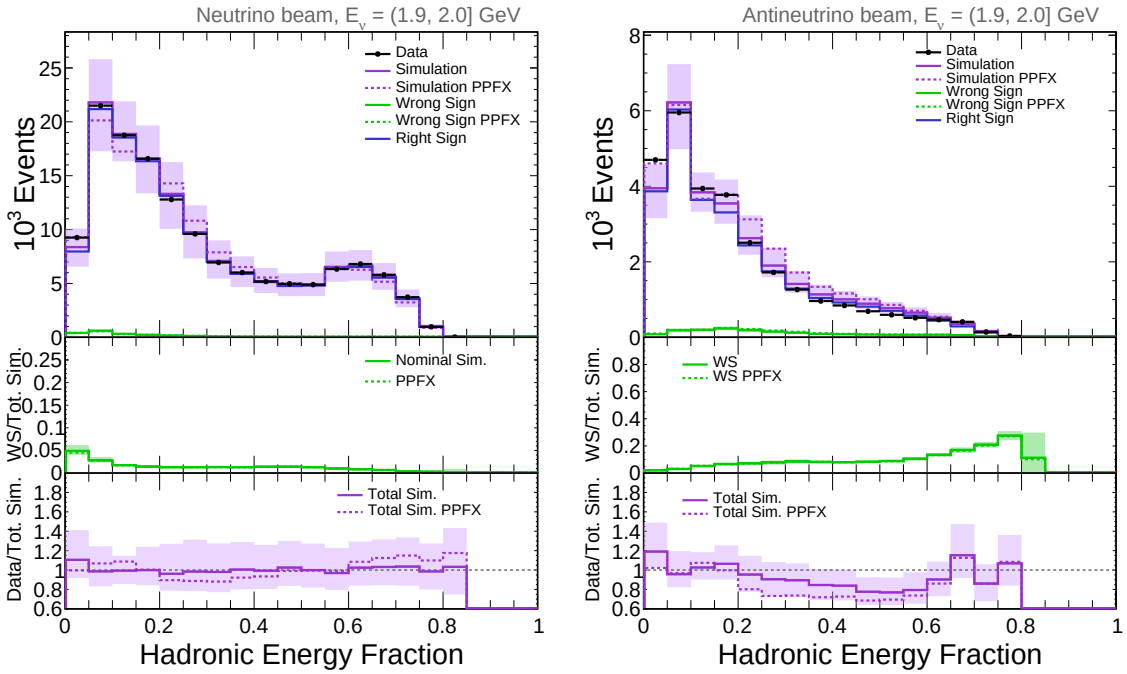


**Figure E.13:** 12th bin of reconstructed $\nu$ and $\bar{\nu}$ energy.

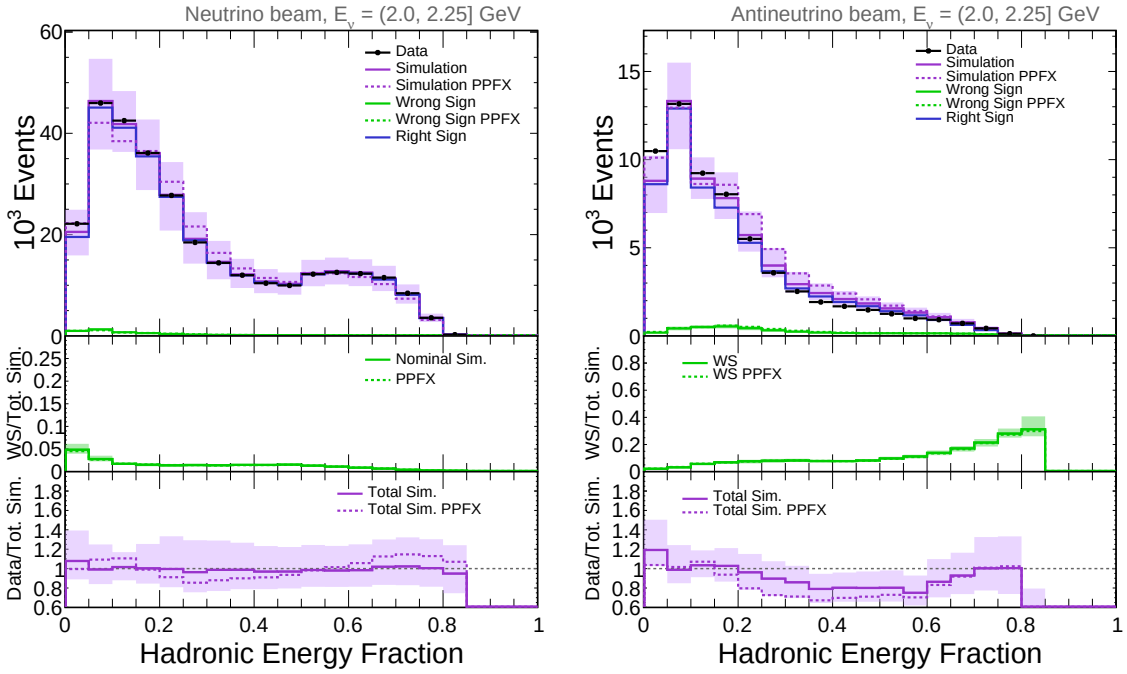


**Figure E.14:** 13th bin of reconstructed $\nu$ and $\bar{\nu}$ energy.

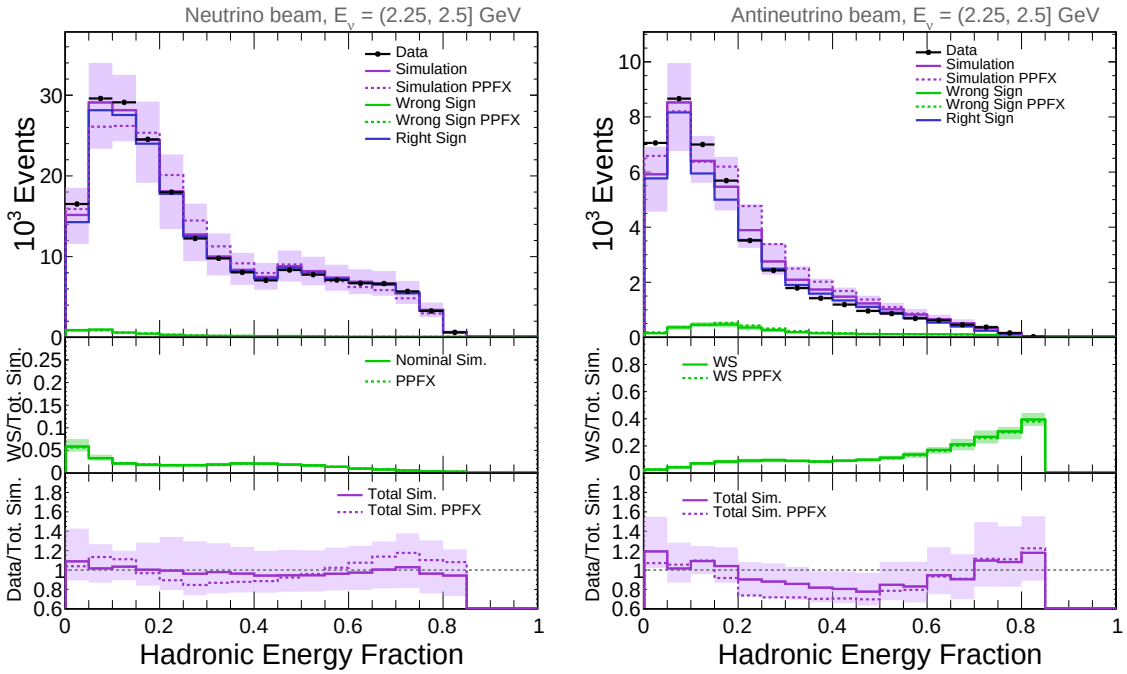


**Figure E.15:** 14th bin of reconstructed $\nu$ and $\bar{\nu}$ energy.

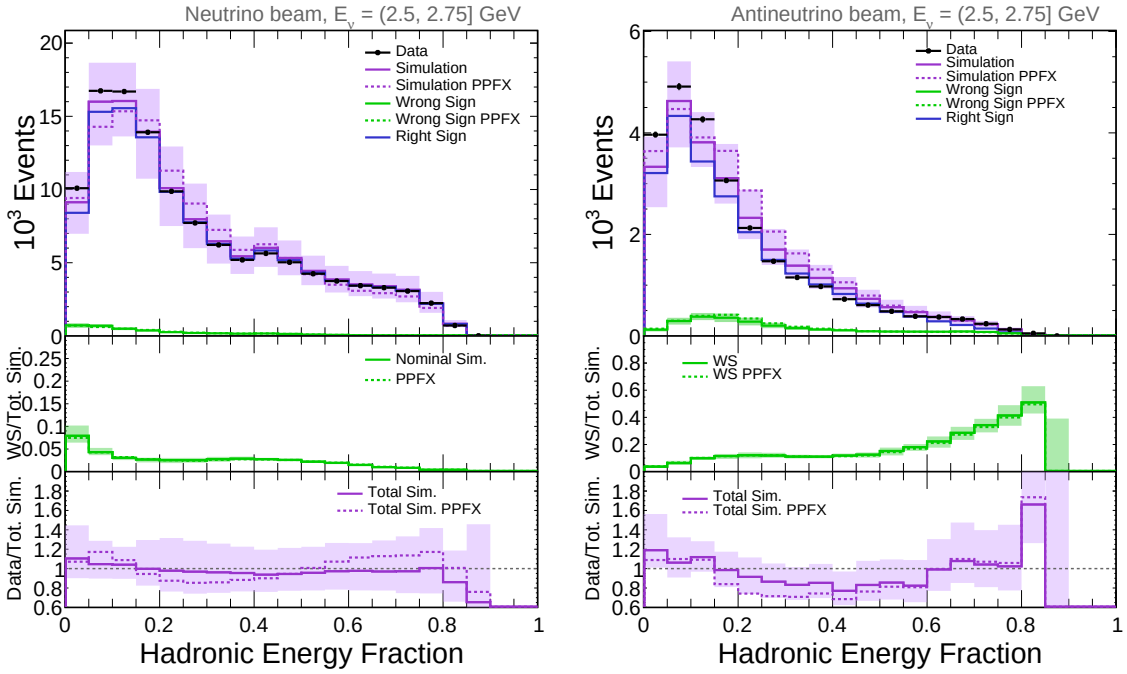


**Figure E.16:** 15th bin of reconstructed $\nu$ and $\bar{\nu}$ energy.

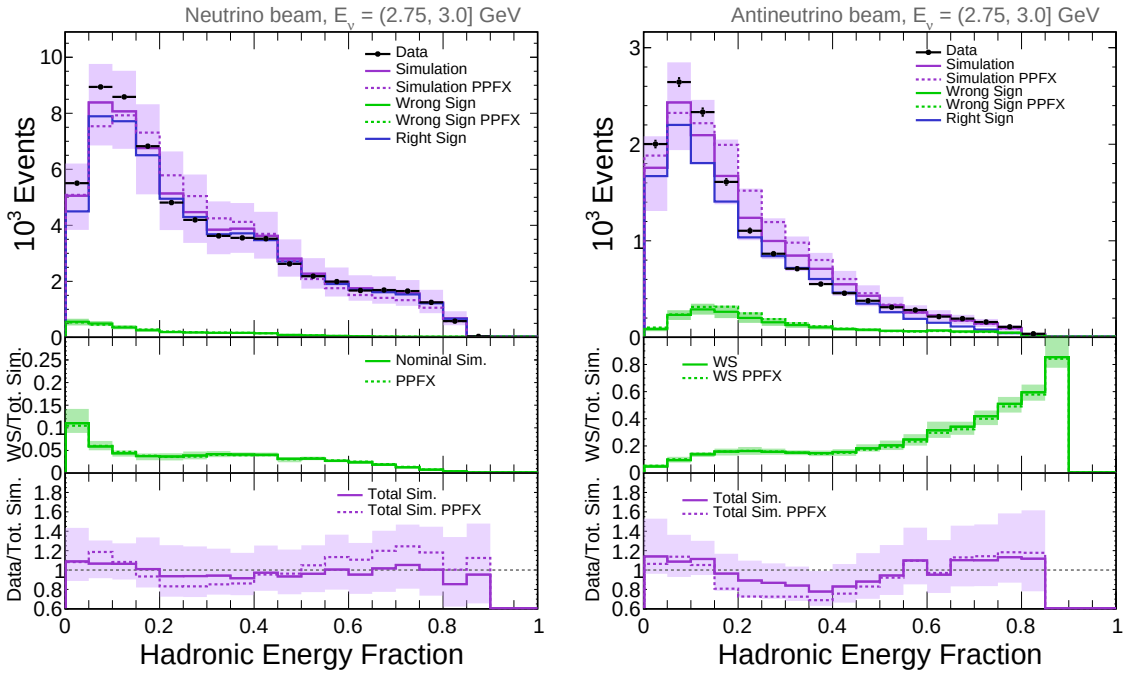


**Figure E.17:** 16th bin of reconstructed $\nu$ and $\bar{\nu}$ energy.

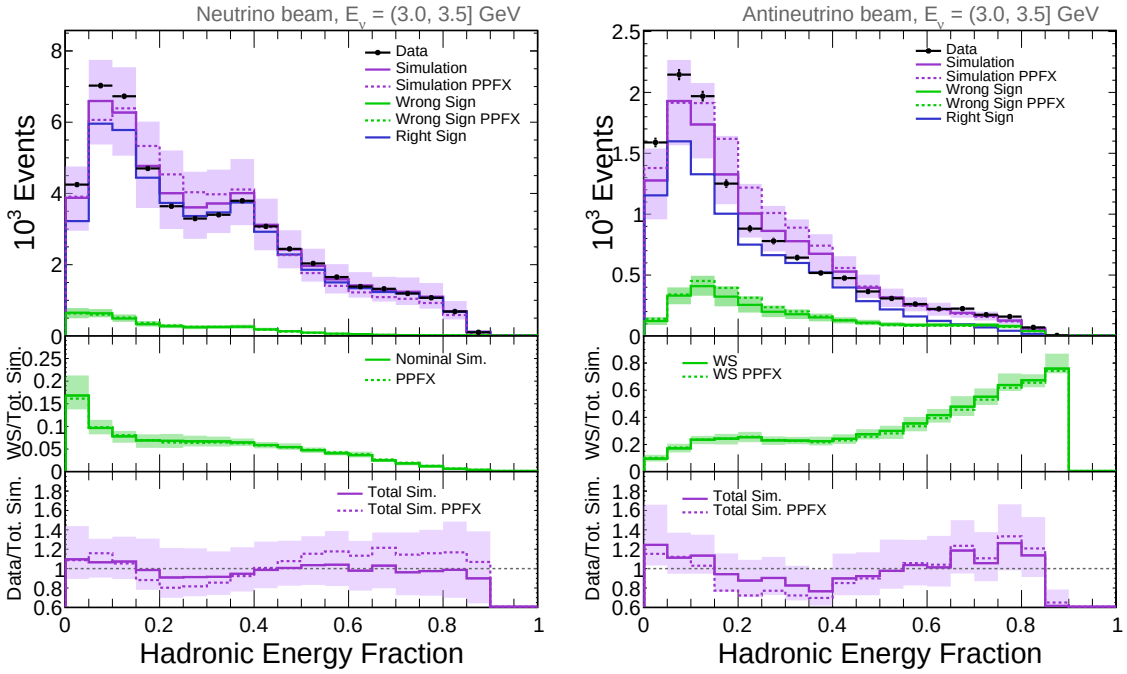


**Figure E.18:** 17th bin of reconstructed $\nu$ and $\bar{\nu}$ energy.

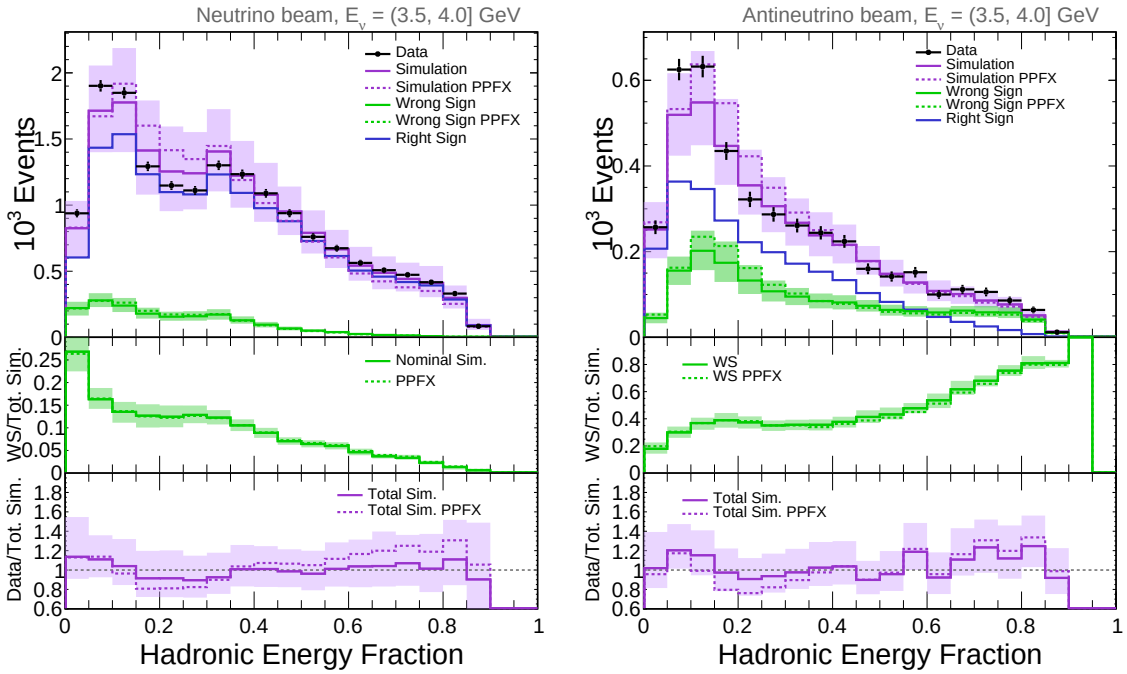


**Figure E.19:** 18th bin of reconstructed $\nu$ and $\bar{\nu}$ energy.

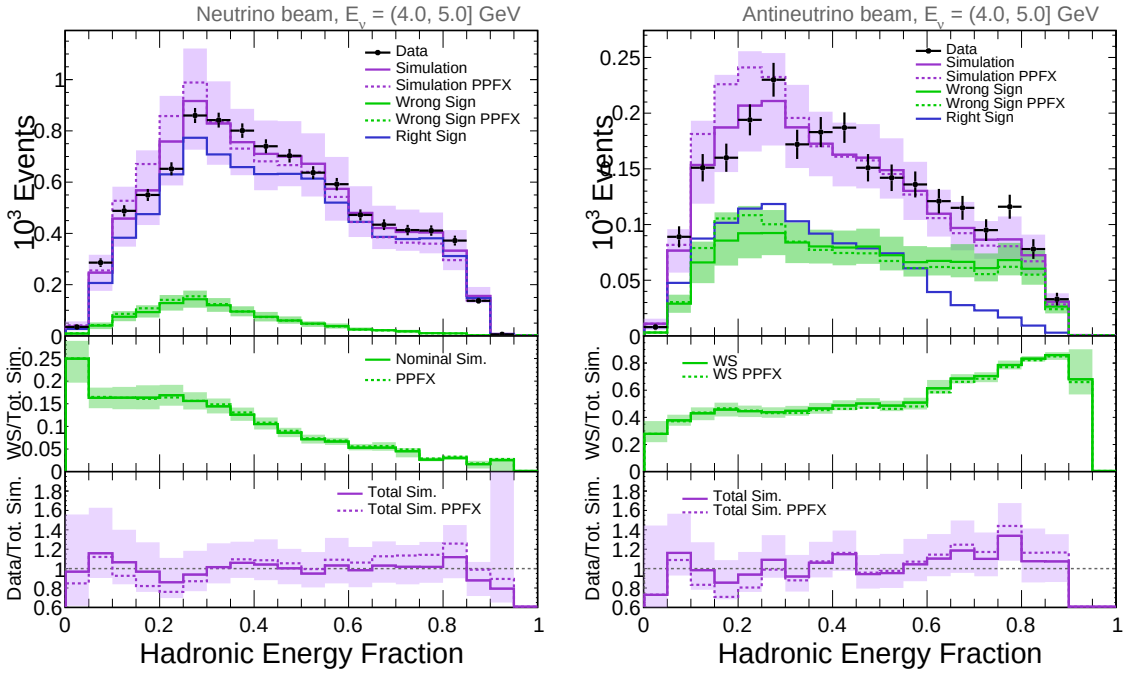


**Figure E.20:** 19th bin of reconstructed $\nu$ and $\bar{\nu}$ energy.

# Acronyms

**2p2h** 2 protons-2 holes

**ADC** Analog Digital Converter

**APD** Avalanche Photo-diode

**ASIC** Application Specific Integrated Circuit

**BDT** Boosted Decision Tree

**Booster** Fermilab's syncrotron accelerator

**CAF** Common Analysis Format

**CAFAna** Common Analysis Format Analysis

**CC** Charged Current

**CL** Confidence Level

**CNN** Convolutional Neural Network

**CRY** Cosmic-ray Shower Library

**CVN** Convolutional Visual Network

**DAQ** Data Acquisition

**DCM** Data Concentrator Module

**DIS** Deep Inelastic Scattering

**ES** Elastic Scattering

**FD** Far Detector

**FEB** Front End Board

**Fermilab** Fermi National Accelerator Laboratory

**FHC** Forward Horn Current

**FLSHits** Fibre Liquid Scintillator Hits

**FOM** Figure of Merit

**FPGA** Field Programmable Gate Array

**FSI** Final State Interaction

**kNN** k-Nearest Neighbour

**LINAC** Linear Accelerator

**MEC** Meson Exchange Current

**MI** Main Injector

**MTU** Master Timing Unit

**NC** Neutral Current

**ND** Near Detector

**NDOS** Near Detector On Surface

**NOvA** NuMI Off-Axis $\nu_e$ Appearance

**NuMI** Neutrinos at the Main Injector

**PC** Principle Component

**PCA** Principle Component Analysis

**PE** Photo-Electron

**PID** Particle Identifier

**POT** Protons On Target

**PPFX** Package to Predict the Flux

**PVC** Polyvinyl Chloride

**QE** Quasi-elastic

**ReMId** Reconstructed Muon Identification

**RES** Resonance

**RHC** Reversed Horn Current

**RPA** Random Phase Approximation

**SSM** Standard Solar Model

**TDR** Technical Design Report

**TDU** Timing Distribution Unit

**TEC** Thermoelectric Cooler

**W** Final state hadronic mass

**WLS** Wavelength Shifting

# Bibliography


[1] J. Chadwick, "The intensity distribution in the magnetic spectrum of beta particles from radium (B + C)," *Verh. Phys. Gesell.*, vol. 16, pp. 383–391, 1914.

[2] W. Pauli, "Open letter to the physicists at the Gauverein meeting in Tubingen," 1930.

[3] E. Fermi, "Versuch einer theorie der beta-strahlen," *Zeitschrift für Physik*, vol. 88, no. 161, 1934.

[4] J. Chadwick, "Possible Existence of a Neutron," *Nature*, vol. 129, p. 312, 1932.

[5] H. Bethe and R. Peierls, "The 'neutrino'," *Nature*, vol. 133, p. 532, 1934.

[6] C. L. Cowan, F. Reines, F. B. Harrison, H. W. Kruse, and A. D. McGuire, "Detection of the free neutrino: A Confirmation," *Science*, vol. 124, pp. 103–104, 1956.

[7] G. Danby, J. M. Gaillard, K. A. Goulianos, L. M. Lederman, N. B. Mistry, M. Schwartz, and J. Steinberger, "Observation of High-Energy Neutrino Reactions and the Existence of Two Kinds of Neutrinos," *Phys. Rev. Lett.*, vol. 9, pp. 36–44, 1962.

[8] R. Davis, Jr., "Attempt to detect the antineutrinos from a nuclear reactor by the Cl37(anti-nu,e-) A37 reaction," *Phys. Rev.*, vol. 97, pp. 766–769, 1955.

[9] M. L. Perl *et al.*, "Evidence for Anomalous Lepton Production in e+ - e- Annihilation," *Phys. Rev. Lett.*, vol. 35, pp. 1489–1492, 1975.

[10] S. Abachi *et al.*, "Observation of the top quark," *Phys. Rev. Lett.*, vol. 74, pp. 2632–2637, 1995.

[11] F. Abe *et al.*, "Observation of top quark production in $\bar{p}p$ collisions," *Phys. Rev. Lett.*, vol. 74, pp. 2626–2631, 1995.

[12] K. Kodama *et al.*, "Observation of tau neutrino interactions," *Phys. Lett.*, vol. B504, pp. 218–224, 2001.

[13] B. Pontecorvo, "Neutrino Experiments and the Problem of Conservation of Leptonic Charge," *Sov. Phys. JETP*, vol. 26, pp. 984–988, 1968. [Zh. Eksp. Teor. Fiz.53,1717(1967)].

[14] Z. Maki, M. Nakagawa, and S. Sakata, "Remarks on the unified model of elementary particles," *Prog. Theor. Phys.*, vol. 28, pp. 870–880, 1962.

[15] R. Davis, Jr., D. S. Harmer, and K. C. Hoffman, "Search for neutrinos from the sun," *Phys. Rev. Lett.*, vol. 20, pp. 1205–1209, 1968.

[16] W. Hampel *et al.*, "GALLEX solar neutrino observations: Results for GALLEX IV," *Phys. Lett.*, vol. B447, pp. 127–133, 1999.

[17] M. Altmann *et al.*, "Complete results for five years of GNO solar neutrino observations," *Phys. Lett.*, vol. B616, pp. 174–190, 2005.

[18] J. N. Abdurashitov *et al.*, "Measurement of the solar neutrino capture rate with gallium metal. III: Results for the 2002–2007 data-taking period," *Phys. Rev.*, vol. C80, p. 015807, 2009.

[19] Y. Fukuda *et al.*, "Evidence for oscillation of atmospheric neutrinos," *Phys. Rev. Lett.*, vol. 81, pp. 1562–1567, 1998.

[20] Y. Fukuda *et al.*, "Measurement of the flux and zenith angle distribution of upward through going muons by Super-Kamiokande," *Phys. Rev. Lett.*, vol. 82, pp. 2644–2648, 1999.

[21] Q. R. Ahmad *et al.*, "Direct evidence for neutrino flavor transformation from neutral current interactions in the Sudbury Neutrino Observatory," *Phys. Rev. Lett.*, vol. 89, p. 011301, 2002.

[22] T. N. Prize, "The Nobel Prize in Physics 2015." `https://www.nobelprize.org/prizes/physics/2015/press-release/`.

[23] E. Catano Mur, *Constraints on neutrino oscillation parameters with the NOvA experiment.* PhD thesis, Iowa State University, 2018.

[24] G. K. Kafka, *A Search for Sterile Neutrinos at the NO$\nu$A Far Detector.* PhD thesis, Harvard University, 2016.

[25] P. Hernandez, "Neutrino Physics," in *Proceedings, 8th CERN Latin-American School of High-Energy Physics (CLASHEP2015): Ibarra, Ecuador, March 05-17, 2015*, pp. 85–142, 2016.

[26] C. Patrignani *et al.*, "Review of Particle Physics," *Chin. Phys.*, vol. C40, no. 10, p. 100001, 2016.

[27] L. Wolfenstein, "Neutrino Oscillations in Matter," *Phys. Rev.*, vol. D17, pp. 2369–2374, 1978.

[28] S. P. Mikheyev and A. Yu. Smirnov, "Resonance Amplification of Oscillations in Matter and Spectroscopy of Solar Neutrinos," *Sov. J. Nucl. Phys.*, vol. 42, pp. 913–917, 1985.

[29] E. D. Niner, *Observation of Electron Neutrino Appearance in the NuMI Beam with the NOvA Experiment.* PhD thesis, Indiana University, 2015.

[30] C. Giunti, C. W. Kim, and M. Monteno, "Atmospheric neutrino oscillations with three neutrinos and a mass hierarchy," *Nucl. Phys.*, vol. B521, pp. 3–36, 1998.

[31] I. Esteban, M. C. Gonzalez-Garcia, A. Hernandez-Cabezudo, M. Maltoni, and T. Schwetz, "Global analysis of three-flavour neutrino oscillations: synergies and tensions in the determination of $\theta_{23}, \delta_{CP}$, and the mass ordering," *JHEP*, vol. 01, p. 106, 2019.

[32] Y. Abe *et al.*, "Indication of Reactor $\bar{\nu}_e$ Disappearance in the Double Chooz Experiment," *Phys. Rev. Lett.*, vol. 108, p. 131801, 2012.

[33] F. P. An *et al.*, "Observation of electron-antineutrino disappearance at Daya Bay," *Phys. Rev. Lett.*, vol. 108, p. 171803, 2012.

[34] J. K. Ahn *et al.*, "Observation of Reactor Electron Antineutrino Disappearance in the RENO Experiment," *Phys. Rev. Lett.*, vol. 108, p. 191802, 2012.

[35] D. Adey *et al.*, "Measurement of the Electron Antineutrino Oscillation with 1958 Days of Operation at Daya Bay," *Phys. Rev. Lett.*, vol. 121, no. 24, p. 241805, 2018.

[36] F. P. An *et al.*, "New Measurement of Antineutrino Oscillation with the Full Detector Configuration at Daya Bay," *Phys. Rev. Lett.*, vol. 115, no. 11, p. 111802, 2015.

[37] N. 2018, "XXVII International Conference on Neutrino Physics and Astrophysics." `https://www.mpi-hd.mpg.de/nu2018/`.

[38] G. Bak *et al.*, "Measurement of Reactor Antineutrino Oscillation Amplitude and Frequency at RENO," *Phys. Rev. Lett.*, vol. 121, no. 20, p. 201801, 2018.

[39] C. Buck, "New Resuslts from the Double Chooz Experiment." `https://doi.org/10.5281/zenodo.1286844`. Talk at XXVIII International Conference on Neutrino Physics and Astrophysics, 4-9 June 2018, Heidelberg, Germany.

[40] K. Abe *et al.*, "Measurements of neutrino oscillation in appearance and disappearance channels by the T2K experiment with $6.6\times10^{20}$ protons on target," *Phys. Rev.*, vol. D91, no. 7, p. 072010, 2015.

[41] K. Abe *et al.*, "Measurement of neutrino and antineutrino oscillations by the T2K experiment including a new additional sample of $\nu_e$ interactions at the far detector," *Phys. Rev.*, vol. D96, no. 9, p. 092006, 2017. [Erratum: Phys. Rev.D98,no.1,019902(2018)].

[42] S. Andringa *et al.*, "Current Status and Future Prospects of the SNO+ Experiment," *Adv. High Energy Phys.*, vol. 2016, p. 6194250, 2016.

[43] M. Altmann *et al.*, "Complete results for five years of GNO solar neutrino observations," *Phys. Lett.*, vol. B616, pp. 174–190, 2005.

[44] J. N. Abdurashitov *et al.*, "Measurement of the solar neutrino capture rate with gallium metal. III: Results for the 2002–2007 data-taking period," *Phys. Rev.*, vol. C80, p. 015807, 2009.

[45] M. Agostini *et al.*, "Comprehensive measurement of pp-chain solar neutrinos," *Nature*, vol. 562, no. 7728, 2018.

[46] M. Ikeda, "Superkamiokande (Solar)." https://doi.org/10.5281/zenodo.1286858. Talk at XXVIII International Conference on Neutrino Physics and Astrophysics, 4-9 June 2018, Heidelberg, Germany.

[47] K. Abe *et al.*, "Search for CP Violation in Neutrino and Antineutrino Oscillations by the T2K Experiment with $2.2 \times 10^{21}$ Protons on Target," *Phys. Rev. Lett.*, vol. 121, no. 17, p. 171802, 2018.

[48] M. H. Ahn *et al.*, "Measurement of Neutrino Oscillation by the K2K Experiment," *Phys. Rev.*, vol. D74, p. 072003, 2006.

[49] M. G. Aartsen *et al.*, "Measurement of Atmospheric Neutrino Oscillations at 656 GeV with IceCube DeepCore," *Phys. Rev. Lett.*, vol. 120, no. 7, p. 071801, 2018.

[50] A. Aurisano, "Recent results from MINOS and MINOS+." https://doi.org/10.5281/zenodo.1286759, 2018. Talk at XXVIII International Conference on Neutrino Physics and Astrophysics, 4-9 June 2018, Heidelberg, Germany.

[51] K. Abe *et al.*, "Atmospheric neutrino oscillation analysis with external constraints in Super-Kamiokande I-IV," *Phys. Rev.*, vol. D97, no. 7, p. 072001, 2018.

[52] B. Abi *et al.*, "The DUNE Far Detector Interim Design Report Volume 1: Physics, Technology and Strategies," 2018. arXiv:1807.10334, FERMILAB-DESIGN-2018-02.

[53] E. Worcester, "DUNE: Status and Science." https://doi.org/10.5281/zenodo.1286763. Talk at XXVIII International Conference on Neutrino Physics and Astrophysics, 4-9 June 2018, Heidelberg, Germany.

[54] M. Shiozawa, "Hyper-Kamiokande." https://doi.org/10.5281/zenodo.1286767. Talk at XXVIII International Conference on Neutrino Physics and Astrophysics, 4-9 June 2018, Heidelberg, Germany.

[55] M. Sanchez, "NOvA Results and Prospects." https://doi.org/10.5281/zenodo.1286757. Talk at XXVIII International Conference on Neutrino Physics and Astrophysics, 4-9 June 2018, Heidelberg, Germany.

[56] P. Adamson *et al.*, "Measurement of Neutrino and Antineutrino Oscillations Using Beam and Atmospheric Data in MINOS," *Phys. Rev. Lett.*, vol. 110, no. 25, p. 251801, 2013.

[57] K. Abe *et al.*, "Updated T2K measurements of muon neutrino and antineutrino disappearance using $1.5{\times}10^{21}$ protons on target," *Phys. Rev.*, vol. D96, no. 1, p. 011102, 2017.

[58] D. S. Ayres *et al.*, "The NOvA Technical Design Report," 2007. doi:10.2172/935497, FERMILAB-DESIGN-2007-01.

[59] P. Adamson *et al.*, "The NuMI Neutrino Beam," *Nucl. Instrum. Meth.*, vol. A806, pp. 279–306, 2016.

[60] "Fermilab Creative Services." `http://vms.fnal.gov/index/vms-home`.

[61] P. Adamson *et al.*, "NOvA Official Plots Database." `https://nusoft.fnal.gov/nova/blessedplots/`.

[62] J.-M. Levy, "Kinematics of an off axis neutrino beam," 2010. arXiv:1005.0574.

[63] S. Mufson *et al.*, "Liquid scintillator production for the NOvA experiment," *Nucl. Instrum. Meth.*, vol. A799, pp. 1–9, 2015.

[64] K. Sachdev, *Muon Neutrino to Electron Neutrino Oscillation in NOνA*. PhD thesis, Minnesota University, 2015.

[65] F. Psihas, *Measurement of Long Baseline Neutrino Oscillations and Improvements from Deep Learning*. PhD thesis, Indiana University, 2018.

[66] P. Antonioli *et al.*, "SNEWS: The Supernova Early Warning System," *New J. Phys.*, vol. 6, p. 114, 2004.

[67] "NOvA FD timing peak monitoring." `http://nusoft.fnal.gov/nova/timing/index.html`.

[68] D. P. Mendez Mendez, "FD time peak technical note," *Internal Document NOvA DocDB 23585*, September 2017.

[69] S. Agostinelli *et al.*, "GEANT4: A Simulation toolkit," *Nucl. Instrum. Meth.*, vol. A506, pp. 250–303, 2003.

[70] Fermilab, "G4NuMI." `https://cdcvs.fnal.gov/redmine/projects/numi-beam-sim/wiki/G4numi`.

[71] L. Aliaga *et al.*, "Neutrino Flux Predictions for the NuMI Beam," *Phys. Rev.*, vol. D94, no. 9, p. 092005, 2016. [Addendum: Phys. Rev.D95,no.3,039903(2017)].

[72] "GENIE Event Generator & Global Analysis of Neutrino Scattering Data." `http://www.genie-mc.org/`.

[73] R. Gran, "Model Uncertainties for Valencia RPA Effect for MINERvA," 2017. arXiv:1705.02932, FERMILAB-FN-1030-ND.

[74] C. Hagmann *et al.*, "Cosmic-ray Shower Library." `https://nuclear.llnl.gov/simulation/main.html`.

[75] C. Backhouse, "The CAFAna framework," *Internal Document NOvA DocDB 9222*, November 2014. `https://cdcvs.fnal.gov/redmine/projects/novaart/wiki/CAFAna_overview`.

[76] "ROOT Data Analysis Framework." `http://root.cern`.

[77] F. James and M. Roos, "Minuit: A System for Function Minimization and Analysis of the Parameter Errors and Correlations," *Comput. Phys. Commun.*, vol. 10, pp. 343–367, 1975.

[78] M. D. Baird, "A Side By Side Comparison of Slicer, Cosmic Slicer, and Slicer4D," *Internal Document NOvA DocDB 9195*, May 2013.

[79] M. D. Baird, *An Analysis of Muon Neutrino Disappearance from the NuMI Beam Using an Optimal Track Fitter*. PhD thesis, Indiana University, 2015.

[80] N. Raddatz, "KalmanTrack Technical Note," *Internal Document NOvA DocDB 13545*, June 2015.

[81] K. Rudolf, "A New Approach to Linear Filtering and Prediction Problems," *Journal of Basic Engineering*, no. 82, pp. 35–45, 1960.

[82] B. Rebel, "Window Tracking Algorithm for Cosmic Ray Muons," *Internal Document NOvA DocDB 15977*, August 2016.

[83] C. Backhouse and A. Radovic, "The Attenuation and Threhold Correction of the NOvA detectors," *Internal Document NOvA DocDB 13579*, June 2015.

[84] D. P. Mendez Mendez, "SA Energy Scale Calibration," *Internal Document NOvA DocDB 27467*, June 2016.

[85] J. Muser and L. Suter, "Second Analysis Data Quality Summary ," *Internal Document NOvA DocDB 15307*, April 2016.

[86] S. Lein, "DCM Edge Metric ," *Internal Document NOvA DocDB 13527*, June 2015.

[87] L. Goodenough and S. Phan-Budd, "Technical Note on the NOvA Beam Monitoring for 2015 Summer Analysis ," *Internal Document NOvA DocDB 13572*, July 2015.

[88] K. Bays, "NOvA Cosmic Rejection package and algorithms technical note," *Internal Document NOvA DocDB 11205*, September 2017.

[89] A. Aurisano, A. Radovic, D. Rocco, A. Himmel, M. Messier, E. Niner, G. Pawloski, F. Psihas, A. Sousa, and P. Vahle, "A convolutional neural network neutrino event classifier," *Journal of Instrumentation*, vol. 11, pp. P09001–P09001, September 2016.

[90] C. Szegedy, W. Liu, Y. Jia, P. Sermanet, S. Reed, D. Anguelov, D. Erhan, V. Vanhoucke, and A. Rabinovich, "Going deeper with convolutions," September 2014. arXiv:1409.4842v1.

[91] K. Bays, "NOvA 2018 numu analysis cosmic background estimation tech note," *Internal Document NOvA DocDB 27878*, March 2018.

[92] G. Davies *et al.*, "CVN 2018 Technical Note," *Internal Document NOvA DocDB 27467*, April 2018.

[93] N. Raddatz, "Reconstructed Muon Identification," *Internal Document NOvA DocDB 11206*, May 2014.

[94] N. J. Raddatz, *Measurement of Muon Neutrino Disappearance with Non-Fiducial Interactions in the NO$\nu$A Experiment*. PhD thesis, Minnesota University, 2016.

[95] L. Vinton, *Measurement of Muon Neutrino Disappearance with the NOvA Experiment*. PhD thesis, Sussex University, 2018.

[96] N. Nayak, "Flux systematics for the 2018 nova oscillation analyses," *Internal Document NOvA DocDB 27884*, April 2018.

[97] C. Backhouse and A. Himmel, "Overview of the 2018 NOvA $\nu_e + \bar{\nu}_e$ appearance analysis," *Internal Document NOvA DocDB 26699*, May 2018.

[98] N. Agafonova *et al.*, "Final Results of the OPERA Experiment on $\nu_\tau$ Appearance in the CNGS Neutrino Beam," *Phys. Rev. Lett.*, vol. 120, no. 21, p. 211801, 2018. [Erratum: Phys. Rev. Lett.121,no.13,139901(2018)].

[99] M. Groh, "Genie Systematics for the 2018 Oscillation Analyses using PCA," *Internal Document NOvA DocDB 27914*, April 2018.

[100] A. Aurisano, "Tech Note: 2017 Light Model," *Internal Document NOvA DocDB 23228*, September 2017.

[101] R. Nichol and B. Zamorano, "Tech note: Calibration executive summary," *Internal Document NOvA DocDB 23558*, September 2017.

[102] T. Alion, "Absolute Calibration and Shape Systematics for 3A," *Internal Document NOvA DocDB 20318*, June 2017.

[103] M. Strait, S. Bending, K. Kephart, and P. Lukens, "NOvA muon energy scale systematic," 2019. arXiv:1902.02805, FERMILAB-FN-1061-ND.

[104] J. Hartnell and A. Radovic, "Summary of the 2018 FHC+RHC $\nu_\mu$ Disappearance Analysis," *Internal Document NOvA DocDB 26702*, March 2018.

[105] T. Alion, "Data-MC Differences in Normalization," *Internal Document NOvA DocDB 27821*, May 2018.

[106] M. Strait, "Tech note on using neutrons to find RHC numu contamination," *Internal Document NOvA DocDB 22955*, May 2018.

[107] S. Baker and R. D. Cousins, "Clarification of the Use of Chi Square and Likelihood Functions in Fits to Histograms," *Nucl. Instrum. Meth.*, vol. 221, pp. 437–442, 1984.

[108] A. Radovic, "Oscillation Parameters for First NOvA Analyses," *Internal Document NOvA DocDB 13640*.

[109] M. Baird and L. Vinton, "Extrapolation Technote for the Numu Third Analysis," *Internal Document NOvA DocDB 23390*, September 2017.

[110] M. A. Acero *et al.*, "First measurement of neutrino oscillation parameters using neutrinos and antineutrinos by NOvA," 2019.

[111] F. An *et al.*, "Neutrino Physics with JUNO," *J. Phys.*, vol. G43, no. 3, p. 030401, 2016.

[112] K. Abe *et al.*, "Hyper-Kamiokande Design Report," 2018. arXiv:1805.04163.

[113] J. Lozier, "ModularExtrap Technical Note," *Internal Document NOvA DocDB 12563*, December 2014.

[114] J. A. Sepulveda-Quiroz, *Measurement of the Kaon Production Normalization in the NuMI Target Using Uncontained Charged-Current Muon Neutrino Interactions in the NOvA Far Detector*. PhD thesis, Iowa State University, 2018.

[115] X. Qian and J.-C. Peng, "Physics with Reactor Neutrinos," *Rept. Prog. Phys.*, vol. 82, no. 3, p. 036201, 2019.